

**Grain scale processes in fault rock -
a comparison between
experimental and natural deformation.**

Inauguraldissertation

zur
Erlangung der Würde eines Doktors der Philosophie
vorgelegt der
Philosophisch-Naturwissenschaftlichen Fakultät
der Universität Basel

von

Nynke Thera Keulen

aus Leeuwarden (Niederlande)

Basel, December 2006

Genehmigt von der Philosophisch-Naturwissenschaftlichen Fakultät auf Antrag von:

Prof. Dr. R. Heilbronner
(Dissertationsleiterin)

Dr. A.-M. Boullier, directeur de recherche
(Korreferentin)

PD Dr. H. Stünitz
(Experte)

Basel, den 19. Dezember 2006

Prof. Dr. Hans-Peter Hauri
Dekan der Philosophisch-
Naturwissenschaftlichen Fakultät

Contents

1	Introduction	3
1.1	General aspects of fault-related rocks	4
1.2	Deformation experiments and natural fault rock	5
1.3	Aim and key issues of the thesis	7
1.4	Layout of the thesis	8
2	Experimental techniques	11
2.1	Sample assembly	12
2.1.1	Sample and pistons	12
2.1.2	Confining pressure medium and temperature measurement	14
2.1.3	Internal heating system	16
2.2	Deformation experiments	18
2.2.1	Deformation apparatus	18
2.2.2	Experimental procedure	18
2.3	Processing of the experimental data	21
2.3.1	Data correction	21
2.3.2	Final displacement measurements	22
3	Grain size and grain shape analysis of fault rocks	25
3.1	Introduction	26
3.2	Fault rock microstructures	28
3.2.1	Deformation experiments	28
3.2.2	Preparation of images for digital image analysis	29
3.2.3	Terminology	31
3.3	Analytical methods	31
3.3.1	Grain size analysis	31

3.3.2	<i>D</i> -mapping	33
3.3.3	Shape analysis	36
3.3.4	Program “ishapes”	36
3.3.5	Shape analysis using automatically digitized outlines	38
3.4	Analysis of experimental fault rock	42
3.5	Discussion	44
3.5.1	The nature of the grain size distribution	44
3.5.2	<i>D</i> -mapping	48
3.5.3	Shape factors	49
3.6	Conclusions	52
4	Grain size distribution of experimental and natural fault rock	57
4.1	Introduction	58
4.1.1	Overview	58
4.1.2	Fault rocks	59
4.1.3	Grain size distributions	59
4.2	Materials and methods	62
4.2.1	Description of samples	62
4.2.2	Rock deformation experiments	64
4.2.3	Grain size analysis	65
4.3	Results	68
4.3.1	Mechanical data	68
4.3.2	Faulted samples	69
4.3.3	Microstructures	72
4.3.4	Grain size analysis of experimental fault rocks	72
4.3.5	Grain size analysis of natural fault rocks	77
4.3.6	Characteristics of GSDs	77
4.4	Discussion	78
4.4.1	Faulting experiments	78
4.4.2	Grain size distributions obtained in experiments	81
4.4.3	Cracked material and gouge	82
4.4.4	Natural fault rock	83
4.4.5	Surface densities of fault rocks	83
4.4.6	Grinding limit	85
4.4.7	Fractal dimension	86
4.5	Conclusions	87

5	Healing microstructures of experimental and natural fault gouge	89
5.1	Introduction	90
5.2	Experimental procedure	91
5.2.1	Samples	91
5.2.2	Experiments	92
5.2.3	Analytical techniques	94
5.3	Results	95
5.3.1	Microstructures of experimental fault rock	95
5.3.2	Natural fault rock	102
5.3.3	An exponential decay law to describe the progress of healing under hydrostatic conditions.	108
5.4	Discussion	110
5.4.1	Healing of fault gouge	110
5.4.2	A hydrostatic healing law for fault gouge	111
5.4.3	Reactivation of fault zones	113
5.4.4	Healing under non-hydrostatic conditions	114
5.5	Conclusions	115
6	Grain scale processes in basalts	117
6.1	Introduction	118
6.2	Experiments	119
6.2.1	Sample material	119
6.2.2	Experimental procedure	121
6.2.3	Experimental results	123
6.3	Microstructural analysis	123
6.3.1	Light microscopy	125
6.3.2	Method of ACF analysis	125
6.3.3	Results of ACF analysis	128
6.3.4	Development of fault zones	131
6.3.5	Grain size analysis	133
6.4	Chemical analysis	136
6.4.1	Reaction within the samples	136
6.4.2	Healing of the samples	139
6.5	Discussion	140
6.5.1	Strength of the basalt samples	140
6.5.2	Mineral reactions in basalt samples	143

6.5.3	Comparison between basalt and granite deformation	144
6.5.4	Implications for the deformation of basalts in nature	145
6.6	Conclusions	146
7	Conclusions	147
7.1	Summary and conclusions	148
7.2	Suggestions for further research	152
A	List of all experiments	155
B	Mechanical data	161
C	Experiments on salt samples	173
C.1	Preparation of the salt samples	174
C.2	Salt experiments	175
C.3	Correction of the mechanical data for friction	179
D	Structural evolution of the Nojima fault	181
D.1	Introduction	182
D.2	The Geodynamic Context of the Nojima Fault	182
D.3	Microstructural Studies of the Fault Rocks	184
D.3.1	Low strain rocks	184
D.3.2	Pseudotachylytes	186
D.3.3	Hydrothermal alteration	187
D.3.4	The latest events: thin fault gouge zones	190
D.4	Remaining Questions and Conclusions	192
E	Setting and structures of the sample localities	195
E.1	Black Forest	196
E.2	Orobic Thrust	204
F	EDX data of basalt samples	213

List of Figures

2.1	Scaled drawing of assembly	13
2.2	Outer salt liners	15
2.3	Overview of sample, pistons, inner salt liners and furnace	16
2.4	Example of a chart-record	17
2.5	Pressure-temperature-time paths for an average experiment	19
2.6	Pure shear and simple shear corrected stress data	22
2.7	Final displacement measurement	23
2.8	Measurements of final shortening	24
3.1	Mechanical data of experimentally deformed granite	28
3.2	Microstructures attained during progressive faulting	30
3.3	Grain size distribution and matrix content of fault rocks	32
3.4	D -mapping of fault rock	35
3.5	Concept of outlines, convex envelopes and angles	37
3.6	Effect of reducing the number of boundary coordinates	39
3.7	Shape analysis of fault rock	41
3.8	Microstructures of experimentally produced fault rocks	43
3.9	Grain size distribution of experimentally produced fault rocks	44
3.10	D -mapping of experimentally deformed quartz	45
3.11	D -mapping at the scale of a sample	46
3.12	Comparative shape analysis of experimentally faulted granite	50
3.13	Shape analysis at different magnifications	51
3.14	Derivation of matrix density as function of fractal dimension	54
4.1	Starting material for experiments and natural fault rocks	63

4.2	Schematics of the procedure for grain size analysis	66
4.3	Mechanical data of deformation of Verzasca Gneiss	68
4.4	Maps of local variations of grain size distribution.	70
4.5	Microstructures of experimentally deformed samples of Verzasca Gneiss	70
4.6	Grain size distribution of experimentally deformed Verzasca Gneiss	73
4.7	D -values of the gouge plotted against magnification of analyzed images	75
4.8	Grain size distribution and D -values of the Nojima Fault Zone	78
4.9	Micrographs of the smallest grains found in gouge	79
4.10	Grain size at the slope change in the GSD	80
5.1	Grain size distribution of quartz fault gouge after deformation	95
5.2	BSE-micrographs showing hydrostatic healing of feldspar and quartz	97
5.3	Grain size distribution and $D_{>}$ -values of the fault gouge	98
5.4	Experiments with non-hydrostatic healing after deformation	99
5.5	Cathodoluminescence and BSE contrast SEM micrographs of fault gouge	100
5.6	$D_{>}$ -values as a function of axial shortening rate during deformation and healing	102
5.7	Mechanical data and micrographs for samples deformed at a low strain rate	103
5.8	Mechanical data of deformation-healing-deformation experiments	103
5.9	Microstructures of deformation-healing-deformation experiment	104
5.10	Microstructures of natural fault gouge	104
5.11	Hydrostatic healing law for fault gouge	109
6.1	BSE micrographs of undeformed basalt	120
6.2	Mechanical data for the deformation of basalt	124
6.3	Light micrographs of basalt in cross-polarized light	126
6.4	Procedure for ACF analysis	127
6.5	ACF-tiles for plagioclase	129
6.6	Preferred orientation and anisotropy of ACF-tiles	130
6.7	Micrographs showing the development of fault zones in Vogelsberg Basalt	132
6.8	Characteristic micrographs of deformed and healed samples	134
6.9	Grain size distribution of Maryland Diabase	135
6.10	Evidence of reaction in deformed basalt samples	137
6.11	ACF-diagrams of basalt	138
B.1	Mechanical data for deformation of Verzasca Gneiss I	162
B.2	Mechanical data for deformation of Verzasca Gneiss II	163

B.3	Mechanical data for deformation of Verzasca Gneiss III	164
B.4	Mechanical data for deformation of Verzasca Gneiss IV	165
B.5	Mechanical data for deformation of Verzasca Gneiss V	166
B.6	Mechanical data for deformation of Verzasca Gneiss VI	167
B.7	Mechanical data for deformation of Verzasca Gneiss VII	168
B.8	Mechanical data for deformation of basalt I	169
B.9	Mechanical data for deformation of basalt II	170
B.10	Mechanical data for deformation of basalt III	171
C.1	Set-up for the creation of salt samples	174
C.2	Examples of salt samples in gold jacket after deformation	176
C.3	Mechanical data for experiments on NaCl samples	177
C.4	Peak strength of salt samples compared to wet halite	178
C.5	BSE-micrograph of salt	179
C.6	Run-in curve before the hit-point	180
D.1	Tectonic framework of Japan and Hyogo-ken Nanbu earthquake epicenter	183
D.2	Geological map of the Awaji Island and sketch of the Hirabayashi borehole	184
D.3	Microphotograph of shortened cleavages in biotite	185
D.4	Histogram of the orientation of shortened biotite cleavage planes	185
D.5	Isochoric lines calculated from fluid inclusions in pseudotachylytes	186
D.6	Textural features in laumontite veins	189
D.7	Textural features in carbonate veins	189
D.8	Grain size distribution obtained from SEM-images of thin sections of fractured rocks	191
E.1	Geological map of the southwestern Black Forest	196
E.2	Geological map of the area around the village Wehr	198
E.3	Localities sampled along the Kandern Fault Zone	199
E.4	Outcrop and sample photographs of the Wehratal and Kandern Fault zone	200
E.5	Micrographs of structures from the Wehratal Fault zone and the Kandern Fault zone	202
E.6	Sample localities and field observation on the Orobic Thrust	205
E.7	Simplified geological map of Orobic Thrust area	206
E.8	Outcrop photographs of cataclasites from the Orobic Thrust	207
E.9	Simplified geological map of the area near Lago di Pescegallo	209
E.10	Micrographs of structures in the Orobic Thrust	211

List of Tables

3.1	Definitions of measurements and shape factors	33
3.2	Shape factors of manually and automatically digitized outlines of test figures	38
4.1	Published data on grain size analyses of fault rocks	61
4.2	Abbreviations and definitions of measurements	64
4.3	Deformation conditions of the experiments on Verzasca gneiss	65
4.4	D -values for cracked grains and gouge	74
4.5	r_K -values determined from grain size distributions	76
5.1	Deformation and healing experiments performed on Verzasca Gneiss	93
5.2	Measured D -values for natural granitoid fault rocks	107
5.3	Rate of material transfer in granular flow	115
6.1	Deformation and heat treatment experiments on basalt	122
A.2	All deformation experiments performed on Verzasca Granite	158
A.3	All deformation experiments performed on basalt	159
A.4	Dimensions of samples used to calculate the final shortening	160
C.1	Overview of the experiments performed on wet-pressed NaCl samples	175
D.1	Occurrences and features of the hydrothermal minerals in the GSJ drillhole	187
E.1	Thin sections of natural samples	212
F.1	Mineral compositions of Maryland Diabase	214
F.2	Mineral compositions of Bransrode Basalt	215
F.3	Mineral compositions of Vogelsberg Basalt	215

With many thanks to:

Renée Heilbronner, Holger Stünitz, Anne-Marie Boullier, Tjerk Heijboer, Behan & Irma Keulen, Auke Barnhoorn, Alfons Berger, Horst Dresmann, Marcel Düggelin, Florian Füsseis, Sebastian Hinsken, Joelle Glanzmann, Konrad Leu, James MacKenzie, Daniel Mathys, Nils Oesterling, Lidia Pittarello, Karl Ramseyer, Almar de Ronde, Hans-Rüedi Rüegg, Verena Scheuring, Stefan Schmid, Claude Schneider, Chris Spiers, Willy Tschudin, Jan Tullis, Katy Waite

... and many thanks to friends, colleagues and visitors for a good time in Basel.

Abstract

The aim of this study is to identify the processes that play a role in and after the formation of fault rock by investigating their microstructures. We apply these observations to interpret the processes related to faulting in natural rocks. This thesis focusses on (1) the development of analytical methods to quantify the grain size and grain shape of fault rock, (2) the investigation of the microstructures that formed during deformation of the rock with emphasis on the grain size distribution of the fault rock, (3) the effect of time, temperature and strain rate on the microstructures of fine grained gouge in the presence of a fluid, and (4) to compare gouge formed under controlled laboratory conditions with natural gouge.

For these purposes a series of deformation experiments with and without subsequent heat treatment on intact granitoid and basalt rock samples were performed at $T = 300 - 500^\circ\text{C}$, $P_c = 500 \text{ MPa}$, at $\dot{\epsilon} = 3.5 \times 10^{-4} - 1.3 \times 10^{-7} \text{ s}^{-1}$ and with 0.2 wt% H_2O . The heat treatment was performed at $T = 200 - 500^\circ\text{C}$, $P_c = 500 \text{ MPa}$ for 4 hours to 14 days under hydrostatic and non-hydrostatic conditions. Thin sections of the samples were investigated with scanning electron and optical polarization microscopy. The results of the laboratory experiments were compared to three natural granitoid fault systems, (1) the Nojima Fault Zone (Japan), (2) fault zones in the Black Forest (Germany), and (3) the Orobic Thrust (Italian Southern Alps).

The grain shape analysis provides a clear distinction between cracked grains and gouge of quartz and feldspar grains with the following shape descriptors (1): aspect ratio (longest / shortest diameter); cracked quartz (range: 1.0–8.0, average 2.9) has a higher ratio than K-feldspar (range: 1.0–4.0, average 2.1), gouge has a low aspect ratio (range: 1.0–3.0, average 1.5), (2) Paris factor and the deltaA (difference between a shape, perimeter and area, respectively, and its convex envelope); cracked grains yield higher values (range: 0–100%, average: 15% for feldspar and 5% for quartz) than gouge (range: 0–20%, average: 2.5%), and (3) Ω -value (fraction of angles $< 0^\circ$ in a histogram of vertex angles); cracked material reaches higher values (30–40%) than gouge (10–20%).

The grain size distributions (GSD) of the deformed samples are quantified using the D -value (slope of $\log(\text{frequency})-\log(\text{radius})$ of the grain size distribution) for quartz and feldspar gouge. Cracked grains and gouges can be distinguished on the basis of their D -value. For both types of fault rocks two slopes are observed: for grain sizes, r , of $\sim 30 \text{ nm} < r < 2 \mu\text{m}$, $D_{<} \approx 0.9-1.1$ for all fault rock; for $r > 2 \mu\text{m}$, cracked material shows $D_{>} \approx 1.5-1.6$, while gouge has $D_{>} \geq 2.0$ for quartz and feldspar, and $D_{>} = 1.8$ for pyroxene gouge. $D_{>}$ of quartz and feldspar gouge is dependent on the deformation conditions; an increase in the confining pressure or temperature,

or a decrease in the strain rate decreases the $D_{>}$ -value. The grain radius at the slope change ($D_{<}$ to $D_{>}$) corresponds to the grinding limit of quartz and may represent a transition in the dominant comminution mechanism from grinding to attrition and shear. Comminution in faults takes place as a two-stage process: rupturing creates cracked grains; further movement on the fault results in further comminution by wear and attrition. Cracked grains rather than gouge are used to calculate the surface energy density associated with faulting; it follows that this energy is small in comparison to the total amount of energy that is set free during an earthquake.

In deformed partially glassy basalt samples, a low strength has been observed. Samples deformed at $T = 500\text{ }^{\circ}\text{C}$ reach a strength of 0.4 GPa. Deformation occurs by viscous flow of the glass matrix; partially glassy basalt deformed at $T = 300\text{ }^{\circ}\text{C}$ displays a strength of 1.3-1.7 GPa and fully crystalline basalt deformed at $T = 500\text{ }^{\circ}\text{C}$ has a strength of 1.1 GPa. The deformation in the samples took place by cataclasis in narrow fault zones.

Heat treatment after deformation caused healing of the gouge. $D_{>}$ decreases from > 2.0 to 1.5 for quartz and feldspar gouge and from >1.8 to 1.6 for plagioclase and pyroxene in diabase. The time-dependent decrease in $D_{>}$ of quartz and feldspar in granitoid gouge is quantified by $\Delta D = D_{>}(t) - D_f = A \cdot e^{(-\lambda t)}$. Under non-hydrostatic conditions healing is more effective. Fine grained gouge deformed at low axial shortening rates can deform by a combination of cataclasis and diffusive mass-transfer induced healing of grains even at $T = 300 - 500\text{ }^{\circ}\text{C}$.

A small volume of mineral reaction products is observed to be associated with glass inside fine grained gouge zones in partially glassy basalt samples. After heat treatment fully crystalline basalt samples also have mineral reaction products: amphibole and biotite have formed at $T = 500\text{ }^{\circ}\text{C}$ and chlorite, amphibole and albite have formed at $T = 300\text{ }^{\circ}\text{C}$.

The GSDs obtained from deformation experiments are nearly identical to results obtained for the Quaternary deformation on the Nojima Fault Zone ($D_{>} = 2.02$ for gouge and 1.64 for cracked grains; $D_{<} = 0.97$). Healed granitoid gouge of the three investigated fault zones that were active during the Tertiary yield $D_{>} = 1.58-1.62$. $D_{>}$ can be used to compare natural and experimental fault rock directly. Healing occurs only in monomineralic aggregates; polymineralic gouge keeps its high $D_{>}$ -value with time, because grain growth processes are inhibited by the intermixing of mineral phases.

Chapter 1

Introduction

1.1 General aspects of fault-related rocks

Faults are zones of localized deformation in the Earth's crust and upper mantle along which rocks are displaced. Faults occur at all scales from plate boundaries separating continents to millimeter sized fractures. Different techniques are necessary to study the deformation associated to them and the integration of the results of these techniques is not always easy. The formation of faults may be related to earthquakes. However, with GPS large amounts of slip on faults without seismicity have been detected as well. Aseismic movement on fault planes also occur after earthquakes (e.g. Heki et al., 1997; Sheu and Shieh, 2004).

Fault reactivation has been observed on many fault zones, e.g. the Torrey Creek zone (Mitra, 1993), the San Andreas Fault (Chester et al., 1993), the Nojima Fault Zone (e.g. Boullier et al., 2004a), the Orobic Thrust (Carminati and Siletto, 2005) or the Gole Larghe fault (Pennacchioni et al., 2006). As many discrete movement zones have been repeatedly active within the same fault zone, these zones are generally regarded as weak areas within a rock. On a large scale, reactivation occurs in the same zone of a few meters in width and leaves the rest of the rock nearly unaffected. On a smaller scale however, it has been observed that some faults can be strong as a result of the precipitation of quartz, feldspar or epidote (Wibberley, 1999; Mitra and Ismat, 2001; Di Toro and Pennacchioni, 2005). In such fault zones deformation may switch to adjoining weaker rock in the same fault. The recurrence time of fault reactivation has been widely studied in order to forecast earthquakes. Inter-plate boundary fault zones have a recurrence time of ca. 20–300 years (Scholz, 1990; Nadeau and McEvilly, 1999).

Faults close to the Earth's surface generally consist of incohesive rocks; the minerals within the fault zones are chaotically distributed (Sibson, 1977). Faults at greater depths are usually cohesive (Sibson, 1977; Schmid and Handy, 1991) and are composed of foliated rocks (Chester et al., 1985). At even larger depths, fault zones grade to shear zones that consist of foliated mylonitic rocks. Unconsolidated rock is usually named gouge or breccia, whereas their consolidated equivalents are called cataclasites (Sibson, 1977; White, 1982). Schmid and Handy (1991) have pointed out that it is not always clear whether the consolidation occurs syn- or posttectonically. Fault rock that has formed as gouge can appear as cataclasite in an outcrop, which may cause confusion about its formation conditions. For post-tectonically consolidated cataclasites the term “healed gouge” may be less ambiguous.

Changes in the ambient conditions at greater depths cause a change in the deformation behavior of the rock and a transition from brittle faults to mylonitic shear zones. This change in deformation behavior is two-fold: (1) the homogeneity of the deformation may change from localized to distributed deformation and (2) the mechanism changes from microscopic cracking

to intracrystalline plasticity or diffusive mass transfer (Rutter, 1986). The nomenclature of the mode of failure in deformed rocks has frequently resulted in confusion. In this thesis, mainly the classification proposed by Rutter (1986), as summarized below, will be followed:

Ductile deformation is delocalized deformation and the transition from brittle to ductile deformation describes the transition from localized fracturing to distributed microcracking (Paterson, 1978). The amount of localization is strongly dependent on the scale of observation and therefore rocks can deform in a brittle and a ductile manner simultaneously (e.g. Rutter, 1986; Schmid and Handy, 1991). Brittle fracturing is sometimes referred to as cataclasis (from the greek *κατα* (down) and *κλαστος* (broken in pieces)), applying to both localized or delocalized fracturing (Rutter, 1986), but more often the term cataclasis is restricted to delocalized fracturing only, as in this thesis. Distributed microcracking is also called cataclastic flow (Borg et al., 1960; Rutter, 1986; Tullis and Yund, 1987). The terms cataclasis, cataclasite ((syn-)tectonically *cohesive* fault rock) and cataclastic flow (*distributed* microcracking) have often led to misunderstanding.

The transition from brittle to plastic deformation is defined by the mechanism of deformation and always describes features occurring at a microscopic scale. Plastic deformation comprises intracrystalline plasticity and diffusive mass transfer; it is characterized by the lack of brittle deformation. Plastic deformation has been referred to as viscous as well (Schmid and Handy, 1991), to avoid confusing the term to crystal-plastic deformation. On the other hand, viscous flow is sometimes limited to Newtonian (linear) viscosity and can lead to misunderstanding in that way. The transition from brittle to plastic deformation is sometimes termed semi-brittle flow (e.g. Kirby and Kronenberg, 1984; Hirth and Tullis, 1994). Mylonites are shear zone rocks in which most or all of the deformation occurs by plastic deformation mechanisms (Sibson, 1977).

1.2 Deformation experiments and natural fault rock

The deformation of rocks in nature is characterized by a combination of a wide range of temperature, pressure, stress and strain rate conditions that act on a system of mainly polymineralic aggregates with various impurities in contact with fluids with a diverse chemistry. This deformation occurs at depths that are mainly inaccessible and span time periods ranging between fractions of seconds to millions of years. In order to obtain a more detailed knowledge of the mechanisms and kinetics that underly these processes, rock deformation experiments have been performed in laboratories. More insight has been gained in the deformation of rocks by systematically varying only one parameter in this complex interplay of phenomena while all others are kept constant. The first apparatuses for triaxial deformation experiments were designed by Kick in 1892 and von Kármán in 1911. This design was improved by Griggs who built an apparatus with two pistons of equal diameter in 1936 and with the possibility for internal heating in

1951 (see Paterson, 1978, for a more detailed overview). The first studies on granite and basalt at elevated pressure and temperature conditions were performed a few years later (e.g. Griggs et al., 1960; Borg and Handin, 1966). Most of the studies on granites and basalts in the sixties and seventies, however, concentrated on the brittle fracturing (e.g. Byerlee, 1967; Kumar, 1968) or frictional sliding behavior of rocks (e.g. Byerlee and Brace, 1968; Stesky et al., 1974; Byerlee, 1978; Dietrich, 1979), and were performed to gain a better understanding of earthquakes. These studies showed, that brittle deformation is mainly dependent on confining pressure.

Around 1980 a renewed interest in semi-brittle and plastic deformation of granites and basalts developed (e.g. Tullis and Yund, 1977, 1980; Kronenberg and Shelton, 1980; Caristan, 1982), which led to the notion that a more detailed study of the rheology of the individual minerals was necessary before the rheology of polymineralic rock could be completely understood (e.g. Avé Lallemant, 1978; Wilson and Bell, 1979; Tullis and Yund, 1987; Hirth and Tullis, 1989, 1994; Den Brok, 1992; Mares and Kronenberg, 1993). These studies showed that plastic deformation is strongly dependent on the temperature, and the axial shortening rate at which a mineral is deformed. In the meantime, the study of friction and fracturing of granites continued. The focus of interest was more directed to the influence of temperature on the deformation and the behavior of pre-formed gouge on friction (Paterson, 1978; Lockner et al., 1986; Fredrich and Wong, 1986; Yund et al., 1990; Karner et al., 1997; Blanpied et al., 1998; He et al., 2006, and many others). The number of experimental deformation studies on intact granites and basalts under conditions leading to cataclastic flow is, in comparison, relatively scarce (but see e.g. Tullis and Yund, 1977; Hacker and Christie, 1991; Kato et al., 2003).

Microstructures provide the link between observations on deformation of natural systems and rock deformation experiments, because the mechanisms that cause the deformation develop the same geometries and fabrics. The fact that microstructures connect experimental data to natural observations was first discussed by Griggs et al. (1960, p40-41):

We feel that, while some of our results may apply only to abnormally high temperatures in the crust, in the majority of cases the effects we find at high temperatures will be found in nature at much lower temperatures because of the lower strain rates. (...) We are encouraged to present our data to geologists, however, by the fact that all the phenomena we have observed have their counterparts in nature.

By studying the microstructures of experimentally and naturally deformed rocks, conclusions inferred from experimental deformation can be extrapolated to natural systems.

1.3 Aim and key issues of the thesis

Faulting causes a grain size reduction in rocks, especially under conditions favoring distributed microcracking. The grain size distribution of fault rock has become one of the major descriptive criteria for fault rock (e.g. Engelder, 1974; Sammis et al., 1987). The most common way to represent this grain size distribution is on a log(frequency)-log(radius) plot, where the slope of the distribution is regarded as a fractal dimension, D :

$$D = \frac{\log N}{\log(1/r)}$$

with N indicating the frequency and r the radius of the grains (Mandelbrot, 1982; Sammis et al., 1987). The assumed power-law distribution has been disputed: Wilson et al. (2005) claim a more irregular distribution.

The fraction of the GSD with grain sizes smaller than 2 μm has not hitherto been investigated very intensively. However, these small grains have a high surface area density and may therefore be important for the calculation of the energy budget of earthquakes, if these small grains have formed during rupturing (Olgaard and Brace, 1983; Kanamori, 1994). Additionally, the small grains have a high surface area to volume ratio and are therefore expected to be chemically the most reactive grains in the gouge after their formation. In this thesis the complete range of grain sizes obtained from experimentally deformed granitoids and basaltic rock is investigated and compared to naturally deformed fault rock. For experimentally deformed granitoids, the influence of deformation conditions on the D -value has been investigated as well. This investigation has led to considerations about the processes causing rupturing and grain size reduction.

The grain size distribution is not the only feature that can be used to quantify the microstructures of fault rocks. Various aspects of the grain shape of fault rock can give information about the evolution of the fault rock from cracked grains to gouge. The grain shape of fragments and its influence on the properties of fault gouge have hardly been investigated (however, see Fernlund, 1998; Mair et al., 2002). In addition, the spatial distribution of gouge and of specific minerals in a fault zone can provide information on the localization of deformation and on the deformation mechanism. These geometrical aspects are addressed in this thesis and have resulted in the development of new grain shape descriptors, as well as the applications of existing tools, like the auto-correlation function (Heilbronner Panozzo, 1992).

The deformation experiments, performed on polymineralic rock samples, are performed under conditions near the brittle-ductile and brittle-plastic transition of those rocks. The first investigations of these transitions were already performed in 1960 by Heard, who studied the influence of confining pressure, temperature, shortening rate and the presence of a fluid on these transitions. However, the exact processes, which occur during the transitions are not completely

understood for polymineralic samples, despite the large progress that has been made over the years (e.g. Tullis and Yund, 1977; Hacker and Christie, 1991; Tullis and Yund, 1992; Hirth and Tullis, 1994; Bos et al., 2000; Kato et al., 2003). Therefore, further microstructural and (micro)-mechanical investigations are performed in this thesis to be able to identify the deformation processes that play a role in the deformation of natural and experimental fault rocks under brittle to ductile and brittle to plastic transition conditions.

After fracturing, grains have a small size and thus a high surface to volume ratio. Small grains are likely to deform by fluid assisted diffusive mass transfer, granular flow, to dissolve and reprecipitate to cause growth of larger grains, or to be involved in mineral reactions (see e.g. Brodie and Rutter, 1985). In this thesis, we will investigate these processes in the fine grained granitoid and basalt gouge. For a better understanding of processes in natural fault rock, it is necessary to know which processes dominate under certain deformation conditions. To do so, we investigate the fine grained gouge under hydrostatic conditions at different temperatures and under different axial shortening rates (i.e., stress).

1.4 Layout of the thesis

- The experimental procedure and the processing of the acquired data is described in detail in Chapter 2.
- In Chapter 3 the geometrical aspects of experimental granitoid fault rocks are described and quantified with newly developed grain shape factors, which are calculated using a new Fortran program, and the D -value for fault rock. It is recognized that cracked grains and gouge have different D -values, and to illustrate this, D -mapping is introduced.
- In Chapter 4 the D -values for granitoid fault rock are further investigated under different deformation conditions and compared to fault rock from the Nojima Fault, Japan. The results are applied to the surface energy of newly formed fault rocks, the mechanism for grain size reduction, the alleged fractal grain size distribution, and the mechanism for rupturing in fault zones.
- The influence of temperature and axial shortening rate on fine grained experimentally and naturally formed granitoid gouge is investigated in Chapter 5. A healing law, based on changes in the D -value with time, is derived for the hydrostatically healed gouge. The non-hydrostatically healed gouge is investigated for brittle-plastic transition microstructures.
- Chapter 6 shows the results for experimental deformation of basalt samples. The deformation mechanisms, grain size distributions, spatial distributions of plagioclase in the samples

and nature and amount of reactions are investigated and combined in a model to explain the differences in strength between the studied samples.

- Appendix A gives details on all deformation experiments and Appendix B shows the mechanical data for most of them. In Appendix C the experiments performed on NaCl samples are discussed. These experiments have been performed to improve the understanding of systematic errors in connection with the deformation apparatus. Appendix D describes the structural evolution of the Nojima Fault, Japan. Appendix E describes the sample areas for the natural fault rocks. The EDX measurements on the basalt samples are listed in Appendix F.

Chapter 2

Experimental techniques

In this Chapter the sample assembly, deformation apparatus, the procedure during an experiment and the processing of the acquired data is described. An overview of all performed experiments and their mechanical data is given in the Appendices A and B, respectively. Appendix C is devoted to the experiments on salt samples, which have been performed in an attempt to improve the data correction of the other experiments.

2.1 Sample assembly

The sample assembly is designed in such a way that a rock sample can be deformed under conditions resembling those in the Earth's crust. Temperature, confining pressure, and differential stress can be controlled separately. Here, a detailed description of the sample assembly that has been used for experiments in this thesis and modifications of this assembly is provided (Fig. 2.1), see also Tullis and Tullis (1986) and De Ronde (2004). Most experiments were performed using a 55 mm high pressure vessel. Most of the early experiments and a few of the later ones were performed using a 58 mm high pressure vessel. Before an experiment the sample assembly is placed in a pressure vessel, which rests on a base-plate. The pressure vessel is cooled internally and with an external cooling ring that is placed on top of the pressure vessel.

2.1.1 Sample and pistons

Five different sample materials have been used; two types of granitoid and three types of basalt. The granitoid rock samples originate from the Val Verzasca and are referred to as Gneiss-Berger and P2. Gneiss-Berger, donated by A. Berger (University of Bern), is a small piece with a smaller grain size and a stronger foliation on the hand specimen scale than P2 (collected by H. Stünitz and R. Heilbronner at the same locality as Gneiss-Berger, swiss coordinates: 704.65–126.30); P2 is a boulder, Gneiss-Berger part of the solid outcrop. Three 20 mm diameter cores of Maryland Diabase have been provided by J. Tullis (University of Brown). A small number of samples have been drilled from these cores. Bransrode Basalt originates from a basalt quarry in Bransrode, state of Hessen, Germany, which is part of the Hoher Meißner region. The Vogelsberg mountain is a mafic intrusion in the state Hessen, Germany. The Vogelsberg samples have been gathered from the Ortenberg quarry. Vogelsberg Basalt is fresher, finer grained and more glass-rich than Bransrode Basalt. Both basalts have been taken by H. Stünitz. Further details on the sample material are provided in the relevant Chapters.

The granitoid samples were obtained by coring with a 6.45 mm inner diameter drill bit, resulting in sample diameters of 6.37 – 6.42 mm. Samples used for experiments 2nk – 11nk have been drilled with a 6.3 mm-drill and have a diameter of 6.28 mm. The larger diameter drill bit was used to avoid ruckling of the (mechanically sealed) 6.5 mm diameter jacket. Some basaltic samples were cored with the 6.59 mm-drill (experiments 12nk – 84nk; 101nk) yielding sample diameters of 6.5 mm. Due to the large sample diameters, later samples were cored with the 6.4 mm-drill (labeled 625–6.3 mm) resulting in 6.38 – 6.41 mm samples.

The flat ends of the samples were polished to two plane-parallel sides. The samples were dried under atmospheric pressure at $T = 110^\circ\text{C}$. 37nk and 38nk (Verzasca Gneiss) were dried under

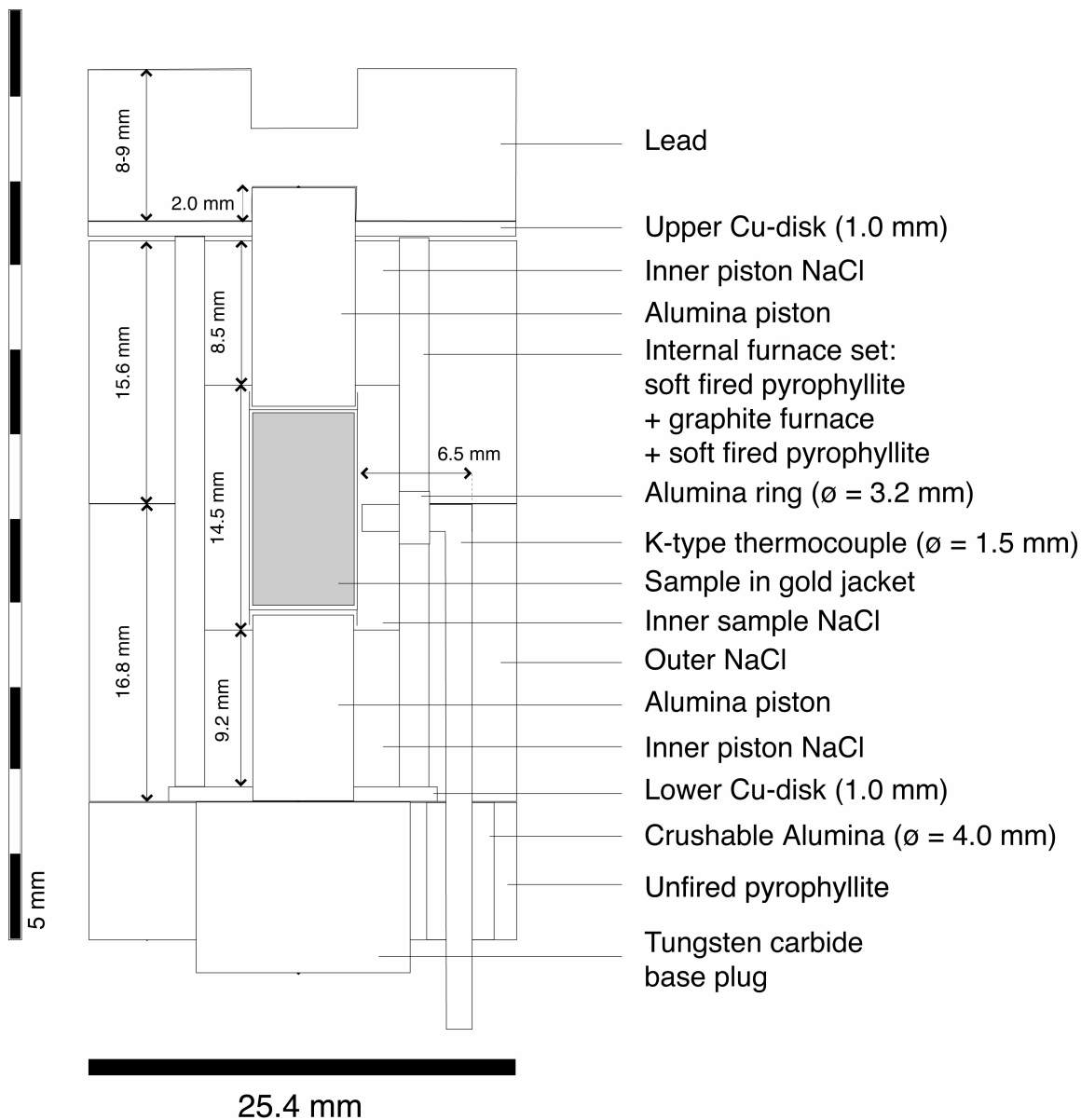


Figure 2.1: Scaled drawing of assembly used for experiments in 55 mm pressure vessel. Due to variations in sample length, vertical differences in the length of pistons and salt occurred. See text for other dimensions and variations due to improvements of the assembly. [Sketch modified after De Ronde (2004).]

atmospheric pressure in a glass vessel flushed with CO_2 gas for 24h at $T = 600^\circ C$. Weight loss during drying was 0.2 wt%. After drying the samples were very friable and one of the undeformed samples showed thermally induced micro-cracks. 39nk and 41nk (Bransrode Basalt) were pre-dried at $T = 900^\circ C$ in a mixture of 13.1 ml CO_2 /min and 3.6 ml CO /min for 24 h. As a result the samples became more brittle. This gas mixture was chosen, because at the resulting oxygen fugacity olivine does not oxidize at high P, T -conditions during experiments.

The samples were wrapped twice in 0.05 mm nickel-foil and placed in a gold tube of 0.25 mm thickness and 6.54 mm diameter. For granitoid experiments 6nk – 29nk a 0.05 mm copper-foil was used. The samples were covered by 0.2 mm thick Au-cups, which were weld-sealed to the top and bottom of the jacket with a carbon-tipped welding pen at 3.8 Ω and 61 V. The samples were cooled in water during the welding to retain the added 0.2 wt% H_2O in the jacket. Samples used in experiments 2nk – 12nk were covered with 0.2 mm disks and closed by mechanically crimping the gold tubing around the sample and these discs; all these experiments were performed without added water. Experiments 2nk, 4nk and 37nk were performed without a foil. Nickel is a better buffer than copper to prevent the oxidation of iron-containing minerals in the sample.

The first granitoid experiments (2nk – 37nk) were performed with zirconia (ZrO_2) pistons. In most of these experiments, with the exception of 27nk and 29nk, the pistons deformed. All other granitoid samples and all basalt samples were deformed with alumina (Al_2O_3) pistons. For the salt tests (test 11 – test 19, see section C.2) zirconia pistons were used. Alumina pistons have a diameter of 6.334 – 6.339 mm, the diameter of zirconia pistons is 6.40 mm.

2.1.2 Confining pressure medium and temperature measurement

The salt liners (see Fig. 2.2) were used as a confining pressure medium. They were wet-pressed from $> 99.5\%$ pure sodium chloride. For the outer salt liners about 11.2 – 11.5 g NaCl was ground, mixed with a few drops of cold water and pressed under a load of 13 tons. After wet-pressing the resulting material has a density of 94% of the single crystal NaCl density. In the lower outer salt liner a 1.0 or 1.6 mm recess was made for the lower copper disk (Fig. 2.1, 2.2). The vertical hole for the thermocouple was drilled with a 1.7 mm diameter drill bit. The horizontal groove for the thermocouple was excised with a knife.

Inner salt liners were pressed with water added under 4.0 – 4.5 tons from 3 – 4 grams of sodium chloride. The piston salt liners (inner diameter of 6.6 mm) and sample salt liners (inner diameter of 7.2 mm) fit exactly around the piston and the welded jacket, respectively. The length of inner salt liners is adjusted to the length of sample, the furnace and the pistons (Fig. 2.3). The inner salt liners rest on the lower copper disk (line A in Fig. 2.3). The lower piston salt liner is

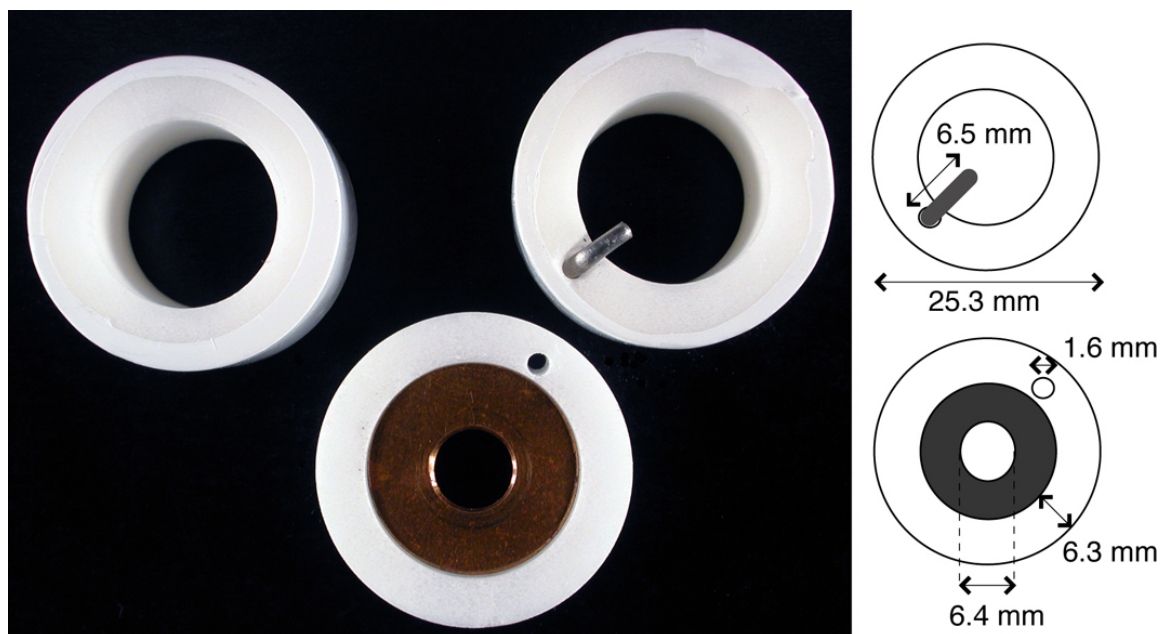


Figure 2.2: Upper outer salt liner wrapped in teflon. Lower outer salt liner, wrapped in teflon; top view with thermocouple. Lower outer salt liner, bottom view with thermocouple hole and copper disk.

shortened such that a small space ($\sim 0.5 - 1$ mm) is left between the jacket and the top of the piston salt liner (line B in Fig. 2.3). The sample salt liner is longer than the jacket with an excess length at line D of ~ 1 mm. This salt liner assembly ensures that the jacket does not rest on the narrower piston salt liner during initial (cold) increase of the confining pressure. All experiments with numbers lower than 53nk were performed with inner salt liners with an inner diameter of 7.0 mm. Salt material was removed, until the welded jacket fitted in the inner salt liners.

A chromel-alumel thermocouple (K-type) was used for all experiments with number 53nk and higher. Earlier experiments were performed using Pt-Pt(10%Rh) thermocouples (S-type) with wires of 0.25 mm in diameter inside a mullite tubing. K-type thermocouples are slightly easier to prepare and less prone to damage during the emplacement of the assembly in the pressure vessel and during initial pumping. The horizontal part of the thermocouple has a length of 6.5 mm (Fig. 2.2); therefore the tip of thermocouple sits at a distance of approximately 0.1 mm from the jacket. The thermocouple did not touch the jacket in the beginning of the experiment, to avoid scratching and tearing of the jacket after a higher amount of shortening. At the end of the experiment, the thermocouple touches the jacket.

The position of the thermocouple is controlled by the length of the lower outer salt liner. An initial position of the thermocouple slightly below the centre of the sample (line C in Fig. 2.3)

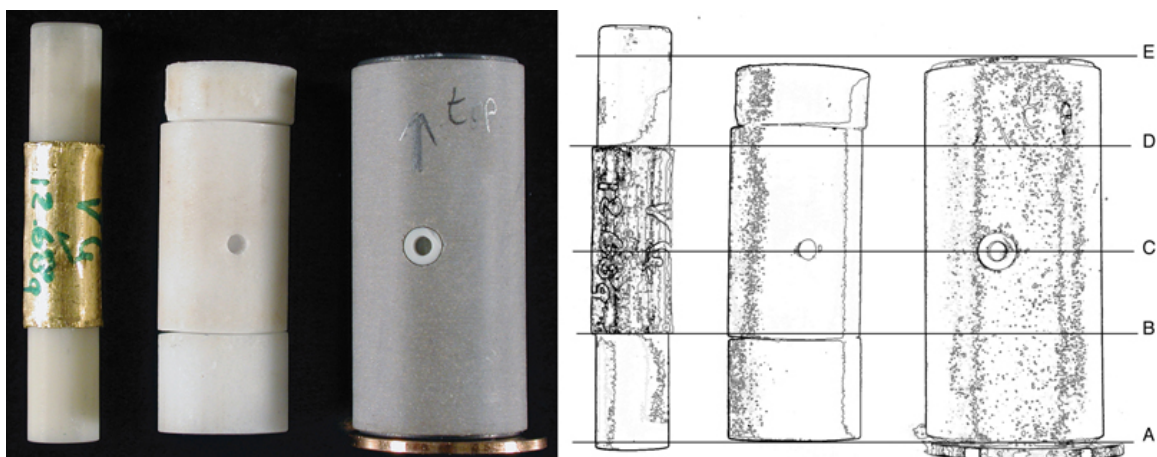


Figure 2.3: Sample with pistons, inner salt liners and furnace with copper disk and alumina ring to position thermocouple. Horizontal lines in sketch show horizontal positions in assembly: A = top of lower copper disc, B = bottom of gold jacket, C = tip of thermocouple, D = top of gold-jacket, E = top of furnace.

leads to a central position at the beginning of the healing period (after deformation).

2.1.3 Internal heating system

The internal heating of the assembly is achieved by a graphite furnace (Fig. 2.1), which has a resistance of $\sim 1 \Omega$ under room conditions and $\sim 16 \Omega$ at $T = 500^\circ\text{C}$. The tungsten carbide base plug, MG12, has a diameter of 12.7 mm. In experiments with numbers higher than 86nk the thicker (1.6 mm) upper copper disks were replaced by thinner (1.0 mm) ones; experiment 97nk was the first with a thinner lower copper disk of 1.0 mm.

Most experiments were performed using a 100% lead top piece. Tests at $T = 300^\circ\text{C}$, $P_c = 500 \text{ MPa}$, $\dot{\epsilon} = 10^{-4} \text{ s}^{-1}$ were made with pieces with 3 – 6 mol% or 10 mol% tin in the lead. Pieces with tin had a steeper run-in curve on the paper chart than pure lead pieces: $\alpha = 8.2^\circ$ versus 12.0° (see Fig. 2.4 for an illustration of α) for a 10% Sn piece (in Rig 1¹ with 2V full scale and chart speed 300 mm/h) and $\alpha = 9.9^\circ$ versus $\alpha = 12.5^\circ$ for a 3-6 mol% Sn piece (in Rig2 with 2V full scale and chart speed 5 mm/min). More tin in lead pieces make these pieces weaker at the PT -conditions of deformation. However, the tin-containing pieces are stronger under room-conditions, which makes it harder to press them into shape before the experiment and more likely to exert a force on the sample during initial (cold) pressure build-up.

¹Rig1 and Rig2 are described in the next section.

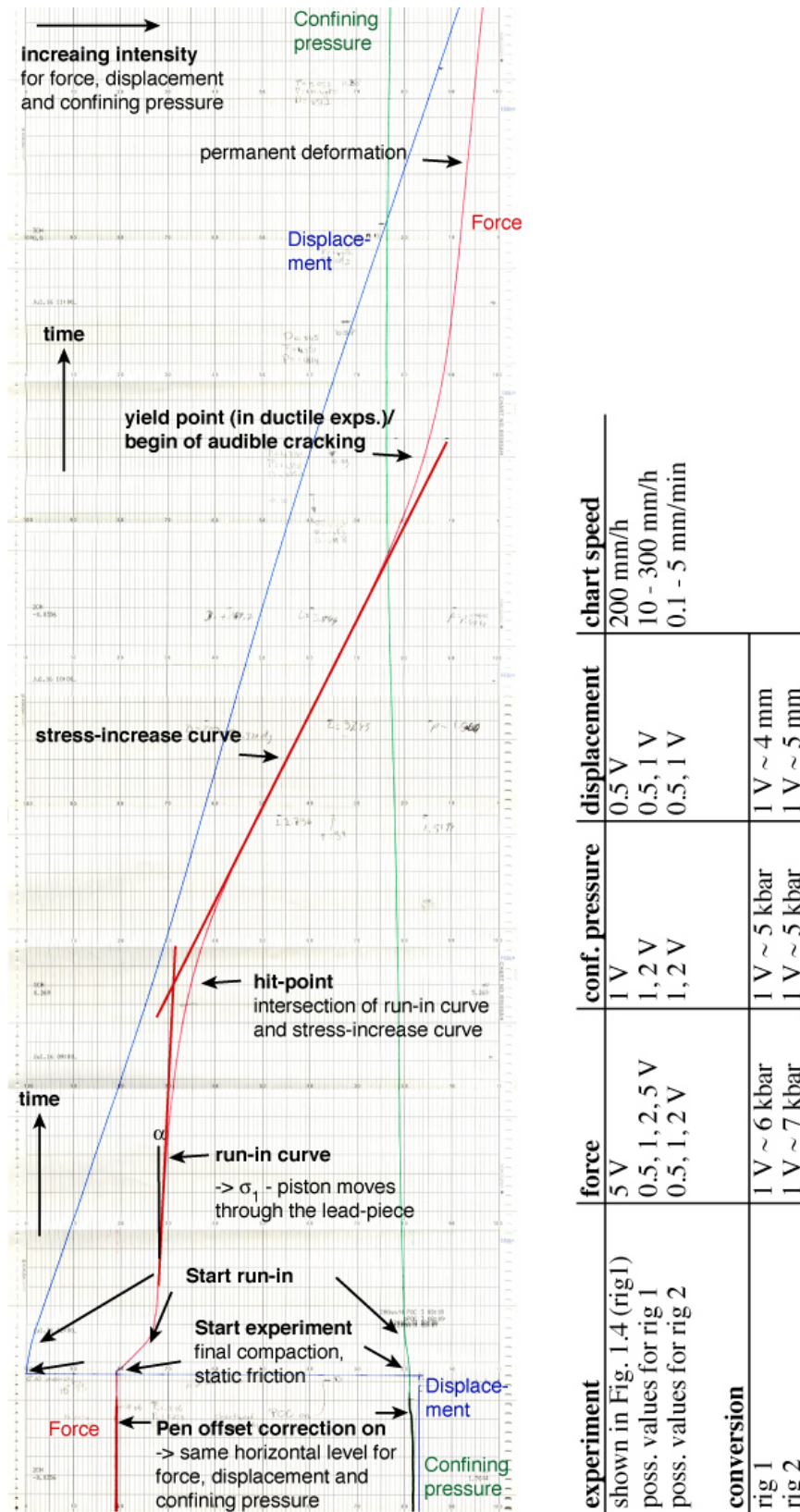


Figure 2.4: Example of a chart-recorder, showing the start of the experiment, the run-in curve, the hitpoint, the stress-increase curve and the yielding towards permanent deformation. Note that the time is increasing upward and therefore the chart should be read from bottom to top. α is the angle that the run-in curve makes with the vertical lines on the chart paper. The table shows the applied settings for force, confining pressure, displacement, and chart speed for the chart recorders of both deformation apparatuses.

2.2 Deformation experiments

2.2.1 Deformation apparatus

The deformation experiments were performed in the Griggs-type solid medium apparatuses (Griggs, 1967) Rig1 and Rig2 of the rock deformation laboratory in Basel. Each apparatus has a servo-controlled internal heating system. The confining pressure is applied by pumping oil in chambers around the hydraulic ram, which presses on the salt liners around the sample. Both apparatuses were improved with an automatic hydraulic pumping system (May 2003 for Rig2 and August 2003 for Rig1). The pumping system in Rig1 is three times faster than in Rig2, using the same frequency (Hz), because of a different gear box.

To apply a differential stress, the samples were loaded by an electro-motor that moves the force actuator downward and is connected to a gear-train of wheels. Experiments were performed with a constant displacement rate, which can be chosen from six rates in steps of an order of magnitude. The original electro-motors, has been replaced by servo-controlled motor (in October 2005 for Rig1 and April 2006 for Rig2). These motors yield an adjustable speed, allowing for a wider range of displacements and can be operated at constant displacement or constant force conditions.

During the experiments the force, confining pressure and axial displacement of the force actuator were registered by a chart recorder. The force applied to the sample is the normal force measured by the load-cell. The confining pressure is measured externally as the oil pressure in the chambers of the hydraulic ram and is recalculated for the area of the σ_3 -piston. The axial displacement of the force actuator is measured by a direct current differential transformer (DCDT). The measurements were also recorded by automatic data registration with the computer program LabVIEW™ (after February 2006 for Rig1). Additionally, the temperature of the sample at the tip of the thermocouple, the output-values of the heating system, the room-temperature (after June 2005), and the vertical movement load-cell with respect to the frame of the deformation apparatus (after June 2006) were measured.

2.2.2 Experimental procedure

Figure 2.5 shows the pressure-temperature and the temperature-time paths for a typical experiment. Data show the average for ten experiments at $T = 300^\circ\text{C}$, $P_c = 500\text{ MPa}$ (77nk – 105nk) and six experiments at $T = 500^\circ\text{C}$, $P_c = 500\text{ MPa}$ (70nk – 113nk).

The sample assembly is placed in the pressure vessel in the apparatus and the cooling water,

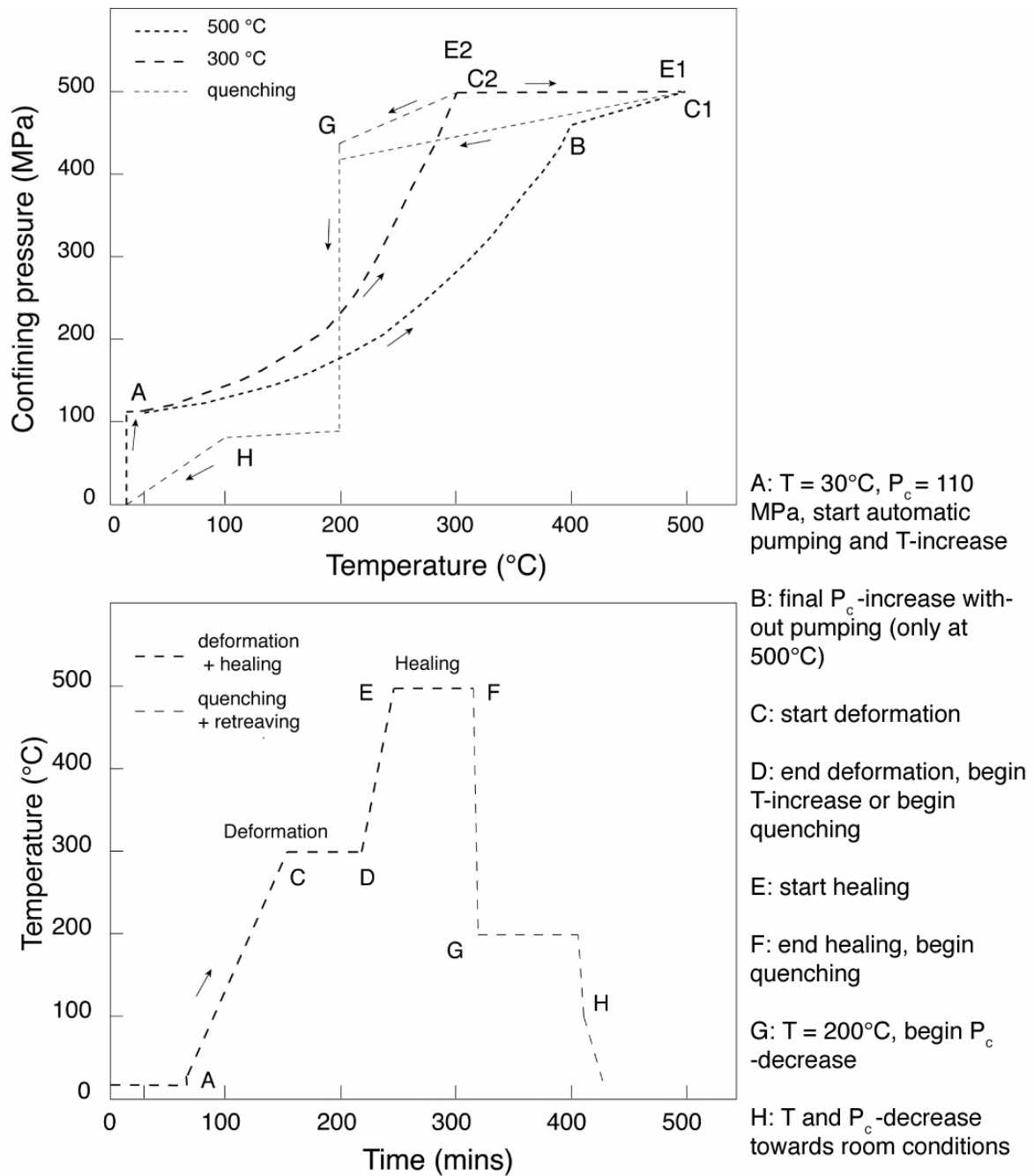


Figure 2.5: a) Pressure-temperature path for an average experiment. Constant T, P_c -conditions during deformation and healing yield: point C = D and E = F. C1/E1 = deformation/healing at $T = 500^\circ\text{C}$, C2/E2 = deformation/healing at $T = 300^\circ\text{C}$. b) Temperature-time path for an experiment with deformation at $T = 300^\circ\text{C}$ and healing at $T = 500^\circ\text{C}$. Run-in time omitted; healing-time is not to scale. Points A–H reflect identical points to a).

heating system and thermocouple are connected. Initial manual pumping is performed at cooling water temperature until a confining pressure of 110 MPa is reached after 44 minutes. Hooks are removed from the 55 mm vertical length pressure vessel after this initial pressure increase. The temperature is increased to $T = 30^\circ\text{C}$ under manual control of the output (point A in Figure 2.5). The automatic hydraulic pumping system is switched on at a low frequency (40-50 Hz for Rig2) to slowly increase the confining pressure. Simultaneously the temperature is increased to $T = 300^\circ\text{C}$ in 60 minutes (0.075°C/s) or to $T = 500^\circ\text{C}$ in 90 minutes (0.087°C/s). In this way, a confining pressure of approximately $P_c = 200$ MPa is reached at $T = 200^\circ\text{C}$ (along path A–B). Temperatures above $T \approx 200^\circ\text{C}$ increase faster in confining pressure with temperature (as an effect of a higher thermal expansion coefficient for NaCl: 0.963% at $T = 100^\circ\text{C}$, 8.932% at $T = 600^\circ\text{C}$, expanded from 20°C (Clark, 1966)). This effect is further enhanced by manually increasing the frequency of the automatic hydraulic pumping system (50-65 Hz for Rig2). For experiments at $T = 500^\circ\text{C}$ the final confining pressure build-up is performed by increasing the temperature from $T = 400$ to 500°C without pumping (point B, only for experiments at $T = 500^\circ\text{C}$). In this way the increase of $P_c = 460 - 470$ MPa to 500 MPa is reached (point C1). For experiments at $T = 300^\circ\text{C}$ it is not possible to reach “piston-out” conditions in this way (point C2). After a run-in period (see Fig. 2.4), the sample is deformed during 10 minutes to 32 days (path C–D).

Samples that are healed after deformation (point D) at a higher (or lower) temperature require an extra heating step: the temperature is increased (or decreased) in 30 minutes to $T = 200$, 400 or 500°C (path D–E), except for the two experiments (95nk, 104nk) with healing during $13.8 \times 10^3\text{s}$, where the temperature increase is performed in 6 minutes. If necessary, the confining pressure is released slowly (at 20 Hz for Rig2 with the automatic hydraulic pumping system) to 500 MPa again. The healing period starts at point E and has a duration of 4 hours to 14 days (path E–F).

After deformation (point D) or after healing (point F1 at $T = 300^\circ\text{C}$ and F2 at $T = 500^\circ\text{C}$) the sample is quenched to $T = 200^\circ\text{C}$ in 2 minutes (path F–G). This causes a decrease in confining pressure to $P_c \sim 410$ MPa (430 MPa for experiments at $T = 300^\circ\text{C}$; point G). The confining pressure is released to 0.8 kbar in 45 minutes, than the temperature is lowered to $T = 100^\circ\text{C}$ (point H). Pressure and temperature are further decreased until room-conditions are reached in 11 minutes.

2.3 Processing of the experimental data

2.3.1 Data correction

The measurements (force, confining pressure and displacement) of the chart recorder are converted to stress, strain and strain rate using the Fortran program RigC4 (R. Heilbronner, <http://pages.unibas.ch/earth/micro/software>). This program uses the corrections for the distortion of the deformation apparatus (stiffness correction). The rig stiffness is 3.316×10^{-6} mm/N for Rig1 and 5.049×10^{-6} mm/N for Rig2 (H. Stüinitz, 2004). The change in cross-sectional area of the samples during deformation and the variations in confining pressure during the experiment are corrected as well. No correction for the strength of the jacket was made.

Friction in the sample assembly and the Griggs-type deformation apparatus is accounted for by the definition of the hit-point (see Fig. 2.4). It is assumed that the dynamic friction in the deformation apparatus has a constant value and that at the hit-point the sample is under hydrostatic conditions. The hit-point is defined as the point where the extrapolated run-in curve (describing the piston movement through the lead piece) intersects with the extrapolated stress-increase curve. Due to reasons described further below (see discussion of the nature of the run-in curve, section C.3) the hit-point is not always a well defined point, but a curvature in the force record (see Fig. 2.4). For strong samples, such as the granitoids and basalt samples described in this thesis, the hit-point is clearly defined and lies close to the cross-cutting point of both curves.

After deformation, the granitoid and basalt samples do not show a consistent shape: some are deformed by a single diagonal fault cutting through the sample, others by a set of multiple conjugated fractures that cause barrelling of the sample. Most samples show a combination of these end-member cases, see Appendix A. The barrelled samples deform largely by pure shear on the scale of the whole sample. A constant sample volume is assumed, and a shortening of the sample therefore leads to an increase in cross-sectional area normal to σ_1 . For samples deforming with a single cross-cutting diagonal fault, the data correction is less straight forward. Part of the deformation takes place along the fault, where instead of enlarging the cross-sectional area this leads to a decrease in contact area between the upper and lower half of the sample. Another part of the deformation is accommodated by the sample, outside the fault zone. In some samples it is not obvious when the cross-cutting fault was developed, i.e. they do not show a stress-drop and the faulting of the sample was not audible during deformation.

To avoid problems arising from these different crack geometries and to be able to compare all mechanical data regardless of geometry, most of the mechanical data is presented as force-displacement curves, which are only corrected for the distortion of the deformation apparatus.

However, this presentation has the disadvantages that (1) it is hard to determine whether the samples show a hardening or weakening behaviour and (2) that in this way it is not possible to correct for the increase in confining pressure during the later stages of deformation.

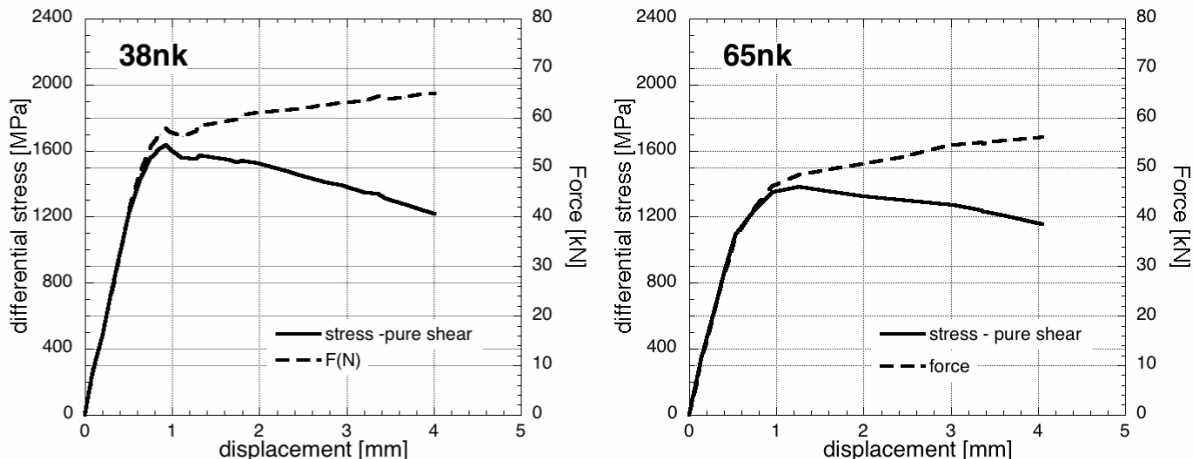


Figure 2.6: 38NK deformed along a single cross-cutting fault plane. Pure shear and simple shear corrected stress data and force data from the same force record. 65NK deformed by a set of conjugated faults, the sample was barreled after deformation.

Figure 2.6 illustrates these problems. Depending on whether force or stress is plotted against displacement, the results are different. For sample 38nk, deformed along a cross-cutting fault, a stress-drop and audible cracking are recorded. The pure shear curve shows – incorrectly – a weakening of the sample. Sample 65nk displays a barreled shape after deformation. The force record of this experiment shows a steady increase, but with a pure shear area correction, this is changed into a weakening behaviour.

2.3.2 Final displacement measurements

Measurements of the samples after deformation reveal that there is a difference between the change in length inferred from the chart record (after correction for distortion) and the final shortening of the samples. The final shortening of the samples has been calculated from measurements of the final length of the samples, which have been obtained in two ways: (1) using a micrometer screw (see Table A.4 in Appendix A) and (2) in the optical microscope from a thin section of the sample. In general, the measured shortening of the sample is less than the value calculated from the chart record (see Fig. 2.7). The precision of the micrometer screw measurements is not very high. The average difference between minimum and maximum length is 0.27mm. This difference is due to the unknown thickness of the gold jacket after deformation and the fact that the samples are usually no longer plane parallel after deformation. Samples

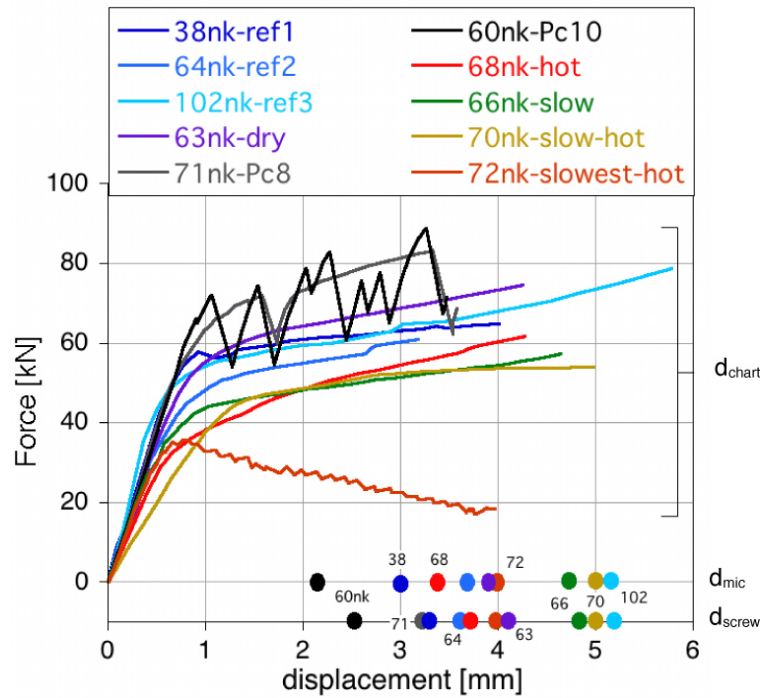


Figure 2.7: Force-displacement data for 10 granitoid deformation experiments, corrected for the rig distortion (d_{chart}). Colored dots indicate the final displacement as calculated from measurements of the sample after deformation; the average value of the micrometer screw measurements (d_{screw}) and the estimation of the shortening measured in the light microscope (d_{mic}). Numbers indicate the sample numbers.

that have been deformed with at a slower rate ($\dot{\epsilon} = 1 \times 10^{-6}$ or 10^{-7}s^{-1} , 66nk, 70nk, 72nk) show the same final length as is calculated from the chart record (see Fig. 2.7). For sample 64nk, the final sample shortening exceeds the length observed from the chart record. Here, clearly, either the initial length of the sample is measured incorrectly or an error has occurred during the recording.

Figure 2.8a compares the values for the final shortening obtained in an optical microscope with the values obtained with a micrometer screw. The samples that are shown are granitoid samples deformed at $\dot{\epsilon} = 1 \times 10^{-4} \text{s}^{-1}$ and have been plotted in (Fig. 2.7). The minimum values for the final shortening obtained with the micrometer screw agree well with those from the optical microscope (blue line in Fig. 2.8a). Therefore, this value is considered to be more representative for the final shortening than the maximum value obtained with the micrometer screw. From Figure 2.8a it can be observed that the discrepancy between the inferred displacement from the chart record and the final displacement is 0.7 mm for these samples.

For the granitoid samples deformed at rates of $\dot{\epsilon} = 1 \times 10^{-6}$ or $1 \times 10^{-7} \text{s}^{-1}$ (Fig. 2.8b) the final shortening obtained after deformation agrees well with the value inferred from the chart

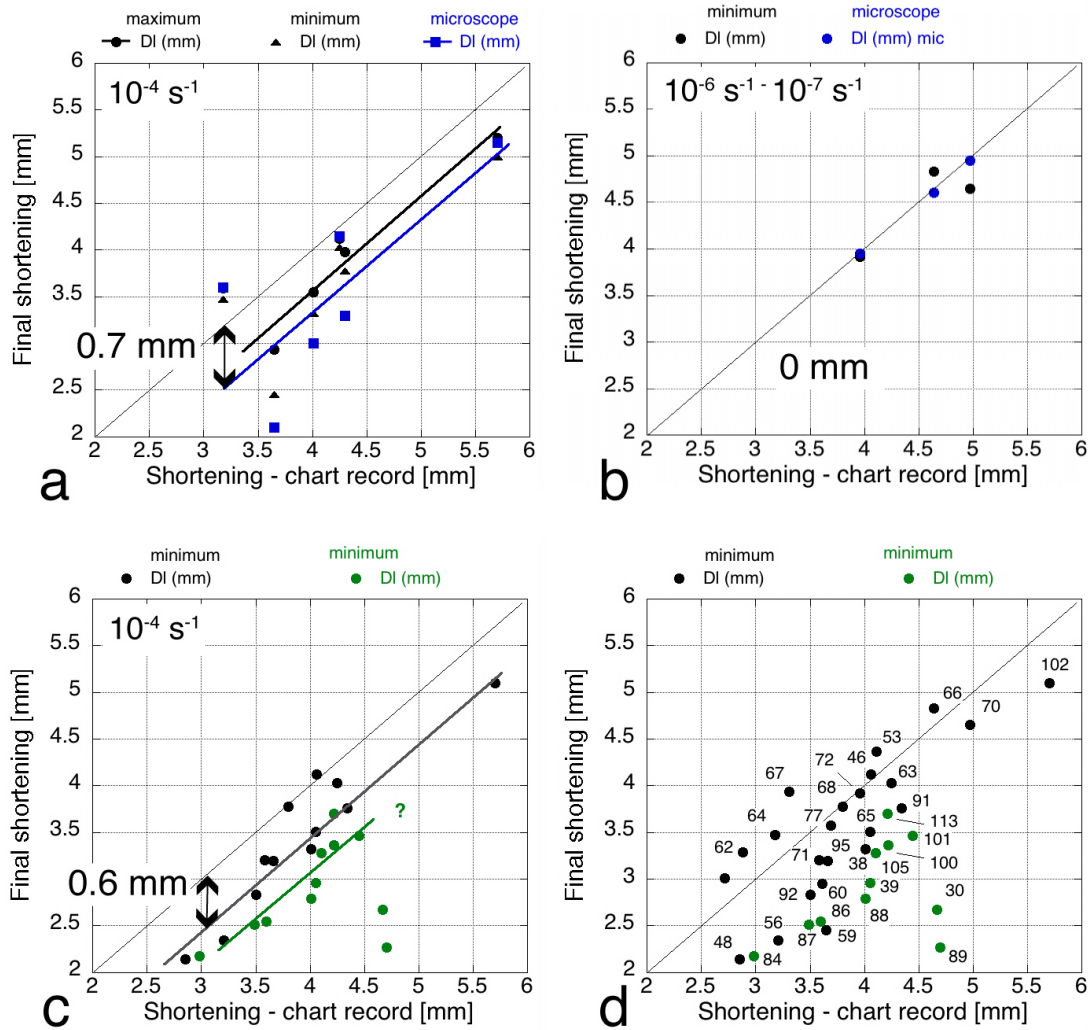


Figure 2.8: Relationship between final shortening, measured with a micrometer screw, and shortening calculated from the chart record output, including a distortion correction. DI = maximum or minimum measured shortening with micrometer screw or the shortening obtained from measurements in the optical microscope. Numbers in (d) indicate the sample numbers.

record. Apparently, for samples deformed at $\dot{\epsilon} = 1 \times 10^{-4} \text{ s}^{-1}$, part of the inferred displacement is absorbed by the deformation apparatus. In Figure 2.8c most experiments performed at $\dot{\epsilon} = 1 \times 10^{-4} \text{ s}^{-1}$ are shown. For granitoid samples the same trend as in Figure 2.8a is observed. For basalt samples, the discrepancy between measured values after deformation and inferred values from the chart record is even larger than for granitoid samples (0.9 mm). The trend through the basalt samples however, is more unclear. The discrepancies in final shortening for granitoid and basalt samples are independent of the deformation apparatus or base-plate utilized for the deformation. For experiments on granitoid samples performed at $\dot{\epsilon} = 1 \times 10^{-4} \text{ s}^{-1}$ 0.7 mm of displacement should be subtracted from the value inferred from the chart record.

Chapter 3

*Grain size and grain shape analysis of fault rocks**

The description and quantification of the geometrical aspects of fault gouge are investigated in this paper. Grain shape factors are developed to distinguish cracked grains and fault gouge. A first investigation of the grain size distribution is performed. The D -value is defined as the slope of the grain size distribution and used as a measure for the visual presentation of the distribution of cracked grains and fault gouge in the fault zone.

*Published as: Heilbronner, R. and Keulen, N. (2006) *Tectonophysics* 427, p.199-216.

Abstract

New methods for microstructural analysis of fault rocks (new shape descriptors for convexity/concavity and angularity) and visualization (D -mapping) were developed and tested on experimentally deformed granites. The samples were deformed at 300 °C, 500 MPa confining pressure, and $10^{-4} s^{-1}$ strain rate. SEM micrographs of the resulting fault rocks were used for digital image analysis.

Cracked fragments and mature gouges can be differentiated on the basis of the slope, D , on a log-log plot of the grain size distribution. Both types of fault rocks exhibit two slopes: For grain sizes $< 2 \mu m$, $D \approx 1.0$ for both types; for grain sizes $> 2 \mu m$, cracked material shows $D \approx 1.6$ while gouge has $D \geq 2.0$. In the case of the gouge, the fractal nature of the grain size distribution is questioned. The D -mapping technique was introduced to visualize the spatial distribution and connectivity of gouge and cracked material in fault rocks.

Grain shape analysis shows clear differences between cracked minerals and fault gouge and between quartz and K-feldspar grains. The aspect ratio is measured as L/S (longest/shortest diameter): L/S of cracked quartz (range: 1.0–8.0, average 2.9) is higher than that of K-feldspar (range: 1.0–4.0, average 2.1). L/S of gouge is always low (range: 1.0–3.0, average 1.5). From the difference between a shape and its convex envelope, two shape descriptors are derived: the paris factor and the area difference ΔA . Both show decreasing values from cracked to gouge material, and the values of cracked K-feldspar (range: 0–100%, average: 15%) are higher than those for quartz (range: 0–100%, average: 5%). Gouge always shows low paris factors (range: 0–20%, average: 2.5%). From the histogram of vertex angles, the Ω -value (fraction of angles $< 0^\circ$) is derived: Ω of cracked material is significantly higher (30–40%) than that of gouge (10–20%). Automatic digitization enhances the distinction between cracked and gouge material.

3.1 Introduction

Fault rocks predominantly result from brittle deformation processes. Throughout geological time fault rocks have been produced in the shallow crust, under relatively low pressure-temperature conditions and at relatively fast strain rates. Fault rocks are intimately associated with earthquakes, and have been studied in boreholes that traverse active faults, such as the Nojima Fault in Japan (e.g. Ito et al., 1999, Appendix D), as well as in experiments that simulate seismic conditions (e.g. Tsutsumi, 1999; Hirose and Shimamoto, 2003, and many other authors).

Fault rocks typically occur along fault surfaces. They are composed of gouge and mineral

and rock fragments of all sizes and shapes (Blenkinsop, 1991; Rawling and Goodwin, 2003; Otsuki et al., 2003; Billi et al., 2003). As faulting is a highly localized deformation process the resulting fault rocks are restricted to within a few meters of the master fault surface. Layers of fragmented particles and gouge of varying grain size and shape are heterogeneously dispersed in the rock, forming a crosscutting and intersecting network (Mitra, 1978, 1993; Anderson et al., 1983; Stewart et al., 2000; Shigematsu et al., 2004).

In the course of fracturing and continued deformation of the fault rocks, the originally angular fragments may be rounded by abrasion, re-fracturing and deformation. The analysis of the shape and shape changes during faulting (and afterwards during healing), and the study of the spatial (re-)arrangement of the particles are therefore of great importance (Mair et al., 2002; Storti et al., 2003). The shape of the fragments can be used to distinguish mature gouges (i.e., gouges which have accommodated large displacements) from fresh gouges or newly fragmented rocks. Increasing roundness is a sign of increasing wear, i.e., increasing deformation or displacement (Cladouhos, 1999; Storti et al., 2003). The spatial arrangement and possible interlocking of fragments has been explored in experiments and the kinematic development has been modeled numerically (Mair et al., 2002; Guo and Morgan, 2002).

The mechanical properties of fault rocks depend on their microstructural characteristics, which is why the quantification of fault rock microstructures is important. Fault rocks are commonly described by their grain size distribution (GSD), by the shape of the fragments, and the spatial distribution or arrangement of the fragments (e.g. Sammis et al., 1987; Marone and Scholz, 1989; Mair et al., 2002; Hirose and Shimamoto, 2003; Wilson et al., 2005, and many others). However, we find that the techniques of grain shape and grain size analysis could be improved. In this contribution we seek to find descriptors for grain size and grain shape that let us discriminate and quantify the complete spectrum of fault rocks, from the first fractured rocks with angular particles and possibly a fractal GSD, to matured gouges with rounded particles and non-fractal GSD. We will introduce a new computer program (“ishapes”) for the derivation of a number of shape factors (including one that addresses angularity). We will also introduce a new approach to grain size analysis (called “*D*-mapping”), which visualizes characteristics of the GSD and thus enables to recognize spatial distribution of fragmented material and localization of gouge. We will demonstrate the application of these methods to experimentally produced fault rocks.

The paper is restricted to the analysis of a small number of samples obtained from experimental deformation and the development of suitable analytical tools. The focus is on differentiating the deformational behaviour of quartz and K-feldspar.

3.2 Fault rock microstructures

The samples analyzed in this study were obtained by experimental deformation of granite rock. The granite was collected in the Val Verzasca, Switzerland, and consists of 35% quartz, 29% plagioclase, 27% K-feldspar and 7% mica (mainly biotite).

3.2.1 Deformation experiments

For the experiments, cylinders of 10.44 to 12.33 mm length and 6.39 mm diameter were cored. The samples were dried during 26 hours at 110 °C and atmospheric pressure and wrapped in a Cu- or Ni-foil. After adding 0.2 wt% water they were sealed in a 0.15 mm thick gold jacket. The axial compression experiments were performed in a Griggs type solid medium apparatus (a detailed description is given by Tullis and Tullis, 1986; De Ronde, 2004) with sodium chlorite as a confining medium. Straight furnaces, zirconia or alumina pistons and Pt/Pt-10%Rh and cromel-alumel thermocouples were used.

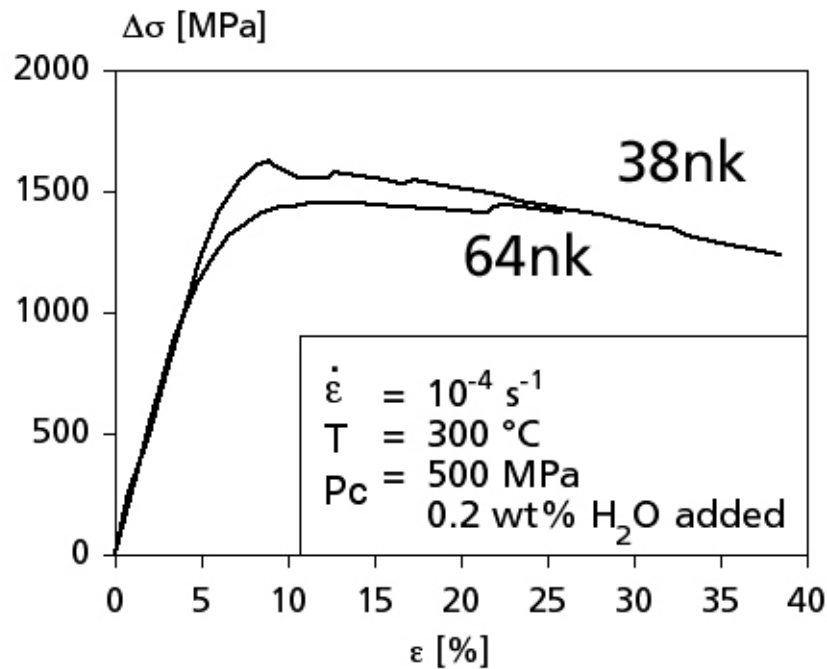


Figure 3.1: Mechanical data of experimentally deformed granite. Stress - strain curves of samples 38nk and 64nk deformed in the solid medium deformation apparatus. Program rigC (www.unibas.ch/earth/micro) was used for data conversion. Experimental conditions are the same for both samples, total axial shortening of 38nk and 64nk is 38% and 26% respectively.

Two samples (38nk and 64nk) were deformed under controlled conditions at $T = 300\text{ }^{\circ}\text{C}$, confining pressure $P_c = 500\text{ MPa}$, and strain rate $= 10^{-4}\text{ s}^{-1}$ (Fig. 3.1). One additional sample (12nk) was deformed under less controlled conditions, at $15\text{ }^{\circ}\text{C}$ (cooling water temperature) and approximately 50 MPa confining pressure. In this experiment, the forcing block was advanced manually; the total axial shortening of 36% was achieved in five pulses with an estimated shortening rate of 10^{-2} s^{-1} . Because of its large content of fault rock material, images of this sample were used for the development of the analytical methods and the computer programs.

After deformation, the samples were vacuum impregnated with epoxy, cut along the cylinder axis from where doubly polished thin sections were prepared. Backscatter SEM images were recorded on a Philips XL30 ESEM (ZMB Basel) using increasing magnifications from $100\times$ to $20,000\times$. The investigated grain sizes span approximately 2.5 orders of magnitude.

3.2.2 Preparation of images for digital image analysis

The SEM images were processed using Adobe Photoshop and ImageSXM (developed from NIH Image, for MacOSX; public domain: <http://reg.ssci.liv.ac.uk/>), as well as a number of macros (“Lazy D -map”, download from <http://pages.unibas.ch/earth/micro/>). Two types of input images had to be prepared. For the shape and grain size analyses of quartz and feldspar, one bitmap for each mineral had to be prepared. In this case, the images were segmented by grey level slicing to differentiate the (dark grey) quartz grains from (intermediate grey) plagioclase grains and (light grey) K-feldspar grains. For the D -mapping technique, a single bitmap separating all grains from the matrix was required. In this case, the average grey levels of quartz, plagioclase and K-feldspar were determined and set to the same brightness (using the Adjust Curves command in Photoshop) and the images were segmented by thresholding, thus separating the (dark) matrix from the (light) grains. Using ImageSXM, a number of segmentation techniques were tested and the results compared visually. Best results were obtained by observing both the image and the grey value histogram during grey level slicing or thresholding. Care was taken to apply consistent segmentation to all images of a given series, such as to ensure unbiased separation of the matrix from grains and fragments. Special ranking filters (Erode7 and Dilate7, “Lazy D -map”) were applied to remove the noise without altering the original shapes of the grains. The resulting bitmaps are the basis for the grain size and grain shape analyses and for the D -mapping method described below. An example of segmentation is shown in (Fig. 3.2a and b).

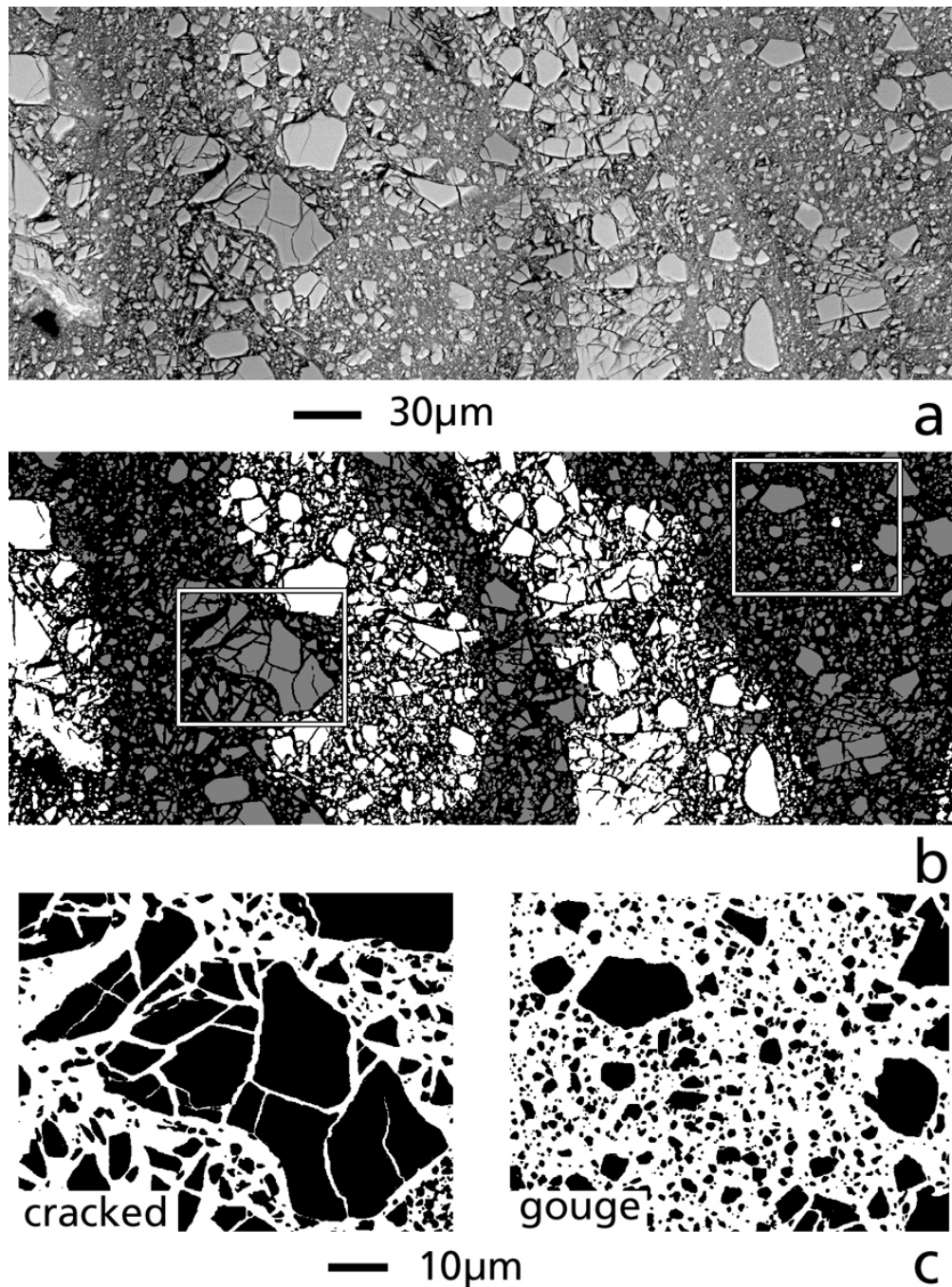


Figure 3.2: Microstructures attained during progressive faulting. a) SEM micrograph (BSE contrast) of fault rock. Sample 12nk (for deformation conditions see text). Scale ($30\ \mu\text{m}$) applies to a) and b). b) Processed image: black = matrix, grey = quartz & plagioclase; white = K-feldspar; frames outlining distinct microstructure types. c) Enlarged view of microstructures: black = particles; white = matrix. Scale ($10\ \mu\text{m}$) applies to cracked and gouge microstructures. Note that both microstructures consist of quartz grains.

3.2.3 Terminology

The terminology used here is illustrated in Figure 3.2c showing two frames of “cracked” and “gouge” microstructures. Typical features of a “cracked” microstructure are angular fragments and a relatively low area fraction of matrix, whereas in gouge, the grains are rounded and the area fraction of matrix is higher. In both cases, the term “matrix” denotes those grains of the fault rock, which are smaller than a given threshold size or smaller than the optical resolution at the given magnification. This terminology is purely geometrical and has no implications for the mechanical properties such as cohesion, etc..

Based on previous analyses, we expect the GSD of both cracked material and gouge to be different; in comparison with published data we would expect different fractal dimensions. In this paper, however, we will not refer to the slope of the GSD (on a log-log plot) as “fractal dimension”; rather we will use the more neutral terms “slope D ” or “ D ”.

3.3 Analytical methods

In this section the analytical tools will be developed and applied to two types of microstructures, “cracked” and “gouge”, from sample 12nk as shown in Figure 3.2.

3.3.1 Grain size analysis

The bitmap (Fig. 3.2c) is opened in ImageSXM and using the Analyze menu the cross sectional areas of the grains are measured. Using a spread sheet program, the equivalent radii, R_{equ} are calculated (for definition of R_{equ} , see Table 3.1), and from these the diameters, d , ($d = 2 \cdot R_{equ}$). The GSDs of the cracked and gouge microstructures are given by the number of grains (#) with a diameter $> d$ versus grain diameter (d) and are shown as a log-log plots in 3.3a. Towards the smallest grain sizes, the linear behaviour drops off. This is due to the limit of resolution (at the magnification of these images) and the resulting inability to detect very small grains. To calculate the fit, therefore, only the numbers of the grains with $d > 2 \mu\text{m}$ have been used. The resulting D -values for cracked and gouge are 2.33 and 1.65 respectively. In practical applications, it is irrelevant whether regular or cumulative GSDs are evaluated, i.e. whether the number of grains of size (d) or ($> d$) are measured, since the resulting curve fits cannot be distinguished (see Appendix).

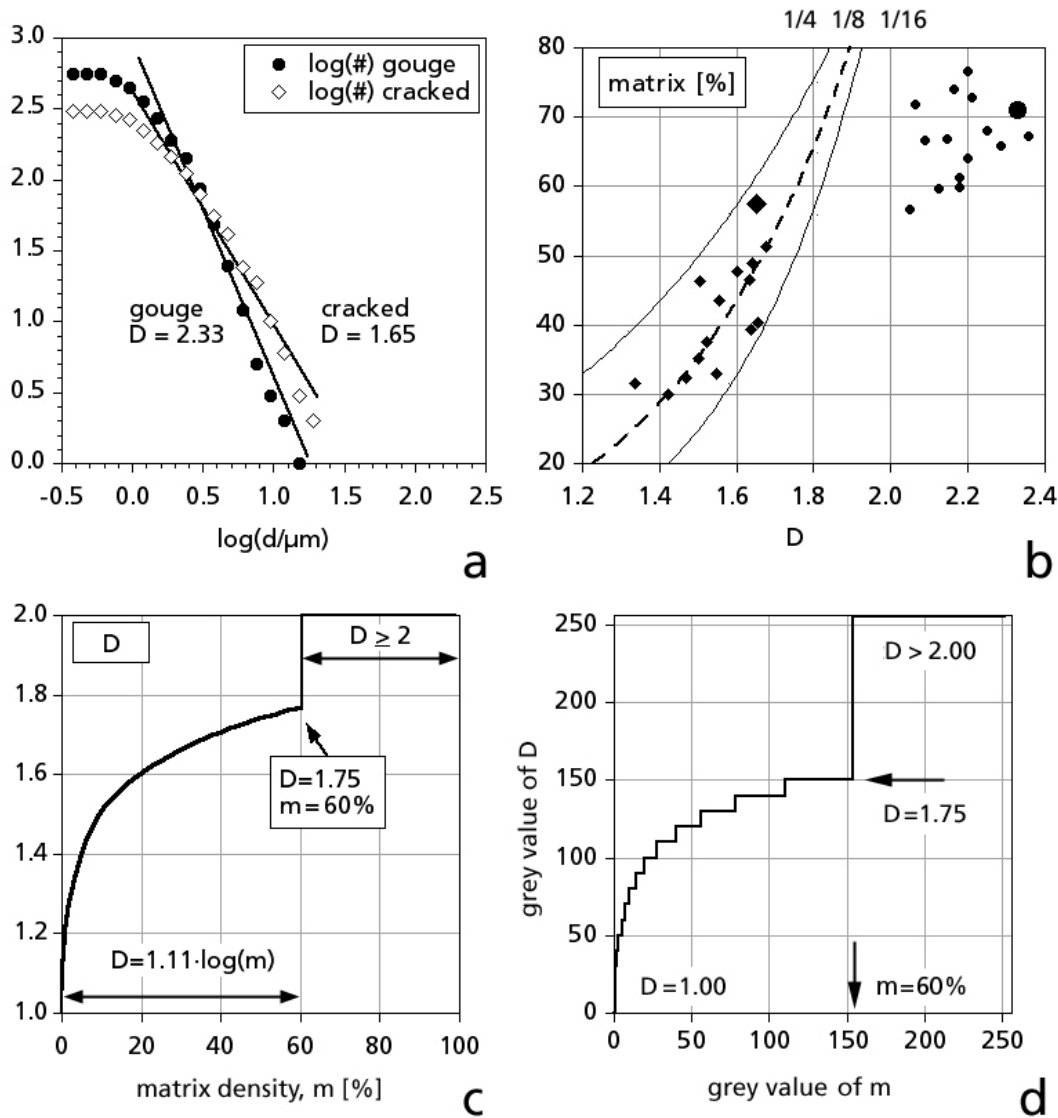


Figure 3.3: Grain size distribution (GSD) and matrix content of fault rocks. a) Cumulative GSD of cracked particles (diamonds) and gouge (circles) of test areas shown in Figure 3.2c. Log(#)-log(d) diagram where d = equivalent diameter of particles in μm ; # = number of particles with diameter $> d$. Least-squares fit for particles with diameter $> 2 \mu\text{m}$ (i.e., $\log(d) > 0.3$) yields slope $D = 2.33$ for gouge, $D = 1.65$ for cracked particles. b) Area percentage (area%) of matrix as function of D (D is the slope of the log-log fit of GSD, as in Figure 3.3a). Rhombs = area% of matrix of images with cracked particles, circles = area% of matrix of images with gouge; large symbols = results of test areas shown in Figure 3.2c; small symbols = results from sample 38nk, discussed later. Superposed thin lines and the dotted line show theoretical area% of matrix assuming that the matrix consists of particles with diameters smaller than 1/4, 1/8 and 1/16 of the diameter of the largest grain. c) D as function of matrix density (m), modeled from Figure 3.3b. d) Look-up Table for converting images representing matrix density to images representing D -values. Horizontal axis (input): grey values (0-255); range 0-154 corresponds to matrix density of 0-60%. Vertical axis (output): grey values (0-255); range 0-150 corresponds to D -values from 1.00 to 1.75; steps of 10 grey levels correspond to increments of 0.05 of D . For input grey values > 154 (matrix density $> 60\%$), the output is 255 (= black) indicating D -values > 2.00 .

	Symbol	Definition
Basic measurements		
Long axis	L	longest projection of rotating shape on x-axis
Short axis	S	shortest projection of rotating shape on x-axis
Perimeter	P	length of original outline
Area	A	area of original shape
Perimeter of envelope	PE	length of outline of convex envelope
Area of envelope	AE	area of convex envelope
Derived measures		
Equivalent radius	R_{equ}	$R_{equ} = \sqrt{(A/\pi)}$
Equivalent perimeter	P_{equ}	$P_{equ} = 2\pi R_{equ}$
Shape factors		
Aspect ratio		L / S
Shape factor F		P / P_{equ}
Paris factor (%) ^a		$2 \cdot ((P-PE) / PE) \cdot 100$
DeltaA (%)		$((AE-A) / A) \cdot 100$
Shape descriptor for angularity		
Fraction of angles < 0 °	Ω (%)	$100 \cdot \sum [h(\alpha)]$ for $\alpha < 0^\circ$

Table 3.1: Definitions of measurements and shape factors as used in this paper.
^afor previous definition of PARIS factor, see Panozzo and Hürlimann (1983).

3.3.2 D-mapping

The aim of this technique is to show the spatial distribution of gouge and cracked material. The gouge is shown as a distinct but homogeneous phase, whereas the cracked material is further differentiated (colour-coded or contoured) according to local variations of the D -value. Three steps are necessary: (1) the image has to be segmented (same as for the grain size analysis), (2) the bitmap has to be Gauss filtered to obtain an image of matrix densities, (3) the matrix densities have to be converted to D -values; in other words, with the help of a special look-up table (LUT), the matrix density image is converted to a D -map. In the following we describe how this LUT is derived.

From the bitmaps of the cracked and gouge microstructures, the area percentages of matrix (white in Figure 3.2c) were calculated. The values are shown in Figure 3.3b together with additional values calculated from microstructures discussed later in the text. A relation between the area percentage of matrix and the value, D , is obvious: smaller D -values correlate with smaller matrix percentages; for $D > 2$, large matrix percentages are reached, but they do not

seem to depend on D .

To explain the relation between matrix density and D -value we consider the fractal fragmentation of a cube (e.g. Turcotte, 1986). Assuming continued fragmentation of cubes into eight cubes of $1/2$ the original edge length and different proportions (from $1/8$ to $7/8$) of the smaller cubes being fragmented further, GSDs with fractal dimensions between 0.00 and 2.81 are obtained. Assuming different maximum grain sizes for the matrix (cut-off grain sizes), it is possible to calculate the theoretical area percentage of matrix as a function of D (see Appendix). The smaller the cut-off grain size, the larger the area percentage of the matrix for any given D . Figure 3.3b displays three such curves, calculated for three different cut-off grain sizes: $d = 1/4$, $1/8$ and $1/16$ where $d = 1$ is the maximum diameter of the GSD. It is obvious that the area percentages of matrix of the cracked microstructures (with D -values between 1.2 and 1.7 and matrix percentages between 20% and 60%) follow the trend of these curves, while the values of the gouges (with D -values above 2 and matrix percentage $> 60\%$) clearly fall outside this correlation and do not depend on the value of D at all.

To obtain the reverse dependence of D on matrix density (m), the axes shown in Figure 3.3b are interchanged (Fig. 3.3c). In the range of ($0\% < m < 60\%$), typical for cracked grains, we find a logarithmic dependence of D on m . In the range ($60\% < m < 100\%$), typical for gouges, D is constant. The resulting matrix- D relation provides the basis for the look-up table (LUT) shown in Figure 3.3d. The input grey values (horizontal axis) range from 0 ($m=0\%$) to 255 ($m=100\%$); the output values (vertical axis) range from 0 ($D = 1.00$) to 150 ($D = 1.75$) to 255 ($D > 2.00$). Between 0 and 150, the output values are stepped: increments of 10 grey values denote D increments of 0.05. Above a matrix density of 60% (input grey value = 154), the LUT assigns a constant grey value of 255 (= black), indicating the presence of gouge.

Figure 3.4a shows a bitmap of a heterogeneous part of a fault rock. The matrix density image (Fig. 3.4b) is calculated by applying a Gaussian filter. The Gaussian filter is used because it ensures that the average density of the filtered image (i.e., the matrix density image) is the same as that of the bitmap. Depending on the size of the filter (filter size is shown on the right of Figure 3.4b) the matrix density image is more or less smooth, revealing more or less local detail. Applying the LUT to this image converts the grey values representing matrix density to grey values that represent D -values (Fig. 3.4c). The effect of the LUT on a matrix density image is such that regions with cracked grains show different shades of grey (D -values in the range of 1 to 1.75), while regions with gouge appear homogeneously black (D -value > 2). The volume fraction of gouge is easily determined by measuring the percentage of the black area.

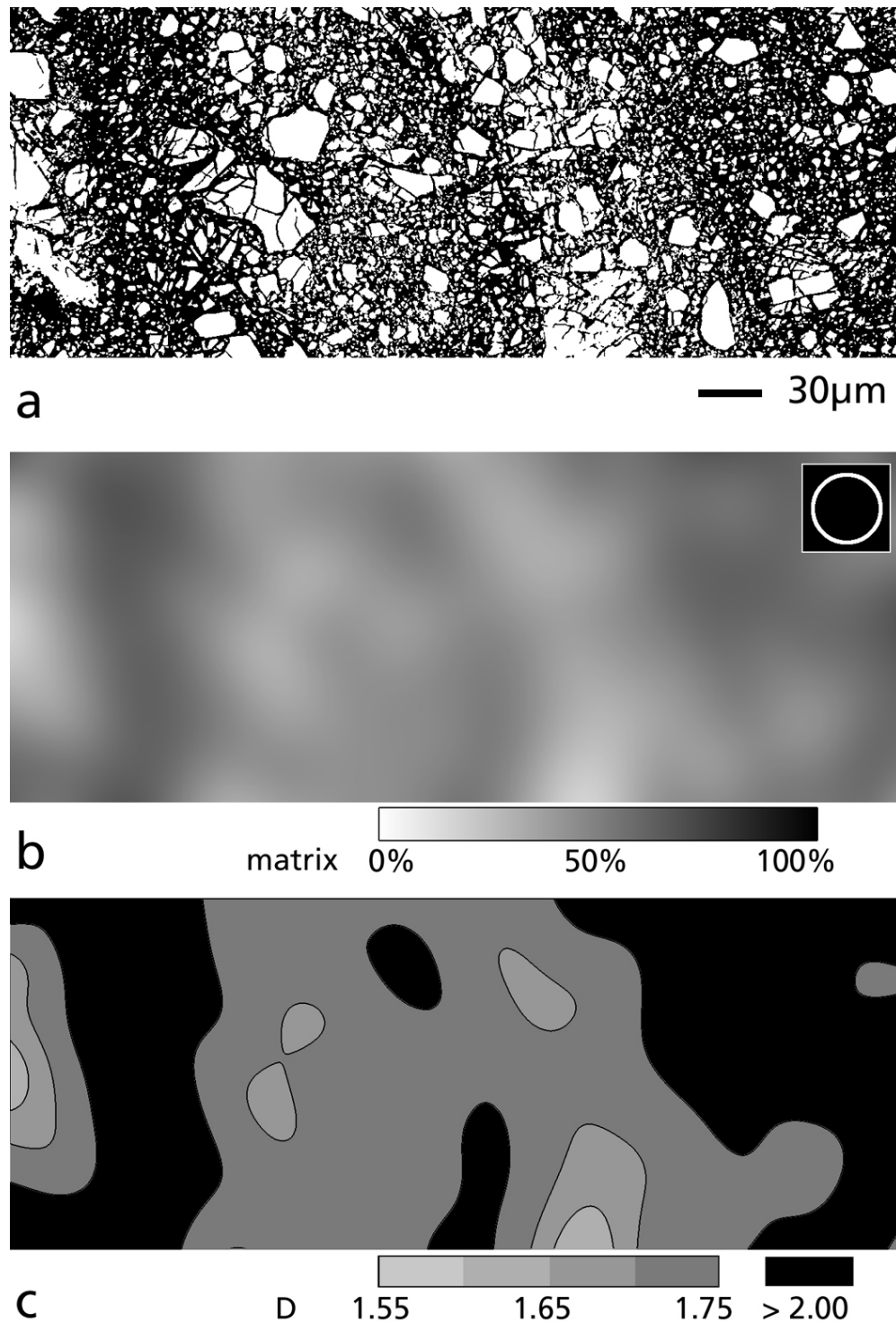


Figure 3.4: D -mapping of fault rock. a) Bitmap of the fault rock shown in Figure 2; white = particles; black = matrix. b) Matrix density image obtained by Gauss filtering of Figure 4a. Filter radius is 50 pixels. Inset shows size of filter. c) D -map obtained by applying the LUT (shown in Figure 3d) to Figure 4b, with superposed D -contours. Grey values represent D -values between 1.55 and 1.75 (lower D -values do not occur in this microstructure), black indicates D -values > 2.00 .

3.3.3 Shape analysis

A number of shape factors have been described in the literature (e.g. Underwood, 1970) and are made available in most image analysis programs. Many are based on best-fit ellipses, cross sectional area and perimeter measurements, others on Feret diameters or projections. In particular, the ratio between the measured perimeter and the perimeter of the equivalent circle (P/P_{equ}) is often used as a measure to describe the lobateness of a given outline. This shape factor is variously called ellipticity (ImageSXM), circularity (imageJ) or even fractal dimension (e.g. Takahashi et al., 1998; Heilbronner and Tullis, 2002). It quantifies any deviation from the circular shape, irrespective of whether the deviation is due to the curvature or angularity of the outline, or the flattening of the shape as a whole.

We used an expanded version of the program "ishapes" (Fortran; download from <http://pages.unibas.ch/earth/micro/>), which addresses the shape of the outline in a more specific manner. In addition to the PARIS factor (Panozzo and Hürlimann, 1983), which is a measure for convexity and concavity based on the PAROR and SURFOR program (Panozzo and Hürlimann, 1983; Panozzo, 1984), it now calculates a number of new shape descriptors (Table 3.1). The basic measurements that are used as input for the "ishapes" program are shown in Figure 3.5. Angles are measured at the vertices (Fig. 3.5a); concave (indenting) angles are counted negative, convex (closing) angles positive. This measure is independent of the sense (clockwise, anticlockwise) in which the particles are evaluated; the sum of all angles of any shape is 360° .

3.3.4 Program "ishapes"

To describe the shape of grains and fragments in fault rocks we used the following measures:

1. The aspect ratio (L/S) is defined as the ratio between the longest and the shortest projection of a particle (Panozzo and Hürlimann, 1983).
2. The "paris factor" is defined as the relative difference between the length of the outline of a shape (P) and the length of its convex envelope (PE) (see Figure 3.5b). It quantifies the lobateness or convexity/concavity of a shape irrespective of aspect ratio or angularity. Round and jagged indentations may yield the same paris factor. Fully convex shapes have a paris factor of 0%. This shape factor yields the same values as the PARIS factor published by (Panozzo and Hürlimann, 1983). We use lower case spelling to indicate that the new "paris factor" and the old "PARIS factor" are derived in two completely different ways.

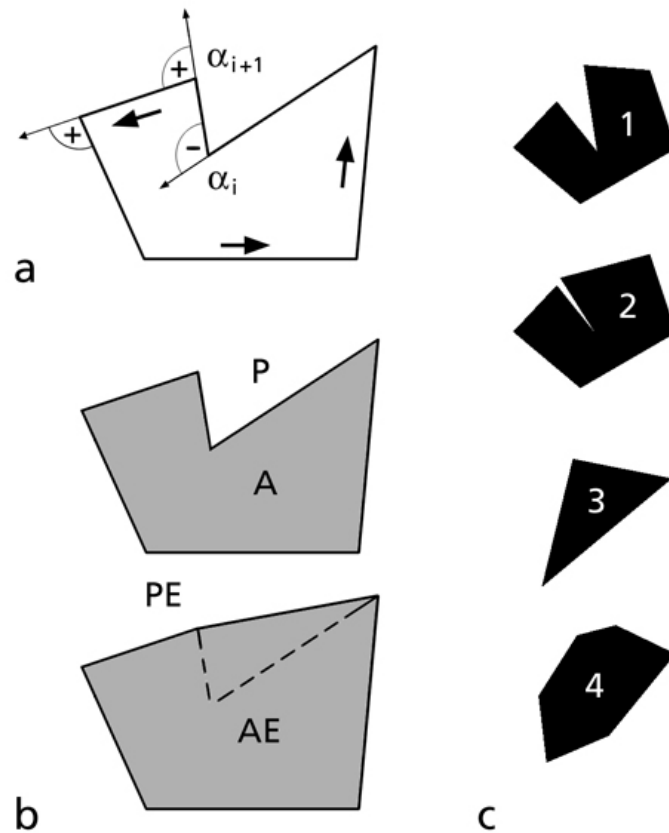


Figure 3.5: Concept of outlines, convex envelopes and angles. a) Definition of the angle at the vertex of an outline: convex (closing) angle = positive; concave angle = negative; sum of angles of polygon = 360° . b) Perimeter (P) and area (A) of outline; perimeter (PE) and area (AE) of convex envelope. c) Four test shapes for shape analysis, results are shown in Table 3.2.

3. The shape factor "deltaA" measures the relative differences between the area of a shape (A) and the area of its convex envelope (AE) (see Figure 3.5b). Note that contrary to the paris factor, deltaA is sensitive to the tightness of the indenting angles: For very small angles (for example, $\alpha < -170^\circ$), deltaA approaches 0% while the paris factor may be very large.
4. On the histogram of angles, the indicator " Ω ", denotes the fraction of vertex angles smaller than 0. Ω is a measure for indentation: the higher Ω the more indented the shape; fully convex shapes do not feature negative angles.

Four simple shapes shown in Figure 3.5c have been digitized manually and evaluated using "ishapes"; the results are listed in Table 3.2. The paris factors of shapes 1 and 2 are similar,

#	n	L/S	F (P/P _{equ})	paris (%)	deltA (%)	Ω (%)	μ (°)
Manually digitized corner points							
1	7	1.37	1.44	47.0	13.1	14.0	51.4
2	7	1.56	1.44	54.2	3.3	14.0	51.4
3	3	2.17	1.39	0.0	0.0	0.0	120
4	6	1.91	1.15	0.0	0.0	0.0	60
Automatically digitized outlines ^a							
1	44	1.37	1.39	42.6	12.7	8.0	8.2
2	58	1.54	1.36	43.9	2.7	5.2	6.2
3	42	2.09	1.35	0.3	1.0	0.0	8.6
4	57	1.89	1.14	0.4	0.7	0.0	6.3

Table 3.2: Results for the shape factors of manually and automatically digitized outlines of the four test figures shown in Figure 3.5c. # = number of shape in Figure 5c; n = number of digitized points; L/S = aspect ratio; F = shape factor; paris (%) = paris factor = excess perimeter; deltA (%) = excess area; Ω (%) = fraction of indenting vertex angles; μ (°) = average vertex angle).

^aminimum distance = 8, vertices with $\alpha = 0^\circ$ excluded.

reflecting the fact that the "excess" length of the outline of the shape compared to the envelope is approximately the same in both cases. However, the deltA-values are different, the relatively low value of shape 2 indicates that the indentation of shape 2 is narrow compared to that of shape 1, i.e., that the "excess" area of the envelope is small. Comparison of the Ω values confirms that fully convex shapes do not have negative vertex angles, hence Ω = 0%. For comparison, two additional measures have been evaluated: the classical shape factor F (= P/P_{equ}) mentioned above, and the average vertex angle, μ . Neither of these measures is very useful for the discrimination of angularity or shape. For example, F cannot discriminate shape 1 from shape 2, while it distinguishes shape 3 from shape 4. Note also that μ is not a measure of indentation or angularity. Since the sum of angles in any given shape is 360° , irrespective of the number and size of indenting angles, μ only reflects the number of points, n , that are digitized on a given outline. $\mu = 360^\circ / n$ (see Table 3.2).

3.3.5 Shape analysis using automatically digitized outlines

With a view towards practical applications, we wanted to make sure that the "ishapes" program can be used with automatically digitized outlines, thus avoiding the effort of manual digitization

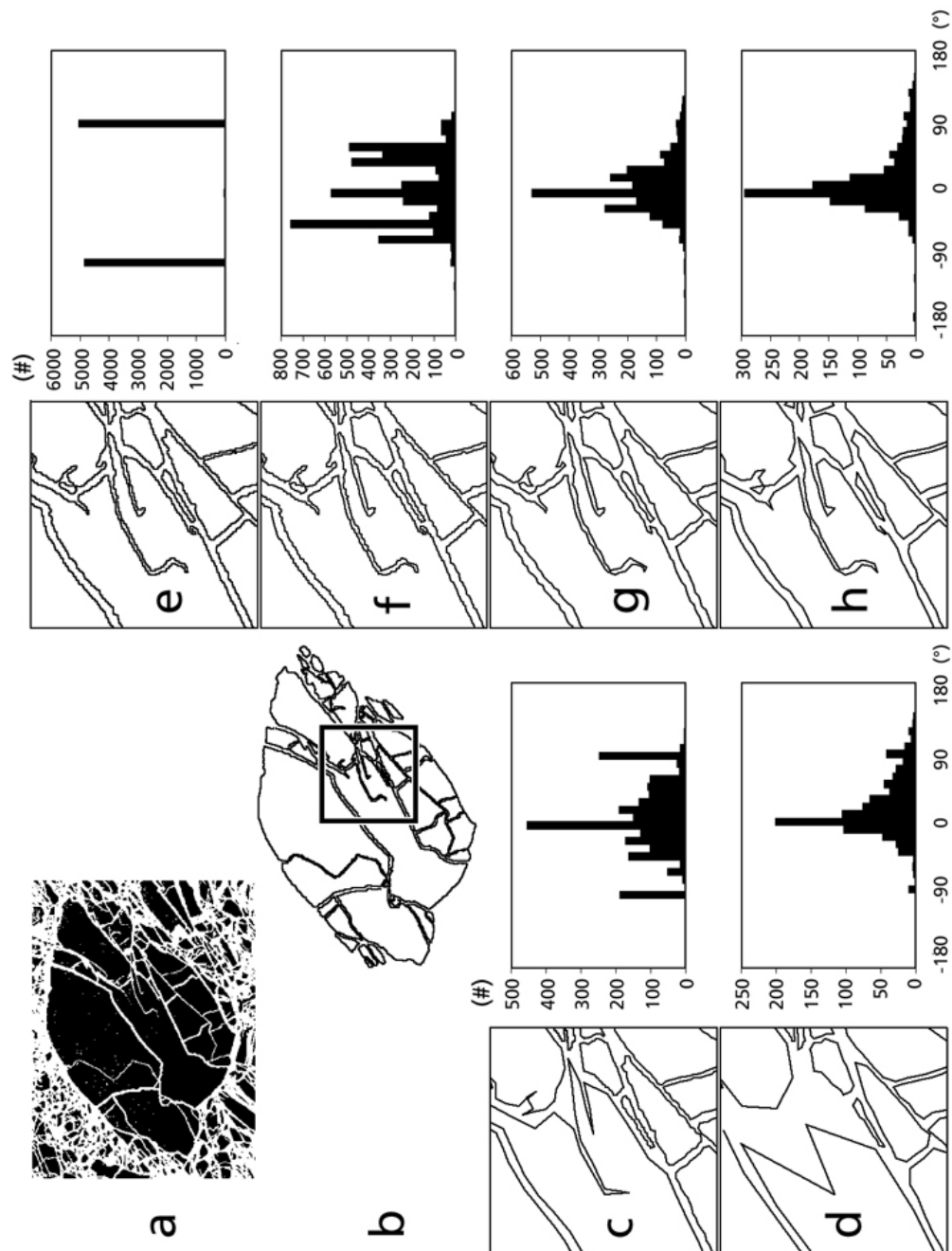


Figure 3.6: Effect of reducing the number of boundary coordinates of automatically digitized outlines. a) Bitmap of fractured quartz grain of sample 12nk. b) Automatically digitized outlines; area in frame is shown enlarged in Figure 3.6c to Figure 3.6h. c) to h) Details of analyzed microstructure (left) and histograms of vertex angles (right) are shown. c) and d) Relative spacing of boundary coordinates: for each grain the smaller of two possible values is selected: 10% of the average segment length (L/n) or 1% of the total boundary length (L) (as shown in c)); 30% of the average segment length (L/n) or 3% of the total boundary length (L) (as shown in d)). e) to h) Absolute spacing of boundary coordinates: the minimum distance between boundary coordinates is 1, 2, 4, or 8 pixels, respectively. Note: points sampled on a straight line (where $\alpha = 0^\circ$) are included.

and the associated bias. To test this, we used ImageSXM and we exported the coordinates of outlines of a number of fragments (shown in Figure 3.6a) as text files. As each pixel of a given outline is recorded, the resulting outline is a zig-zag line with 90° corners (Fig. 3.6e). Not only does the outline consist of horizontal and vertical segments only, the number of coordinates saved per outline is excessive. For a meaningful analysis the number of points must be reduced.

It is well known that the orientation distribution function of lines that connect points on a square grid is far from being homogeneous (Panozzo Heilbronner, 1988) and that orientation distribution functions (ODFs) prepared from digitized lines display discretization artefacts. However, if the coordinates are digitized at distances of 10 pixels and if the bin size of the ODF is $\leq 5^\circ$, the artefacts are strongly reduced. Therefore, in order to minimize the orientation artefact, widely spaced coordinates are useful. Program “ishapes” proposes two ways by which this goal can be achieved:

1. by prescribing a minimum relative distance between digitized points defined with respect to the size of the particle (see Figure 3.6c and Figure 3.6d) or
2. by prescribing a minimum absolute pixel distance between coordinates points (see Figure 6e to 6h) defined with respect to pixel coordinates (pixel size).

The effect of the minimum distance between digitized points along the outline, i.e., of the minimum length of the segments, on the result of the analysis of angles is evident in the histograms of Figure 3.6. If the minimum distance is 1 pixel (Fig. 3.6e), i.e., if all points are used, the resulting histogram contains only two angles: (-90°) and ($+90^\circ$). If the pixel distance is 2 (Fig. 3.6f), the diagonal angles, ($+45^\circ$) and (-45°) appear. At a minimum distance of 8 pixels (Fig. 3.6h), a reasonable histogram is produced. If relative distances are selected in a microstructure with large grain size variations, the situation is slightly more complicated: small particles have short minimum distances and large particles long ones, the resulting histograms are mixed, the artificial peaks at ($+90^\circ$) and (-90°) persist (compare Figure 3.6c and Figure 3.6d).

For the test analysis of the four shapes (Fig. 3.5c) we used an absolute minimum distance of 8 pixels. The results are shown in Table 3.2. Comparison with the manual digitization shows that μ , Δ and Ω are closely reproduced. Deviations are due to the circumstance that during “blind” sampling of coordinates along the outline (picking points at fixed minimum distances), the exact corner points may be missed and accordingly the acute angles may be blunted. Note again, that the average angles, μ , only reflect the number of points sampled on the outlines.

For the analysis of our type microstructures (“cracked” and “gouge”, shown in Figure 3.2c) we also used an absolute minimum distance (of 8 pixels). The outlines of 55 cracked and 58 gouge

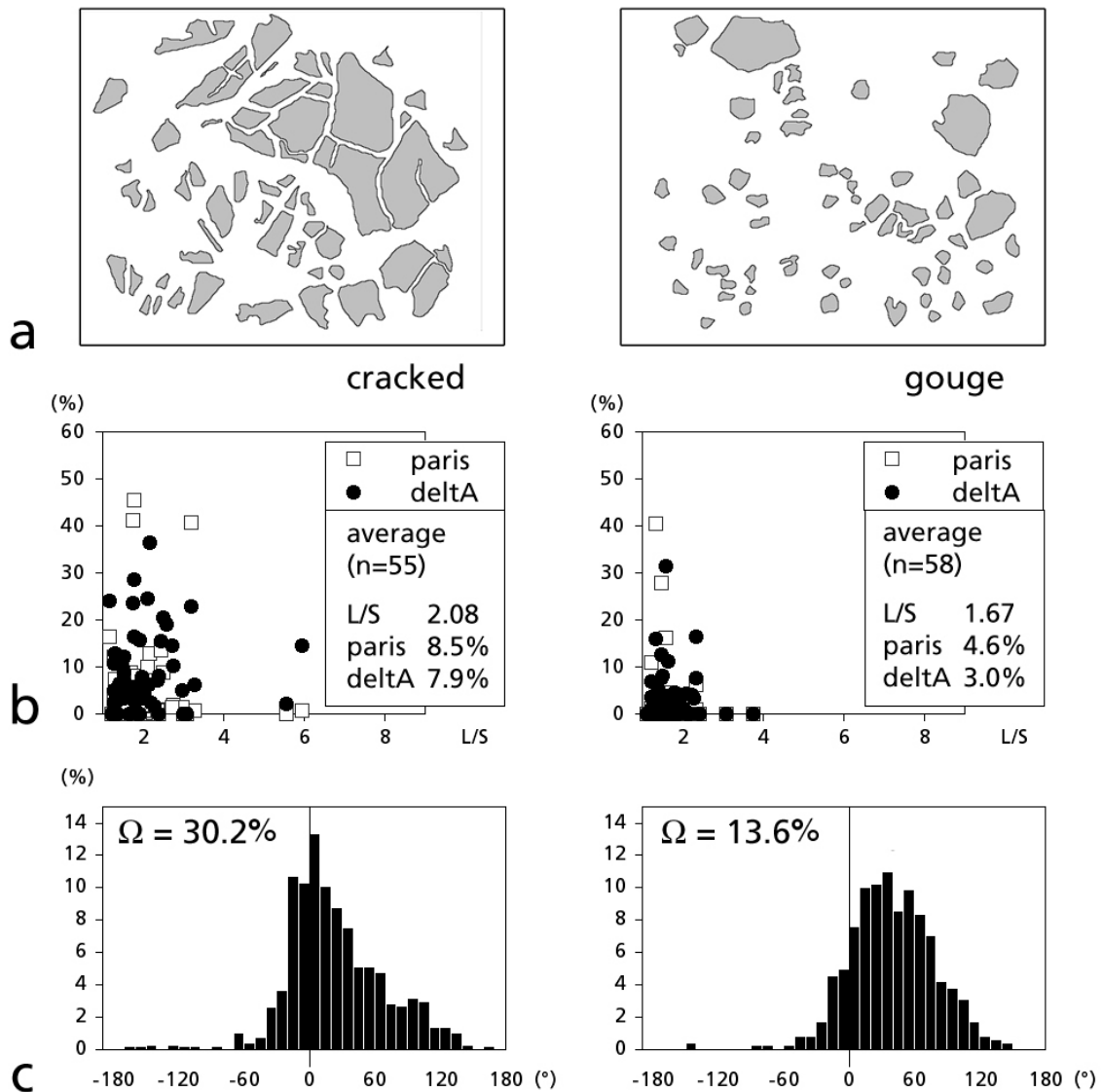


Figure 3.7: Shape analysis of fault rock. a) Automatically digitized outlines of microstructures shown in Figure 3.2c. b, c) Result of analysis using outlines shown in Figure 3.7a with minimum distance setting = 8 pixel. b) Shape factors (paris and deltaA) versus aspect ratio (L/S); number of evaluated particles and average values are indicated. c) Histograms of angles, values for percentage of angles $< 0^\circ$ (Ω) are indicated.

grains are shown in Figure 3.7a. The paris factor and deltaA are plotted against aspect ratio (Fig. 3.7b). The analysis shows that the cracked grains display a higher variability of shapes than the gouges. The variation of the paris factors is not identical to that of deltaA. Very high paris

factors are due to cracks that terminate inside particles and which cause substantial additional (excess) perimeter but do not produce much excess area, thus do not cause a comparably high ΔA value. The histograms of vertex angles are shown in Figure 3.7c. For fully convex particles, all vertex angles are $> 0^\circ$; the more concave the fragments, the more negative angles appear. The histograms of vertex angles of the cracked and the gouge site show that the proportion, Ω , of angles $< 0^\circ$ is much larger for the cracked fragments than for the gouge. In summary, the average values of cracked grains and gouge differ as follows: cracked grains have higher aspect ratios (L/S), higher Paris factors, higher ΔA values and higher Ω values than gouges (Fig. 3.7b and Fig. 3.7c).

3.4 Analysis of experimental fault rock

We now discuss the application of our new methods of analysis to experimentally produced fault rocks. We have selected two sequences of SEM images taken at increasing magnifications (Fig. 3.8) to determine the complete GSD of cracked grains and gouge separately for quartz and feldspar. The results of the grain size analysis are shown in Figure 3.9. All GSDs show the same characteristics: for small grains ($d < 2 \mu\text{m}$), the slope, D , is 1.0; for large grains ($d > 2 \mu\text{m}$), the slopes are considerably steeper, with D attaining values up to 2.26 (Fig. 3.9). At grain sizes larger than $2 \mu\text{m}$, both quartz and feldspar show higher D -values for gouge than for cracked material.

Figure 3.10 shows the D -mapping of a fractured quartz grain at relatively high magnification. The diameter of the Gaussian filter ($11 \mu\text{m}$) defines the spatial resolution of the matrix density image (Fig. 3.10b) and of the D -map (Fig. 3.10c). The lowest D -value attained with this filter size is 1.45. A value of $D > 1.5$ is more typical for cracked quartz (compare Figure 9). A value < 1.5 is not entirely unrealistic, however, it may also be an artefact, which is due to the small filter size. The smaller the Gaussian filter the lower the (local) D -value may become. In the extreme, if the filter would fit inside an intact grain, the measured D -value for the interior would be $D = 1.0$. The advantage of small filter sizes is to highlight details of the microstructure such as the spatial distribution of gouge material.

Figure 3.11 shows the D -mapping of sample 12nk at relatively low magnification. As the sample was broken, the thin section contains a number of gaps which were widened during vacuum impregnation of the glue and which the SEM image displays as black areas (Fig. 3.11a). From these black parts a (white) mask was prepared and overlaid on the D -map shown in Figure 3.11b to distinguish these apparent gouge areas from true gouge.

Figure 3.12 shows the results of the “ishapes” analysis, for manually digitized outlines

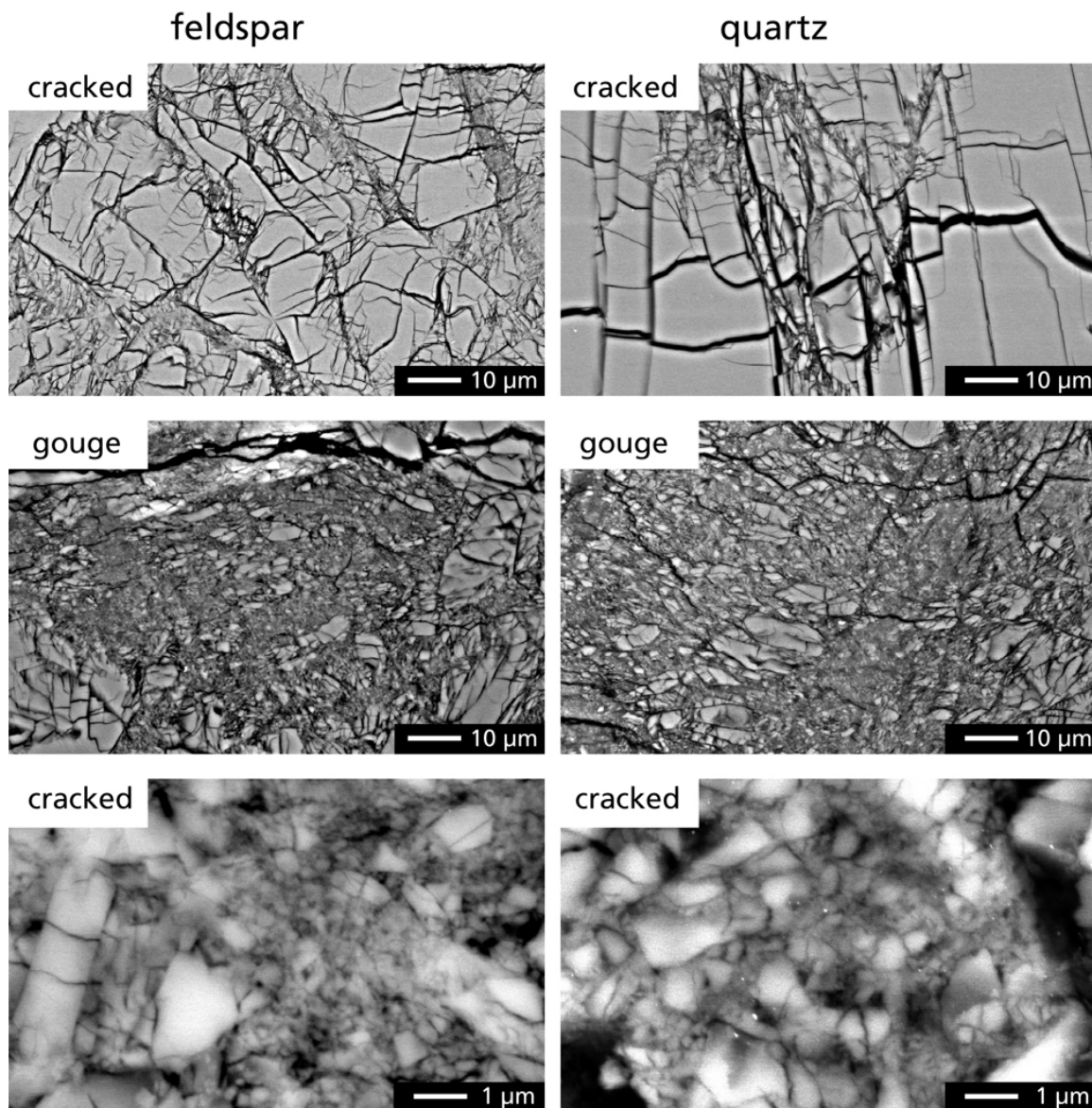


Figure 3.8: Microstructures of experimentally produced fault rocks. Cracked grains and gouge of feldspar and quartz are shown at two different magnifications (1000x and 10,000x). All microstructures are from sample 38nk.

(Fig. 3.12a) and for automatically digitized (exported) outlines and using minimum sampling distance of 8 pixels (Fig. 3.12b). In each case the results for quartz and feldspar and for cracked grains and gouge are shown separately. Note that the average values and the variability of the aspect ratio (L/S), the shape descriptors (paris factor and ΔA) are much larger for cracked grains than for gouge. Note also that the aspect ratios of cracked quartz are higher than for

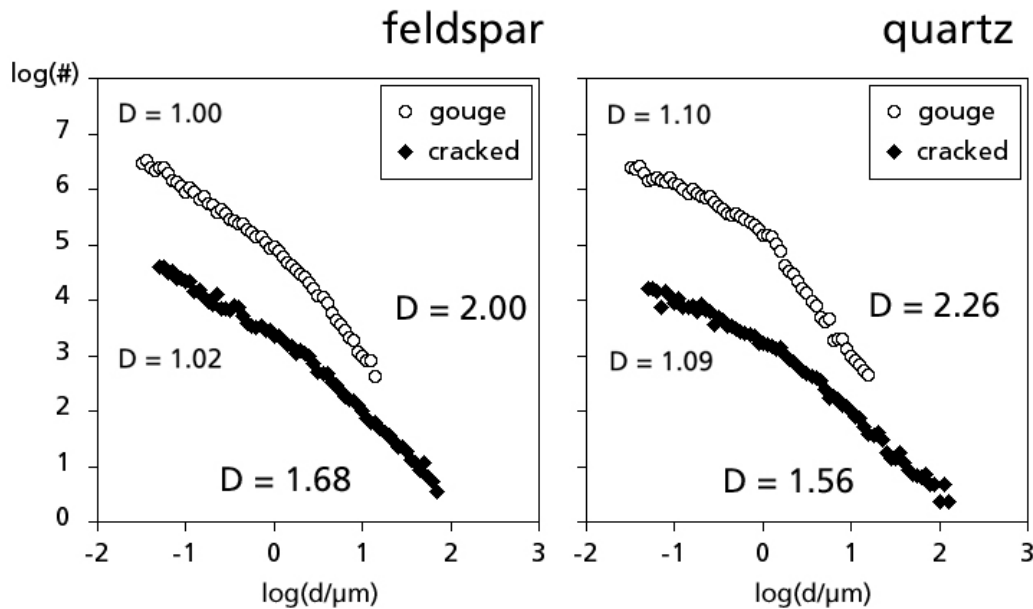


Figure 3.9: Non-cumulative grain size distribution (GSD) of experimentally produced fault rocks. Separate GSDs are shown for cracked grains and gouge and for feldspar and quartz; sample 64nk. Log($\#$)-log(d) diagram where d = equivalent diameter of particles in μm ; $\#$ = number of particles with diameter d . Separate power-law fits to grain sizes $> 2 \mu\text{m}$ and $< 2 \mu\text{m}$ are shown; derived D -values are indicated. This study is only concerned with D -values for grain sizes $> 2 \mu\text{m}$.

feldspar. The histograms showing the vertex angles are different for manually and automatically digitized cracked grains, while those for gouges are all very similar. However, the Ω values of manually and automatically digitized lines are approximately the same. They show significant differences between cracked grains and gouge. Figure 3.13 shows the values of the paris factor of quartz and feldspar, cracked grains and gouge, evaluated at 4 different magnifications.

3.5 Discussion

3.5.1 The nature of the grain size distribution

It has become a standard procedure to characterize fault rocks by their GSD. The measurements are done either in two dimensions on images (Biegel et al., 1989; Monzawa and Otsuki, 2003) or three dimensions by sieving or other methods (Anderson et al., 1980, 1983; Sammis et al., 1986; An and Sammis, 1994), for review Blenkinsop (see 1991). The GSDs are presented as log($\#$)-log(d) plots (Sammis et al., 1987; Marone and Scholz, 1989; Tsutsumi, 1999) and characterized by the slope D , the so-called “fractal dimension” (Mandelbrot, 1982; Sammis et al., 1987; Monzawa and Otsuki, 2003; Storti et al., 2003). Both types of representations of the GSD are used:

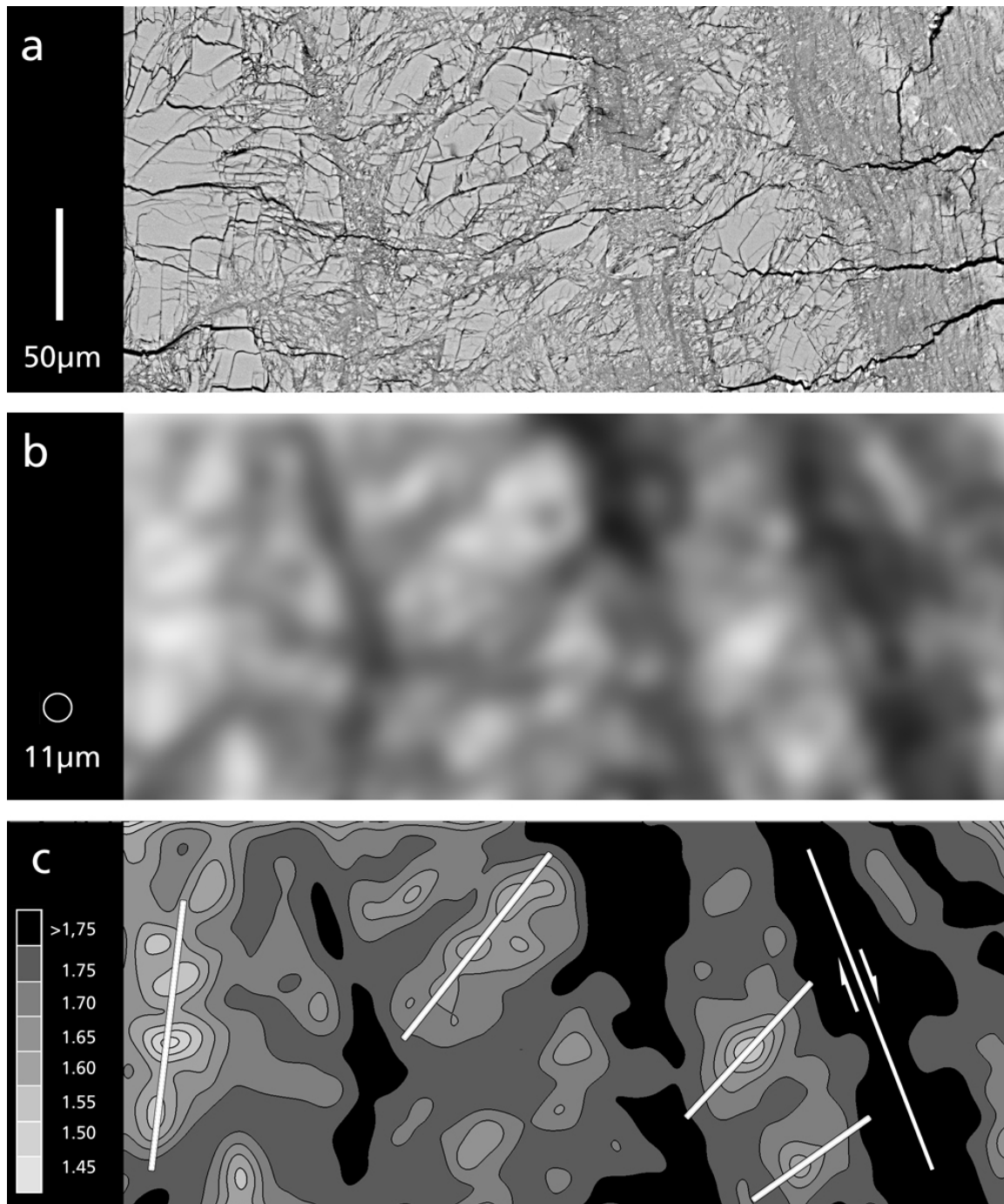


Figure 3.10: D -mapping of experimentally deformed quartz. a) SEM backscatter image of sample 38nk, showing cracked grains and gouge; constant grey value indicates 100% quartz. b) Matrix density image, obtained by Gaussian filtering of Figure 3.10a using a filter diameter of $11\ \mu\text{m}$; circle on left shows size of filter. c) D -map of Figure 3.10b with superposed D -contours; black = areas where $D = 2$ (gouge); grey shades = regions with cracked grains; lowest D -value attained is 1.45. White lines indicate axes of coherent regions with low D -value, shear sense along gouge zone is indicated; compression direction is vertical.

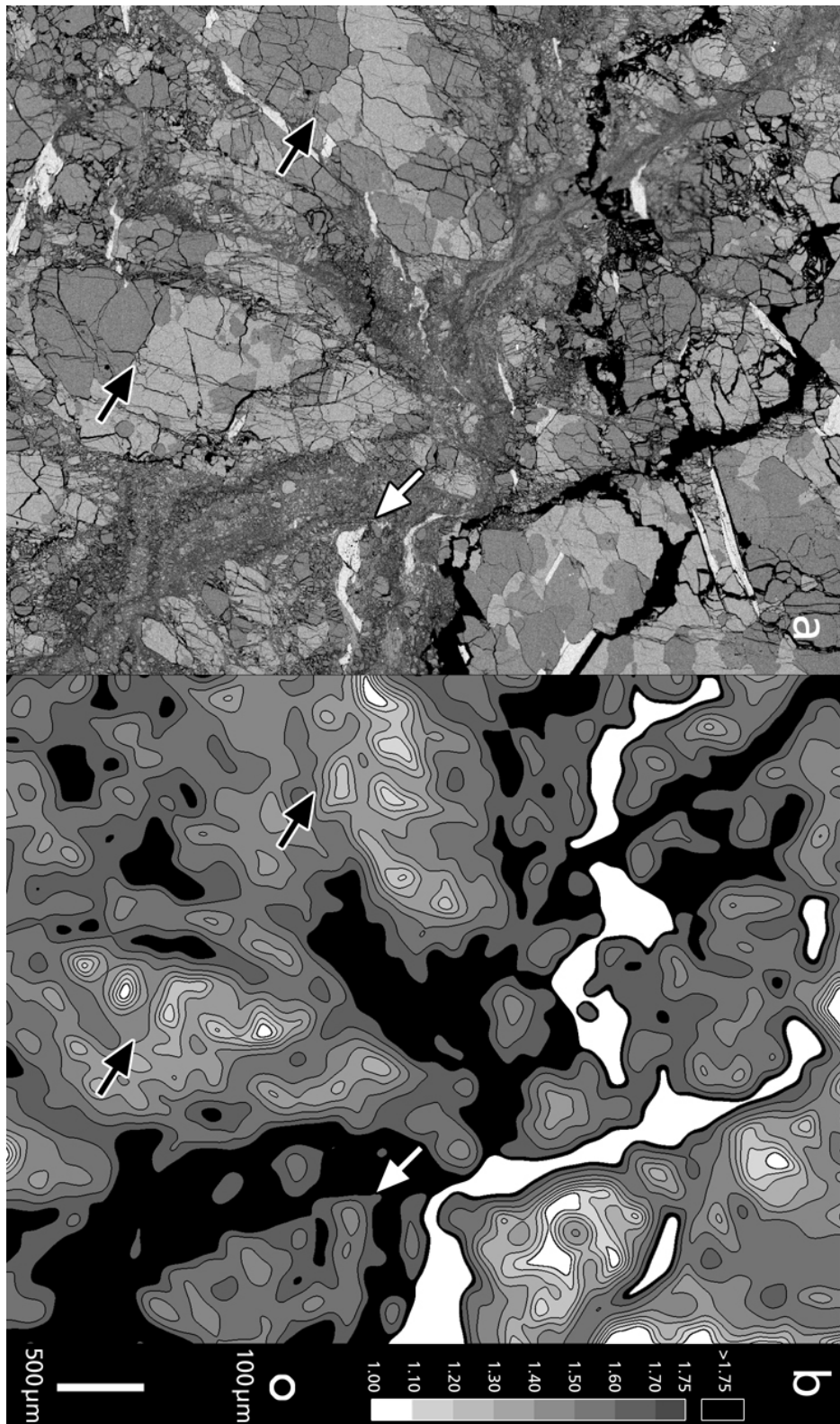


Figure 3.11: D-mapping at the scale of a sample. a) SEM backscatter image of sample 12nk, showing cracked grains and gouge; light grey = K-feldspar, dark grey value = quartz + plagioclase. b) D-map of matrix density images of Figure 3.11a with superposed D-contours; grey shades = regions with cracked grains; black = areas where $D = 2$ (gouge); white areas within gouge indicate holes; size of Gauss filter is indicated. Arrows point to details discussed in text.

cumulative ones with $\log(\# > d) - \log(d)$ and regular ones with $\log(\#) - \log(d)$. Fractal dimensions between 0.3 and 2.6 have been reported.

In a comparison of image analysis and sieving it has been shown that the shape of the grains is an important parameter influencing the sieving size distribution of fractured objects (Fernelund, 1998; Rawling and Goodwin, 2003). Especially angular and curved grains are more accurately measured with image analysis. We measure our GSDs in two dimensions, present the data in the form of log-log plots, and derive characteristic slopes, D . However, we do not generally interpret these slopes in terms of the fractal dimensions of the GSD. First, because we always find two D -values, a lower one for small grain sizes and a higher one for larger grain sizes. Secondly, because the D -values derived for the larger grain sizes of the gouge attain values in excess of 2, while $D > 2$ is an impossible value for a fractal dimensions measured in two dimension (see Appendix).

Our data consistently show that the GSDs of cracked material and of gouge have two separate slopes, D . The slope change occurs between 1 and 3 μm grain size and may be associated with the so-called grinding limit (Kendall, 1978), which is 1.7 μm for quartz (Prasher, 1987). For grain sizes smaller than 1 to 3 μm , the D -value for the GSD is ~ 1 for all types of fault rock, for cracked material and gouge, and for quartz and feldspar. At grain sizes above 1 to 3 μm , the D -values differ: for cracked quartz and feldspar, D is below 2, on the order of 1.6 and 1.7, respectively; for quartz and feldspar gouge, D is above 2, on the order of 2.3 and 2.0, respectively (see Figure 3.3a and Figure 3.9).

The process of self-similar cataclasis has been invoked to explain the fractal dimension of the GSD of fault gouges (Sammis et al., 1986). Based on the model of a progressively fragmented cube (Turcotte, 1992), GSDs with fractal dimensions between 0 and 3 can be calculated (see Appendix), where high D -values are typical for intensive comminution, indicating large proportions of relatively fine grain sizes at all scales (Mandelbrot, 1982; Turcotte, 1986). Applying stereological concepts for random sectioning (Underwood, 1970), one can show that if a given fractal GSD (of 3-d grains) is sampled on a random two-dimensional section, the fractal dimension of the corresponding size distribution of 2-d sections is lowered by 1 (Turcotte, 1986; An and Sammis, 1994). In other words, the maximum fractal dimension of two-dimensional sections is 2 (see Appendix). However, D -values > 2 have been reported repeatedly (e.g. An and Sammis, 1994; Otsuki et al., 2003; Storti et al., 2003; Hadizadeh and Johnson, 2003; Monzawa and Otsuki, 2003, Appendix D, Chapter 4). Also in this study, we find that the D -value of gouge material is always in excess of 2 (see Figure 3.3a and Figure 3.9). Only the cracked material shows D -values < 2 and thus is compatible with an interpretation as fractal.

Self-similar fragmentation processes cannot explain fractal dimensions in excess of 3, and there-

fore the interpretation of the slope D of the GSD (on a log-log plot) in terms fractal dimension is misleading. In the case of gouges it is possible to invoke additional (non-fractal) comminution processes such as abrasion and spalling (Storti et al., 2003, Chapter 4) to explain D -values > 3 . However, since these processes are clearly non-fractal, it would be better not to refer to the slope of the power-law fit to the GSD as “fractal dimension”.

3.5.2 D -mapping

In a general way, the GSD and the area percentage of what appears as matrix on a given image (Fig. 3.3b) are related to one another. At a given magnification we define as “matrix” that fraction of a material that cannot be resolved optically, i.e., that fraction of a GSD that has a grain size smaller than a given threshold (cut-off) grain size. The fractal model provides a means to quantify this relation for cracked materials. We use the E value ($E = 3 - D$), which describes the volume distribution of the fractal size distributions (Turcotte, 1986), to calculate the apparent matrix content (see Appendix). In Figure 3.3b, the curves for three different cut-off grain sizes are shown. Obviously, if only the three largest size classes ($d = 1, 1/2$ and $1/4$) are considered as grains and grains smaller than $1/4$ as matrix (curve $1/4$), a GSD with a slope D of 1.5 (in 2 dimension), i.e. with a fractal dimension of 2.5 (in 3 dimensions) has an area percentage of matrix of 50%. If the matrix only includes grains that are smaller than $1/16$ of the largest grain size, the corresponding area percentage of matrix is only 25%, and 50% matrix is reached only if $D = 1.75$.

Figure 3.10 shows the D -map of fractured quartz. A number of gouge zones (black, $D > 2.0$) separate layers of cracked material (grey, $D < 1.75$). From the increasing rotation of coherent and semi-coherent aggregates of cracked material (see rotation of superposed white axes) a dextral shear along the gouge band is inferred and this is in accordance with microscopic investigations of the sample. From left to right, both the width of the gouge bands (i.e., the amount of gouge material) and the amount of rotation increase. D -maps such as these are useful for identifying regions of cracked and gouge material for further analysis.

Figure 3.11 shows the D -map of a major part of an experimental sample (compression direction is vertical). The black areas (gouge) form two poorly connected zones dipping from the upper left to the lower right, and a short conjugate segment in the center. Black arrows point to quartz - K-feldspar grain boundaries (Fig. 3.11a). The corresponding sites in the D -map (Fig. 3.11b) show that in one case (on the left), the change of mineral composition is associated with a change of D -value. In the other case (on the right) the major change of D is approximately vertical (subparallel to the conjugate segment of the gouge zone) while the quartz - K-feldspar boundary

is approximately horizontal. In other words, the variations of D that are visible on this D -map do not depend on mineral composition but on fragmentation intensity.

The white arrow (in Fig. 3.11) points to a biotite grain. This grain is fractured and plastically deformed and consequently it produces a low D -value. In as much as the D -map measures the fragmentation intensity, the rendering of micas as areas of low fragmentation intensity is correct. However, “low fragmentation intensity” has a different meaning for biotite than for quartz or K-feldspar, in one case it indicates soft and plastic behaviour, in the other hard and rigid behaviour. In other words, if biotites are not eliminated (masked from the picture), the D -maps cannot easily be interpreted as mechanical maps, where low D -values indicate less fragmentation or rigid behaviour and high D -values indicate intensive fragmentation and cataclastic flow.

Assuming that the portion visible in Figure 3.11 is representative of the entire sample, the total area percentage, i.e., the volume percentage of gouge produced in sample 12nk is 19%. Such a high proportion of fault gouge is unusual and was obtained only in this un-confined experiment. Under controlled conditions formation of gouge is more localized and the yield is considerably lower.

3.5.3 Shape factors

The program “ishapes” calculates a number of shape descriptors, of which we use the aspect ratio ($L/S = \text{longest/shortest projection}$), the excess perimeter (paris factor), the excess area (deltA), and the histogram of the angles at the vertices. Comparing the paris factor and deltA permits the distinction of grains with narrow cracks (high paris factor - low deltA) and grains with more rounded indentations (lower paris factor - higher deltA).

Both the paris factor and the deltA values display considerable scatter (Fig. 3.12a): the cracked material has higher paris factors and higher deltA values than the gouge. Being rounded, the gouges always show low L/S ratios and low paris factors and deltA values. Cracked feldspar shows lower aspect ratios (L/S) and higher paris factors and deltA values than quartz. Feldspars have two perpendicular cleavage planes, causing indented shapes. Feldspars fracture more effectively than quartz (Tullis and Yund, 1977), a circumstance which does not only explain the higher D -value of cracked feldspar measured in the previous section, but which may also explain the lower aspect ratio.

Automatic digitization (as in Fig. 3.12b) reproduces the discrimination of cracked and gouge material. Comparing these results with the corresponding manual digitization (Fig. 3.12a), one notes that - with the exception of the paris factor for cracked feldspar - automatic digitization

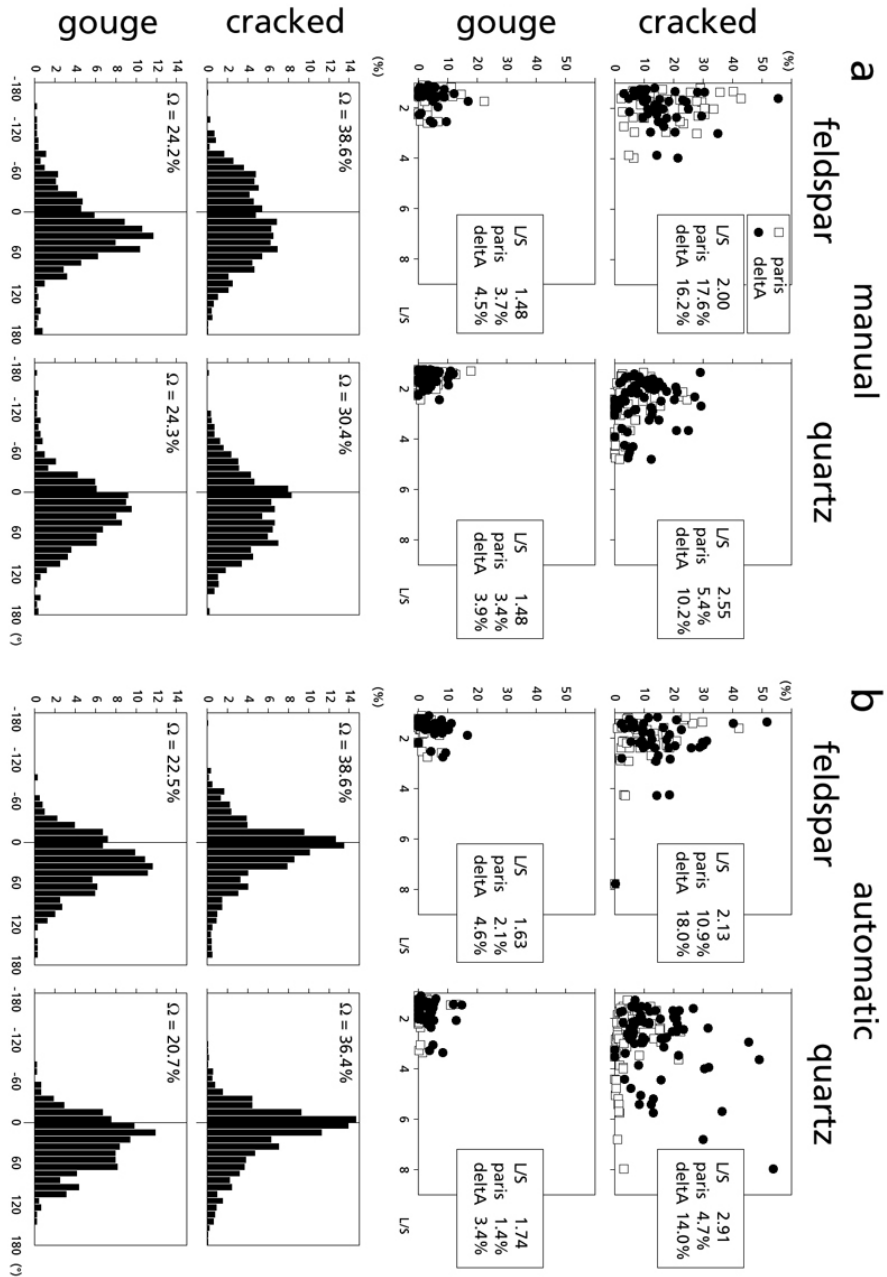


Figure 3.12: Comparative shape analysis of experimentally faulted granite. a) Using manually digitized outlines; b) using automatically digitized outlines and a minimum spacing of 8 pixels. Identical grains of samples 64nk and 38nk were used, magnification of SEM image = 500x. Top: diagrams showing shape factors (paris and delta) as a function of aspect ratio (L/S); separate results for cracked grains and gouge, developed in feldspar and quartz; average values are indicated. Bottom: corresponding histograms of vertex angles; values for percentage of angles $< 0^\circ$ (Ω) are indicated. Points sampled on a straight line (where $\alpha = 0^\circ$) are eliminated.

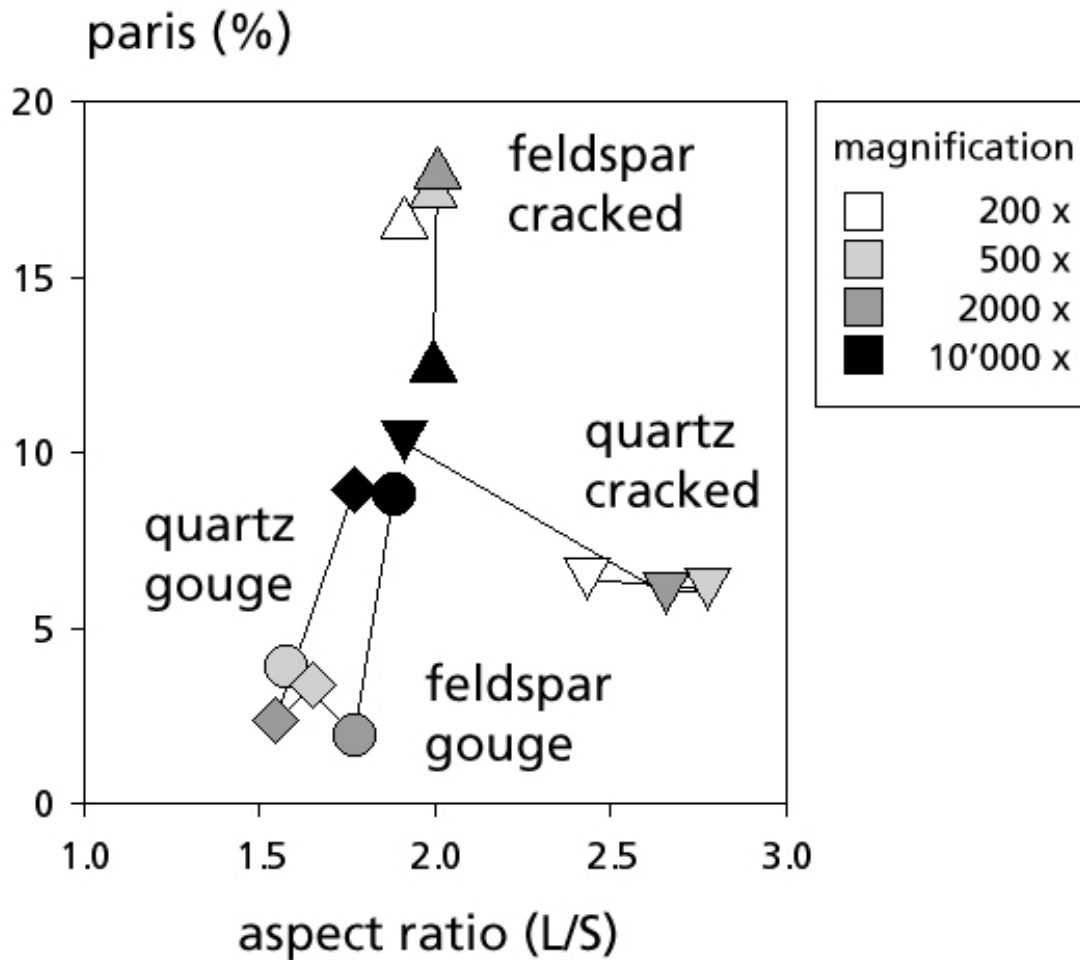


Figure 3.13: Shape analysis at different magnifications. Average values of the paris factor are shown as a function of aspect ratio (L/S); manually digitized outlines from samples 38nk and 64nk were used. Different symbols denote feldspar and quartz, cracked and gouge; grey shades from white to black indicate increasing magnification of SEM images. Note convergence of results at the highest magnification.

yields the same results as manual digitization. The general observation is that cracked grains can be distinguished from gouge, and that, in the cracked state, quartz and feldspar behave differently. From the point of view of shapes, all gouges are quite similar. The paris factor is always slightly lower than ΔA , indicating that the concavities are gentle and rounded. Similar differences have been found by Lin (1999a), who described the roundness of clasts in ultracataclasites and pseudotachylytes by comparing radius of curvature within angles of the grain with the radius of the total grain and has observed that cataclasites are less rounded than pseudotachylyte clasts.

At low magnifications, i.e., for larger grain sizes, the shapes of cracked feldspar and quartz are quite different, while the gouges are similar, as has been discussed above. At the highest magnifications, however, gouge and cracked grains are virtually indiscernable (Fig. 3.13). This may imply that, at the smallest investigated scale, the fragmentation process has a different effect on grain shape or is a different process altogether than at the large scale. Small cracked grains are "rounder" than large cracked grains: in feldspar they are less jagged (lower Paris factors), in quartz they are less elongate (lower aspect ratios). Also, gouge formation does not affect the smallest grains or, if it does, it does not affect their shape: the Paris factor remains constant or decreases only very slightly from 11–12% to 9–10%.

The vertex angles histograms of cracked and gouge materials are significantly different (Fig. 3.12). As one would expect the fraction of angles $< 0^\circ$, i.e., indented angles are much more frequent in cracked materials than in gouges and, as a consequence, the Ω -values of cracked materials are higher than those of gouges. In fact, the Ω -value is a very sensitive descriptor of fault rock development, decreasing from $\Omega \approx 38\%$ for cracked fragments to $\Omega \approx 20\%$ for mature gouge material. In view of the strong dependence of the histogram of vertex angles on the digitizing procedure (automatic or manual), in particular on the number of points digitized per grain, we have not as yet explored, whether other statistical parameters such as the maximum values, the standard deviation, the range of values or the skewness could be used to distinguish cracked material from gouge.

3.6 Conclusions

We used the public domains software "ImageSXM", a number of macros ("Lazy D -map"), and an improved version of the image analysis program "ishapes" to quantify the microstructures of granitoid fault rock, in particular to distinguish cracked material and gouge through grain size distributions (GSDs) and grain shapes.

1. The GSDs of fault rocks have been measured and the slopes, D , on a log-log plot have been determined. For all fault rocks, two slopes are recognized: below grain sizes of approximately $2 \mu\text{m}$, $D \approx 1$ for both cracked and gouge material. For $d > 2 \mu\text{m}$, $D \approx 1.6$ for cracked material and $D \leq 2$ for gouge (the values apply to 2-d grain size measurements).
2. The results comply with a self-similar process of fragmentation for the cracked material, but the alleged fractal nature of gouge is questioned.
3. D -mapping (spatial visualization of the slope D of GSDs) is shown to be a useful exploratory tool; it can be used to identify the spatial distribution of cracked material or gouge and to trace shear zone networks.

4. The aspect ratio of particles (L/S) of cracked material (1.0–5.0) is higher than that of gouge (1.0 to 2.0). L/S of cracked quartz (1.0–5.0) is higher than L/S of cracked feldspar (1.0 to 3.0).
5. The paris factors and ΔA values of cracked material display a wide scatter. Average values of the paris factor are $\sim 15\%$ for feldspar and 5% for quartz; average values of ΔA are 15 to 20% for feldspar and 10–15% for quartz. Since $\Delta A \approx$ paris factor, indentations are wide (no cracks). In gouges, the paris factors and ΔA values are low ($< 5\%$) and show less scatter. Again, paris factor $\approx \Delta A$, and indentations are small and rounded.
6. The histogram of vertex angles discriminates cracked materials from gouges: Ω -values of cracked materials (35–40%) are significantly higher than the Ω -values of gouges (20–25%).
7. Automatic digitization lowers the bias and improves the distinction between cracked material and gouges.

Appendix: Derivation of a look-up table for D -mapping

The fragmentation of a cube (size = d_1) into eight cubes (size $d_2 = \frac{d_1}{2}$) is considered, with different proportions of crushing ($\frac{N_2}{N_1} = 1$ to 7) see (e.g. Turcotte, 1986). Using a spreadsheet program, the numerical and volume densities and the cumulative volume densities were calculated (Appendix Figure 3.14 a, b, c).

The fractal dimension, D , of the resulting grain size distribution (GSD) is given by:

$$D = \frac{\log(N_2/N_1)}{\log(d_1/d_2)} \quad (3.1)$$

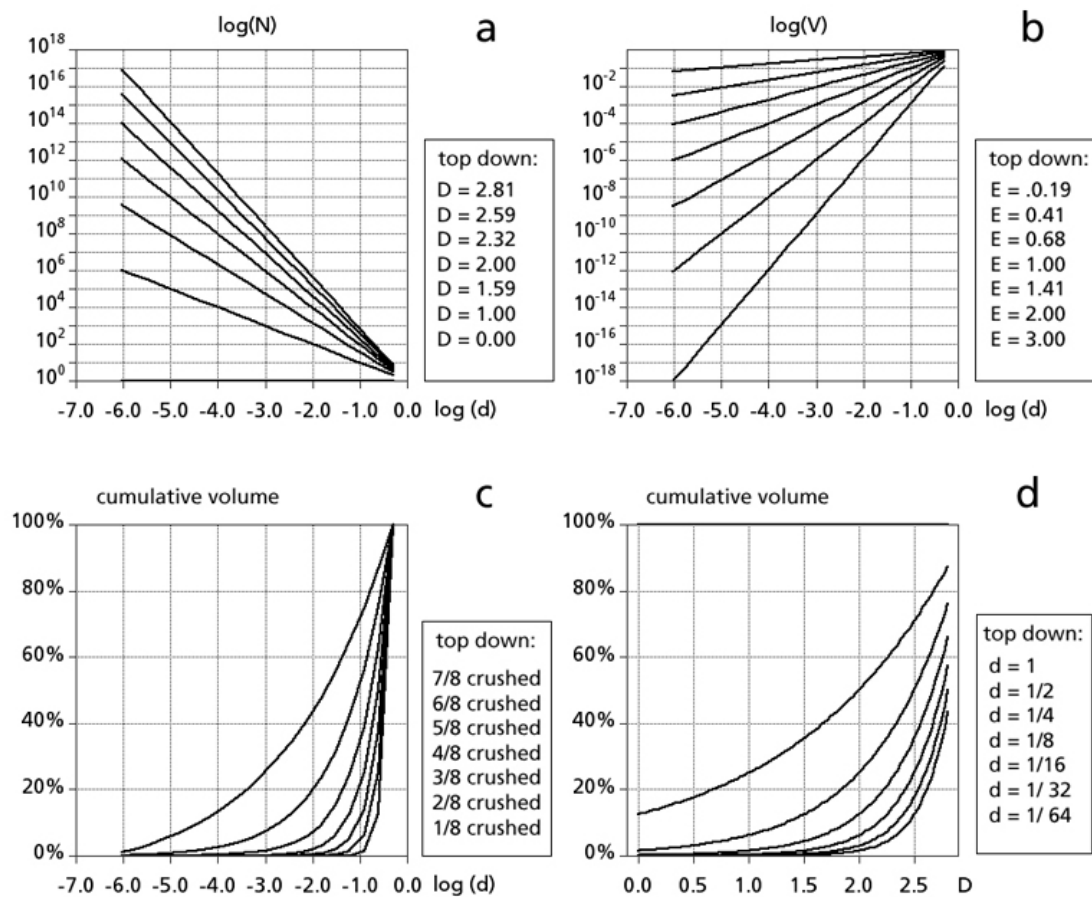


Figure 3.14: Derivation of matrix density as function of fractal dimension. a) $\log(N)$ versus $\log(d)$, where N = number of grains, d = diameter of grains, for various fractal dimensions, D . b) $\log(V)$ versus $\log(d)$, where V = volume of grains, for various volume fractions, E . c) cumulative matrix volume (%) versus $\log(d)$, for various proportion of crushed grains; d = largest grain size that is counted as matrix ($d = 1$ equals largest grain size). d) volume density of matrix (%) versus fractal dimension, D , for various cut-off grain sizes, d .

D is the slope of the $\log(N) - \log(d)$ plot of the GSD, where d is the grain size and N is either $N(d)$, the number of grains of size d , or $N(>d)$, the number of grains larger than d . For proportions $N_2 / N_1 = 1$ to 7 of crushed cubes, the following D -values are obtained: 0.18, 1.02, 1.60, 2.01, 2.33, 2.59, and 2.81, respectively, if N is $N(>d)$; and 0.00, 1.00, 1.59, 2.00, 2.32, 2.59, and 2.81, if N is $N(d)$. For $D > 1$, the difference becomes negligible.

In 2 dimensions, the probability of sectioning a fragment is proportional to its size. Therefore, N_2 in equation (3.1) becomes $(N_2 \cdot d_2)$ and the slope D is reduced by 1.

The volume density is given by:

$$E = \frac{\log(V_1/V_2)}{\log(d_1/d_2)} \quad (3.2)$$

where V is the volume of a given the grain size.

$$E + D = 3.00 \quad (3.3)$$

Transposing the spread sheet that was used to calculate the cumulative volume as function of d , yields the cumulative volume up to d_1 , $d_1/2$, $d_1/4$ etc. for different D . If matrix is defined as the volume fraction below a given cut-off grain size, these different volume densities correspond to different matrix densities, m , which are defined for decreasing cut-off grain sizes. The cut-off grain size defines the largest grain size that is counted as matrix. The matrix densities are plotted as a function of D (Appendix Figure 3.14 d). The curve fits yields increasing exponents for decreasing cut-off grain size. Inverting the exponential function $m \sim \exp(D)$ for a given cut-off grain size yields the logarithmic dependence of $D \sim \log(m)$.

To convert area percentages to volume densities we use the simple stereological relation:

$$\frac{A_\alpha}{A_{total}} = \frac{V_\alpha}{V_{total}} \quad (3.4)$$

where A_α = the area of phase α , A_{total} = the total area, V_α = the volume of phase α and V_{total} = the total volume (see Underwood, 1970).

Chapter 4

*Grain size distributions of fault rocks: a comparison between experimentally and naturally deformed granitoids.**

In this contribution, the grain size distribution and its D -values are further investigated. From these measures, conclusions are drawn on the process of rupturing and grain size reduction and on the alleged fractal nature of fault rock. The results from laboratory experiments are compared to a natural fault zone.

*Published in the Journal of Structural Geology as: Keulen, N., R. Heilbronner, H. Stünitz, A.-M. Boullier and H. Ito, Grain size distributions of fault rocks: a comparison between experimentally and naturally deformed granitoids, Volume 29, Issue 8, Pages 1282-1300

Abstract

We have investigated the grain size distribution (GSD) of granitoid fault rock by comparing experimentally produced gouge with fault rock from the Nojima Fault Zone. Triaxial experiments were carried out on wet and dry intact samples of Verzasca Gneiss at $T = 300\text{--}500\text{ }^\circ\text{C}$, $P_c = 500$ and 1030 MPa, $\dot{\epsilon} = 0.013\text{--}1.6 \times 10^{-4}\text{ s}^{-1}$. The GSD has been determined from SEM-micrographs and is characterized by the slope, D , of its log(frequency)-log(radius) histogram. The GSD is not fractal; we observe two slopes for all GSDs. The larger grains in experimentally deformed samples have a D -value, $D_{>}$, of 2.04 and 2.26 for feldspar and quartz gouge. Cracked grains yield values of $D = 1.5\text{--}1.6$. Increasing the confining pressure or temperature decreases the D -value. For grains smaller than $\sim 2\text{ }\mu\text{m}$ another D -value, $D_{<}$, of 0.9–1.1 is observed. The grain radius at the slope change, r_K , corresponds to the grinding limit of quartz, so that r_K probably represents a change in the dominant comminution mechanism from grinding to attrition-processes. The GSD obtained from deformation experiments agrees well with results for the Nojima Fault Zone: $D_{>} = 2.02$ for gouge and 1.64 for cracked grains; $D_{<} = 0.97$. Grain size reduction in fault zones develops by a two-stage process: rupturing creates cracked grains; further displacement of fragments causes further comminution by wear and attrition. Cracked grains have been used to calculate the surface energy associated with faulting; it follows that this energy forms a small fraction in the total energy-budget of earthquakes.

4.1 Introduction

4.1.1 Overview

Major fault zones and earthquakes in the upper crust typically develop highly localized zones of deformation. At the macroscopic scale, faults usually appear as narrow, highly deformed zones or networks embedded in wide damage zones of relatively low deformation. Observations on natural fault zones have shown that this localization of deformation along faults occurs both in space and time (e.g. Mitra, 1993; Faulkner et al., 2003; Wilson et al., 2003). Most of the displacement takes place in very narrow zones within the gouge of typically a few to 1 mm wide, leaving the rest of the gouge inactive (e.g. Wibberley and Shimamoto, 2005; Chester et al., 2005). Bos et al. (2000) have made this same observation for laboratory experiments on halite.

Within these narrow deformation zones gouge with a wide range of grain sizes has been produced (e.g. Storti et al., 2003; Boullier et al., 2004a, Appendix D). At the microscopic scale, the fault rock consists of cataclasite or gouge with properties that change as a function of time and space. Displacement on a fault zone causes the evolution from a thin fracture to a wider gouge

zone. The microstructures of the fault rocks influence and reflect the mechanics of faulting, i.e., earthquakes. For example, evidence for coseismic hydraulic fracturing (Boullier et al., 2004b) or for a change in the frictional properties of faults resulting from their grain shape (Mair et al., 2002) has been obtained through microstructural studies. Despite experimental data and field observations on gouge, the properties of fault rock and the evolution of cracked grains to gouge still remain rather poorly understood.

4.1.2 Fault rocks

A number of definitions for fault rocks can be found in the literature (e.g. Sibson, 1977; White, 1982; Wise et al., 1984; Chester et al., 1985; Schmid and Handy, 1991). Usually, cohesive and non-cohesive fault rocks are attributed to cataclasis, a process involving fracturing, frictional sliding, dilatancy, and rigid-body rotation between grain fragments, grains, or clusters of grains. Sibson (1977) has defined gouge as a cataclastic rock without cohesion; the cohesive rock is called cataclasite. Many cohesive cataclasites in nature are thought to be the product of syn- or post-tectonic healing processes (Schmid and Handy, 1991).

In this study, however, we will distinguish different fault rocks on the basis of microstructures rather than inferred mechanical properties (see Heilbronner and Keulen, 2006). We will use the term “cracked grains” for angular fragments that have fractured without much displacement (such that the original geometrical relationship of the fragments can still be recognized). The term “gouge” will be used for more highly deformed fault rocks where the grains are more rounded and the original spatial relationship between the fragments is lost. The term “fault rocks” thus applies to both cracked grains and gouge.

4.1.3 Grain size distributions

A large number of studies has been dedicated to measuring and analyzing grain size distributions of fault rocks (e.g. Mitra, 1993; Blanpied et al., 1995; Lin, 1999b; Bos et al., 2000; Stewart et al., 2000; Kato et al., 2003). The grain size distribution (GSD) is considered as an important parameter for the characterization of the gouge (e.g. Sammis et al., 1987; Marone and Scholz, 1989; Hadizadeh and Johnson, 2003; Wilson et al., 2005; Chester et al., 2005). Within a certain size range the GSD may be self-similar (scale invariant) and in this case can be described by a power-law relationship (Mandelbrot, 1982). The slope of some power-law distributions, D , is called the fractal dimension (Turcotte, 1992; Korvin, 1992, and references in both). This D -value has often been used to compare the GSD of natural earthquake and fault zones, like the San Andreas Fault zone (e.g. Anderson et al., 1980; Blenkinsop, 1991), the Moine Thrust

(Blenkinsop and Rutter, 1986) or fault systems in Japan (Monzawa and Otsuki, 2003; Otsuki et al., 2003) with fault rocks derived from experiments (e.g. Marone and Scholz, 1989; Morrow and Byerlee, 1989; Amitrano and Schmittbuhl, 2002).

For the measurements of the GSD, several different methods have been used (see Table 4.1). The most classical one, originating from sedimentology, is sieving. By this method a distribution of mass against size is obtained (Anderson et al., 1980; Sammis et al., 1986). Other studies have used the Coulter counter (An and Sammis, 1994; Amitrano and Schmittbuhl, 2002; Wilson et al., 2005) or optical microscopy on thin sections (Biegel et al., 1989; Monzawa and Otsuki, 2003) these methods provide a description of the GSD in terms of frequency versus grain size. A disadvantage of sieving and the use of light microscopes is that the size of smallest detectable grains is $\sim 2 \mu\text{m}$ (Table 4.1).

An easy way to measure the sizes of the grains smaller than $2 \mu\text{m}$ is scanning electron microscopy (SEM), as was done by Sammis et al. (1987) and Shao and Zou (1996), but in their samples no small grains were observed. Olgaard and Brace (1983); Yund et al. (1990); Chester et al. (2005) found grains as small as 15–50 nm with the TEM, but the TEM is unsuitable for measuring large numbers of grains necessary to obtain a size distribution. Wilson et al. (2005) used a Coulter counter and measured grains of 40 nm to $300 \mu\text{m}$. Nevertheless, the frequency distribution of grains sized between 30 nm and $2 \mu\text{m}$ is not very well known. We find that using scanning electron micrographs of impregnated and polished sections of gouge, reliable GSD in the size range larger than 60 nm can be obtained.

In a previous study (Chapter 3) two types of fault rock can be distinguished: cracked grains and gouge. Cracked grains and gouge can be discriminated on the basis of particle shape and grain size distributions. The D -values of gouge are always higher than those of cracked grains. Composition (quartz versus feldspar) influences various aspects of the particle shape of cracked grains and gouge (elongation, paris factor, etc.).

Table 4.1 shows a compilation of published results on the GSD of fault rocks: values of the fractal dimension vary between 0.8 and 2.6, but values of D between 1.5 and 2.1 are the most common for granitoid rocks. High D -values are generally obtained for more recently active fault zones, though a wide spread of D -values within a single fault zone can be observed.

As there appears to be link between fault rock microstructure (shape and GSD) and the mechanical behavior of faults, and since fossil fault rocks are important clues to seismic activity in the past, this study focuses on the microstructures of naturally and experimentally produced faults. In this paper we examine the influence of experimental conditions on the fault rock microstructure and we compare the results to a natural fault rock cored from a recently active segment of

Authors	year	rock type	location	nat/exp	method of analysis	(2D)-fractal dimension	smallest diam., μm
Samimis et al.	1987	granite	Lopez Canyon	natural	LM, manual	1.6	2
Samimis & Biegel	1989	granite		natural	manual	1.6	
Marone & Scholz	1989	quartz sand (porous)	Ottawa	experimental ^a	SEM, manual	1.6	1.5
Blenkinsop	1991	granite, gneiss	SAF,	natural ^b	LM, digitizer	0.8 - 2.1	3
		arkose	Cajon Pass Drillhole	natural ^b	LM, digitizer	1.6 - 2.0	5
An & Sammis	1994	granite	SAF, Tejon Pass	natural	sieve + Coult. Count.	1.4 - 2.6	2
		gneiss	San Gabriel	natural	sieve + Coult. Count.	1.6 - 1.9	2
		tonalite	Lopez Canyon	natural	sieve + Coult. Count.	1.5 - 1.9	2
Shao & Zou	1996	schist and gneiss	Qinling Mountain	natural	LM, manual	1.6	6
Monzawa & Otsuki	2003	granite	Tanakura	natural	LM, manual	1.7	10
		granite	It.-Shimotsutaki	natural	LM, manual	2.1	11
		granite	Koi	natural	LM, manual	2.1	8.1
		granite	Nojima	natural	LM, manual	2.3	7.7
Hadizadeh & Johnson	2003	quartz sandstone	Nojima	experimental ^c	LM, digitizer	1.9-2.5	3.5
Wilson et al.;	2005	granite	Masillon, Ohio	natural	Coult. Count.		0.04
Reches & Dewers	2005	granite	SAF, Tejon Pass	natural	Coult. Count.		0.04
Chester et al.	2005	granite	Bosman fault, R.S.A.	natural	LM + TEM, manual	2.0	0.05
Heilbronner & Keulen	2006	granitoids	SAF, Punchbowl	natural	SEM, digital	1.4 - 2.3	0.03
This study		granitoids	Verzasca	experimental ^d	SEM, digital	1.6 - 2.4	0.03
		granitoids	Nojima	natural	SEM, digital	1.4 - 2.3	0.03
		granitoids	Verzasca	experimental ^e	SEM, digital	1.4 - 2.3	0.03

Table 4.1: Published data on grain size analyses of fault rocks. Method of analysis: LM = light microscope image of thin section, SEM = scanning electron microscope image, manual = analogue box counting, digitizer = instrument for digital analysis of photomicrographs, digital = analyzed with computer, Coult.count. = laser diffraction particle size analysis. The indicated fractal dimension (D -value) is for 2-dimensional analysis. S.A.F. = San Andreas Fault, R.S.A. = Republic of South Africa.

^a $P_c = 100$ MPa, T_{room}

^b3.5 km depth, 90-250 °C

^c $P_c = 15 - 200$ MPa

^d $T = 15$ & 300 °C, $P_c = 50$ & 500 MPa

^e $T = 300 - 500$ °C, $P_c = 490-1030$ MPa

the Nojima Fault (Japan). The focus of the paper is on the grain size distributions (D -values cracked grains and gouge) and on the geometry and spatial distribution of the fault rock in the samples (D -mapping). The aim is to study the influence of temperature, confining pressure, axial shortening rate, total axial shortening, and fluid content on the grain size development of gouge material in deformed granitoids.

4.2 Materials and methods

4.2.1 Description of samples

Verzasca gneiss: The starting material for the study of experimental fault rocks is cored from a gneiss that was collected in the Val Verzasca (location: Swiss coordinates 704.65 - 126.30, Figure 4.1a). The composition is granitic, consisting of $\sim 29\%$ plagioclase, $\sim 27\%$ K-feldspar, $\sim 35\%$ quartz and $\sim 7\%$ mica, mainly biotite. The average grain size is $\sim 280 \mu\text{m}$ and the rock exhibits a faint foliation and lineation, while appearing isotropic at the thin section scale.

Nojima fault rock: The samples for the study of natural fault rocks are taken from the Nojima fault, which transects a Cretaceous granodiorite and the overlying sediments of the Kobe Group and Osaka Group (Figure 4.1b). The modal composition of the granodiorite is $\sim 33\%$ quartz, $\sim 34\%$ plagioclase, $\sim 19\%$ K-feldspar, $\sim 11\%$ biotite and $\sim 4\%$ hornblende. One year after the Hyogo-ken Nambu Earthquake (Kobe Earthquake, 17 January 1995, $M_w = 7.2$) three bore holes have been drilled through the Nojima fault at different depths (Ito et al., 1999; Ohtani et al., 2000; Tanaka et al., 2001; Murakami et al., 2002). The fault rock samples studied here (Figure 4.1c and 4.1d) are from the Hirabayashi drill core, which have reached the fault zone at a depth between 623.1 to 625.3 m (the thin sections are provided by the Geological Survey of Japan).

The history, as derived from the cores, can be divided into two major deformation episodes (Appendix D). An earlier deformation episode is related to a left-lateral movement on the Nojima Fault (Fabbri et al., 2004) prior to the deposition of the Middle to Late Eocene Kobe Group. Pseudotachylytes associated with this episode have been dated at 56.4 Ma by fission-tracks on zircons (Murakami and Tagami, 2004). A more recent Quaternary deformation episode is associated with a right-lateral movement along the Nojima fault and offsets the Plio-Pleistocene unconformity at the base of the Kobe Group Group (Murata et al., 2001). The studied thin sections are from the Quaternary deformation episode.

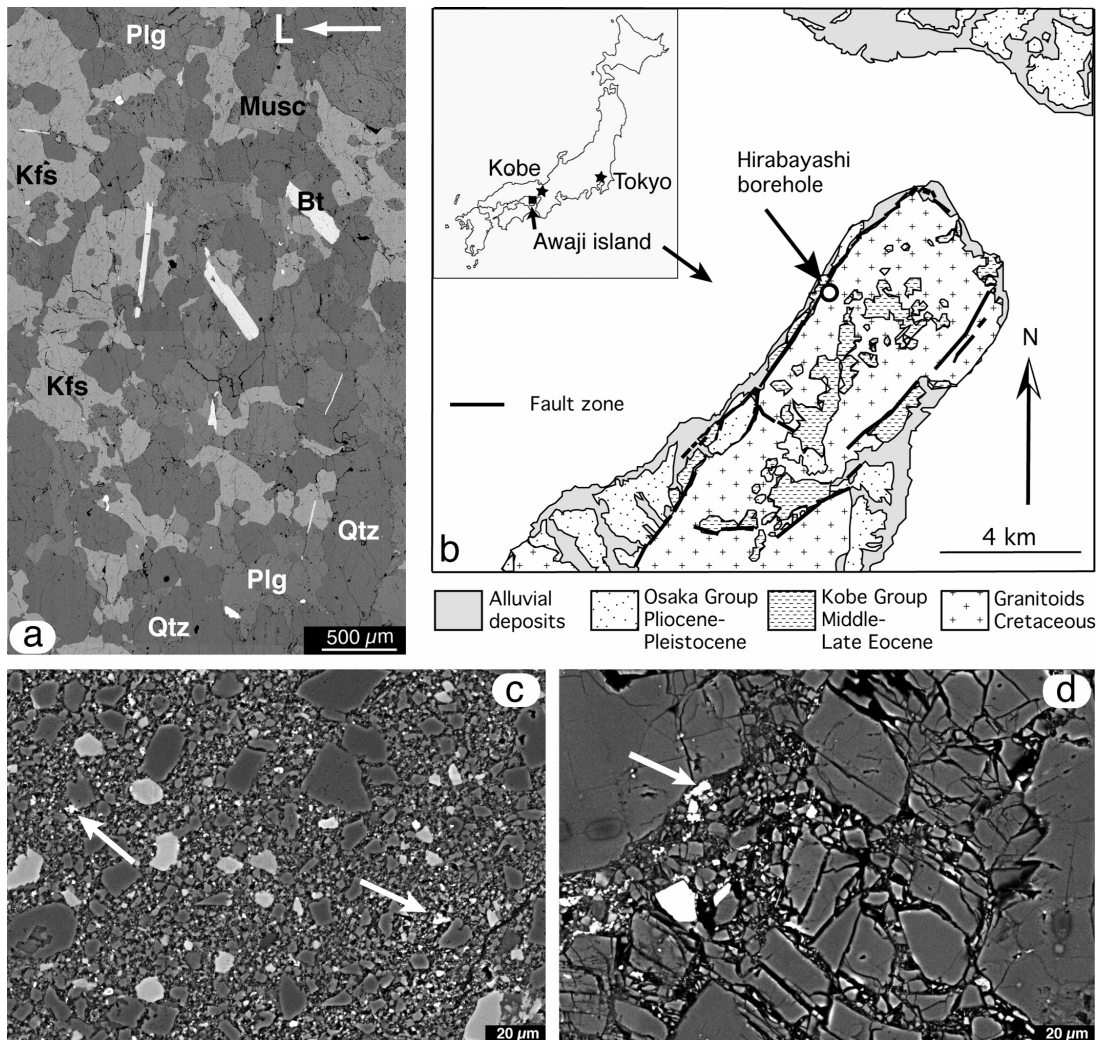


Figure 4.1: Starting material for experiments and natural fault rocks used in study. (a) Undeformed sample material from the Val Verzasca, Switzerland; scanning electron micrographs, back scatter contrast. This gneiss is isotropic at the scale of a thin section and has a granite composition. L = lineation. Minerals, in order of increasing brightness: quartz (Qtz), Na-rich plagioclase (Plg), muscovite (Musc), K-feldspar (Kfs), biotite (Bt). (b) Map of the northern part of Awaji Island, Japan, showing the locality of the Hirabayashi drill site in the Nojima Fault [after Ohtani et al. (2000)]. In-set shows the cities Tokyo and Kobe (stars) and the enlarged area (black square). (c, d) Fault rocks of the Nojima Fault Zone (recent event); scanning electron micrographs, back scatter contrast. (c) Gouge with rounded siderite fragments (white arrows) and pseudotachylyte fragment (black arrow). 623.50 m depth. (d) Cracked grains: individual parts can still be fitted together. The white arrow indicates siderite grains. 633.08 m depth.

4.2.2 Rock deformation experiments

Samples of Verzasca gneiss measuring 6.39 mm in diameter and 10.1 – 12.9 mm in length (L_0) are cored parallel to the mesoscopic lineation. Table 4.2 lists the used abbreviations. At this size, the sample width corresponds to approximately 25 grains. After polishing their flat ends, the samples are dried in an oven at 110 °C and atmospheric pressure for at least 24 hours. The samples are wrapped in Ni-foil and placed in a gold jacket. In all cases except for experiment 63nk, a “room-humidity” sample, approximately 0.2 wt% H₂O (1.68 to 2.14 μ l) is added and the jacket is weld-sealed. During welding, the jacket and sample are cooled in order to avoid water loss. The exact water content of the “wet” and “room-humidity” experiments is not known, we assume that even in the “room-humidity” experiment, some water may have be present along the grain boundaries.

Symbol	Definition
$D_{<}$	slope of power law fit for small grain sizes ($r < r_K$)
$D_{>}$	slope of power law fit for large grain sizes ($r > r_K$)
r_K	radius of grains at slope break of GSD
d_K	grain diameter at slope break of GSD
L_0	original length of sample
Δ_L	axial shortening of sample
r_{min}	minimum grain size used for calculation of GSD
r_{max}	maximum grain size used for calculation of GSD
A	cross sectional area of grain (pixel ²)
P	perimeter of cross section of grain (pixel)

Table 4.2: Abbreviations and definitions of measurements as used in this paper.

Deformation is carried out in a Grigg’s solid medium deformation apparatus as described by Tullis and Tullis (1986) and De Ronde (2004), using straight furnaces, alumina pistons and sodium chloride as the confining medium. The pistons are slightly bevelled, thus reducing their diameter from 6.39 mm to 6.2 mm at the sample-piston interface. Temperature is measured with Pt/Pt-10%Rh or Cromel/Alumel thermocouples. The standard or reference deformation conditions are “wet” samples, 300 °C temperature, 500 MPa confining pressure, $10^{-4}s^{-1}$ shortening rate, and a total axial displacement of 3.5 - 5.0 mm (samples 38nk and 64nk). In separate runs, one or more parameters are varied: 500 °C temperature, 1030 MPa confining pressure, up to 5.8 mm total displacement, $10^{-6}s^{-1}$ strain rate or no H₂O is added (see Table 4.3). During the experiment, pressure, load and displacement are recorded on a strip chart. Using the rigC4 program (www.unibas.ch/earth/micro/software/), with a correction for rig stiffness, the force-displacement and stress-strain curves are calculated.

After the experiment, the samples are quenched. To avoid loss or damage of the non-cohesive

Deformation conditions							
sample nr.	T	P_c	ax. $\dot{\epsilon}$	L_0	d_{chart}	$d_{(chart-1mm)}$	H_2O
	$^{\circ}C$	MPa	$\times 10^{-4}s^{-1}$	mm	mm	$\%wt$	
38nk	300	510	1.5	10.44	4.01	3.0	0.2
64nk	300	500	1.3	12.33	3.18	2.2	0.2
102nk	300	510	1.3	10.17	5.78	4.8	0.2
60nk	300	1030	1.5	10.13	3.47	2.5	0.2
68nk	500	520	1.4	10.32	4.28	3.3	0.2
63nk	300	530	1.4	12.11	4.25	3.3	0.0
66nk	300	490	0.015	12.37	4.64	3.6	0.2
70nk	500	500	0.013	12.95	4.97	4.0	0.2

Table 4.3: Deformation conditions of the experiments on Verzasca gneiss. T = temperature, P_c = confining pressure, e = axial shortening rate rate, L_0 = starting length of sample; d_{chart} = axial displacement from chart strip, $d_{(chart-1mm)}$ = corrected axial displacement, H_2O = amount of added water. Samples were quenched immediately after deformation.

fault rocks, the jackets are punctured and the samples are impregnated with epoxy. The samples are cut along the compressional axis and the deformed length of the sample is re-measured. Thin sections are prepared (polished and carbon coated) for observation in the light and scanning electron microscope.

4.2.3 Grain size analysis

For the grain size analysis, images with a wide range of magnifications are used. The micrographs of the experimental microstructures are collected using a Philips XL30 ESEM scanning electron microscope (20kV acceleration voltage; backscatter contrast); those of the Nojima Fault Zone are acquired with a Leica Stereoscan 440 SEM. For each sample a cascade of micrographs is prepared, starting with overviews at low magnifications (100x) and zooming in (to 20'000x) on selected areas with a factor of 2 to 2.5 from one magnification to the next. At each magnification, three or four images are taken of each kind of fault rock (quartz, feldspar, cracked grains and gouge). The total range of grain sizes (radius, r) observable at these magnifications is from <20 nm to >200 μm , however, because of the scarcity of measurable grains at either end of the distribution, the statistically reliable range does not exceed three orders of magnitude.

We use Image SXM (<http://reg.ssci.liv.ac.uk/>) and ImageJ (<http://rsb.info.nih.gov/ij/>) and special Macros and Plug-Ins (<http://www.unibas.ch/earth/micro/software>) for segmentation and image analysis. First, the images are pre-processed (removal of noise) and scaled to pixels (Figure 4.2a). Bitmaps of quartz and feldspar grains are obtained by density slicing at the corresponding grey levels and subsequent separation of grains (Figure 4.2b). The cross sectional

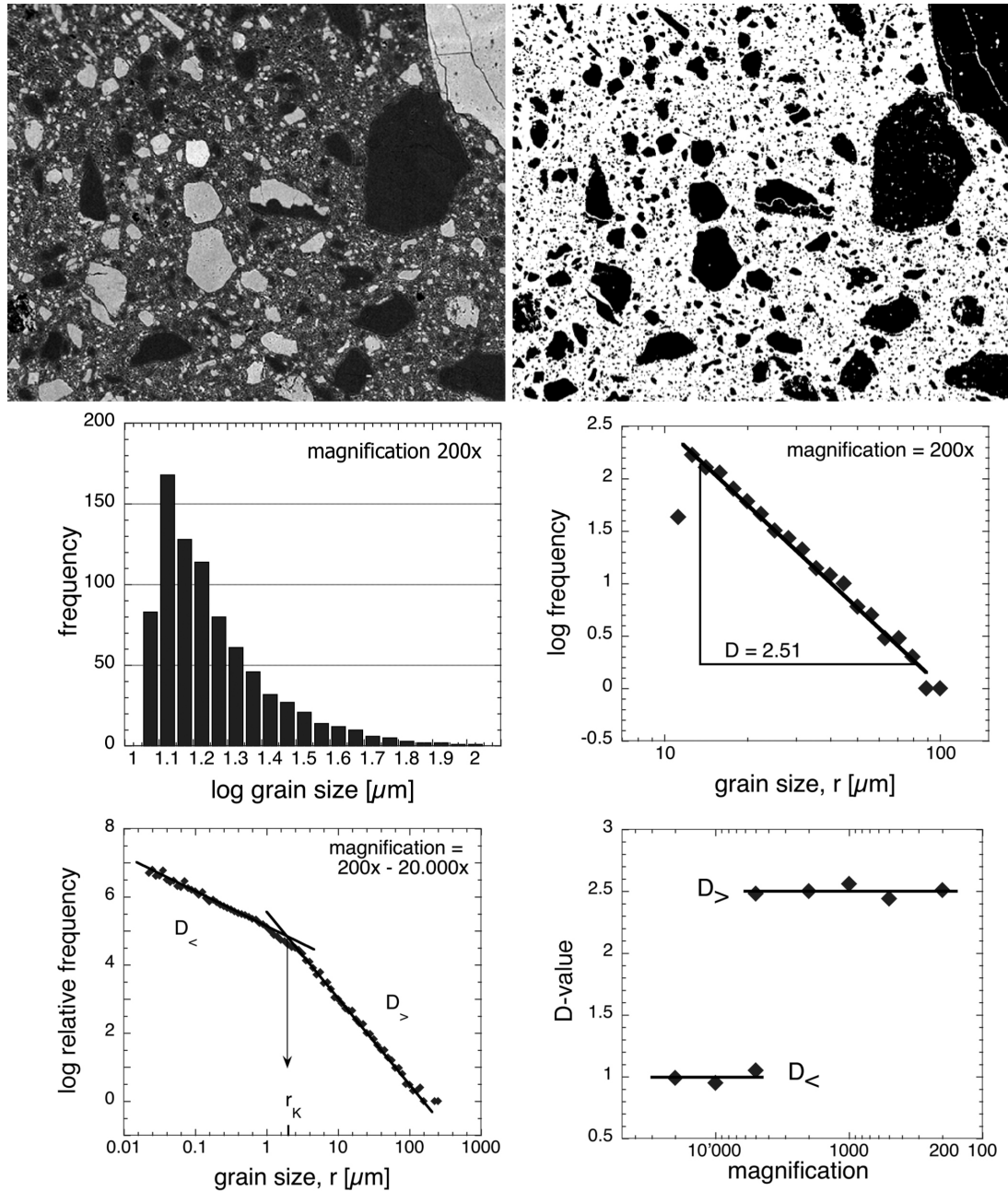


Figure 4.2: Schematics of the procedure for grain size analysis. (a) Starting image: gouge of Nojima Fault Zone; scanning electron micrographs, backscatter contrast. (b) Binary image. (c) Histogram of equivalent radii (1285 grains). (d) Log-log plot of frequency versus equivalent radius (20 bins per order of magnitude). The slope of the line fit yields the D -value. (e) Combined log-log plot for entire range of magnification, showing two distinct average D -values ($D_{<}$ and $D_{>}$ and r_K (see text)). (f) D -values versus magnification. Note that intermediate magnifications yield both D -values ($D_{<}$ and $D_{>}$).

areas, A (pixel²), and the perimeters, P (pixel), of the grains are measured using the Analyze menu of the software. After removing grains with areas smaller than 20 pixel², 300 to 1200 grains per image could be used. Some of the images taken at the highest magnification could not be processed automatically; in this case the grain boundaries are traced manually.

The resulting files of areas and perimeters were transferred to a spreadsheet program. The areas were restored by adding the pixel values of P , i.e., the band of pixels outlining the grain, to the area A within the outline. The equivalent radii, r , were calculated as

$$r = \sqrt{\frac{A + P}{\pi}} \quad (4.1)$$

and collected in a histogram (Figure 4.2c). On a log(frequency)-log(size) plot with 20 bins per order of magnitude of grain size, the slope (D) of the power-law fit is determined (Figure 4.2d). The results from all magnifications are then combined into a single plot, (Figure 4.2e), multiplying the frequency in each bin by a factor that reflects the relative magnification of the images and corrects for areas in the micrograph that were not investigated (e.g. large grains at edge of the micrograph, cracks). Overlapping bins of grain radii have been analyzed to check the correct up-scaling; the average frequency of the overlapping bins is used to draw the combined GSD plot. Figure 4.2f shows the individual D -values as a function of magnification.

In all samples, two distinct D -values are obtained: a shallower slope ($D_{<}$) at smaller grain sizes and a higher slope ($D_{>}$) at larger grain sizes. The change from $D_{<}$ to $D_{>}$ occurs at r_K . The point r_K is determined in the following manner: On grain size plots derived from the magnifications around r_K , the curves for $D_{<}$ and $D_{>}$ are drawn. The intersection of the corresponding line yields r_K .

From the experimentally deformed Verzasca Gneiss, only limited fault rock material is available. We therefore use only one combined log-log plot and one (average) $D_{>}$ and $D_{<}$ value per magnification. In the case of the Nojima fault zone, we have more fault rock samples. We have been able to evaluate a number of cascades from different samples of the drill cores and derive 4 to 5 $D_{<}$ and $D_{>}$ values per magnification.

For the evaluation of the largest grain sizes, light micrographs (taken with a ZEISS Axioplan Polarisation microscope) are included. The difference between the slopes ($D_{>}$) determined from light and scanning electron micrographs is less than 0.05. We have also tested the reliability of the semi-automatic segmentation by comparing the derived D -values to D -values obtained from manual tracings of the outlines. On two sets of test images taken at magnifications of 500x and 2000x, the difference in $D_{>}$ is less than 0.04.

4.3 Results

4.3.1 Mechanical data

The results of the triaxial compression experiments are shown as force-displacement diagrams (Figure 4.3a). With the exception of sample 60nk all samples display the same general behavior. Yield strength is reached after approximately 1 mm displacement, after that the load increases steadily, the differential stress decreases slowly after an axial shortening of 8-10%. In some of the experiments deformed at $T = 300^\circ\text{C}$, reaching the yield strength was accompanied by audible cracking. Sample 60nk (run at the highest confining pressure) is different from all others in that it has produced distinct acoustic events, which accompany load drops on the order of 20 kN (corresponding to approximately 500 MPa).

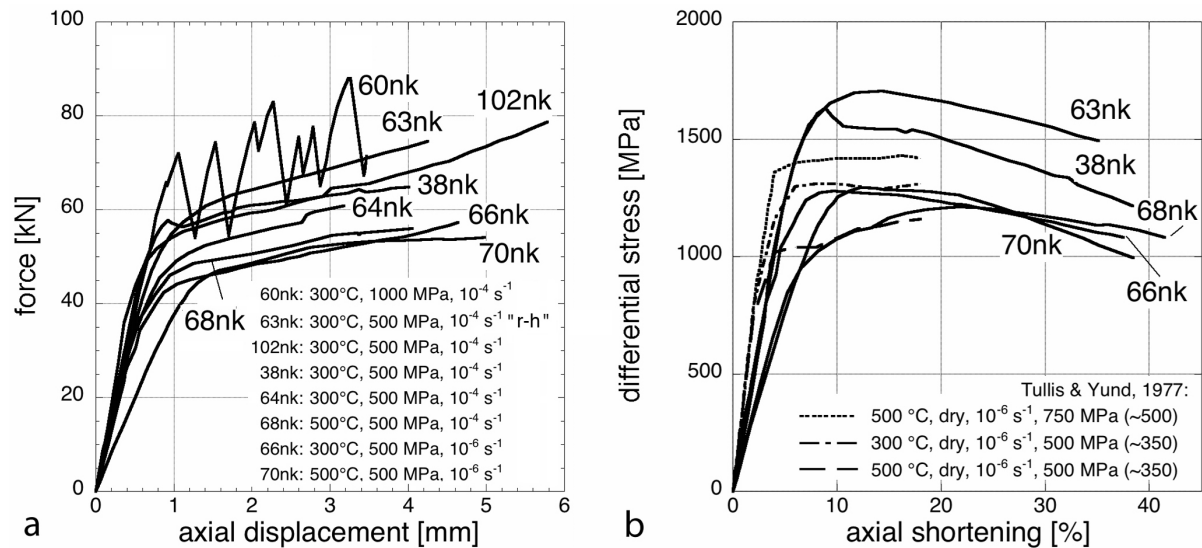


Figure 4.3: Mechanical data. (a) Force versus axial shortening of samples of Verzasca Gneiss. For experimental conditions see Table 4.3. r-h = room-humidity. (b) Differential stress versus axial shortening, calculated using program rigC4 (see text). For comparison, 3 experiments on Westerly Granite by Tullis and Yund (1977) are included. Since pyrophyllite or talc was used as confining medium, the true P_c -values (indicated in brackets) are approx. 2/3 of the values given in the literature (see text).

At 45kN (1000-1200 MPa), sample 70nk, deformed at relatively high temperature (500°C) and low axial shortening rate (10^{-6}s^{-1}), is the weakest. At 60–75 kN (1750 MPa) sample 63nk, which is run under dry conditions, is the strongest. Samples deformed at standard conditions (64nk and 38nk) support loads of 55–65 kN, corresponding to strengths of 1300–1500 MPa.

For comparison with published data, we also show a stress-strain diagram (Figure 4.3b). The differential stress is calculated with a correction for an increase in cross-sectional area, assuming

constant volume. The Verzasca Gneiss has approximately the same strength as Westerly Granite (Fig. 4.3b) deformed by Tullis and Yund (1977). The main differences with respect to Westerly Granite experiments are the higher shortening at yield stress (with typical values $\sim 5\%$ versus $\sim 10\%$), the higher shortening rate (mainly 10^{-4} s^{-1} , see Table 4.3) and the amount of added water. In both sets of experiments, a temperature increase from 300°C to 500°C produced a strength reduction of approximately 200 MPa. Note that Tullis and Yund have used pyrophyllite or talc as confining medium, which means that the true confining pressures were only $\sim 2/3$ of the published values (J.Tullis, pers.comm., 2004).

We noted a difference between the measured lengths of the deformed samples and the deformed lengths calculated from the total axial displacements derived from the force-displacement records (compare Figure 4.3a and Table 4.3). The calculated displacements exceeded the measured displacements by up to 1 mm. In the rest of the paper, we will therefore use the more conservative values of the measured displacements, not the displacements shown in Figure 4.3. This difference in measured length is not critical for the results, as the displacement is used semi-quantitatively in this study.

4.3.2 Faulted samples

In most samples deformed at $T = 300^\circ\text{C}$ and $P_c = 500 \text{ MPa}$, through-going fault zones are formed accommodating the axial displacement within a single gouge zone. At $T = 500^\circ\text{C}$, $P_c = 500 \text{ MPa}$ and occasionally at $T = 300^\circ\text{C}$, $P_c = 500 \text{ MPa}$, conjugate fault zones have developed and partitioned the axial displacement over at least two fault zones, leading to a smaller displacement on any given fault. Sample 60nk deformed at $P_c = 1030 \text{ MPa}$ shows a set of parallel faults. The corresponding load-displacement curve (Figure 4.3) shows an equivalent number of load drops. It is likely that each drop in the differential stress is related to the creation of a new fault plane.

The samples are deformed along relatively wide fault zones of 1.0–1.4 mm width, which become narrower with higher confining pressure or higher temperature; with increasing displacement, they tend to broaden. Most of the gouge zones are formed around mica grains or the connection of two mica grains. At a temperature of 300°C and strain rates of 10^{-4} s^{-1} biotite deforms by gliding, kinking and occasionally by fracturing.

Using the D -mapping technique described elsewhere (Heilbronner and Keulen, 2006), maps of local variations of the grain size distribution are prepared for three of the experimental samples (Figure 4.4). Cracking and gouge formation occur throughout the samples. In samples 38nk and 102nk gouge regions coalesce; in sample 60nk there is less coalescence. The volume proportion of gouge formed during the deformation is determined by measuring the black area (indicating

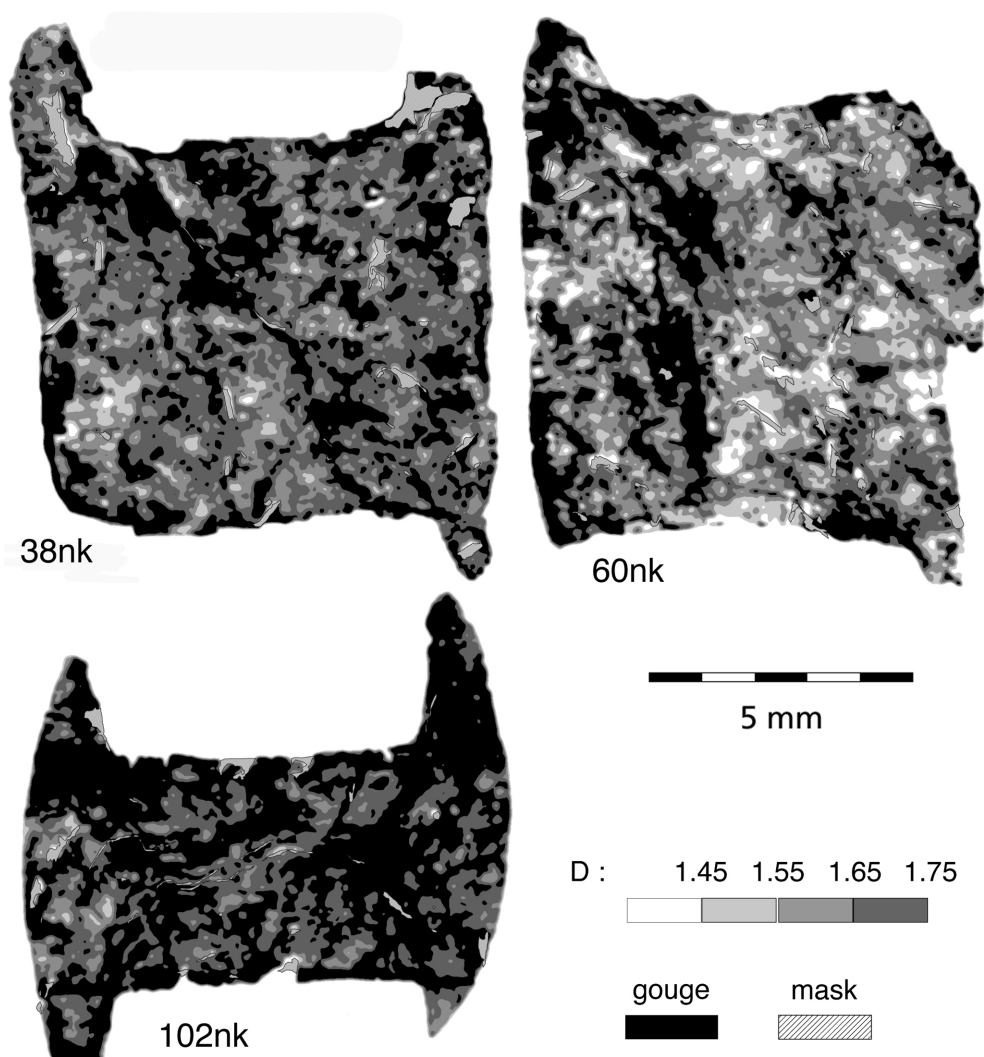
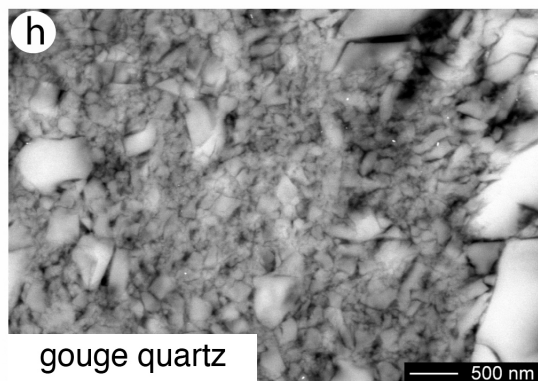
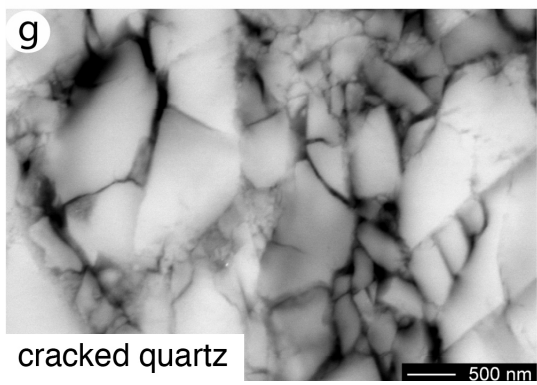
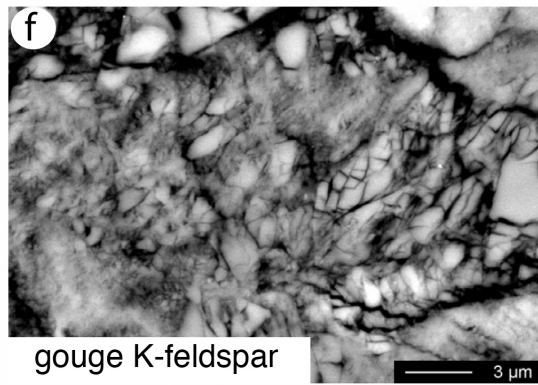
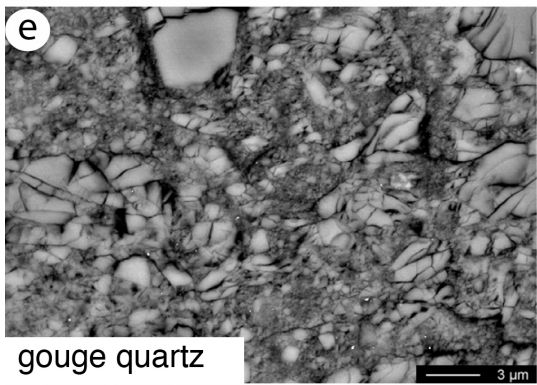
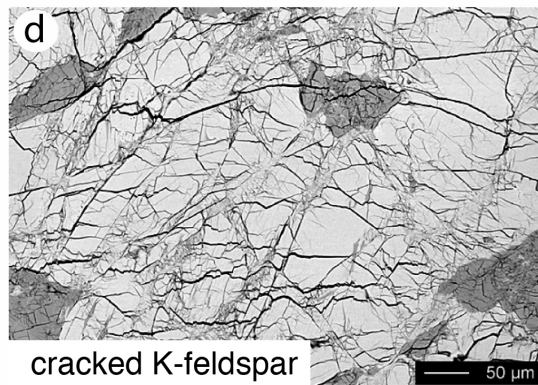
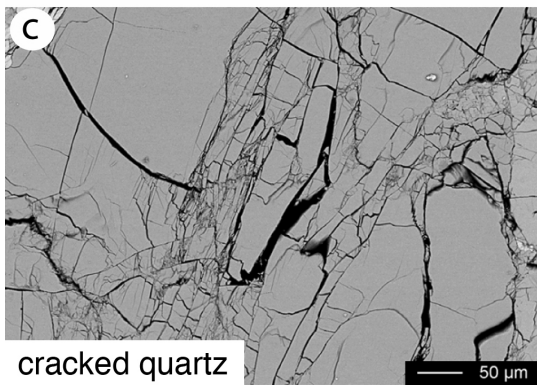
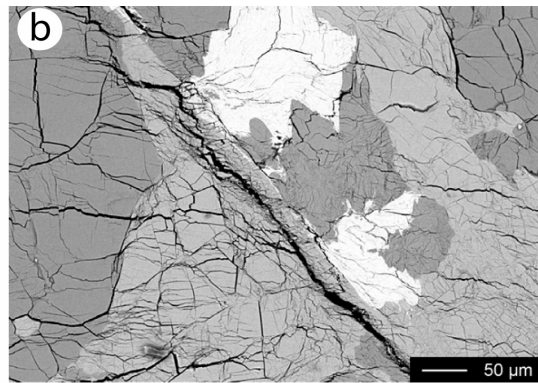
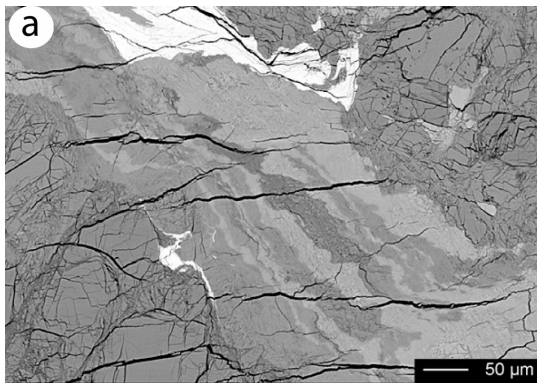


Figure 4.4: Maps of local variations of grain size distribution. The radius of the Gauss-filter was 5 pixels ($= 40 \mu\text{m}$); for D -mapping technique, see Chapter 3. D -values > 1.75 indicate gouge, D -values < 1.75 indicate cracked grains. Holes and biotite in samples are masked. Three samples are shown: 38nk (reference sample): $d = 3 \text{ mm}$; 102nk: $d = 4.8 \text{ mm}$; 60nk: $d = 2.5 \text{ mm}$. Fault surfaces are indicated. Scale applies to all samples.

Figure 4.5: Microstructures of experimentally deformed samples of Verzasca Gneiss. Scanning electron micrographs, backscatter contrast. Minerals, in order of increasing brightness: quartz, Na-rich plagioclase, muscovite, K-feldspar, biotite. (a) Fault zone consisting of gouge with adjacent cracked grains (reference sample 38nk). (b) Relatively narrow gouge zone (sample 60nk, high confining pressure). (c) Reference sample 64nk. (d) Reference sample 38nk. (e) Reference sample 38nk. (f) Reference sample 38nk. (g) Cracked quartz grains at high magnification (high displacement sample 102nk). (h) Quartz gouge at high magnification (reference sample 38nk).

fault rock with $D > 1.75$) in Figure 4.4 and dividing this proportion by the total sample area. For increasing axial displacement, d , increasing amounts of gouge are formed. After $d = 4 \text{ mm}$,



sample 38nk (reference sample) has 24.5% of gouge; after $d = 5.8$ mm, sample 102nk (deformed at the same conditions) has 54.8%. At higher confining pressures, there is less gouge: after $d = 3.5$ mm, sample 60nk ($P_c = 1000$ MPa) has only 15.5% gouge.

4.3.3 Microstructures

In the experiments at $P_c = 500$ MPa and $T = 300$ °C, the original grains in the gouge zone form broad and elongated arrays of fractured particles (Figure 4.3.2a); at higher confining pressures, these arrays are much narrower (Figure 4.3.2b). Quartz and feldspar are both strongly fractured; at higher confining pressures, quartz is less intensively fractured than feldspar. A variation in grain shapes can be observed: quartz grains are more elongated, feldspar grains are more irregularly shaped (Figure 4.3.2c & 4.3.2d); the same variation in shape has been observed for a sample deformed at low PT -conditions (Chapter 3).

Within the gouge zones, quartz and feldspar are fractured to very small grain sizes in all experiments (Figure 4.3.2e & 4.3.2f). The gouge is equidimensional and subangular in shape. In the cracked grains and the gouge, the grains smaller than $2 \mu\text{m}$ diameter do not show any intragranular fractures, while grains larger than $10 \mu\text{m}$ are usually fractured into a spectrum of smaller grains (Figure 4.3.2g & 4.3.2h). Also, grains smaller than $1 \mu\text{m}$ are equiaxial and appear weakly indented. Within the gouge these small grains show more rounded edges.

4.3.4 Grain size analysis of experimental fault rocks

Dependence of grain size distribution on type and composition of fault rock: The grain size distributions of all of our experiments display the same general characteristics (Figure 4.6). On log-log plots of frequency versus equivalent radius, two distinct parts can be discriminated (compare also Chapter 3). Both for cracked grains and gouge, two D -values are obtained: a lower value, $D_<$, for small grain sizes and a higher value, $D_>$, for larger grain sizes. The grain size, r_K , at the intersection of the two curve fits is on the order of $1 - 2 \mu\text{m}$. In gouge, the lower range of grain sizes extends from $r_{min} \approx 20$ nm to $r_K \approx 2 \mu\text{m}$ with $D_< \approx 1.0$ and the upper range extends from r_K to $r_{max} \approx 20 \mu\text{m}$ with $D_> \approx 2.0$. In cracked grains, the lower range of grain sizes extends from $r_{min} \approx 50$ nm to $r_K \approx 1.5 \mu\text{m}$ with $D_< \approx 1.0$ and the upper range extends from r_K to $r_{max} \approx 100 \mu\text{m}$ with $D_> \approx 1.5$.

Comparing feldspar and quartz we note that the $D_<$ values are approximately identical under almost all experimental conditions ranging from 0.72 to 1.02 in cracked feldspar, 0.74 to 1.09 in cracked quartz, from 0.91 to 1.12 in feldspar gouge and 0.78 to 1.10 in quartz gouge (Table 4.4).

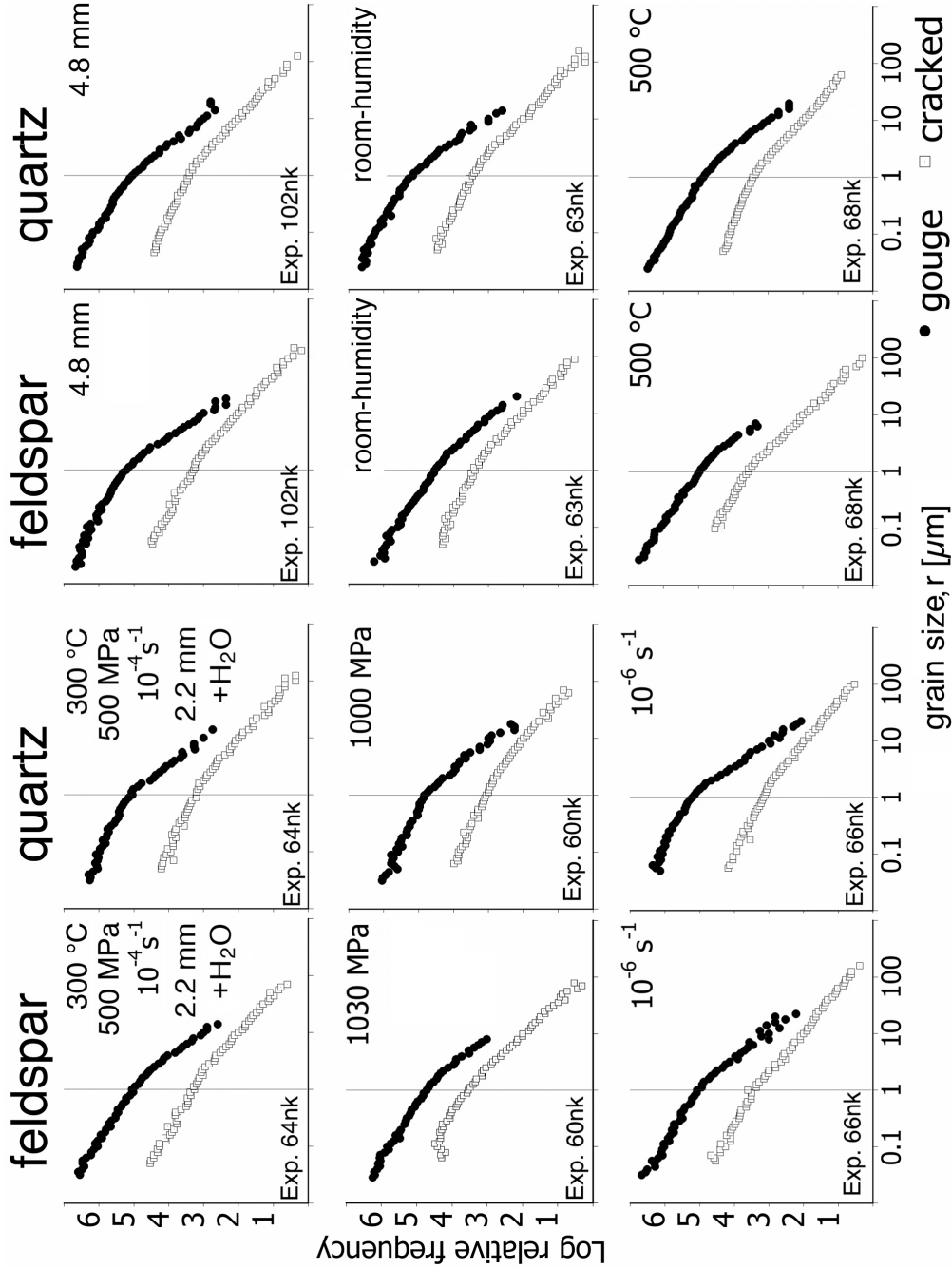


Figure 4.6: Grain size distribution of experimentally deformed Verzasca Gneiss plotted in a log(frequency)-log(equivalent radius) histogram. Results for quartz and feldspar are shown in separate graphs, results for cracked grains and gouge are shown with separate symbols. The frequency is normalized to 100 grains with a radius of 10 μm for cracked grains and to 1000 grains with a radius of 10 μm for gouge. Note the slope change in most of the curves at the slope change, r_K , and the grain size at the slope change, r_K , are listed in the Table 4.4 and 4.5, respectively.

<i>D</i> -values for cracked grains and gouge								
sample nr.	feldspar				quartz			
	cracked		gouge		cracked		gouge	
	$D_{<}$	$D_{>}$	$D_{<}$	$D_{>}$	$D_{<}$	$D_{>}$	$D_{<}$	$D_{>}$
38nk	1.02	1.68	1.00	2.03	1.09	1.56	1.10	2.26
64nk	0.95	1.52	1.05	2.06	0.74	1.44	1.05	2.26
102nk	0.87	1.52	1.01	2.07	0.92	1.55	1.00	2.27
60nk	0.74	1.37	0.91	1.85	0.96	1.72	0.78	1.94
68nk	0.92	1.67	1.01	1.95	0.92	1.47	1.01	2.07
63nk	0.72	1.62	1.12	2.12	0.78	1.55	0.83	2.32
66nk	0.86	1.37	1.05	2.09	0.96	1.46	0.97	2.26
Nojima Fault Zone								
	cracked		gouge					
	$D_{<}$	$D_{>}$	$D_{<}$	$D_{>}$				
	0.97	1.64	0.97	2.02				

Table 4.4: *D*-values ($D_{<}$ and $D_{>}$ of cracked grains and gouge. In experiments, quartz and feldspar were measured separately; in natural samples (Nojima), all mineral grains were combined.

The $D_{>}$ values, in contrast, are usually higher for quartz than for feldspar ranging from 1.37 to 1.68 in cracked feldspar, 1.44 to 1.72 in cracked quartz, from 1.85 to 2.12 in feldspar gouge and 1.94 to 2.32 in quartz gouge (Table 4.4).

On average, the grain size, r_K , of cracked grains is slightly larger than in gouge (Table 4.5). However, this effect is more pronounced in quartz than in feldspar. The grain size, r_K , of cracked quartz ranges from 1.1–1.8 μm and is smaller than r_K of cracked feldspar which ranges from 1.6–2.0 μm . Similarly, in gouge, r_K of quartz is 1.1–1.4 μm while r_K of feldspar is 1.4–2.0 μm .

Dependence of grain size distribution on experimental conditions: The GSD of the experimentally deformed granitoid samples are shown in Figure 4.6 & 4.7, the derived values of $D_{<}$, $D_{>}$, and r_K are shown in Tables 4 & 5. The d_K grain diameter is two times the r_K grain radius indicated in Figure 4.6, and has been used to compare our data to other studies. We consider the samples 64nk and 38nk as reference samples. The experiments are performed at $T = 300^\circ\text{C}$, confining pressure $P_c = 500$ MPa, strain rate $\dot{\epsilon} = 1.5 \times 10^{-4} \text{s}^{-1}$, 0.2 %wt H_2O was added to the samples. The total axial displacement, ΔL , of 64nk and 38nk is 2.2 and 3 mm, respectively. In Figure 4.6, each of the plots shows the GSDs resulting from the change of one of the experimental conditions with respect to 64nk.

The reference values derived from the GSDs of sample 64nk and 38nk are the following: $D_{<}$

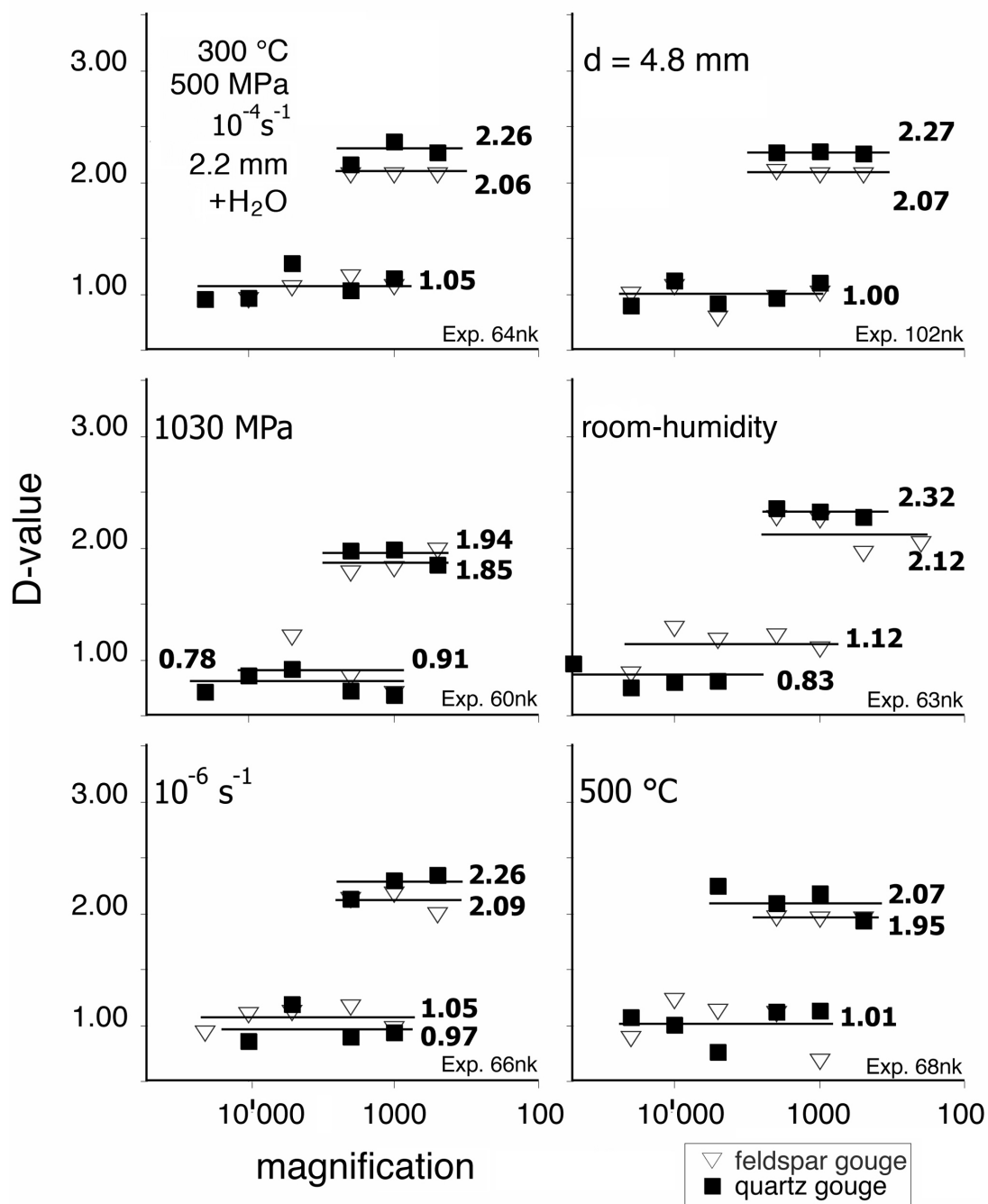


Figure 4.7: D -values of the gouge plotted against magnification of analyzed images. Average D -values are indicated by the horizontal lines. Feldspar and quartz are shown separately. Analyses at 1000x and 2000x magnification yield a value for $D_{<}$ and $D_{>}$, because r_K lies in the range of analyzed grain sizes.

r_K : Grain radius at slope change [μm]

sample nr.	feldspar				quartz			
	cracked		gouge		cracked		gouge	
	r_K	range	r_K	range	r_K	range	r_K	range
38nk	1.6	1.4 - 1.7	1.5	1.4 - 1.7	1.5	1.3 - 1.6	1.1	0.9 - 1.1
64nk	1.9	1.7 - 2.0	1.6	1.5 - 1.7	1.3	1.2 - 1.4	1.1	1.0 - 1.3
102nk	1.8	1.7 - 2.0	1.5	1.3 - 1.7	1.4	1.4 - 1.5	1.1	0.9 - 1.1
60nk	1.7	1.6 - 1.7	1.8	1.6 - 1.9	1.8	1.8 - 2.0	1.1	1.0 - 1.2
68nk	1.8	1.6 - 1.9	1.9	1.9 - 2.0	1.5	1.4 - 1.6	1.3	1.3 - 1.5
63nk	1.8	1.7 - 1.9	1.5	1.5 - 1.6	1.1	1.1 - 1.3	1.1	1.0 - 1.3
66nk	1.6	1.3 - 1.	1.3	1.3 - 1.6	1.8	1.6 - 1.9	1.4	1.4 - 1.6
Nojima Fault Zone								
	cracked		gouge					
	r_K	range	r_K	range				
	1.9	1.6 - 2.0	1.5	1.2 - 1.6				

Table 4.5: r_K -values determined from grain size distributions. In experiments, the values for quartz and feldspar were determined separately; in natural samples (Nojima), all mineral grains were combined.

ranges from 0.95 to 1.07 ($D_<$ of cracked feldspar = 1.00; $D_<$ of feldspar gouge = 1.02; $D_<$ of cracked quartz = 0.95; $D_<$ of quartz gouge = 1.07), cracked grains have somewhat lower values than gouge. r_K is 1.1–1.8 μm (cracked feldspar = 1.8 μm ; r_K of feldspar gouge = 1.6 μm ; r_K of cracked quartz = 1.6 μm ; r_K of quartz gouge = 1.1 μm), quartz yields lower values than feldspar and cracked grains have higher values than gouge. $D_>$ is 1.5 – 1.6 for cracked grains ($D_>$ of cracked feldspar = 1.6; $D_>$ of cracked quartz = 1.5) and 2.04–2.26 for gouge ($D_>$ of feldspar gouge = 2.04; $D_>$ of quartz gouge = 2.26), quartz has a lower D -value than feldspar for cracked grains and a higher value for gouge.

Increasing the confining pressure from 500 MPa to 1030 MPa leads to a marked reduction of both $D_<$ and $D_>$, both for cracked grains and gouge. The grain sizes, r_K , at the slope break of cracked grains and gouge do not change significantly, with the possible exceptions of r_K of feldspar gouge and cracked quartz: these values increase from 1.6 to 1.8 μm and from 1.5 to 1.8 μm , respectively. This variation is within the error of the measurements.

Reducing the strain rate from 10^{-4}s^{-1} to 10^{-6}s^{-1} does not affect the values of $D_>$; of the $D_<$ -values only those of cracked feldspar and of quartz gouge appear to be lowered: from 1.00 to 0.86 and 1.07 to 0.97, respectively. The grain size r_K of feldspar remains unchanged, while that of cracked quartz and quartz gouge increases from 1.5 to 1.8 μm and from 1.1 to 1.4 μm respectively.

Increasing the axial shortening from 2.2 mm to 4.8 mm has no significant effect on any of the measured values. As has been mentioned before, the only difference between samples 64nk ($\Delta L = 2.2$ mm), 38nk ($\Delta L = 3.0$ mm) and 102nk ($\Delta L = 4.8$ mm) is the width of the fault zone(s), i.e., the amount of fault rock (cracked grains and gouge) created during deformation.

Deforming the sample without adding any water (under “room-humidity” conditions) has a marked effect on the GSD. With the exception of feldspar gouge, all $D_{<}$ values are lowered significantly to values as low as 0.72 to 0.83. At the same time, all values of $D_{>}$ increase. The grain size at the slope break is not affected except for r_K of cracked quartz, which is lowered from 1.5 to 1.2 μm .

Increasing the temperature from $T = 300^\circ\text{C}$ to 500°C affects the $D_{>}$ -values. In particular, the values for feldspar gouge and quartz gouge are lowered from 2.04 to 1.95 and from 2.26 to 2.07, respectively. The major effect on r_K is to increase the values for feldspar and quartz gouge from 1.6 to 2.0 and from 1.1 to 1.4 μm , respectively.

4.3.5 Grain size analysis of natural fault rocks

For the Nojima samples the GSDs are given as bulk results, i.e., the different mineral phases, in particular, quartz and feldspar, were not separated. Comparing the GSDs of cracked minerals and gouge to the experimental results, we note that the values of $D_{<}$ (1.64 and 2.02), $D_{>}$ (0.97) and r_K (1.9 μm and 1.5 μm) are very close to the corresponding values obtained for feldspar cracked grains and gouge (see Table 4.4, Figure 4.8).

4.3.6 Characteristics of GSDs

The GSDs of both the experimental and natural fault rocks display a number of characteristics that we want to highlight (compare Figure 4.6, 4.7 & 4.8). The lower limit of grain sizes that could be used for the calculation of statistically reliable distributions is $r_{min} = 30$ to 60 nm for experimentally produced and $r_{min} = 100$ to 200 nm for naturally produced gouge and cracked grains, respectively. Similarly, the upper limit is $r_{max} = 50$ – 100 μm for experimentally produced and $r_{max} = 100$ – 200 μm for naturally produced gouge and cracked grains, respectively. In other words r_{min} and r_{max} of gouge are always smaller than r_{min} and r_{max} of cracked grains by a factor of ~ 2 . Note, however, that r_{min} is not the absolutely smallest grain size that can be detected in the SEM (Figure 4.9). Grains as small as $r \approx 5$ nm have been detected both in experimental and in natural fault rocks, but not in numbers large enough to be included in the grain size analysis.

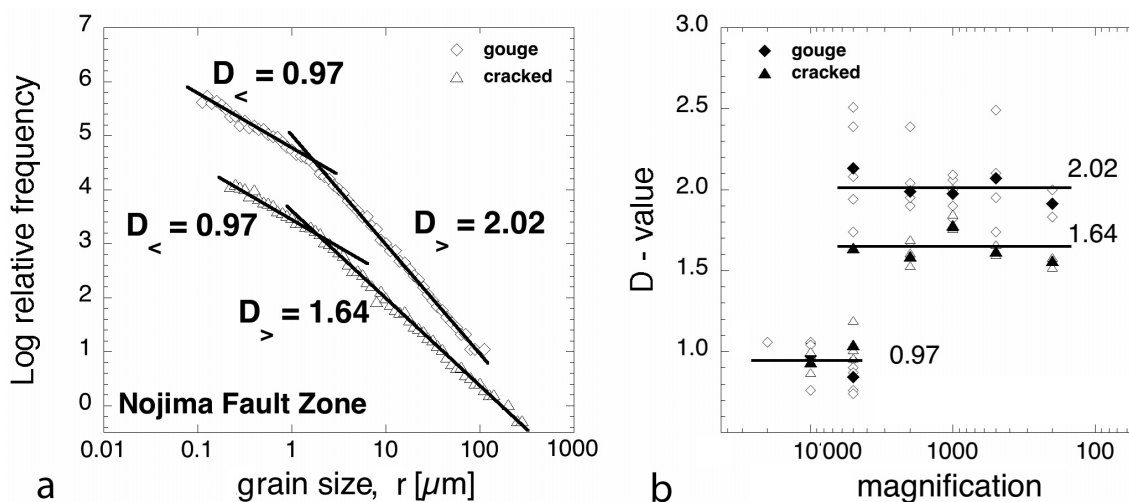


Figure 4.8: Grain size distribution and D -values of the Nojima Fault Zone. (a) Grain size distribution of cracked grains and gouge (all minerals). The frequency is normalized to 100 grains with a radius of $10 \mu\text{m}$ for cracked grains and to 1000 grains with a radius of $10 \mu\text{m}$ for gouge. (b) D -values versus magnification, compiled from 9 cascades (see text). The average values per magnification are indicated with solid symbols. Overall average values for $D_{<}$ and $D_{>}$ are indicated by solid lines. The thin-sections used for the analyses originate from the following locations in the cores: a) HR4-1 (522.79 m), HR4-11 (633.08 m) b) HR4-11, HR2-52 (626.90 m), HR256 (643.10 m) and HR3-10 (623.46 m).

The grain size r_K at the slope break of the power law fit to the GSD has a remarkably constant value. In contrast to the marked decrease of minimum and maximum grain size from cracked grains to gouge, the r_K values remain approximately constant or decrease by $< 30\%$ from an average value of 1.7 to $1.4 \mu\text{m}$ in experimental and from 1.9 to $1.5 \mu\text{m}$ in natural fault rocks (Figure 4.10).

4.4 Discussion

4.4.1 Faulting experiments

Brittle deformation experiments on granitoid rock at elevated pressure-temperature conditions have been performed by Griggs et al. (1960); Stesky et al. (1974); Carter et al. (1981); Blanpied et al. (1995); Kato et al. (2003) and others. Our experiments on Verzasca Gneiss compare best with the data on Westerly Granite published by Griggs et al. (1960) and Tullis and Yund (1977, 1980). The geometry and distribution of strain in our samples is variable (Figure 4.4). Therefore, we prefer to present our mechanical data in terms of force versus axial displacement rather than stress and strain (Figure 4.3a). For comparison with published data, we have converted our force data to stress data (Figure 4.3b).

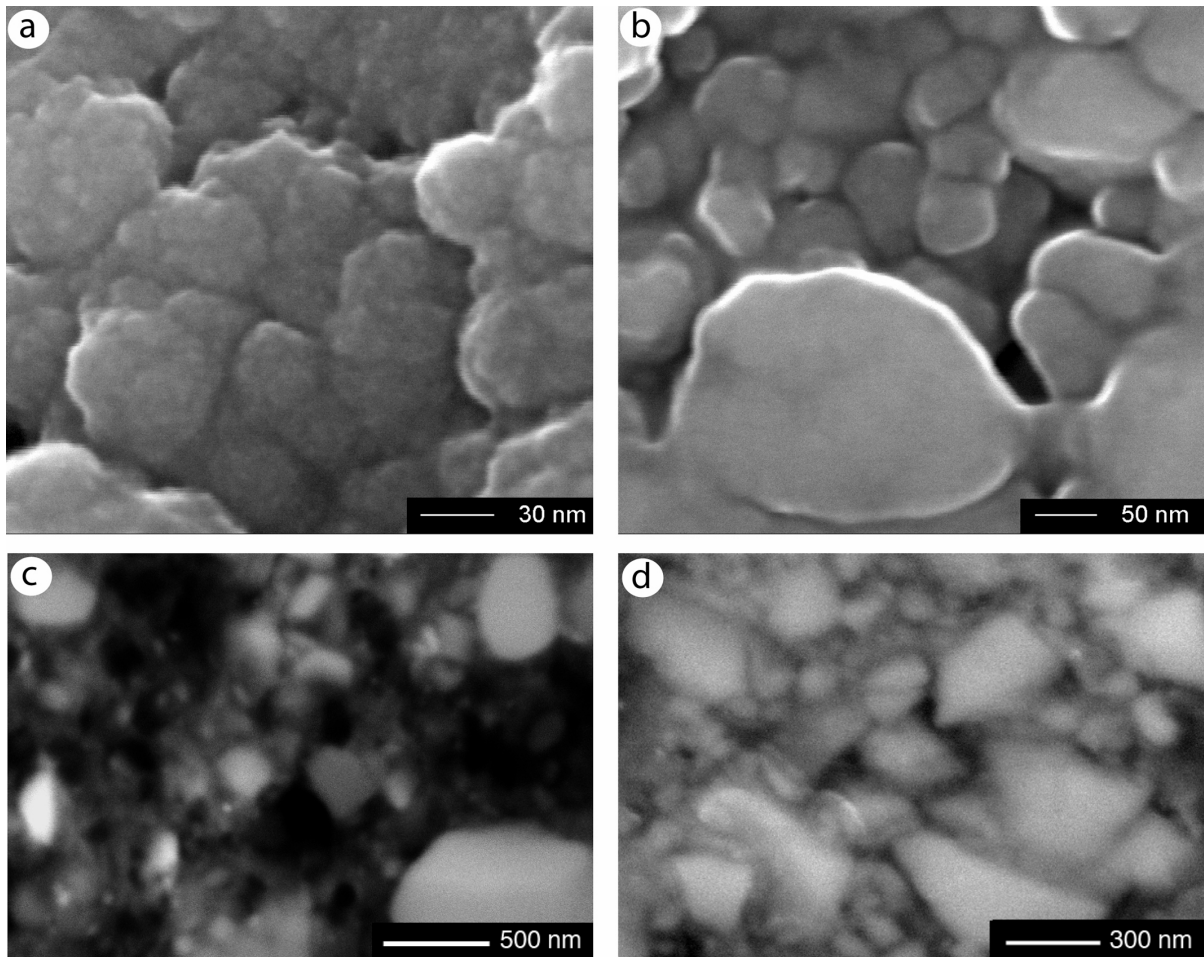


Figure 4.9: Scanning electron micrographs of the smallest grains found in gouge. (a,c) Nojima Fault Zone. (b,d) Experiment 63nk (room-humidity). (a,b) Secondary electron mode. (c,d) backscatter contrast mode. The pockmark structure in (a) is an effect of the carbon coating and does not show individual atoms or another substructure.

The experiments on Westerly Granite at $P_c = 500$ and 750 MPa have been performed without added water; samples have been pre-dried at a higher temperature (300°C) than ours (Tullis and Yund, 1977). Since pyrophyllite or talc has been used as outer confining medium, the confining pressure has been reduced to approximately 350 and 500 MPa. Their experiments at 750 MPa are therefore best compared to ours at 500 MPa, because we use NaCl as outer confining medium. The strengths of Westerly Granite and Verzasca Gneiss are comparable showing strengths of 1200 to 1600 MPa under similar conditions, although no experiments have been performed under identical conditions. The variation of the bulk shortening rate between 10^{-4} and 10^{-6}s^{-1} does not show any mechanical effect, consistent with the results of Tullis and Yund (1980, 1992).

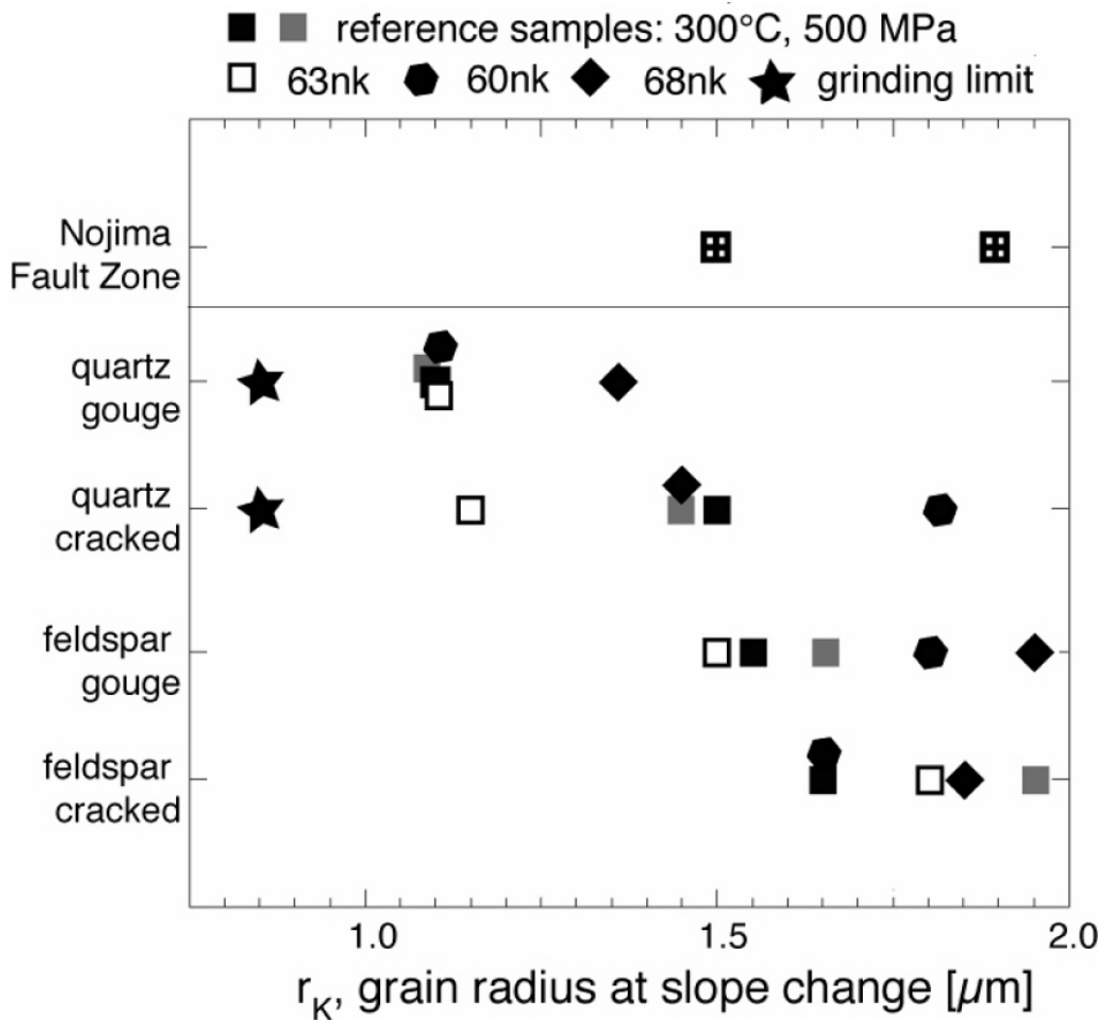


Figure 4.10: Grain size, r_K , at the transition from $D_<$ to $D_>$ (slope change in GSD plots) and grinding limit for quartz, after Steier & Schönert (1972) in Prasher (1987). The uncertainty in the position of r_K is $\pm 0.3 \mu\text{m}$.

The effect of a high confining pressure (~ 1 GPa) is comparable to experiments by Tullis and Yund (1977, 1980). Very narrow slip zones accommodate the axial shortening. According to Tullis and Yund (1977) and Hirth and Tullis (1994), the formation of these narrow zones and the decrease in volume of fault rock is related to the transition from mode I to mode II cracking above $P_c \approx 600\text{--}800$ MPa. The number of these narrow zones corresponds to the number of audible cracking events in the experiment 60nk. This observation suggests that the mechanical behavior is not a case of stick-slip as described in the literature (e.g. Byerlee and Brace, 1968; Stesky et al., 1974; Lockner et al., 1986). Instead, the apparent stick slip character of the mechanical data (Figure 4.3) is produced by multiple rupture events, demonstrating the great

strength of already ruptured material at high confining pressure.

4.4.2 Grain size distributions obtained in experiments

Changing the physical parameters of experimental deformation also affects the grain size distribution. The effects are discussed with reference to sample 38nk and 64nk, which have been deformed under identical temperature, pressure and strain rate conditions.

The largest effect is observed for increasing the confining pressure to ~ 1 GPa. It causes a reduction in the $D_{>}$ -values (Figure 4.6, 4.7, Table 4.4) and a decrease in the total amount of gouge and cracked grains in the fault zone (see Figure 4.4). This smaller amount of gouge is related to the transition from mode I to mode II cracking: mode I fracturing is dilatant; in mode II fracturing sharp shear fractures are formed when dilatancy is suppressed. Dilatancy suppression appears to inhibit the formation of large amounts of surface (small grains) and thus may reduce the $D_{>}$ -value.

At higher temperatures, there is a decrease in the $D_{>}$ values of the gouge (Figure 4.7, Table 4.4). Several authors report a transition in the behavior of experimentally deformed granites around $T = 300^\circ\text{C}$ (e.g. Stesky et al., 1974; Blanpied et al., 1995; Kato et al., 2003), related to the critical slip distance. In feldspar deformed at $T = 500^\circ\text{C}$ we observe undulatory extinction and deformation bands, which are developed by micro-cracking at a very small scale, as described by Tullis and Yund (1987). At a temperature of 500°C , Hirth and Tullis (1994) have found an increased dislocation activity in quartz. The less efficient grain size reduction at elevated temperature may be caused by a semi-brittle behavior.

The effects of not adding water and slower strain rate are either unsystematic (higher $D_{<}$ -values for feldspar and lower $D_{<}$ values for quartz in gouge of non-water added sample 63nk; Table 4.4) or not existent (sample 66nk, Table 4.4). The D -values are the same regardless of the amount of shortening of the sample (samples 38nk, 64nk, 102nk; Table 4.4, Figure 4.7).

After 4 mm axial shortening a gouge of ≈ 1.0 mm thickness has been formed. Once a mature zone with gouge is established, this zone is growing wider at greater displacement, but $D_{>}$ of the gouge is not changing. Marone and Scholz (1989) have also observed similar D -values for different shear strains. In general, it can be concluded that the effects of changing the physical conditions of deformation on the grain size distribution are of minor importance except for the increase in confining pressure, and, to a lesser extent, temperature.

4.4.3 Cracked material and gouge

All experimental and Nojima fault rock samples show the same type of grain size distribution (GSD). For small grain sizes ($d < 2 - 3 \mu\text{m}$) the GSD is characterized by D -values of ~ 1 , whereas for the larger sizes the D -values range between ~ 1.5 and ~ 2.3 (Table 4.4). The gouge always shows higher D -values than the cracked material (Figure 4.6, 4.8, Table 4.4). It is interesting to note that the values of $D_{<}$ in cracked material and gouge, in quartz and feldspar, and in experimental and in Nojima fault rocks all have very similar values and the same range of variation (Table 4.4). Furthermore, this grain size range is not affected by changing the experimental deformation conditions. In contrast, $D_{>}$ of gouge is the parameter that has been measured in several other studies before (Table 4.1). It is the most suitable of the D -values to compare natural fault zones of different regions or to compare natural fault rock with experimentally obtained values.

Higher D -values indicate a more efficient grain size comminution producing a larger number of smaller grains. The difference between gouge and cracked grains clearly demonstrates that the initial rupturing process does not produce the full amount and size fraction of small grains observed in gouge (Figure 4.6, 4.8). Instead, slip on the fault zone causes further comminution of grains in the gouge and an increase in $D_{>}$. Thus, it can be concluded that after the initial fragmentation of the rock by rupturing there is a post-rupture processing during slip which takes place in the gouge to produce the higher values of $D_{>}$. If the evolution of the GSD is a two-stage process involving initial rupturing and further grain comminution in the gouge, probably by attrition, shearing, grinding, etc., it is questionable whether the surface energy calculated from the GSD can directly be related to the seismic energy release as proposed by Wilson et al. (2005) and Chester et al. (2005).

Further comminution of grains in gouge has been observed by Sammis et al. (1986, 1987) and Hadizadeh and Johnson (2003). However, any quantitative characterization of fault displacement by GSD measurements appears impossible because an increase in sample shortening from 2.2 to 4.8 mm in our experiments (64nk and 102nk) does not change any of the D -values or r_K -values systematically (Figure 4.6, 4.10, Table 4.5). Thus, the more efficient grain comminution in gouge must take place in the first stages of the fault displacement after rupturing.

In the experiments performed under identical conditions (38nk, 64nk, 102nk) the variation of D -values of the cracked material is always larger than in the gouge (Table 4.4). The only systematic difference appears to be the consistently higher $D_{>}$ values of quartz gouge compared to feldspar gouge, i.e., for the coarser grain size fraction ($> 2 \mu\text{m}$) quartz shows a more efficient comminution of grains than feldspar. The $D_{>}$ -values for quartz and feldspar gouge are almost

identical in these three experiments and indicate that this D -value is very well reproducible and therefore forms a reliable parameter to compare the GSD of fault zones. Another difference is the lower r_K -value for quartz compared to feldspar. Thus, the change in the GSD occurs at $\sim 1 \mu\text{m}$ in quartz, while it occurs at $\sim 2 \mu\text{m}$ in feldspar (Table 4.4).

4.4.4 Natural fault rock

The range of values in the natural samples from the Nojima fault is approximately the same as those of the feldspars in experiments (Figure 4.6, 4.8, Table 4.4) so that the natural fault rock appears to behave in a similar way as feldspar.

The recently formed fault rock of the Nojima Fault zone shows the same D -values as the experimentally deformed granitoid rock, especially for feldspar minerals. If we compare the D -values of the recent deformation episode with feldspar in experiment 64nk and 38nk, performed at $T = 300 \text{ }^\circ\text{C}$, $P_c = 500 \text{ MPa}$, $\dot{\epsilon} = 1.5 \times 10^{-4} \text{ s}^{-1}$, with $\sim 4 \text{ mm}$ shortening and with 0.2 wt% H_2O added to the sample, all D -values are the same within the error of 0.05. Temperature and pressure conditions during Nojima deformation were lower than in the deformation experiments.

$D_{>}$ of the Nojima Fault gouge ($D_{>} = 2.02$) is in fairly good agreement with data from coarser grain size fractions by Monzawa and Otsuki (2003); they obtain $D_{>} = 2.192$ to 2.559, for ve different samples of the surface outcrop of the Nojima Fault Zone, with a mean of 2.347. Monzawa and Otsuki (2003) data is more similar to the values of $D_{>}$ for the experimentally deformed quartz so that all data appears to be within the variation of the experimental data.

Our results are consistent with studies of other fault zones (Table 4.1). Blenkinsop (1991) and An and Sammis (1994) describe both low ($D_{>} < 1.6$) and high ($D_{>} > 2.0$) values for analyses of gouge originating from the same fault zone. Several other studies describe high $D_{>}$ values (e.g. Blenkinsop, 1991; Hadizadeh and Johnson, 2003). In some gouge the lower limit of $D_{>}$ is 1.4 to 1.6, except for the San Andreas Fault Cajon Pass Drillhole granite ($D = 0.8$ Blenkinsop, 1991). We speculate that this gouge with $D_{>}$ below 1.6 might be monomineralic gouge where fluids and temperature caused healing (e.g. Sammis et al., 1987; Keulen et al., 2008) or were only cracked (e.g. Marone and Scholz, 1989).

4.4.5 Surface densities of fault rocks

The surface energy in gouge can be used to calculate a part of the energy release during an earthquake event (Kanamori, 1994; Wilson et al., 2005; Chester et al., 2005). The grain size distribution allows the calculation of the total surface area of the fault rock (Chester et al.,

2005; Wilson et al., 2005). The estimates of Chester et al. (2005) for the Punchbowl fault are based on GSDs with an assumed minimum grain size, r_{min} , of 1.6 nm and a constant D -value of 3 (= 2 in 2 dimensions) for the entire grain size range. In contrast, we find that in all of our experimental and natural samples the D -value below $r \approx 1$ to $2 \mu\text{m}$ is $D_{<} \approx 1$.

We have calculated the surface density for our cracked minerals and gouge assuming a fractal fragmentation of a cube. We use the size range between $r_{min} = 15 \text{ nm}$ and $r_{max} = 100 \mu\text{m}$ assuming values of $D_{<} = 1.00$ (i.e., $D = 2$ in three dimensions) for $r < r_K$ ($r_K = 0.5$) and $D_{>} = 1.50$ and 2.00 (i.e., $D = 2.5$ and 3 in three dimensions) for $r > r_K$. For cracked minerals we obtain surface densities of $1.3 \times 10^6 \text{ m}^{-1}$, for gouge we get $6.0 \times 10^6 \text{ m}^{-1}$. Using the same approach to calculate surface densities for the Punchbowl Fault using the data ($r_{min} = 1.6 \text{ nm}$ and $r_{max} = 100 \mu\text{m}$, $D = 2.0$) given by Chester et al. (2005), we obtain $6.8 \times 10^8 \text{ m}^{-1}$. If we now compare our value of cracked grains of $1.3 \times 10^6 \text{ m}^{-1}$ to a value of $4.2 \times 10^8 \text{ m}^{-1}$ (corresponding to $4.2 \times 10^5 \text{ m}^2$ in the 1mm thick layer of the fault, given by Chester et al., 2005) or $2.7 \times 10^8 \text{ m}^{-1}$ (corresponding to $80 \text{ m}^2\text{g}^{-1}$ given by Wilson et al., 2005) we note that in our case, the surface density, and accordingly, the energy required to generate it, is smaller than the values assumed by Wilson et al., (2005) and Chester et al. (2005) by a factor of 200 to 300. For this comparison we use the surface density of cracked grains because we assume that this is the material, which is created by the rupture process during the seismic event, while the higher surface density of gouge is due to the combined effect of fracturing and subsequent deformation during slip. Finding that the surface densities in cracked rocks and even in gouge are so low suggests to us that the creation of those surfaces cannot play a major role in the energy budget of a seismic event.

The discrepancy between our data and the data published by Chester et al. (2005) can be explained by the fact that they have measured their small grain size fraction (down to $r = 25 \text{ nm}$) in the TEM, which is a notoriously difficult method for obtaining good statistics of any parameter observed. Thus, they did not detect the change of D -values at $r \approx 1 \mu\text{m}$. Using $D = 2.0$ over the entire range of grain sizes results in a total surface area which is 2 orders of magnitude too high. Furthermore, they assumed $r_{min} = 1.6 \text{ nm}$ and thus obtained many tiny grains with a high surface area density. Note, that finding lower surface densities rather supports and strengthens their general conclusion that the surface energies do not contribute in any major way to the energy dissipated during earthquakes. Pittarello et al. (2006) came to the same conclusion, using GSD measurements on pseudotachylytes.

4.4.6 Grinding limit

Grains with very small radii formed by comminution have been found before in deformation experiments ($d = 10$ nm; Yund et al., 1990), in mining induced fault zones (~ 40 nm; Olgaard and Brace, 1983; Wilson et al., 2005) and in natural fault zones (40 nm; Wilson et al., 2005, Chester et al. 2005). We observe grains of 30 nm in both experimental and natural fault rock (Figure 4.9). r_K is 1.2 ± 0.3 μm for quartz and 1.8 ± 0.3 μm for feldspar grains. The slope change is observed for both cracked grains and gouge (Figure 4.6, 4.8, Table 4.5). Very small grains are already formed upon cracking of the grains; they are not only a product of gouge formation. $D_{<}$ is less dependent on deformation conditions, the type of mineral (quartz or feldspar) and is more similar for cracked grains and gouge than $D_{>}$.

Kendall (1978) has demonstrated that a critical diameter exists below which particles cannot be comminuted further by grinding. This critical diameter, called the grinding limit, is 0.5 μm for SiO_2 glass, 1.7 μm for quartz and 4.4 μm for calcite (Steier and Schönert, 1972 Prasher, 1987). Small particles have a different internal stress distribution and are stronger due to smaller flaw sizes and flaw size density (Prasher, 1987) so that very high stresses are required to break them (Mitra, 1978). This is consistent with our observation that no intragranular cracks within grains smaller than 2 μm in diameter are observed.

The r_K -values for quartz are slightly higher than the grinding limit (indicated as radius) for quartz (Figure 4.10). There is no data for the feldspar grinding limit available but the higher r_K -values for feldspar (Figure 4.10) are consistent with the observation that the critical grain size for grinding is linearly dependent on the elastic modulus E of the mineral (Kendall, 1978), because the bulk E -modulus of feldspar is approximately 2 times that of quartz (Bass, 1995).

Thus, it appears likely that r_K represents approximately the grinding limit in the comminution of fault rock. For smaller grain sizes, where grinding is inhibited, comminution is less efficient, leading to a lower $D_{<}$. Grinding is performed by compressional fracturing of grains: a network of cracks will develop and the grain will break into several smaller ones (Jaeger, 1967). Other processes, like shearing or attrition also produce comminution. Reches and Dewers (2005); Dor et al. (2006) describe comminution as dynamic pulverization (explosive granulation followed by dynamic contraction) at earthquake crack tips. For grains smaller than r_K compressional fracturing appears inhibited, but shearing or attrition remain significant. From the difference between D -values in cracked grains and gouge, it is clear that grinding, shearing and attrition during slip cause further comminution in gouge.

4.4.7 Fractal dimension

Fractal dimensions are used to describe geometries that are scale invariant (Turcotte, 1992). To describe a GSD as fractal, this distribution should lie on a straight line over several orders of magnitude in a log(frequency)-log(size) distribution. The GSD of both the experiments and the Nojima Fault Zone gouge does not show a fractal distribution. The data cover 3.5 orders of magnitude, but cannot be fitted with a single straight line. Furthermore, there are statistical problems because most fault rock grain size measurements only cover 1 to 4 orders of magnitude.

The advantage of having a fractal distribution is the scale invariance of the measurements. Analyses performed on laboratory experiments or on hand specimens could easily be extrapolated to large fault systems. However, Turcotte (1992) emphasizes that not every power-law distribution can be described by a fractal dimension. Fractal dimensions are limited to D -values between 0 and 2 in 2D (Turcotte, 1992), so that gouge with $D_{>}$ larger than 2.0 cannot be described as fractal.

Several authors have commented on the ideal nature of a fractal dimension or D -value of 1.6: a GSD with a D -value of 1.6 appears the most ideal for close packing (Monzawa and Otsuki, 2003). Hoffmann and Schönert (1971) and Sammis et al. (1987) describe a D -value of 1.6 (for constrained comminution) as ideal, because the probability that grains of the same size are neighboring each other and the amount of pore space for a close-packed array of spherical grains are minimized. Morgan (1999); Morgan and Boettcher (1999) have shown with numerical simulations of gouge that a D of 1.6 marks the onset of shear localization, inter-particle rolling, and a decrease in the general comminution rate. Biegel et al. (1989) and Marone and Scholz (1989) find a D -value of 1.6 for the onset of shear localization in their experimentally formed gouge. Therefore, it seems that the onset of gouge evolution from cracked grains, leading to an increase of $D_{>}$ above 1.6, is causing dilatancy (a less close packing) and the possibility of inter-particle rolling. This will increase the possibility for grinding and is in this way creating more small grains, thus a higher $D_{>}$. The smaller D -values of gouge in high confining pressure experiments support such an interpretation, because of the effective suppression of dilatancy at high pressures.

Storti et al. (2003) report measurements in carbonate fault zones, in which the D -values at the boundary of the shear zone are between 0.9 and 1.4 and evolve to D -values between 1.6 and 2.5 for the interior shear bands. These observations are consistent with our observations: gouge ($D > 1.6$) is localized in slip zones, whereas cracked grains ($D < 1.6$) make up a larger part of the sample without major slip.

4.5 Conclusions

The analyzed fault rocks derived from experimentally faulted granite and from the Nojima fault zone consist of two different types of material, cracked grains and gouge. These can be distinguished on the basis of their microstructures and their grain size distribution (GSD). On log-log plots the GSDs display two distinct power-law fits: $D_<$ for grain sizes smaller than r_K and $D_>$ for grain sizes larger than r_K . $D_>$ is the value that corresponds to other published D -values (so-called “fractal dimensions”).

$D_<$ is 0.9–1.0 for cracked grains and 0.9–1.1 for gouge and more or less independent of the deformation conditions or the type of mineral. The lower limit of grain sizes in experimentally and naturally produced gouge is $r = 15$ nm.

$D_>$ is 1.5–1.6 for cracked grains and 2.0–2.3 for gouge and depends on the deformation conditions or the type of mineral. The upper limit of grain sizes evaluated in this study, r_{max} , is $100 \mu\text{m}$. $D_>$ for gouge is a good parameter to compare natural and experimental fault rock.

Cracked grains result from initial fragmentation by rupturing. They develop into gouge by subsequent grain comminution, grinding, attrition, or shear during slip along the fault zone. These processes produce larger $D_>$ -values and therefore represent a more efficient grain size reduction for quartz and feldspar grains in the size range greater than $1\text{--}2 \mu\text{m}$.

The grain size, r_K , at the slope break of the log(frequency)-log(size) histogram of the GSD occurs at $1.2 \pm 0.3 \mu\text{m}$ for quartz and at $1.8 \pm 0.3 \mu\text{m}$ for feldspar. The grain size r_K coincides approximately with the grinding limit in quartz and probably corresponds to a change in the physical process of grain comminution. Attrition and shear may dominate below the transition value r_K .

Most of the experimental conditions during deformation (temperature, confining pressure, H_2O -content, displacement rate) have a minor effect on the GSD. Most noticeable is an increase in confining pressure (~ 1 GPa), which reduces the efficiency of grain comminution.

The gouge of the Nojima Fault Zone shows $D_> = 2.02$ for gouge and 1.64 for cracked grains. These values are the same as for the experimentally deformed granitoids. Experiments and natural seismic fault rocks from the Nojima fault zone show the same GSD, although the experiments have been carried out at higher PT -conditions and at presumably slower displacement rates than in nature.

The development of the GSD is a two-stage process. First rupturing of the rock causes cracked grains that evolve to a gouge as a result of further movement on the fault zone. The surface

densities calculated from the GSD of cracked minerals and gouge are 200–300 times lower than published data, confirming that the creation of surface plays a minor role in the energy budget of earthquakes.

Chapter 5

*Healing microstructures of experimental and natural fault gouge**

In this Chapter effects of temperature, time and axial shortening rate on grain size distribution and other microstructures of the fault gouge is studied. For monomineralic fault gouge that is healed under hydrostatic conditions, an empirical healing law is derived, which is based on the change in $D_{>}$ -value. For non-hydrostatically healed gouge the relationship between the shortening rate, the deformation mechanism and the $D_{>}$ -value are investigated. More details on the natural fault rock are given in Appendices D and E.

*Published as: Keulen, N., Stünitz, H. and Heilbronner, R., "Healing microstructures of experimental and natural fault gouge" in: The Journal of Geophysical Research, Vol. 113, B06205, doi: 10.1029/2007/B005039.

Abstract

The healing of fault gouge was studied by examining microstructures of naturally and experimentally produced granitoid fault rock. We performed deformation experiments on intact granitoid rock samples at $T = 300 - 500\text{ }^\circ\text{C}$, $P_c = 500\text{ MPa}$, at $\dot{\epsilon} = 1.2 \times 10^{-4} - 1.3 \times 10^{-7}\text{ s}^{-1}$ with 0.2 wt% H_2O added. Healing experiments were carried out on deformed samples at $T = 200 - 500\text{ }^\circ\text{C}$, $P_c = 500\text{ MPa}$, for 4 hours to 14 days under hydrostatic and non-hydrostatic conditions. The grain size distributions (GSD) of the deformed samples were quantified using the $D_{>}$ -value (slope of $\log(\text{frequency})$ - $\log(\text{radius})$ of the GSD) for quartz and feldspar fault gouge. Healing causes a decrease in the $D_{>}$ -value from > 2.0 to ~ 1.5 . The time dependence of the $D_{>}$ -decrease is described by a hydrostatic healing law of the form: $\Delta D = D_{>}(t) - D_f = A \cdot e^{(-\lambda t)}$. The results of the laboratory experiments were compared to three natural fault systems, (1) Nojima Fault Zone (Japan), (2) Fault zones in the Black Forest (Germany), and (3) Orobic Thrust (Italian Alps). Natural and experimental gouges have similar $D_{>}$ -values. Healing is only observed in monomineralic aggregates; polymineralic (i.e. mixed) fault gouges retain their high $D_{>}$ -value after extended healing times because grain growth is inhibited. Healing under non-hydrostatic conditions is more rapid than hydrostatic healing. The low strain rates, which were measured during non-hydrostatic healing, are temperature-dependent and suggest that diffusive mass transfer processes take place during deformation. Thus, fault rocks at upper to mid-crustal depth may deform by combined cataclasis and diffusive mass-transfer.

5.1 Introduction

Laboratory studies were performed to measure the healing rate (identified as the rates of fault strength recovery) of experimentally produced fault gouge in slide-hold-slide friction experiments in order to extrapolate these data to natural fault systems (e.g. Dietrich, 1979; Marone et al., 1995; Bos and Spiers, 2002; Muhuri et al., 2003). Therefore, other experiments were carried out on sodium chloride (Bos et al., 2000; Bos and Spiers, 2002; Voisin et al., 2007) and gypsum (Muhuri et al., 2003) as models for healing of silicate fault gouge under higher temperature conditions. Healing experiments on quartz and granitoid fault gouge at higher temperature conditions were performed by (Rutter and Maddock, 1992; Blanpied et al., 1995; Karner et al., 1997; Olsen et al., 1998; Kanagawa et al., 2000; Tenthorey et al., 2003; Nakatani and Scholz, 2004; Tenthorey and Cox, 2006). The efficiency of healing processes in friction experiments is related to the size of the contact area of the sliding surfaces (e.g. Scholz and Engelder, 1976; Dietrich and Kilgore, 1994). Healing of natural faults on a geological timescale is less well understood. It is generally assumed that high temperatures and fluids enhance the healing processes. Healing under hydrostatic conditions can be caused by cementation, i.e. filling pore

space by precipitation of material from a fluid. Healing under non-hydrostatic conditions is additionally driven by pressure solution and/or cementation processes (Sleep, 1994; Olsen et al., 1998; Kay et al., 2006).

In order to study fault rock healing experimentally at elevated temperatures and pressures, samples are kept at P and T conditions for extended periods of time. Hydrothermal alteration of gouge was documented in cases where fracturing and healing was carried out in different experimental machines (Karner et al., 1997; Tenthorey and Cox, 2006). The approach of this study is to carry out healing in-situ after fracturing and gouge formation in the same solid medium deformation apparatus. The effect of healing was quantified microstructurally. The grain size distribution ($D_{>}$ -value) was used as the critical parameter by which to characterize the progress of healing in the fault gouge (Chapter 4). The experimentally derived rate of change of the grain size distribution during healing at different temperatures and healing periods is used to infer the time needed for fault gouge healing under natural conditions. The grain size distribution of the experimentally deformed samples were compared to natural fault rocks from the Nojima Fault Zone, central Japan; the Black Forest, southwestern Germany; and the Orobic Thrust, Italian Alps.

In this study fault rocks are described based on the definitions given in Chapter 3: (1) “Cracked material” is a ruptured fault rock in which the individual, usually angular, pieces retain their original geometric relationship with respect to the original grain shape. (2) “Fault gouge” refers to grains in a fault zone for which the relationship of the original grain geometry is lost due to displacement and rotation of fragments. (3) In this study “healing” is identified by the closure of microcracks, cementation, clustering of grains, dissolution of small grains, growth of large grains, and rounding of larger grains. Thus it is primarily a geometrical concept. (4) The term “polymineralic” is used for well-mixed fault gouge, consisting of more than one mineral, and (5) The term “monomineralic” is used for parts of the fault gouge of a single mineral composition. Thus, the terms monomineralic and polymineralic refer to the degree of local mixing of individual fragments in a gouge (at a given scale of observation), not to the overall mineral composition of the whole rock.

5.2 Experimental procedure

5.2.1 Samples

Verzasca gneiss is a very weakly foliated, fine grained gneiss with a granitoid composition and a mean grain radius, r , of ~ 0.14 mm. Samples were collected from blocks in the river directly south of Brione in the Val Verzasca, Ticino, southern Switzerland, and cored parallel to the weakly

developed lineation. Cylinders measured 11 mm length on average and 6.4 mm diameter and were dried at 110 °C under atmospheric pressure for at least 24 hours. The samples were placed in weld-sealed Au-jackets with 0.2 %wt H₂O added. The experiments were performed in a Griggs type solid medium deformation apparatus with sodium chlorite as confining medium (Tullis and Tullis, 1986; De Ronde et al., 2005). Experiments were divided into five groups; all experiments are listed in Table 5.1. For the modal composition of Verzasca gneiss, see Table 5.2.

5.2.2 Experiments

Deformation-only experiments (*d*):

Granitoid samples were deformed at temperatures (T) of 300 °C and 500 °C, a confining pressure (P_c) of 500 MPa, and with an axial shortening rate ($\dot{\epsilon}$) of $1.4 \times 10^{-4} s^{-1}$.

Deformation & hydrostatic healing experiments (*dh*):

As a first step, the samples were deformed as described for the deformation experiments (*d*), above. At the end of the deformation the differential load was removed to achieve hydrostatic conditions ($P_c = 500$ MPa). The samples were healed at different temperatures (200, 300, 400 and 500 °C). If healing was carried out at a temperature different from the deformation, the temperature was changed over a time span of 30 minutes, except for experiments 92nk and 95nk (change in 6 minutes). The samples were kept under hydrostatic conditions for 4 hours to 14 days (Table 5.1). The thermocouple for the temperature control was located at the center of the sample. At 900 °C, the maximum temperature drop is approximately 20 °C from the center to the ends of the sample. As the experimental temperatures used here are only 300 to 500 °C, the temperature differences are expected to be much smaller than 20 °C.

Deformation & non-hydrostatic healing experiments (*dnh*):

To investigate the influence of a small remaining axial load on the sample during the healing period, three experiments were performed. In two experiments (77nk and 67nk) the load on the samples was not removed after deformation. Instead, the displacement was stopped and the load was allowed to decrease over a period of 14 days. The shortening of the samples during the stress relaxation occurred at very low rates (10^{-8} to $10^{-9} s^{-1}$). In another experiment (62nk) an initial axial shortening (15%) and fracturing at a high rate ($\dot{\epsilon} = 1.4 \times 10^{-4} s^{-1}$) was followed by 19% shortening at a lower rate of $\dot{\epsilon} = 2 \times 10^{-7} s^{-1}$ for 14 days.

Deformation experiments with a lower axial shortening rate (*d*):

To study the influence of a low shortening rate on the deformation directly, samples were deformed under the same temperature and pressure conditions ($T = 300$ °C - 500 °C and $P_c = 500$ MPa) as for short term deformation experiments using axial shortening rates of $\dot{\epsilon} = 1 \times 10^{-6} s^{-1}$

sample	deformation				healing				D -values	
	T °C	P_c MPa	$\dot{\epsilon}$ $\times 10^{-4} s^{-1}$	ax. ϵ %	T °C	P_c MPa	time d/h	time $\times 10^{+3} s$	feldspar	quartz
<i>deformation (d)</i>										
38nk ^a	300	510	1.5	38					2.03	2.26
64nk ^a	300	500	1.3	26					2.06	2.26
102nk ^a	300	510	1.3	57					2.06	2.27
91nk	400	530	1.3	38					1.99	2.18
68nk ^a	500	520	1.4	37					1.95	2.07
<i>hydrostatic (dh)</i>										
116nk	300	530	1.4	35	200	500	14d	1209.30	1.87	2.01
97nk	300	500	1.3	29	300	520	4h	13.80	1.99	2.12
58nk	300	500	1.3	27	300	510	14d	1202.80	1.74	1.89
104nk	300	490	1.2	31	400	500	4h	13.80	1.92	2.08
119nk	300	550	1.4	34	400	520	4d	330.12	1.73	1.93
92nk	300	500	1.4	31	400	500	14d	1209.12	1.68	1.76
95nk	300	540	1.3	31	500	540	4h	13.80	1.73	1.82
46nk	300	560	1.6	39	500	520	4d	326.22	1.59	1.57
48nk	300	600	1.4	27	500	520	14d	1255.30	1.54	1.57
56nk	500	490	1.6	28	500	480	7d	608.88		
65nk	500	530	1.4	32	500	530	14d	1226.50	1.55	1.50
<i>dnh</i>										
62nk ^b	300	490	1.4+0.002	15+19	500	480	14d	1207.62	1.67	-
77nk ^c	300	580	1.3	27	300	550	14d	1198.91	1.61	
67nk ^c	300	530	1.4	31	500	510	14d	1213.38	1.47	
<i>d - lower $\dot{\epsilon}$</i>										
66nk ^{a,d}	300	490	0.015	38					2.09	2.26
70nk ^{a,d}	500	530	0.013	38					1.83	1.87
72nk ^e	500	470	0.0013	39					1.68	-
<i>dhd</i>										
59nk ^f	500	520	1.4	26+15	500	490	11min	0.66	1.96	2.06
53nk ^g	500	600	1.4	26+15	500	520	14d	1177.38		
54nk ^g	500	560	1.4	26+15	500	530	14d	1188.18		

Table 5.1: Overview of deformation and healing experiments performed on Verzasca Gneiss and resulting $D_{>}$ -values. All samples were deformed with 0.2 wt% H_2O added. Symbols: T = temperature, P_c = confining pressure, $\dot{\epsilon}$ = axial shortening rate, ax. ϵ = axial shortening, d = days, h = hours, dnh = non-hydrostatic healing, dhd = deformation-healing-deformation.

^aExperiment described in Chapter 4

^b15% shortening at $10^{-4} s^{-1}$ + 19% shortening at $10^{-7} s^{-1}$

^cnon-hydrostatic healing experiment

^dtime needed for experiment: 4 days

^etime needed for experiment: 30 days

^fdeformation (26%), hydrostatic conditions (11 min), deformation (15%)

^gdeformation (26%), hydrostatic conditions (14 days), deformation (15%)

and $\dot{\epsilon} = 2 \times 10^{-7} \text{ s}^{-1}$; these experiments lasted 4 days and 30 days, respectively.

Deformation-healing-deformation experiments (*dhd*):

Two experiments were carried out that consisted of two deformation phases with an intermediate healing period; they were performed at $T = 500^\circ\text{C}$, $P_c = 500 \text{ MPa}$. The samples were first shortened by approximately 26% (first deformation) and subsequently kept under hydrostatic conditions for 11 minutes or 14 days. After the healing period, the samples were reloaded in a second deformation event to obtain a total axial shortening of approximately 41%. The first deformation and the hydrostatic healing were carried out in the same way as in the *dh*-experiments.

5.2.3 Analytical techniques

After deformation and healing, samples were quenched and retrieved from the deformation apparatus. A small opening in the Au-jacket was made to vacuum-impregnate the samples with very low viscosity epoxy (BASF Laromin C260). After evacuation (20 min), the liquid epoxy took 2 to 3 hrs to harden. One or more polished thin sections were made from a single sample, prepared parallel to the median axial plane. Final polishing was performed with $0.5 \mu\text{m}$ diameter diamond powder. The microstructures of the samples were studied using polarized light microscopy (LM), scanning electron microscopy (SEM), and cathodoluminescence microscopy (CL; Ramseyer et al., 1989). The CL-images were taken with an acceleration voltage of 25 kV and with exposure times of 10 s for feldspars and $\geq 180 \text{ s}$ for quartz using $10 \mu\text{m}$ thick thin sections. The luminescence of the minerals under CL reflects the amount and nature of trace elements, of defects in the crystal lattice and changes in the fluid composition (Ramseyer and Mullis, 2000; Nakamura et al., 2005). This method was used successfully to study healed fault gouge (Shimamoto et al., 1991).

For the grain size distribution analysis the public domain software, ImageSXM*, combined with the macro “Lazy Grain boundaries”† (Heilbronner, 2000) was used. The grain size distribution of the fault gouge in the samples was analyzed from two or three series of characteristic backscattered electron contrast SEM micrographs (BSE) with a range of magnifications of 500x to 20,000x and from manual tracings of grain boundaries. The size of the smallest grains was verified with the SEM in SE-contrast mode (see Chapter 4). The grain size distribution is displayed as a log(frequency)-log(radius) histogram and is characterized by two slopes (D-values): a $D_{>}$ -value for grains larger than a critical grain size r_K and a $D_{<}$ -value for grains smaller than

*<http://reg.ssci.liv.ac.uk/>

†<http://pages.unibas.ch/earth/micro/software>

r_K (Figure 1). The radius at the transition between $D_<$ and $D_>$, r_K , is $\sim 1.1 \mu\text{m}$ for quartz fault gouge (Fig. 1) and $\sim 1.6 \mu\text{m}$ for feldspar fault gouges (Chapter 4). As the grain size fraction below r_K disappears during healing, we will only use changes of $D_>$ to quantify the progress of the healing process.

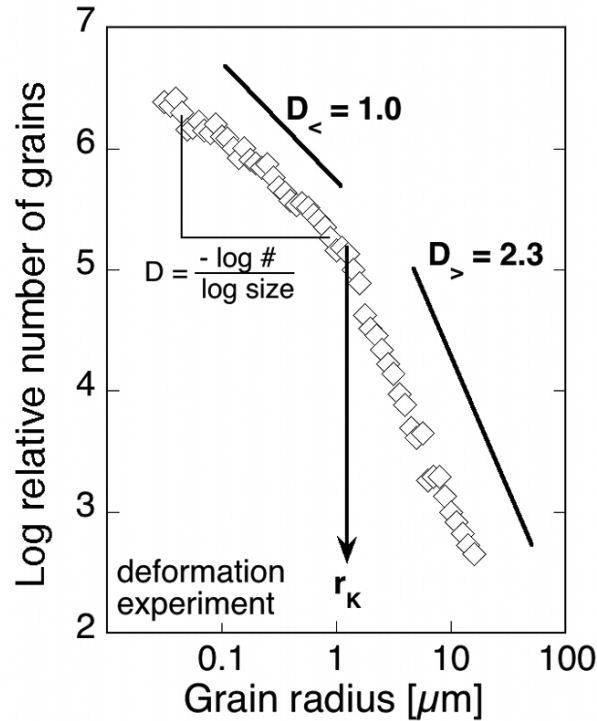


Figure 5.1: Grain size distribution of quartz fault gouge after deformation (no healing; sample 64nk). $D_>$ and $D_<$ values represent the slopes of the grains with $r < r_K$ and $r_K < r$, respectively. For quartz gouge in this sample $r_K = 1.1 \mu\text{m}$.

5.3 Results

5.3.1 Microstructures of experimental fault rock

Deformation-only experiments (*d*):

After deformation at $T = 300^\circ\text{C}$ and $P_c = 500 \text{ MPa}$, the fault gouge is only partially cohesive. Details concerning the nature and geometry of the faults are given in Keulen et al. (2007). In the experiments we mostly find monomineralic gouge because the displacement is not sufficient to produce a mixing of fragments derived from different minerals (e.g. quartz and feldspar). In other words, although the bulk sample material is polymineralic (granitoid), small monomineralic domains derived from individual minerals persist and can be distinguished. In naturally deformed gouge, however, two types of gouge can be observed: monomineralic gouge domains

derived from fragmented minerals without mixing, and polymineralic gouge, where mixing of fragments has taken place during displacement.

The grain size distributions show two distinct relationships with a $D_{>}$ -value for larger grains and a $D_{<}$ -value for smaller grain sizes (Fig. 5.1; see Keulen et al., 2007, for a further explanation). Feldspar and quartz have a $D_{>}$ -value of 2.03 and 2.26, respectively (Fig. 5.1, Table 5.1), while the $D_{<}$ -values (below r_K) are on the order of ~ 0.9 to 1.0 and the same for both minerals (Keulen et al., 2007). The $D_{>}$ -values decrease with increasing temperature of deformation; the $D_{>}$ -value of quartz is higher than that of feldspar under all deformation conditions. The radius of the smallest grain size found in fresh fault gouge is 7-8 nm.

Deformation & hydrostatic healing experiments (*dh*):

The progress of healing of feldspar and quartz fault gouge are shown in Figure 5.2. The fresh fault gouge (Fig. 5.2a) shows loose, angular, equidimensional grains with very small grains (< 50 nm). After a short healing period (4 hours, Fig. 5.2b) the angular edges of grains are more rounded and fewer small grains remain. Bridges of material form between the grains (arrows in Fig. 5.2b) and small grains are cemented to larger ones. With increasing time the fault gouge becomes more cohesive and small cracks are closed. These microstructural changes are further enhanced after longer healing periods (Fig. 5.2c,d). The bridges between grains grow wider and grains increase in size. In samples with a long healing time or during healing at 500°C , most grains smaller than $r \approx 2 \mu\text{m}$ disappear (Figs. 5.2d, 5.3.1). Healed fault gouges are cohesive; they do not disintegrate when the jacket is opened after deformation and healing.

In healed samples, grain sizes with $r < 1 \mu\text{m}$ have not been detected (Fig. 5.3.1a), so that only a single slope, $D_{>}$, of the grain size distribution, for grains larger than r_K , can be determined. The $D_{>}$ -value of the fault gouge decreases with increasing healing time and temperature. At $T = 500^\circ\text{C}$ the $D_{>}$ -value decreases from 1.95 – 2.06 (after deformation) to 1.59 for feldspar and from 2.06 – 2.27 (after deformation) to 1.57 for quartz within 4 days (Table 5.1). Significantly lower $D_{>}$ -values could not be achieved by longer healing durations at 500°C (Table 5.1); after 14 days, $D_{>}$ is 1.54 for quartz and 1.57 for feldspar. At $T = 400^\circ\text{C}$, $D_{>}$ -values below 1.80 are reached after 14 days, and at $T = 300^\circ\text{C}$, $D_{>} = 1.74$ for feldspar and $D = 1.89$ for quartz (Table 5.1). In the investigated temperature range ($T = 200 - 500^\circ\text{C}$), the decrease in $D_{>}$ -value is systematic with time and temperature, so that the $D_{>}$ -value offers itself as parameter to quantify the healing process.

Deformation & non-hydrostatic healing experiments (*dnh*):

Samples that have undergone non-hydrostatic healing (67nk and 77nk) show a slow decrease in load by approximately 20 – 25kN in 14 days after deformation (Figure 5.4a) resulting in a further 1 – 2% shortening of the sample by creep. The creep rate decreases to $\dot{\epsilon} = 10^{-8} - 10^{-9} \text{s}^{-1}$

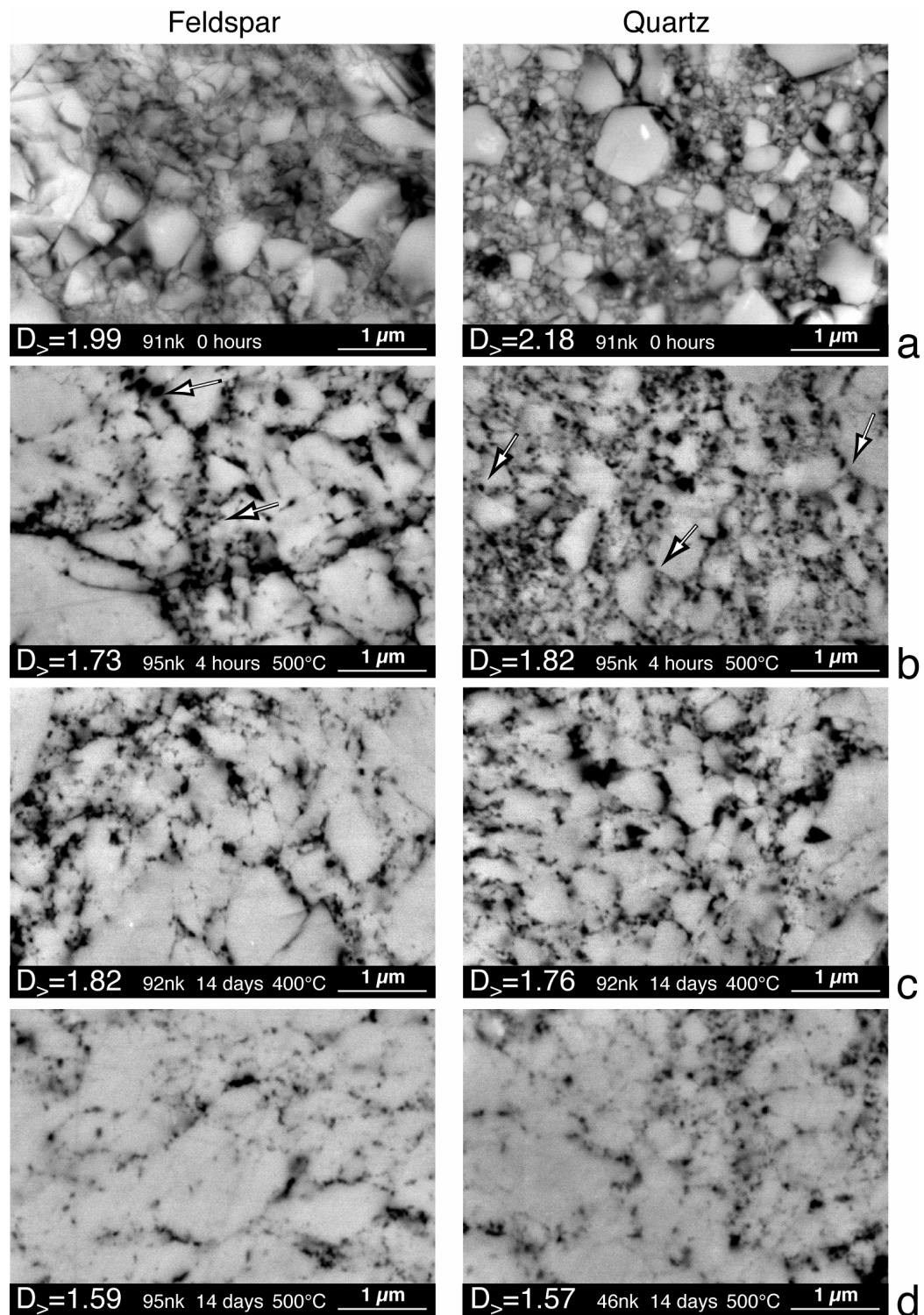


Figure 5.2: BSE-contrast SEM micrographs showing hydrostatic healing of feldspar (left column) and quartz (right column). $D_{>}$ -value of the fault gouge, sample number, healing time and temperature are indicated. Arrows indicate initial grain growth with bridges connecting grains. Maximum compression during deformation was oriented vertically.

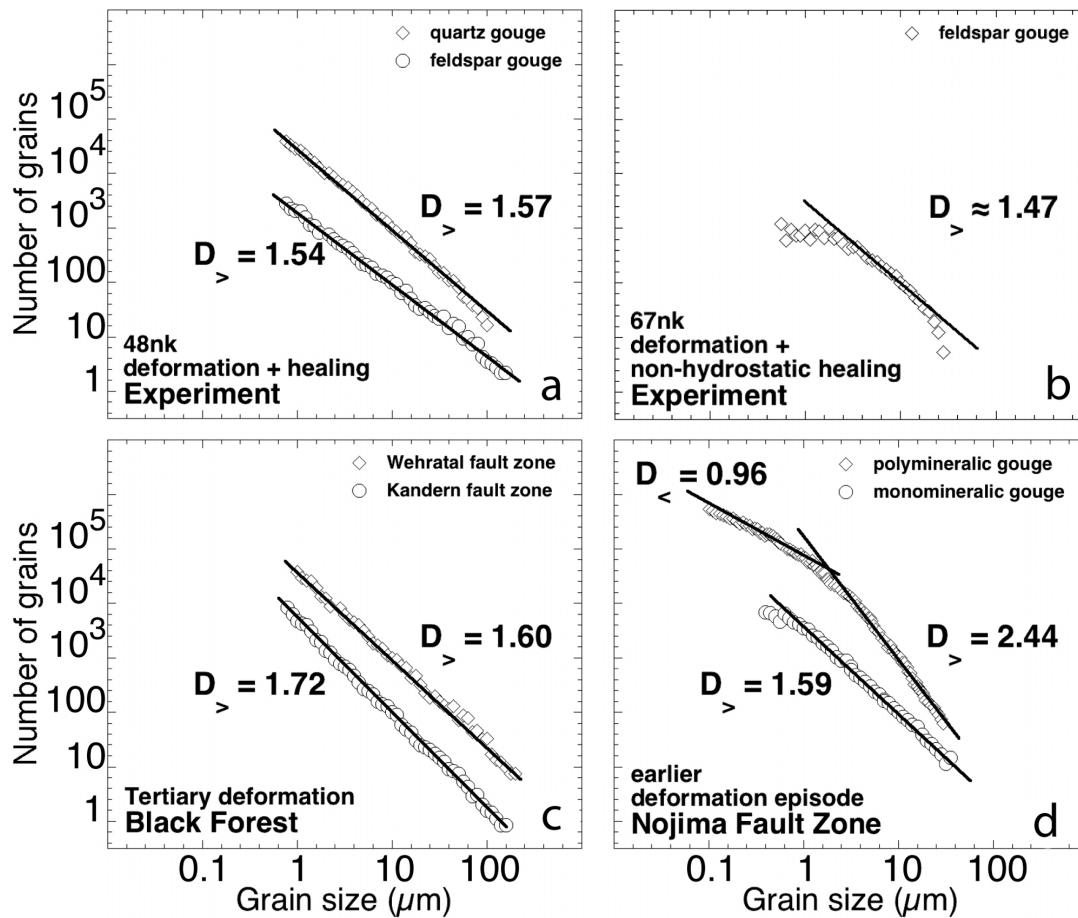


Figure 5.3: Grain size distribution and $D_{>}$ -values of the fault gouge from (a) hydrostatic healing experiment ($n = 6303$; $n=6712$ grains), (b) non-hydrostatic healing experiment ($n = 4820$), (c) Black Forest ($n = 5891$; 6487) and (d) Nojima Fault Zone ($n = 18674$; 7846). To be able to fit two distributions in one plot, the grain size distributions are normalized to a frequency of 100 and 1000 grains with a radius of $10 \mu\text{m}$.

after 14 days (Fig. 5.4). Experiment 67nk at $T = 500^\circ\text{C}$ shows a faster creep rate than the one at $T = 300^\circ\text{C}$ (77nk) despite the lower axial load (Fig. 5.4), demonstrating a clear temperature dependence of the deformation rates.

Comparing BSE and CL micrographs of movement zones one notes that very small fragments have been healed by cementation and precipitation of chemically different material (Fig. 5.4). Two brightness levels of luminescence can be distinguished in the deformed and healed samples: the newly deposited material displays low luminescence colors, whereas the fragments show bright colors. A BSE and CL images of the *dh*-sample 48nk (Fig. 5.4a) reveal fine-grained healed fault gouge in K-feldspar, plagioclase, and quartz. In the BSE micrograph, the *dnh*-sample 67nk appears completely homogeneous (Fig. 5.4b, arrow) while in the CL image the

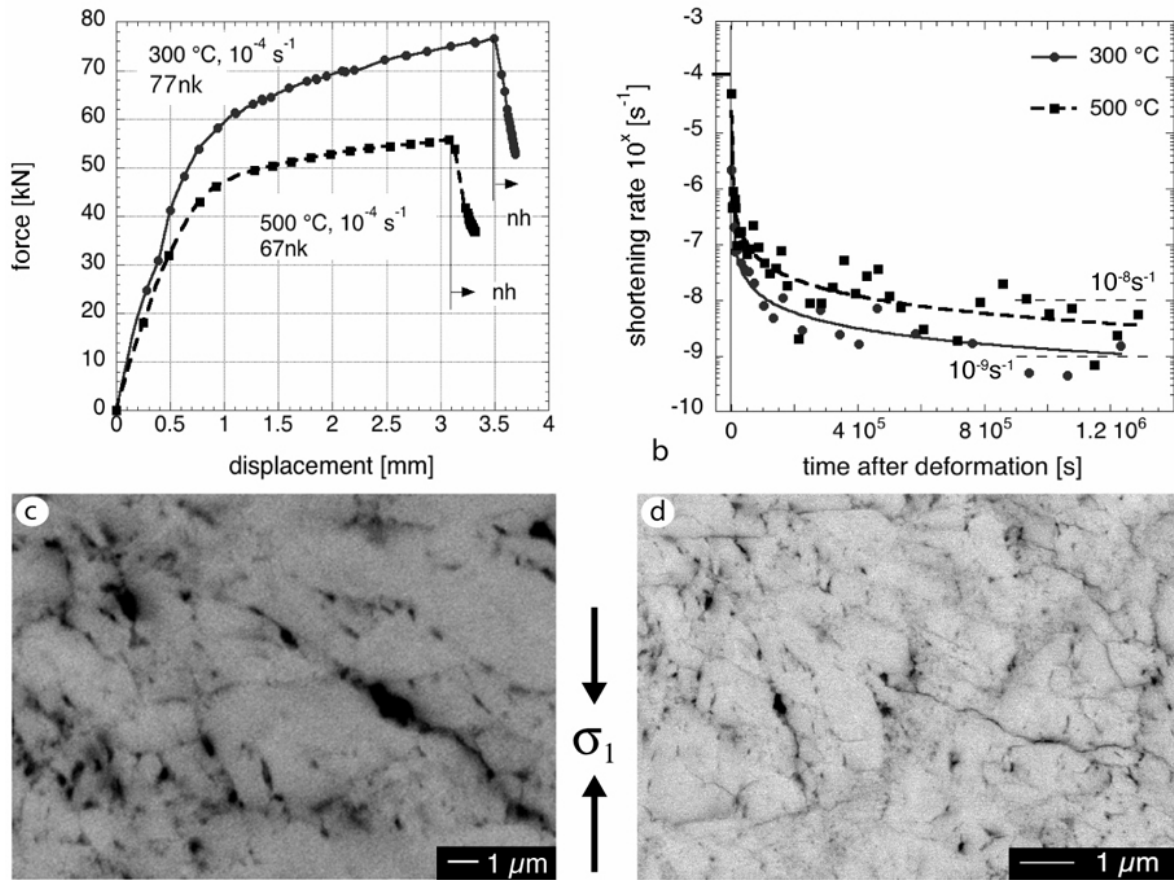


Figure 5.4: Experiments with non-hydrostatic healing after deformation. Non-hydrostatic healing caused an additional axial shortening with a low shortening rate. (a) Force versus axial shortening, nh = non-hydrostatic healing (b) axial shortening rate versus time for the non-hydrostatic healing period.

presence of fine-grained fragments can be recognized. Comparison of the *dnh*-samples 67nk and 77nk (Fig. 5.4b and c) shows that the material of the fault gouge healed at $T = 300^\circ\text{C}$ is less luminescent (dark blue and brown instead of blue and purple) compared to that healed at $T = 500^\circ\text{C}$.

For non-hydrostatic healing at $T = 500^\circ\text{C}$ (67nk) a $D_{>}$ -value of 1.47 is obtained (Fig. 5.3.1b). However, the grain size distribution of this particular sample is unusual in that it does not show a clear power-law behavior (Fig. 5.3.1b); the value of 1.47 is an approximation for the central part of the grain size range only. As in the hydrostatically healed samples, no grains smaller than $\sim 1\mu\text{m}$ can be detected. The $D_{>}$ -values for the *dnh*-samples are slightly lower than those of the *dh*-samples (Fig. 5.6). The low $D_{>}$ -values obtained under non-hydrostatic healing conditions indicate that healing is more efficient under non-hydrostatic than under hydrostatic conditions (see also Table 5.1).

Figure 5.5: Healing visible as increase of cohesion in cathodoluminescence micrographs (left column) and backscatter-contrast SEM micrographs (right column). Arrows point to corresponding locations in the thin section. Cathodoluminescence: K-feldspar = light blue, plagioclase = light green/yellow, bright red, and salmon-colors, quartz = dark blue/black, biotite = black, epoxy resin = dark green. BSE-contrast micrographs: K-feldspar = light grey, plagioclase = medium grey, quartz = dark grey, biotite = white, epoxy resin = black. (Sub-)horizontal cracks are extension cracks developed during unloading of the sample after deformation related to a vertical maximum compression orientation during deformation. For deformation conditions of the samples see Table 5.1.

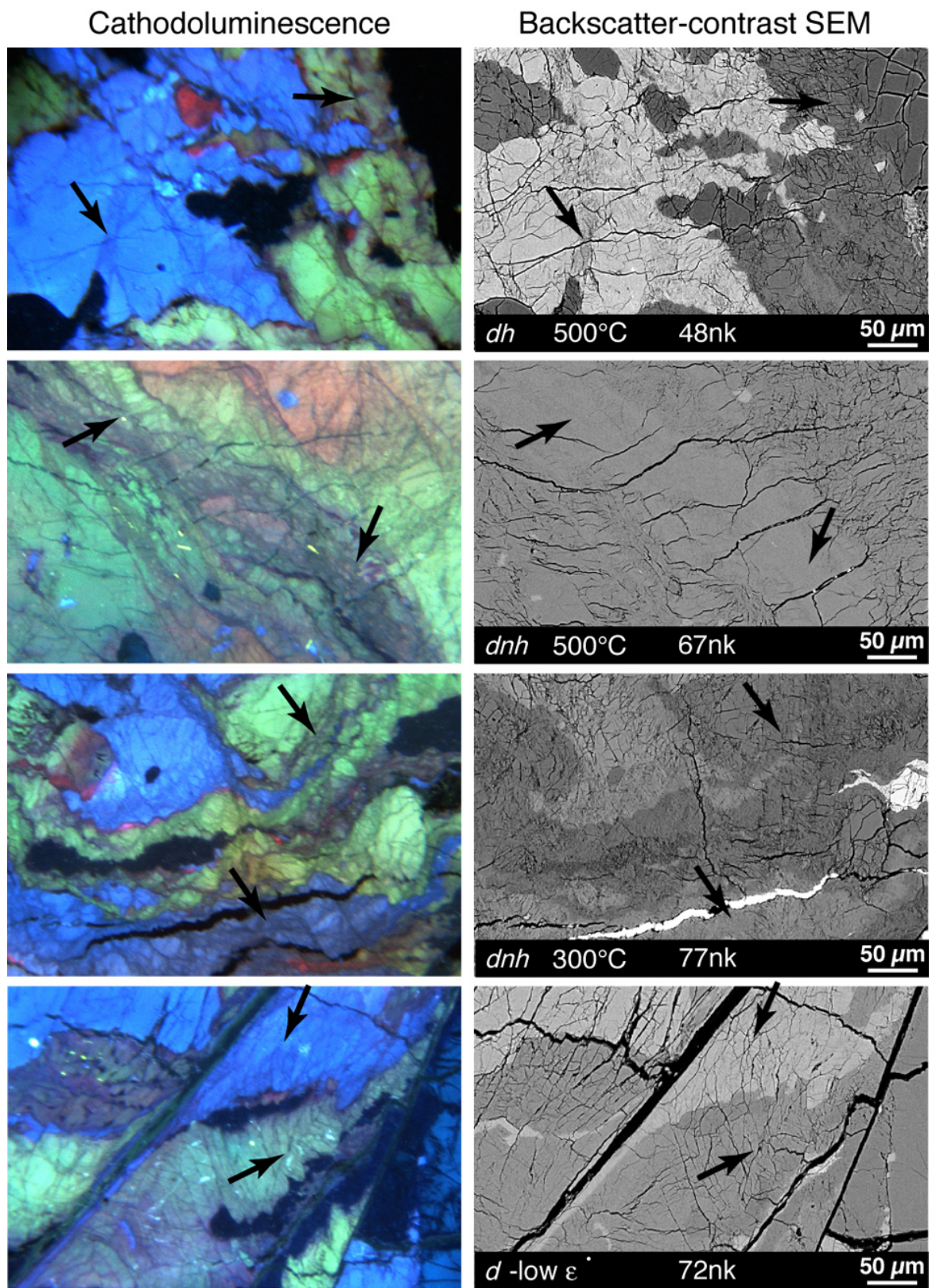
Deformation experiments with a lower axial shortening rate (*d*):

Three samples have been deformed at 500 °C, $P_c = 500$ MPa and with different axial shortening rates (68nk: $\dot{\epsilon} = 10^{-4} s^{-1}$, 70nk: $10^{-6} s^{-1}$ and 72nk: $10^{-7} s^{-1}$). At $10^{-7} s^{-1}$ (Fig. 5.7a), the sample shows a clear weakening behavior; thus, a switch to a different dominant deformation mechanism is suspected. The fault zone developed in sample 72nk ($\dot{\epsilon} = 10^{-7} s^{-1}$) consists of a single narrow diagonal fault along which all of the displacement has occurred. At all temperatures, the $D_{>}$ -values decrease with a decrease in axial shortening rate from values of $D_{>} \approx 2$ at $\dot{\epsilon} = 10^{-4} s^{-1}$ to $D_{>} < 1.5$ at $\dot{\epsilon} = 10^{-8} s^{-1}$ and $T = 500$ °C; and from values of $D_{>} > 2$ at $\dot{\epsilon} = 10^{-4} s^{-1}$ to $D_{>} < 1.6$ at $\dot{\epsilon} = 10^{-9} s^{-1}$ and $T = 300$ °C (see Fig. 5.6 and Table 5.1). This indicates that at slow displacement rates and elevated temperatures, healing processes may become important during deformation.

Deformation-healing-deformation experiments (*dhd*):

Figure 5.8 shows the force-displacement for samples that were deformed twice at $T = 500$ °C, $P_c = 500$ MPa and $\dot{\epsilon} = 10^{-4} s^{-1}$, with a hydrostatic healing period between both deformation phases. The force required to deform the sample for the second time is the same as in the first and independent of the intermediate healing time.

On BSE micrographs at high magnification, two generations of fault gouges can be distinguished (Fig. 5.9a,c). The first generation of fault gouge formed during the first deformation stage and was healed at 500 °C for 14 days (as *dh*-samples 56nk, 65nk, Table 5.1). The second generation of fault gouge displaced the healed fault gouge and was not healed. The fault zones were identified on the basis of their cross-cutting relationships and by their state of cohesion (fresh or healed). The fresh fault gouge formed a network of conjugate fractures, often next to the healed fault gouge of the first deformation stage. The fault gouge formed in experiment 59nk has approximately the same $D_{>}$ -values as the experiment performed under the same conditions with a single deformation phase (*d*-Experiment 68nk, see Table 5.1).



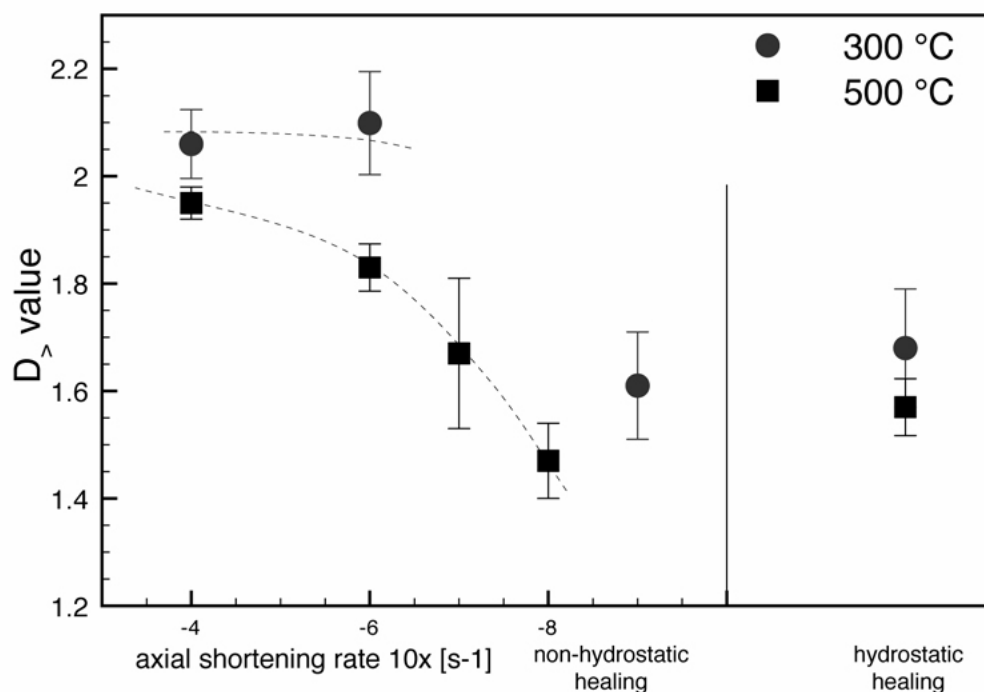


Figure 5.6: $D_{>}$ for feldspar as a function of axial shortening rate and for samples healed under (non-)hydrostatic conditions for 14 days. The values for the axial shortening rate during non-hydrostatic healing are derived from Figure 5.4b.

5.3.2 Natural fault rock

The experimentally produced microstructures have been compared with granitoid fault gouge samples collected from four different natural fault zones.

Nojima Fault Zone:

The thin sections studied here originate from a Cretaceous granodiorite affected by a left-lateral movement of the Nojima Fault (Ito et al., 1999; Fabbri et al., 2004) that off-sets the base of middle-late Eocene Kobe Group. Pseudotachylytes related to this deformation episode (Boullier et al., 2001) were dated at 56 ± 4 Ma by fission-tracks on zircons (Murakami and Tagami, 2004). The deformation was followed by an alteration producing laumontite (Fujimoto et al., 2001) which indicates temperatures of 150°C – 280°C (Zen and Thompson, 1974; Boullier et al., 2004a). Samples were taken from a depth of 623.5–624.6 m (i.e., within a meter of the main fault zone) of the Hirabayashi drill core through the Nojima Fault Zone (UTM 53, E53494456/N3823093). The studied fault gouge was formed during pre- to middle Eocene movement of the Nojima Fault. Parts of the fault gouge consist of well-mixed mineral phases (Fig. 5.3.2a). BSE-contrast SEM micrographs show rounded grain shapes indicating healing of the monomineralic fault gouge

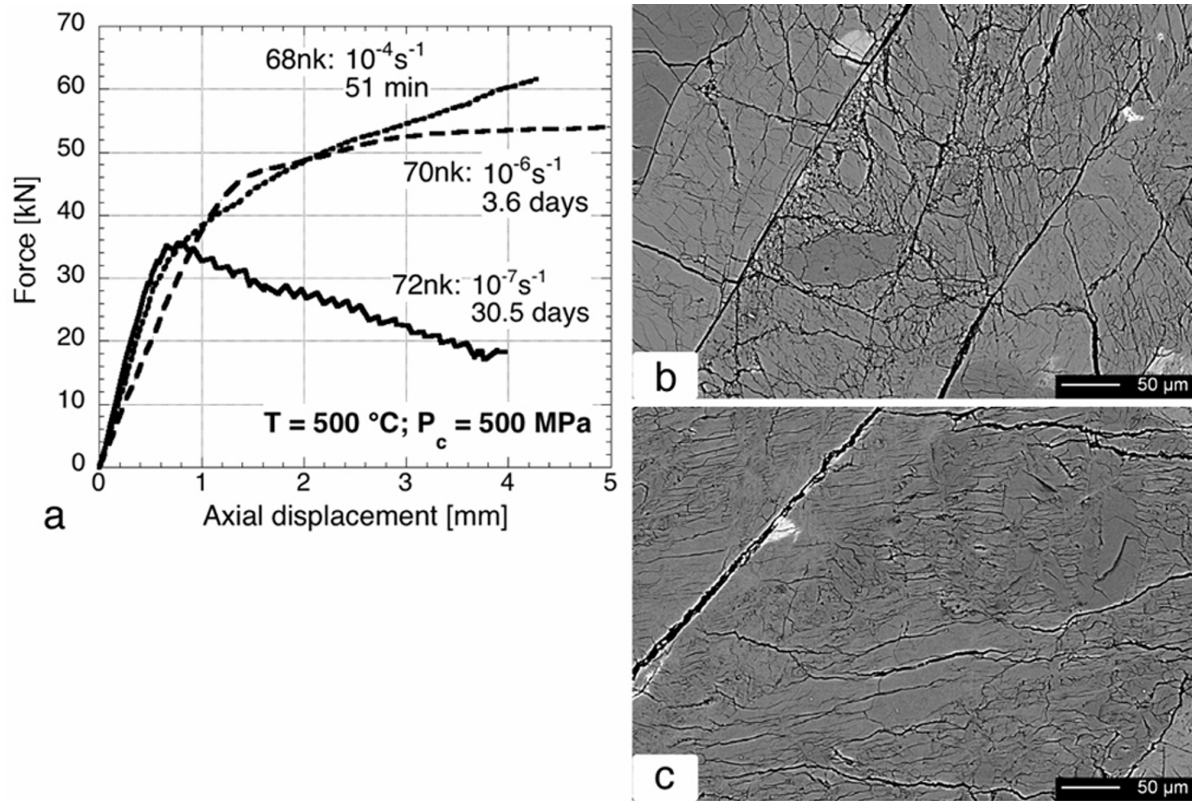


Figure 5.7: Mechanical data and microstructures of samples deformed at different axial shortening rates. Mechanical data, axial shortening rates and duration of the experiments are indicated.

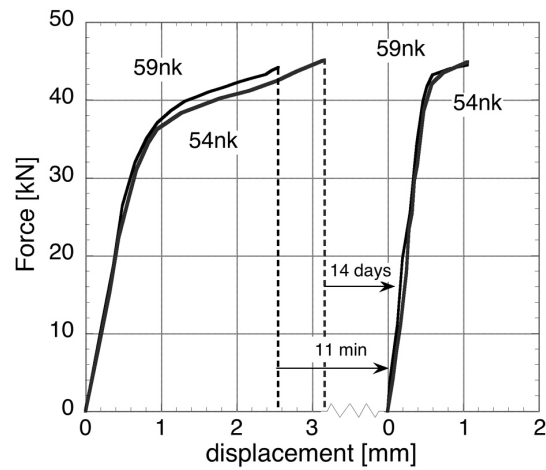


Figure 5.8: Mechanical data of deformation-healing-deformation experiments. Samples were deformed, unloaded (schematically indicated by dashed line). Both deformation phases and the hydrostatic period between deformation occurred at $T = 500 \text{ }^\circ\text{C}$, $P_c = 500 \text{ MPa}$.

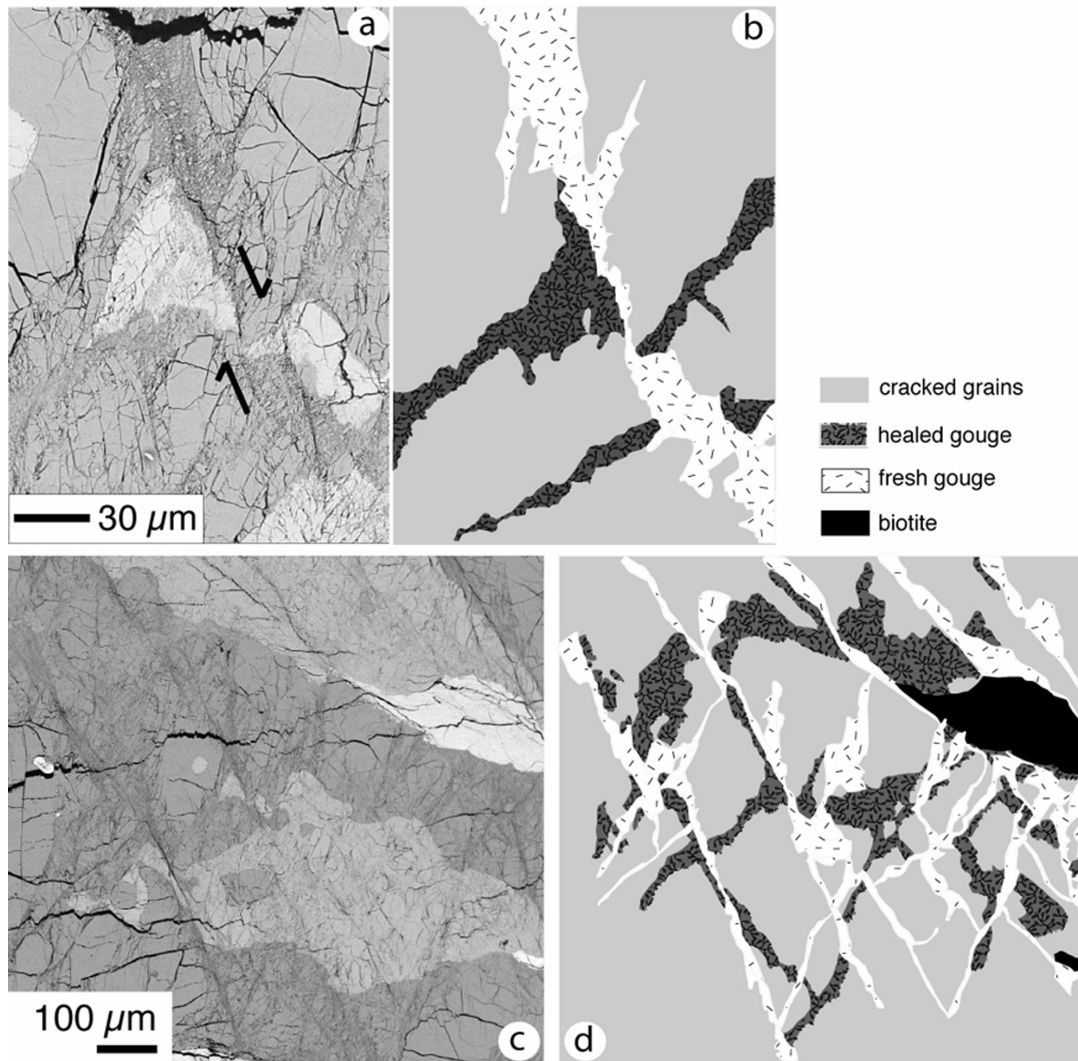
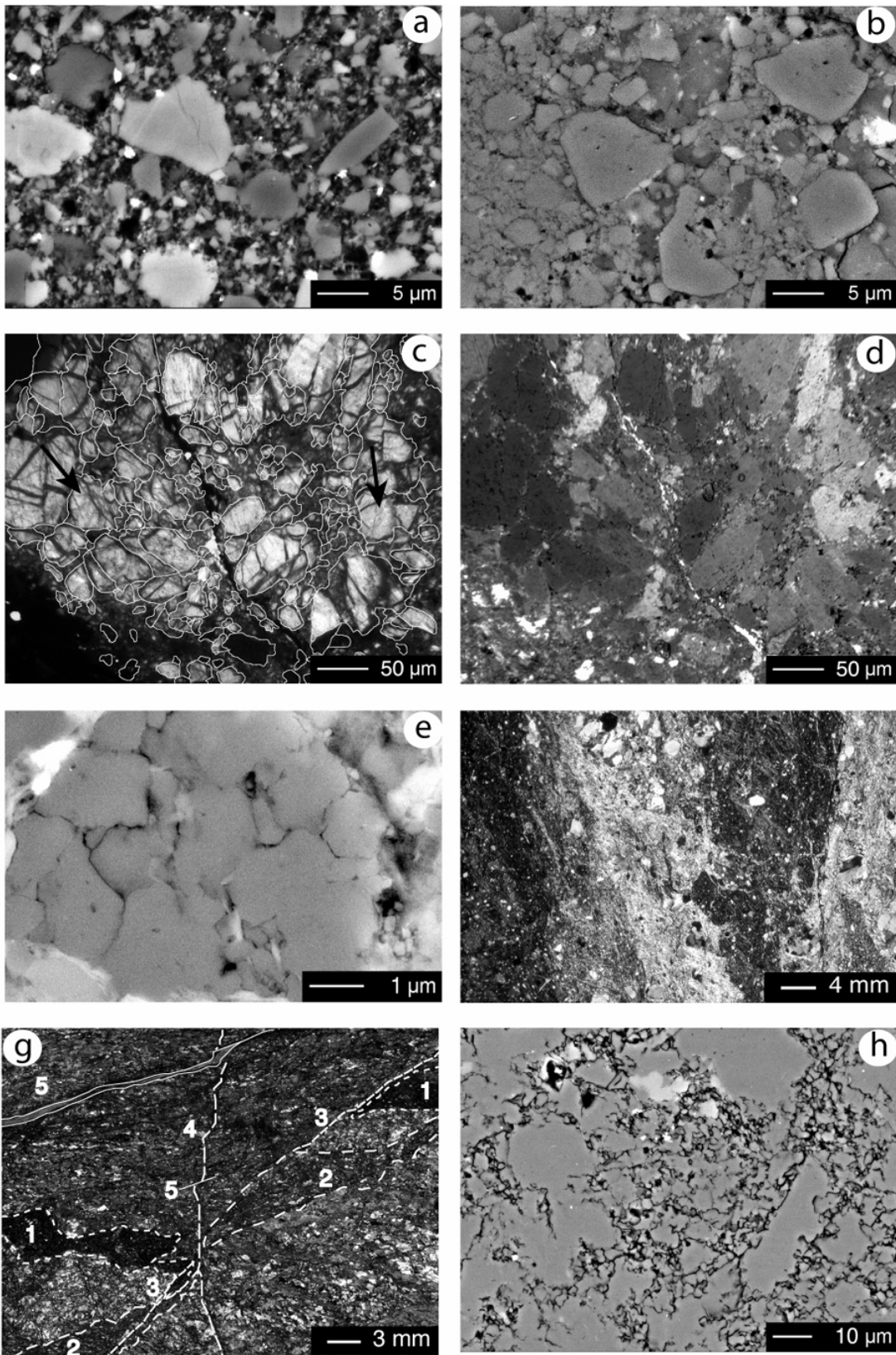


Figure 5.9: Microstructures of deformation-healing-deformation experiment. (a) BSE contrast SEM micrograph of fault gouge zone formed in experiment 54nk, arrows show the displacement. (b) Interpreted distribution of cracked grains, healed fault gouge and fresh fault gouge in (a). The fault gouge of the first deformation is cross-cut and offset by the second deformation. (c) BSE contrast SEM micrograph of a large part of the fault zone network in the same sample. (d) Interpreted structure of the fault zone network in (c), created by combining detailed observations on the fault gouge as in (a) into one map.

Figure 5.10: Microstructures of natural fault gouge. (a,b) backscatter-contrast SEM (BSE) micrographs of the Nojima Fault, (a) polymineralic fault gouge, (b) monomineralic fault gouge. (c,d,e) Wehratal Fault Zone, (c) CL image corresponding to (d) polarization light micrograph (LM) of the same location. Arrows point to corresponding sites. (e) BSE-micrograph showing healed quartz. (f,g,h) Orobic Thrust, (f) Reactivated fault zone in Gneiss Chiari, with several layers of cataclasites cross-cutting each other. (g) LM-image of fault rock from Passo di Verrobbio showing repeated fracturing. Possible sequence of gouge formation and fracturing is indicated by numbers. (h) Pescegallio fault gouge, consisting of plagioclase in BSE-micrograph.



(Fig. 5.3.2b). No healing microstructures were observed in the polymineralic fault gouge (Fig. 5.3.2a).

Black Forest Fault Zone:

The Wehratal Fault (UTM zone 32: E32418869/N5277964) and the Kandern Fault Zones (UTM zone 32: E32400833/N5285457) in the southern Black Forest, Germany have been reactivated during the formation of the Upper Rhine Graben (late Eocene to present) (Ziegler and Dèzes, 2005). Earlier brittle deformation on these fault zones occurred in the Permian or Mesozoic (Echtler and Chauvet, 1992). The Kandern Zone forms the junction between the Rhine Graben normal fault and the EW-striking transtensional Kandern-Hausen fault in the southern Black Forest. The samples studied here originate from the leucogranitic Schlächtenhausen Granite and the K-feldspar-rich Marlsburg Granite (Hinsken, 2003), derived from a road section east of the village Kandern. Zircon and apatite fission tracks analyses indicate that deformation occurred at approximately Late Eocene time (Dresmann et al., 2009). The Wehratal normal fault is coeval with the Kandern fault and cuts through the Albtal Granite (Huber and Huber-Aleffi, 1990). The samples were taken at the northern shore of the Wehra water reservoir.

CL observations of thin sections of the samples indicate cementation of non-luminescent material around the grains and crack healing in both fault zones (Fig. 5.3.2c,d). The LM image shows that several fragments have healed to grains with a single optical orientation (Fig. 5.3.2d). Black arrows in Figure 5.3.2c point to fragments of an earlier fracturing cycle cemented with more luminescent material, indicating a higher temperature during cementation. The grains have a roughly equidimensional shape; grain growth is clearly expressed by a clustering of the grains (Fig. 5.3.2e). Alteration reactions occurred after the cataclastic deformation, especially in the fine-grained fault gouge.

Orobic Thrust:

The Orobic Thrust is one of the major thrusts of the Lombardic Alps, Northern Italy, where the Variscan Basement is thrust over a series of Permian to Mesozoic sediments (e.g. De Sitter and De Sitter-Koomans, 1949; Schoenborn, 1992). Alpine deformation in the Orobic area started before the Adamello intrusions (42–30 Ma Del Moro et al., 1983) and occurred under lower greenschist facies or very low-grade conditions, as is indicated by the occasional growth of chlorite, stilpnomelane and albite (Milano et al., 1988). Carminati and Siletto (2005) suggest that Alpine deformation on the Orobic Thrust occurred in two phases: first top-to-SSE thrusting and subsequently strike-slip movement.

We sampled Variscan paragneisses (Passo di Verrobbio) and orthogneisses (Gneiss Chiari from Lago di Pescegallo; UTM zone 32: E544236/N5098326) deformed by the Orobic Thrust in the area west of the Passo di San Marco (UTM: E545615/N5098687). Hundreds of small cataclastic

locality	analysed minerals for GSD	degree of mixing	temperature °C	D _{>} -values
Kandern, Black Forest	qtz, Ksp	-	70-120 ^b	1.58
Kandern, Black Forest	qtz, plag, Ksp	+/-	70-120	1.72
Wehratal, Black Forest	qtz, plag, Ksp	-	<120	1.60
Verrobbio, Orobic Thrust	plag (Ksp)	-	250-400 ^c	1.59
Verrobbio, Orobic Thrust	qtz	-	250-400	1.62
Pescegallo, Orobic Thrust	plag (qtz, Ksp)	--	250-400	1.59
Nojima Fault Zone	qtz (plag, Ksp)	++	150-280 ^a	2.44
Nojima Fault Zone	qtz, plag (Ksp)	-/-	150-280	1.59
Verzasca Gneiss (experiments)	qtz, Ksp, plag	-	500	1.54-1.59

locality	composition
Kandern, Black Forest	qtz, plag, Ksp, bt, wm
Wehratal, Black Forest	Ksp, qtz, plag, bt, wm
Verrobbio, Orobic Thrust	qtz, plag, Ksp, bt, gnt, chl, wm, st
Pescegallo, Orobic Thrust	plag, qtz, Ksp, wm
Nojima Fault Zone	qtz (33%), plag (34%), Ksp (19%), bt (11%), hbl (4%)
Verzasca Gneiss (experiments)	qtz (35%), plag (29%), Ksp (27%), bt (5%), wm (2%)

Table 5.2: Measured D-values for natural granitoid fault rocks. qtz = quartz, plg = plagioclase, Ksp = K-feldspar. Mixing describes the amount of mixing of the minerals within the fault gouge; ranging from (++) = very well to (-) = absent.

^a (Zen and Thompson, 1974), ^b (Dresmann et al., 2009), ^c(Milano et al., 1988)

fault-zones can be seen in the field, alternating with and cross-cutting pseudotachylytes. These fault zones cross-cut one another even at the thin-section scale (Fig. 5.3.2f,g). Flattened grains with straight boundaries, indentations and the presence of stylolites indicate that healing in these fault zones involved pressure solution. With CL we can observe that newly deposited material was cemented around these fragments. Locally, in fractions up to 30%, the orthogneiss fault gouge is monomineralic on a mm to cm-scale and here bridges between the plagioclase grains produce irregular and rounded grain shapes (Fig. 5.3.2h).

Grain size distribution of natural fault rocks:

The $D_{>}$ -values of natural fault rocks depend primarily on whether the fault gouge consists of a polymineralic mixture or monomineralic aggregates (Table 5.2). Polymineralic fault gouge always shows a higher $D_{>}$ -value than monomineralic gouge ($D_{>} = 2.44$ for the Nojima Fault gouge; $D_{>} = 1.72$ for the Kandern Fault gouge) although both gouge types have the same deformation history (i.e., formed under the same PTt conditions). In the polymineralic fault gouge of the Nojima Fault Zone, very small grains (smaller than 150 nm diameter) can still be observed. These distributions are similar to those of fresh experimental gouge without healing (Table 5.1). For monomineralic fault gouge, $D_{>}$ lies in a range from 1.58 to 1.62 (Fig. 5.3, Table 5.2), similar to monomineralic healed experimental samples.

5.3.3 An exponential decay law to describe the progress of healing under hydrostatic conditions.

The evolution of the fault gouge from cohesionless material to a consolidated rock is reflected by a change of the $D_{>}$ -values as a function of healing temperature and time. Final (healed) values, D_f , of 1.5 - 1.6 are reached after 4 days if the healing temperature is high (500 °C) and after longer periods if healing temperatures are lower. Once the healed value is reached, it does not decrease any further. Even after healing times of several million years (as in the case of the Nojima fault), values of 1.58 - 1.59 are observed. As a first approximation we therefore describe the decrease of $D_{>}$ by an exponential function in the following form:

$$\Delta D = \Delta D(t) = D_{>}(t) - D_f = A \cdot e^{(-\lambda t)} \quad (5.1)$$

where λ [s^{-1}] is the temperature dependent decay constant and A the temperature-dependent pre-exponential constant.

Although the $D_{>}$ values of freshly deformed quartz and feldspar are different (~ 2.3 versus ~ 2.1 , respectively), they both decay towards a common final value of $D_{>}$ (Fig.5.11a and b, Table 5.1). Therefore, we fitted one common decay function for each of the healing temperatures ($T = 300$,

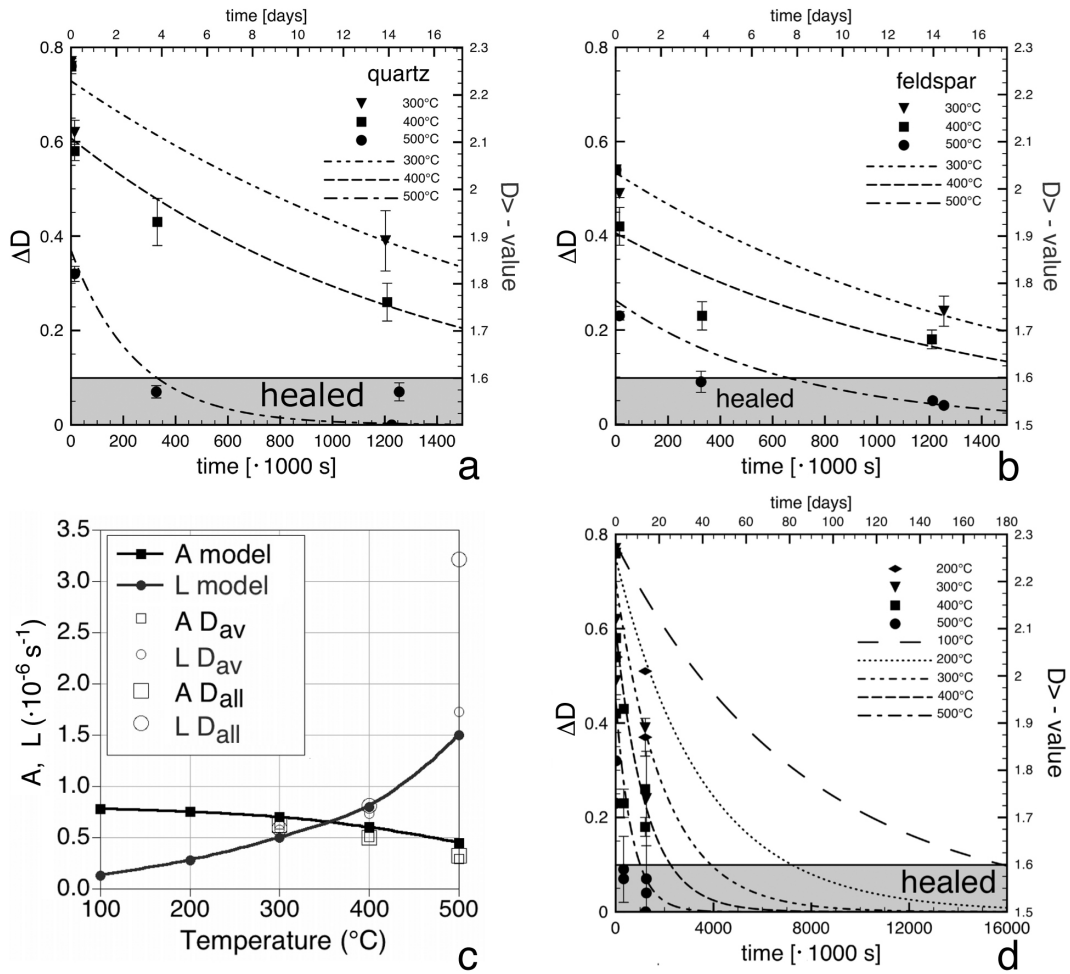


Figure 5.11: Decay of $D_{>}$ and $\Delta D = D_{>}(t) - D_f = D_{>} - 1.5$ as a function of healing time for different temperatures. Data are taken from Table 5.1. (a,b) $D_{>}$ -values for quartz and feldspar, including exponential curve fits. (c) Dependence of A and $L = \lambda$ on temperature. “ D_{av} ”: A and λ are obtained by fitting the average $D_{>}$ -values of quartz and feldspar; “ D_{all} ”: all $D_{>}$ values of quartz and feldspar are used; “mode”: values of A and λ selected for most conservative long time extrapolation. Note: no experimental data for $T = 100^{\circ}\text{C}$ and 200°C . (d) Decay curves of $D_{>}$ and ΔD calculated for larger time periods using the values for A and λ from (c): $T = 500^{\circ}\text{C}$: $A=0.45 / \lambda=1.5$; 400°C : $A=0.60 / \lambda=0.80$; 300°C : $A=0.70 / \lambda=0.5$; 200°C : $A=0.75 / \lambda=0.28$; 100°C : $A=0.78 / \lambda=0.13$.

400 and 500°C) and derived A and λ values for the individual $D_{>}$ values of quartz and feldspar (D_{all} in Fig. 5.11c) and for the average $D_{>}$ values of quartz and feldspar, (D_{av} , Fig. 5.11c) at any given temperature. We then selected maximal values for A and minimal values for λ with the intention of obtaining the most conservative decay laws.

Extrapolating the values of A and λ (Fig. 5.11c) we plotted a decay curve for 200°C . An additional healing experiment at 200°C and 14 days reproduced the expected values of $D_{>}$. It

is important to note that the decay functions are based on a few experiments and may have large errors. Also, the decay of ΔD describes a geometrical change; no physical process is implied. Figure 5.11d shows the decay of ΔD within one half year for temperatures between 200 and 500 °C. Note also that at geological time scales, healing is very fast.

5.4 Discussion

5.4.1 Healing of fault gouge

The rate of change in the microstructures of fault gouge depends on time and temperature. In the fault gouge the grain size fraction smaller than $\sim 1 \mu\text{m}$ is no longer observable with the SEM after the samples are kept at $T = 500^\circ\text{C}$ for 14 days (Fig. 5.3). Qualitatively, the microstructures of the fault gouge show that the fragments are more rounded, small cracks have closed and the gouge is more cohesive (less plucking of particles when the sample is sectioned after the experiment; Fig. 5.2).

For fresh fault gouge, the log(frequency)-log(radius) histogram of the grain size distribution shows two different slopes ($D_>$ and $D_<$, Fig. 5.1). The grain size distribution of fault gouge kept at an elevated temperature for two weeks displays only a single slope ($D_>$, Fig. 5.3). A decrease of $D_>$ with time and an enhancement of the decrease in $D_>$ with increasing temperature (Table 5.1) can be observed as an effect of healing.

Similarities between our *dh*-type healing experiments and observations on (non-hydrostatic) healing from slide-hold-slide experiments emerge. Like Dietrich (1972) we observe that the amount of healing (or $\Delta\mu_s$) increases with an increasing holding period. Marone (1998) shows that the healing rate depends on the loading rate, as we do with different axial shortening rates. A lower rate enhances the healing effect. Blanpied et al. (1995); Olsen et al. (1998); Tenthorey et al. (2003); Nakatani and Scholz (2004) show that healing of wet fault gouge is enhanced at the beginning of the healing period at higher temperature, as is the case for our experiments. They conclude that the healing mechanism is different from that for dry friction under lower temperature conditions. Muhuri et al. (2003) have calculated that frictional healing of quartz gouge at $T = 300^\circ\text{C}$ will take 3 years, extrapolated from their own data and those of Karner et al. (1997). Tenthorey and Cox (2006) find that the recovery of fault cohesion to a strength of 20 MPa at $T = 200^\circ\text{C}$ takes 3.2 years extrapolated from isostatic healing experiments at $T = 700 - 927^\circ\text{C}$ and $P_{eff} = 50 \text{ MPa}$. Giger et al. (2006) find in similar experiments that quartz gouge with a grain size $\leq 37 \mu\text{m}$ reduces its permeability about one order of magnitude every 16 years at 200°C . These values indicate a similar timescale of healing as our calculated healing period of 1 year at $T = 200^\circ\text{C}$, where our value is at the shorter end of the range. This small

difference might be explained by the higher P_c in our experiments, allowing for better solubility of silica and therefore a decrease in the time needed for healing.

Fresh gouge has many grains as small as 60 nm diameter, whereas in healed monomineralic gouge hardly any grains smaller than 2 μm are observed. Thus, apart from the decrease in $D_{>}$ -value, the lower limit of observed grain size is increasing. The increase in the lower grain size limit appears, at a first approximation, to be exponential with time and linear with temperature. However, the counting statistics for these very small grains become insufficient for a quantitative analysis as the lower detection limit is approached.

5.4.2 A hydrostatic healing law for fault gouge

We have formulated a hydrostatic healing law based on the grain size development of fault gouge during hydrostatic healing under a confining pressure of $P_c = 500$ MPa and in the presence of water. The observed decrease in $D_{>}$ -value is due to a decrease of the small grain size fraction and / or an increase of the large size fraction.

Very small grains disappear from the grain size distribution during healing (Figs. 5.1,5.3, Table 5.1). Two processes may be responsible for this: (1) Small grains are dissolved preferentially because of their large surface to volume ratio (Sleep, 1994). (2) Small grains may be cemented together to form larger ones. Growth of small fragments at the expense of their neighboring fragments with high defect densities has been documented in cataclasites by (Stünitz et al., 2003). The cementation of small grains is documented by the combined SEM and CL images (Fig. 5.3.1).

During healing the pore space of gouge decreases (Fig. 5.2). In general, a decrease in pore space lowers the permeability and inhibits the transport of dissolved material. Also, larger mean grain sizes lead to a lengthening of the transport paths for the dissolved material. As a consequence, the healing progress slows down with time, as is observed experimentally. The time-dependence is expressed in the exponential healing law (Table 5.1, Fig. 5.11).

$D_{>}$ -values of experimentally deformed and subsequently healed samples approach 1.58 for quartz and for feldspar. For healed monomineralic natural fault gouges of the Nojima Fault Zone, the Orobic Thrust, the Kandern Fault zone and the Wehratal Fault Zone, the $D_{>}$ values are in the range of 1.58–1.62 (Table 5.2). They coincide with the experimental values and $D_{>}$ -values of 1.60 for granitoid fault gouge formed in gneisses from the Qinling Mountain (Shao and Zou, 1996) and a $D_{>}$ -value of 1.60 for the Lopez Canyon fault gouge (Sammis et al., 1987). Therefore, a rounded lower-end final $D_{>}$ -value of 1.5 to 1.6 is characteristic for a completely healed fault

gouge in experimentally and naturally samples.

Unhealed natural fault gouge associated with pseudotachylytes has $D_{>}$ -values of 2.0 – 2.3 (An and Sammis, 1994; Monzawa and Otsuki, 2003; Pittarello et al., 2006). These values are very similar to those of unhealed experimental fault gouge deformed at $T = 300\text{ }^{\circ}\text{C}$ and 500 MPa confining pressure (Chapter 4). The similarity of $D_{>}$ -values of unhealed fault gouge of experimentally deformed samples at $\dot{\epsilon} \approx 10^{-4}\text{ s}^{-1}$ and those of natural seismic fault gouges indicates that it may not be possible to distinguish between seismically and aseismically produced fault gouges and cataclasites on the basis of their $D_{>}$ -values.

The difference in $D_{>}$ values between the monomineralic fault gouge ($D_{>} = 1.58 - 1.62$) and polymineralic fault gouge ($D_{>}$ up to 2.44) in the Nojima fault is remarkable, considering that both types of gouge have formed contemporaneously and have remained under the same pressure and temperature conditions after deformation. The difference can be explained by the mixing of different phases in the fault gouge. The fact that phase mixing inhibits the healing process suggests that normal grain growth is an important process during healing (see also Sleep, 1994), because mixing of different phases inhibits the growth of grains (e.g. Olgaard and Evans, 1988). In a well-mixed polymineralic fault gouge, the $D_{>}$ -value acquired during deformation may be preserved and can be used as an indicator for the conditions during deformation.

In equation 5.1, one expects the pre-factor A to be equal to ΔD , the difference between the $D_{>}$ -value of freshly formed gouge and the value $D_f (= 1.5)$ after complete healing, and independent of the healing temperature. However, a temperature dependence is noticeable in Fig. 5.11c. This is due to the following circumstance: Healing was always carried out at the same temperature as the deformation. As the $D_{>}$ -value of freshly formed gouge does not only depend on mineral composition but also on deformation temperature, the starting values for the different healing experiments was different. $D_{>}$ varies between 1.95 for experimentally deformed feldspar (at $500\text{ }^{\circ}\text{C}$) and 2.26 for quartz (at $300\text{ }^{\circ}\text{C}$). The corresponding range of values for A are 0.45 to 0.76. Our fit values are 0.45 to 0.70 for 500 and $300\text{ }^{\circ}\text{C}$ respectively. In nature even higher values occur (Fig.5.3, Table 5.2): $D_{>} = 2.44$ ($A = 0.94$) for naturally formed polymineralic gouge (estimated deformation temperature $< 200\text{ }^{\circ}\text{C}$). This temperature dependence of $D_{>}$, added to the fact that our data base is still rather small, lets us anticipate rather large errors for A .

For the long time extrapolation however, the value of the decay constant is much more important. As we assume that water is the main agent transporting dissolved material and furthermore that healing ceases below the freezing temperature of water, the decay constant λ is assumed to be 0 at $0\text{ }^{\circ}\text{C}$. Even though healing may well continue down to 0K, it must be by another process, at much lower rates. However, a temperature setting of $< 0\text{ }^{\circ}\text{C}$ is not of great geological significance.

Using our extrapolated values for A and λ for 200 and 100 °C, we obtain healing times of 3 and 6 months, if we accept that reaching a value of $D_{>} \leq 1.6$ means that the gouge is healed. Again, the exact value of the healing time is not important, only the order of magnitude counts: healing takes a year or a few years, not thousands or millions of years!

This hydrostatic healing law can only be extrapolated to other pressure and temperature conditions with caution: the chemistry of the pore fluid plays an important role. The solubility of silica does not only increase with temperature, but also with confining pressure (Manning, 1994). For example at $T = 400$ °C, $P_c = 500$ MPa the solubility is five times higher than at 250 MPa and the same temperature. Salts or volatiles dissolved in water may increase or impede the dissolution-, diffusion- or precipitation-rate of the minerals involved (see e.g. Dove and Crerar, 1990; Xie and Walther, 1993). Furthermore, faults in nature are open systems, and therefore fluids are not necessarily always saturated with silica and other components.

5.4.3 Reactivation of fault zones

The *dhd*-experiments (53nk, 54nk, 59nk) took place at confining pressures similar to those inferred for the base of the seismogenic zone. Under these conditions, faults without elevated pore pressures are strong. Repeated deformation of samples takes place at the same strength regardless of whether healing has taken place or not (Fig. 5.8). Furthermore, repeated deformation affects intact rock and does not produce slip on the existing fault zones (Fig. 5.9). Thus, new fractures form instead of repeating slip events on existing fractures suggesting that deformation takes place by cataclastic flow at confining pressures above the brittle-ductile transition (Paterson, 1978; Rutter, 1986; Kohlstedt et al., 1995).

Tenthorey et al. (2003); Tenthorey and Cox (2006) have studied the extent to which strength is recovered after healing at low confining pressure. They observe partial strength recovery after hydrostatic treatment at $T = 927$ °C. Sample strength increases with increasing healing time and temperature (Karner et al., 1997; Tenthorey et al., 2003; Tenthorey and Cox, 2006). Microstructures of our *dhd*-samples show that a second deformation after healing develops a new fault gouge zone adjacent to the earlier one instead of reactivating the existing fault gouge zone (Figs. 5.9, 5.3.2g,h), a feature that has been observed by other workers in experimental fault rock (Tenthorey et al., 2003, see especially their Figure 4f) and in natural fault rocks Mitra (1992); Otsuki et al. (2003).

Rutter and Maddock (1992) found a similar behaviour for kaolinite-quartz gouge deformed at conditions up to $P = 200$ MPa and $T = 600$ °C. Their mechanical data displayed a hardening and brittle failure upon reloading after stress-relaxation at high temperatures and over long

times. Microstructures for this fault gouge show recrystallisation and the formation of new minerals, cementation and the healing of cracks.

5.4.4 Healing under non-hydrostatic conditions

In samples healed during slow deformation under non-hydrostatic conditions ($\dot{\epsilon} < 10^{-8} s^{-1}$) the healing process is more efficient, producing lower $D_{>}$ -values at shorter times than under hydrostatic conditions (Fig. 5.6). The hydrostatic healing law for granitoid fault gouge (equation 5.1) cannot be used for samples healed under non-hydrostatic conditions. A further set of experiments would be required to determine the stress or strain rate dependence for samples healed under non-hydrostatic conditions.

The temperature dependence of the creep rate, the effective reduction of pore space, and reduction in $D_{>}$ -value suggest that creep is accommodated by diffusive processes (solution-precipitation/diffusion creep). This is in contrast to experiments by Karner et al. (1997), who find that cementation is inhibited during healing under load. We think that their results differ from ours because they used different pore and confining pressures. For deformation at sufficiently slow shortening rate and, depending on the grain size and the temperature, non-hydrostatic healing of the fault gouge by diffusion creep appears to be more efficient than the creation of new fault gouge by micro-cracking (the brittle-plastic transition, Rutter, 1986; Kohlstedt et al., 1995).

For deformation at a strain rate of $\dot{\epsilon} = 10^{-7} s^{-1}$ and $T = 500^{\circ}C$, especially in the case of quartz, brittle deformation and healing seem to progress simultaneously, especially for quartz. Undulatory extinction, deformation bands and micro-kinking in quartz were observed and are explained by fracturing, fragment rotation, and subsequent healing (Fig. 5.7b). Similar features were described by Tullis and Yund (1987); Den Brok (1992); van Daalen et al. (1999); Vernooij et al. (2006) for low and intermediate temperature regimes.

Paterson (1995) has formulated a constitutive relationship for granular flow accommodated by material transfer through an intergranular fluid in the form of an adapted island-channel model. Source to sink diffusion is assumed to control the rate of this process in natural fault rock and in laboratory investigations at intermediate pressure-temperature conditions. For a quartz-water system with a grain size of $10 \mu m$, deformed at $T = 327^{\circ}C$, $P_c = 200$ MPa and low differential stress, Paterson's relationship yields a strain rate of $\dot{\epsilon} = 5 \times 10^{-9} s^{-1}$ for granular flow controlled by source-sink diffusion (Table 1 in Paterson, 1995). After fracturing at $T = 300 - 500^{\circ}C$ and $P_c = 500$ MPa, very fine-grained fault gouge is observed in our samples (particle size as small as 30 nm).

	Paterson'95	smaller grain sizes				
grain diameter [μm]	10	1	1	0.1	0.1	1
island diameter [μm]	0.2	1	0.1	0.1	0.05	0.02
strain rate [s^{-1}]	5×10^{-9}	2×10^{-9}	2×10^{-7}	2×10^{-6}	7×10^{-6}	5×10^{-6}

Table 5.3: Rate of material transfer in granular flow, recalculated from Paterson (1995) for source-sink diffusion control, $T = 600\text{K}$, $P_c = 200\text{ MPa}$.

If we apply Patersons calculation (Eq. 34 in Paterson, 1995), using temperature and confining pressure of 327°C and 200 MPa , respectively, we obtain a strain rate of 10^{-6}s^{-1} for grains of $0.1\ \mu\text{m}$ with islands of $0.05\ \mu\text{m}$ in diameter (Table 5.3), and strain rate of 10^{-9}s^{-1} for grains of $1\ \mu\text{m}$ with islands of $1\ \mu\text{m}$. These calculations are performed for a differential stress of one third of the effective confining pressure. In our deformation experiments, the differential stress is more than one order of magnitude higher, from which we expect an increase of the creep rate by at least one order of magnitude. The results of the Paterson model for diffusion creep and our observed creep rates are similar, if a mean grain size of $1\ \mu\text{m}$ is considered for the experimental samples. To us this confirms that diffusion creep may be probable dominant mechanism for the observed creep during non-hydrostatic healing experiments.

Increasing the temperature in experiments to 500°C increases the displacement rate by about one order of magnitude (Fig. 5.4). Samples may deform simultaneously by fracturing and viscous flow. The same combination of brittle and viscous deformation has been shown for experimental deformation of halite fault gouge in a NaCl-saturated fluid (Bos et al., 2000). Fousseis et al. (2006) describe the evolution of brittle precursor faults to mylonitic zones that deform by a combination of cataclasis and simultaneous viscous creep of the fine-grained material in shear zones at the Cap de Creus, Spain. The calculated rates show that diffusion creep can achieve relatively high deformation rates (e.g. 10^{-9}s^{-1}) in natural fault zones at moderate temperatures (e.g. $T = 300^\circ\text{C}$). These processes constitute likely mechanisms for post-seismic creep.

5.5 Conclusions

We deformed granitoid samples in a Griggs type deformation apparatus at $T = 300^\circ\text{C}$, $P_c = 500\text{ MPa}$, $\dot{\epsilon} = 10^{-4}\text{s}^{-1}$ with $0.2\ \text{wt}\%$ H_2O added. After deformation, samples were subsequently healed at $T = 200 - 500^\circ\text{C}$, $P_c = 500\text{ MPa}$ for 4 hours to 14 days under hydrostatic or non-hydrostatic conditions. The microstructures and grain size distributions of the experimental samples were compared to those of naturally deformed and healed samples. From the

comparison, the following conclusions are drawn:

- In natural fault rocks, the monomineralic (un-mixed) parts of the gouge show the same healing microstructures and grain size distributions as the experimental fault gouges. In polymineralic domains of the gouge the initial grain size distribution is preserved after long periods of healing. Thus, mixing of different mineral phases may effectively prevent healing. The fact that healing strongly depends on the mixing of phases suggests that normal grain growth plays an important role in the healing process.
- The grain-size distribution for healed experimental and natural fault gouge asymptotically approaches a $D_{>}$ -value of ~ 1.5 .
- A hydrostatic healing law for quartz and feldspar minerals in granitoid fault rocks is formulated to estimate different healing times, t , at different temperatures: $\Delta D(t) = D_{>}(t) - D_f = A \cdot e^{(-\lambda t)}$, where $D_f = 1.5$ is the final value for completely healed gouge. The best estimates for A are between 0.45 (500 °C) and 0.78 (100 °C) and for λ between $1.5 \times 10^{-6} s^{-1}$ (500 °C) and $0.13 \times 10^{-6} s^{-1}$ (100 °C). The hydrostatic healing law is valid for monomineralic fault gouge or monomineralic parts of any gouge. Extrapolation shows that healing of monomineralic domains of granitoid fault gouge under hydrostatic conditions may occur in ~ 1 year at a temperatures between 100 °C and 200 °C.
- Healing under non-hydrostatic conditions is even more efficient than hydrostatic healing. Deformation under low axial shortening rates causes simultaneous deformation and healing by means of diffusion mass transfer (diffusion creep). The presence of a very small grain size fraction in the fault gouge promotes the operation of this process.
- In *dhd*-experiments with repeated deformation, at $P_c = 500$ MPa, fault zones created in the first deformation event are not reactivated during the second deformation. Frictional sliding on pre-existing faults does not occur regardless of whether the fault gouge is healed or not. Even though more experiments are necessary to fully understand the mechanical implications of fault gouge healing, our results already now suggest that in natural rocks, the degree of healing may not play a major role in brittle fault reactivation at high confining pressures.

Chapter 6

Experimental investigation of grain scale processes during and after deformation of diabase and glassy basalt.

In this Chapter the experiments performed on basalt samples are described. The mechanical data, microstructures and mineral reactions of basalt samples are investigated. The observations on the grain size distribution and its D -value and the development of fault zones are compared to the granitoid experiments. Investigations of the spatial distribution of plagioclase in the deformed samples and of mineral reactions in the fine grained gouge have been performed.

6.1 Introduction

Although basalt is a very common rock type in the Earth's crust, only a few studies have concentrated on the mechanical properties of these rocks and their coarser grained equivalents, diabase and gabbros. Hardly any investigation has been performed in the temperature range of $T = 300\text{--}500^\circ\text{C}$ and upper to mid-crustal confining pressures, although the base of the seismogenic zone of oceanic crust is estimated at ca. $T = 400^\circ\text{C}$ (Tapponnier and Francheteau, 1978; Hyndman and Wang, 1995). It is therefore necessary to study basalt deformation at the brittle-ductile and brittle-plastic transition to gain a better understanding of the processes acting in transform faults and during early stages of subduction.

Most experiments on partially glassy basalts and diabase concentrate on the rheology of partially molten mafic rock (e.g. Mei et al., 2002; Yoshinobu and Hirth, 2002). They show that, compared to the anhydrous high temperature experiments of Mackwell et al. (1998) on diabase, the presence of melt strongly weakens the rock. Dry diabase has a strength of ca. 500 MPa at temperatures of ca. 1000°C and $\dot{\epsilon} = 10^{-6}\text{s}^{-1}$. Only a few experiments have been performed under lower temperature conditions, mainly to investigate the frictional properties (e.g. Stesky et al., 1974; He et al., 2006), and to show that these rocks have a high coefficient of friction. Kronenberg and Shelton (1980) and Caristan (1982) have experimentally investigated the transition from fracturing to dislocation creep for Maryland Diabase in samples without added water. Kronenberg and Shelton (1980) concentrated on the microstructural transition between microcracking and dislocation creep and Caristan (1982) on the mechanical strength of the samples. The transition from fracturing to crystal-plastic deformation occurs between $T = 800^\circ\text{C}$, $P_c = 500\text{ MPa}$ and $T = 600^\circ\text{C}$, $P_c = 1500\text{ MPa}$ for samples shortened at $\dot{\epsilon} = 10^{-6}\text{s}^{-1}$. Unfortunately, neither of the studies report strength data of their samples deformed at temperatures below $T = 1000^\circ\text{C}$. Carmichael (1989) reports unpublished experiments performed by J. Tullis (1979) on Maryland Diabase. Dry samples deformed at $T = 600^\circ\text{C}$, $P_c = 500\text{ MPa}$, $\dot{\epsilon} = 3 \times 10^{-6}\text{s}^{-1}$ have a strength of ca. 1.2 GPa. Early experiments on basalt and diabase have been performed by Griggs et al. (1960) and yielded comparable strength. Rutter et al. (1985) report a strength of 1.4 GPa for wet, glass-free basalt deformed at $P_c = 200\text{ MPa}$ and $T = 20^\circ\text{C}$.

In contrast to basalts many studies have been performed on granitoid rock in the temperature range of $T = 300\text{--}500^\circ\text{C}$ (e.g. Stesky et al., 1974; Tullis and Yund, 1977, 1980; Blanpied et al., 1995; Kato et al., 2003, Chapters 3 and 4). Granite and basalt are the most common and typical rocks of the basement of the Earth's crust and are known to show a different mechanical behavior depending on the $PT\dot{\epsilon}$ -conditions. We will compare experimentally deformed basalt samples to granitoids to obtain information on the differences in the behavior of crustal rocks. Both rock types have been deformed under similar conditions and have been investigated for

their fault rock microstructures.

Unlike in most previous deformation experiments the basalt rock samples investigated in this study have been deformed and heat treated under conditions where metamorphic reactions are possible. The absence of chemical reactions in laboratory experiments is one of the largest discrepancies between such studies and rocks from natural fault and shear zones. Earlier studies by Rutter et al. (1985) and Hacker and Christie (1991) investigated the relation between deformation and metamorphism in basalts. Rutter and co-workers have reported that no decrease in strain rate due to the formation of hornblende in their samples deformed at $T = 600^\circ\text{C}$, $P_c = 200$ MPa, $P_p = 0\text{--}154$ MPa occurred. Hacker and Christie describe the formation of dark mica and glass, consuming up to 50% of the original glass pods in their samples at $T = 675\text{--}875^\circ\text{C}$, $P_c = 1.0$ GPa. This reaction did not cause a weakening of their samples. However, other studies showed that metamorphic reactions during experimental deformation can cause significant weakening (Stünitz and Tullis, 2001; De Ronde et al., 2004, 2005).

We have performed deformation experiments on Maryland Diabase (MD) and two partially glassy basalts, Bransrode Basalt (BB) and Vogelsberg Basalt (VB) at $T = 300$ and 500°C , $P_c = 500$ MPa with $\dot{\epsilon} = 0.01\text{--}3.4 \times 10^{-4} \text{ s}^{-1}$ in order to study their microstructures and strength. We observe a high strength for all samples deformed at $T = 300^\circ\text{C}$, whereas a remarkable weakening occurs in partially glassy basalts deformed at $T = 500^\circ\text{C}$, but not in fully crystalline diabase deformed under these conditions. Focusing on possible causes of the observed weakening, the deformation microstructures and mineral reaction products in the deformed samples are studied. It is investigated whether this weakening may be caused by metamorphic reactions. Furthermore, we will compare our results with the corresponding data on granitoid rock.

6.2 Experiments

6.2.1 Sample material

MD is fully crystalline with a grain size of approximately $120 \mu\text{m}$. It consists of ~ 40 vol% plagioclase (bytownite) with albite-rich rims, ~ 55 vol% clinopyroxene and $\sim 3\%$ ore minerals. The modal amounts of MD, BB and VB have been measured, with an error of 6%, with point counting on thin sections of undeformed material. The mineral composition was determined semi-quantatively using an electron dispersion X-ray detector (EDX) connected to a scanning electron microscope (SEM) in back-scattered electrons contrast mode (BSE). Pyroxene shows $0.01\text{--}5 \mu\text{m}$ wide exsolution bands. Kronenberg and Shelton (1980) measured the composition for their MD samples using TEM and electron diffraction patterns as: $\text{An}_{71}\text{Ab}_{27}\text{Or}_{02}$ (bytownite) and $\text{En}_{46}\text{Fs}_{16}\text{Wo}_{38}$ (augite), and reported exsolution bands of augite and pigeonite. Opaque

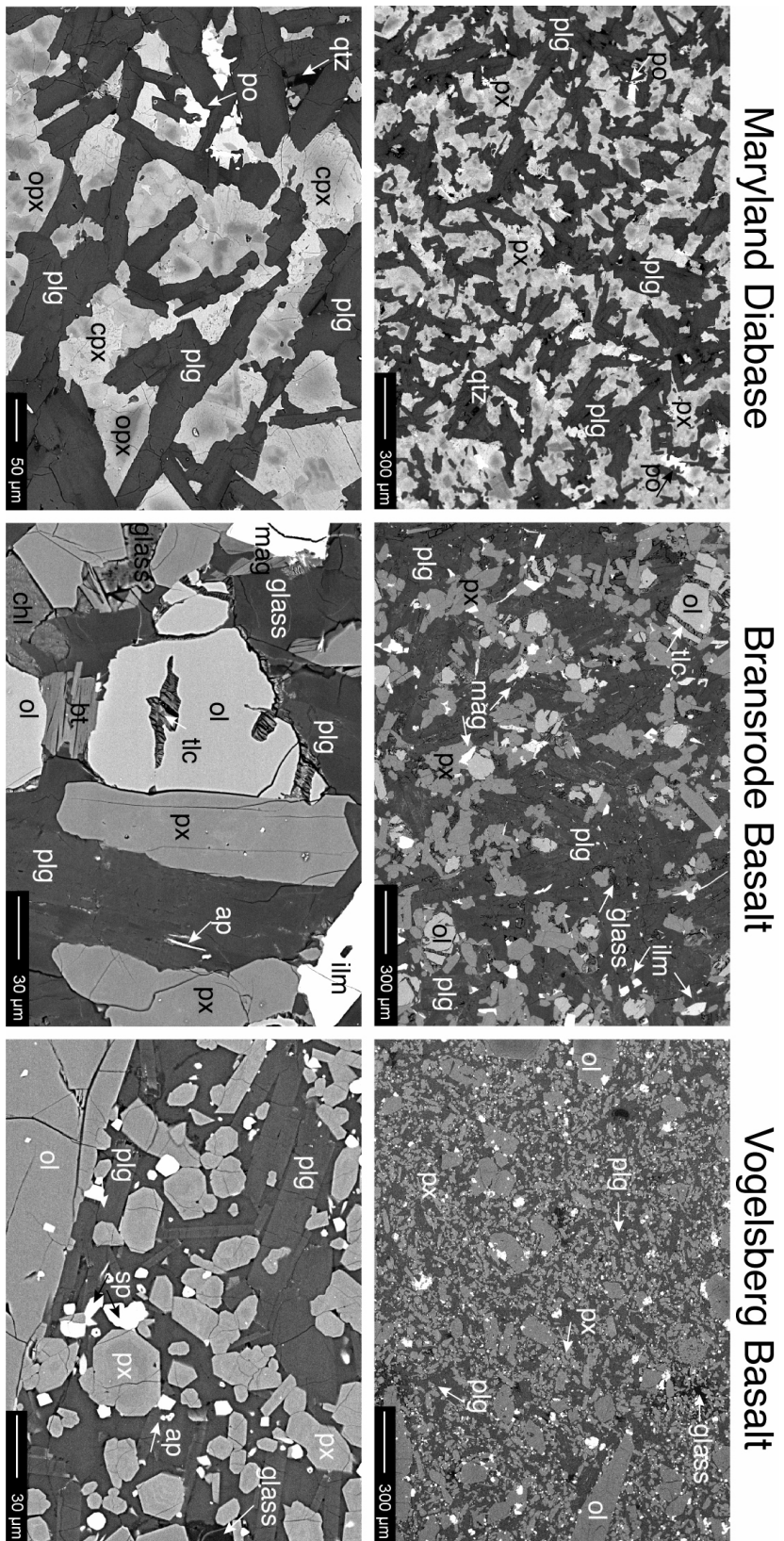


Figure 6.1: Back-scatter contrast SEM micrographs of undeformed Maryland Diabase, Bransrode Basalt and Vogelsberg Basalt. Mineral abbreviations after Kretz (1983): px = pyroxene, plg = plagioclase, po = pyrrhotite, qtz = quartz, cpx = clinopyroxene, opx = orthopyroxene, ol = olivine, ilm = ilmenite, mag = magnetite, tlc = talc, ap = apatite, chl = chloride, bt = biotite, sp = spinel.

minerals are mostly pyrrhotite and some cronstedtite*. We observe some quartz and biotite, and one spot of K-Al-Si glass, which has reacted with enstatite to quartz and mica before deformation.

BB is a Miocene alkali-olivine basalt, whose formation is associated to rifting activity in the Rhine Graben. The samples come from Groß Almerode am Hohen Meißner, Germany. The composition of the basalt is ~ 45 vol% plagioclase (bytownite), ~ 12 vol% Fe-rich olivine, ~ 23 vol% pyroxene (titano-augite), 10 vol% glass pods, 6 vol% ore minerals (Mg-Ti-magnetite and ilmenite), $\sim < 1$ vol% apatite and ~ 4 vol% alteration products, mainly chlorite. Locally the rock is more intensively altered. Care has been taken to select only unaltered sample cores; some of the samples had to be excluded from analysis after deformation. The average grain size of the matrix is $60 \mu\text{m}$, including the smaller olivine grains. Olivine grains can measure ~ 0.5 mm. Pyroxene is smaller ($\sim 25 \mu\text{m}$) than plagioclase ($\sim 90 \mu\text{m}$).

VB is an alkali-olivine basalt and originates from the Ortenberg quarry in Hessen, Germany. The development of the Vogelsberg is related to crustal extension in the Rhine Graben area (Geyer and Gwinner, 1986). VB consists of ~ 30 vol% plagioclase (labradorite), ~ 35 vol% pyroxene (titanaugite), ~ 11 vol% olivine (forsterite), $\sim 9\%$ spinel (spinel-titanomagnetite), $< 1\%$ apatite and 12 vol% glass pods, and ~ 2 vol% alteration products; a K-white mica (probably illite), phlogopite and talc inside some of the olivines. Feldspars and pyroxene have a broad variation in composition. The glass pods have a composition near the high temperature ternary feldspar composition (Carpenter, 1992). The rims are enriched in MgO, SO_3 , P_2O_5 , TiO_2 , and FeO, this may be associated with the formation of micro-crystalline grains. Glass pods occur as roughly equi-dimensional pods of up to 0.2 mm in size, though usually about the same size as the matrix grains. VB is very fine grained, with an average matrix grain size of $20 \mu\text{m}$ and clasts of olivine of up to 2 mm. This basalt is enriched in incompatible trace elements and radiogenic Sr relative to a MORB-mantle (Wittenbecher, 1992).

6.2.2 Experimental procedure

Cylinders of 6.39 mm in diameter and 11.6 ± 0.2 mm in length are cored (except sample 30nk: 13.786 mm length, 6.50 mm diameter). The ends of the cylinders are polished to plane parallel surfaces. The samples are dried for at least 24 hours under atmospheric pressure at $T = 110^\circ\text{C}$. The dry samples are wrapped twice in 0.05 mm nickel-foil and placed in a 0.25 mm thick gold tubing together 0.2%wt H_2O . The samples are deformed in a Griggs-type solid medium

*Phyllosilicate of the serpentine group with the formula $\text{Fe}_2^+\text{Fe}^{3+}[(\text{Si}, \text{Fe}^{3+})\text{O}_5](\text{OH})_4$, which is commonly associated with pyrite or pyrrhotite. Identified with EDX on a SEM.

sample	deformation				heat treatment			
	T °C	P _c MPa	ė x 10 ⁻⁴ s ⁻¹	ax. ε %	T °C	P _c MPa	time x 10 ⁺³ s	time days
<i>Maryland Diabase</i>								
100nk	300	480	1.3	39	500	560	1205.80	14
113nk	300	510	1.3	37				
30nk	500	480	0.013	34				
<i>Bransrode Basalt</i>								
39nk	300	480	0.018	39				
101nk	500	560	1.3	37				
41nk	500	510	0.01	15				
<i>Vogelsberg Basalt</i>								
105nk	300	520	3.4	35				
88nk	300	510	1.3	35				
87nk	300	490	1.3	30	300	500	1202.04	14
86nk	500	510	1.2	30				
89nk	500	540	1.3	40				
84nk	500	500	1.0	25	550	480	1206.48	14

Table 6.1: Deformation and heat treatment experiments performed on the three types of basalt. 0.2 wt% H₂O was added to all samples. T = temperature, P_c = confining pressure, $\dot{\epsilon}$ = axial shortening rate, ax. ϵ = axial shortening.

deformation apparatus (Tullis and Tullis, 1986) at the University of Basel, using NaCl as confining medium, Al₂O₃ as pistons. The temperature is measured with a K-type (chromel/alumel) thermocouple during deformation. For more details on the experimental method, the reader is referred to the Chapters 2 and 4.

Samples are deformed at $T = 300$ and 500°C , $P_c = 500$ MPa and $\dot{\epsilon} = 1 \times 10^{-6}\text{s}^{-1}$ – $3.4 \times 10^{-4}\text{s}^{-1}$ (see Table 6.1). Most of the samples are quenched after deformation and retrieved from the deformation apparatus. Three samples are heat treated by keeping them in the deformation apparatus at $T = 300$ or 500°C , $P_c = 500$ MPa, under hydrostatic conditions, for 14 days (heat treatment period). Samples are cut along their median plane and one half is used to make a thin section. The samples are studied using a Philips XL30 SEM (ZMB Basel) in BSE-mode and with a Zeiss Axioplan optical polarization microscope (LM).

6.2.3 Experimental results

MD is strong under the investigated conditions with peak stresses of 1700 MPa at $T = 300^\circ\text{C}$, $\dot{\epsilon} = 10^{-4}\text{s}^{-1}$ and 1100 MPa at $T = 500^\circ\text{C}$, $\dot{\epsilon} = 10^{-6}\text{s}^{-1}$ (Fig. 6.2). Samples deformed at $T = 300^\circ\text{C}$ (100nk, 113nk) show displacement along a single diagonal fault with a 25–50 μm wide gouge zone. The sample deformed at $T = 500^\circ\text{C}$, $\dot{\epsilon} = 10^{-6}\text{s}^{-1}$ (30nk) has two conjugated faults, each with ca. 50 μm wide gouge zones. Some of the samples have rotated with respect to the compressional axis during the deformation (as a result of shearing on biotite or due to an imperfect sample shape) and in these cases broader gouge zones are formed along the edges of these samples.

The BB sample deformed under $T = 300^\circ\text{C}$ and $\dot{\epsilon} = 10^{-6}\text{s}^{-1}$ (39nk) shows two conjugated faults with ca. 100 μm wide gouge zones and much deformation (cracked grains and smaller gouge zones) in the rest of the sample. Both BB samples deformed at $T = 500^\circ\text{C}$ (41nk, 101nk) show very broad fault zones with mainly cracked minerals and no well developed fault gouge.

The VB samples deformed at $T = 300^\circ\text{C}$ show a strength of 1.7 GPa for deformation at $\dot{\epsilon} = 3.4 \cdot 10^{-4}\text{s}^{-1}$ (105nk) and 1.4 GPa for deformation at $\dot{\epsilon} = 1 \times 10^{-4}\text{s}^{-1}$ (88nk). The samples deformed at $T = 500^\circ\text{C}$, $P_c = 500$ MPa (86nk, 89nk, 84nk) yield a maximum strength of only 400 MPa. VB deformed at $T = 300^\circ\text{C}$ has formed several weakly developed narrow conjugated faults in one sample (88nk) and a single diagonal fault with an upto 100 μm (87nk) and 300 μm (105nk) wide gouge zone in the other two samples. The samples deformed at $T = 500^\circ\text{C}$ are homogeneously broadened and shortened; gouge or cracked material are only rarely observed.

In general, it is observed that deformation is more localized in fully crystalline basalt (MD) than the partially glassy basalt samples (VB, BB). At $T = 300^\circ\text{C}$ all basalt rock samples show a similar strength, however at $T = 500^\circ\text{C}$, BB and VB are remarkably weaker than MD.

6.3 Microstructural analysis

The deformed samples have been studied in LM to investigate the nature of the deformation of the individual minerals and the spatial distribution of minerals within the sample to understand the difference in localization of the deformation and the strong decrease in the strength of partially glassy basalts deformed at $T = 500^\circ\text{C}$. Afterwards the samples have been investigated with BSE to study the development of fault zones in the fractured samples and the grain size distribution of these fault zones.

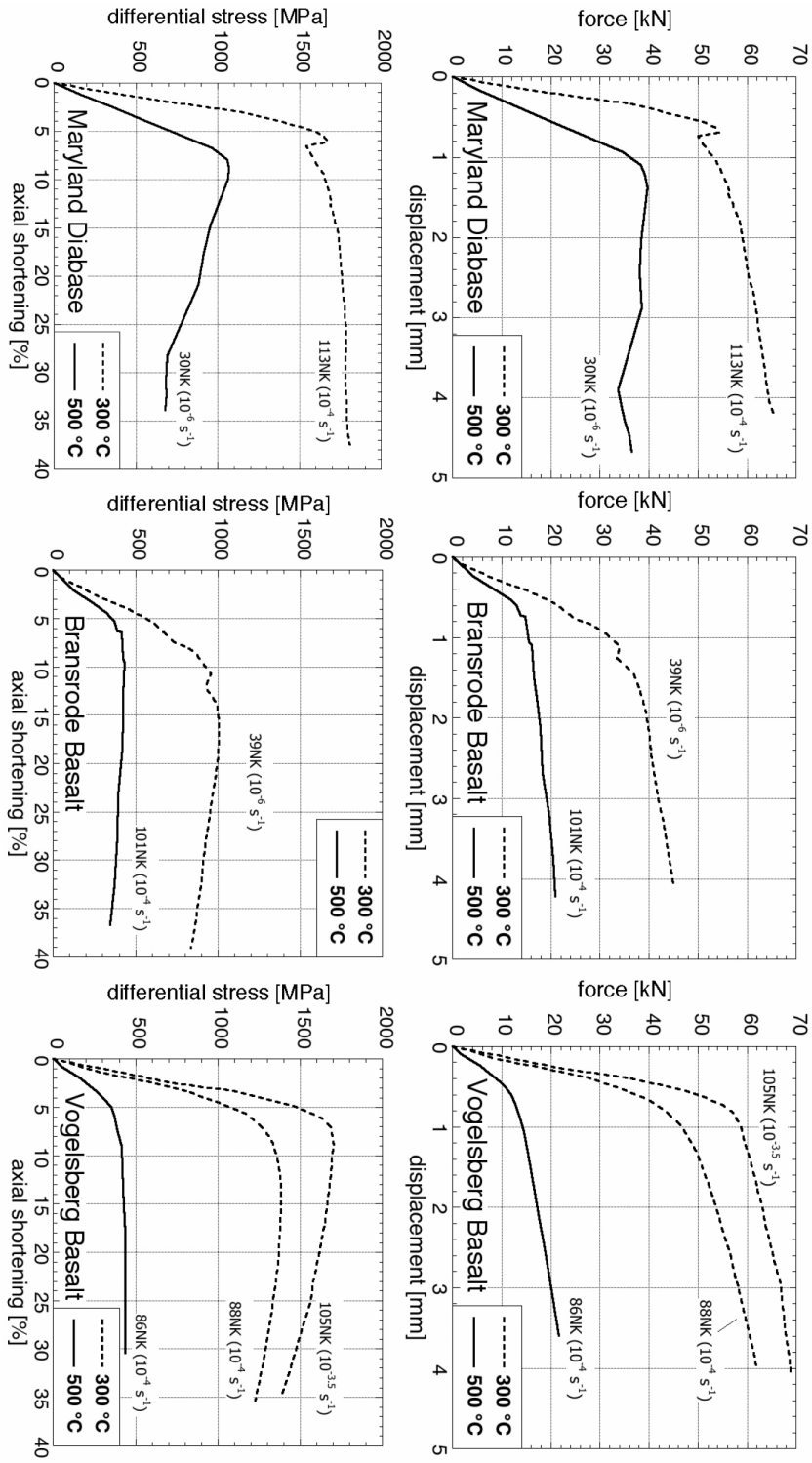


Figure 6.2: Mechanical data for the deformation of Maryland Diabase, Vogelsberg Basalt and Bransrode Basalt. All experiments have been performed at $P_c = 500$ MPa and with 0.2 wt% H₂O. Note the difference in strength between diabase and partially glassy basalt for deformation at $T = 500$ °C.

6.3.1 Light microscopy

The microstructures of the deformed basalt samples show considerable variation (Fig. 6.3). MD deformed at $T = 300^\circ\text{C}$ shows an extensive grain size reduction of both plagioclase and pyroxene (Fig. 6.3a). Plagioclase is more intensively fractured than pyroxene and forms the largest portion of the fault gouge. At $T = 500^\circ\text{C}$ both plagioclase and pyroxene are deformed by fracturing at grain scale. Most of the fractured material consists of cracked grains, not of gouge (Fig. 6.3b). The most intense deformation is found near narrow fault zones, while the remaining part of the samples is more or less unaffected by deformation. See Chapter 3 and 4 for a definition of cracked grains and gouge.

BB deformed at $T = 300^\circ\text{C}$ shows a strong grain size reduction of pyroxene and plagioclase forming cracked grains and, especially in case of plagioclase, gouge (Fig. 6.3c). Olivine and magnetite also occur as cracked grains. The glass pods have an elongated shape and with internal fractures. In the experiments at $T = 500^\circ\text{C}$ olivine, pyroxene and magnetite form relatively large clasts that are surrounded by finer grained plagioclase (Fig. 6.3d). Plagioclase grains have been bent and rotated to a position with their long axis more or less perpendicular to σ_1 (Fig. 6.3d). The glass pods are elongated and do not show internal cracks. Glass pods lie between the fine grained plagioclase and pyroxene. No evidence of melting during the time of the experiments is found and part of the glass is devitrified. Within the cracks of olivine pre-existing chlorite and serpentine are observed. Locally, olivine fragments are displaced along these alteration products. From BSE observations, no increase in the volume of alteration products within olivine during deformation is assumed.

At $T = 300^\circ\text{C}$ the VB samples show only a weak comminution of the grains outside the fault zones after deformation. Within the narrow fault zones, gouge is formed from plagioclase, pyroxene, and olivine. Most of the deformation however, including the barrelling of the sample, seems to be accommodated by deformation of the glass pods and fracturing of plagioclase (Fig. 6.3e). At $T = 500^\circ\text{C}$, hardly any fractured material is detected. Plagioclase grains are aligned perpendicular to the main principal stress; as a result, some of the grains are fractured (Fig. 6.3f). The glass pods are very elongated without any internal fractures and locally recrystallized to albite. Alteration products occur in very small amounts and are hardly ever associated with displacement and have not influenced the deformation of the sample.

6.3.2 Method of ACF analysis

The spatial distribution of the plagioclase minerals within the samples has been investigated by means of the auto correlation function (ACF), to study the difference in deformation behavior

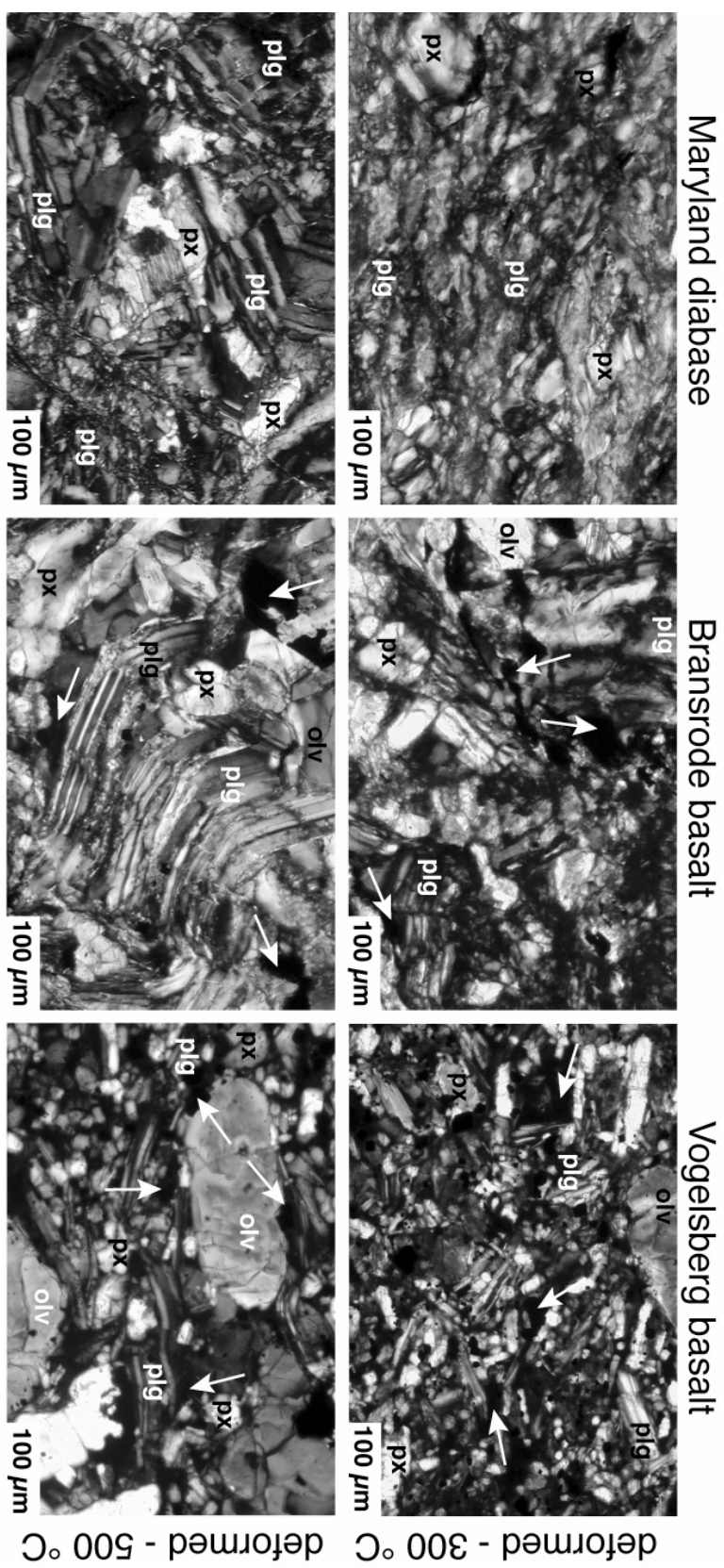


Figure 6.3: Light micrographs of Maryland Diabase, BB and VB in cross-polarized light. Samples have been deformed at $T = 300$ and $500\text{ }^{\circ}\text{C}$, $P_c = 500$ MPa. Arrows point at glass. The shortening direction is vertical in all images. px = pyroxene, plg = plagioclase, ol = olivine.

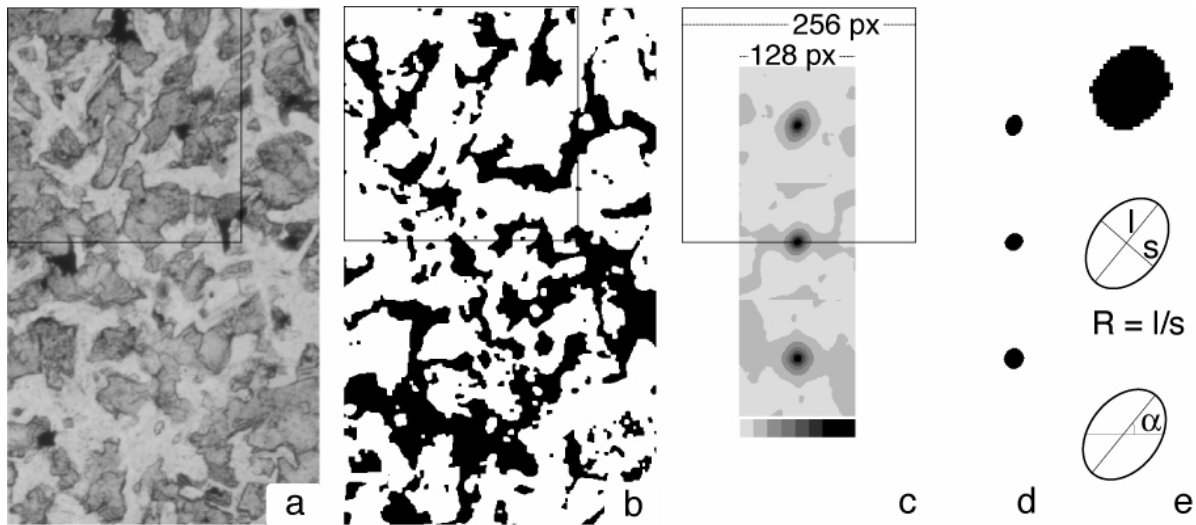


Figure 6.4: Procedure for ACF analysis. a) Plane polarized light Maryland Diabase micrograph, plagioclase is light grey, pyroxene dark grey. b) Bitmap showing plagioclase grains in black. c) ACF-tiles calculated from the bitmap in b). Square of 256x256 pixel shows the area used to calculate the upper ACF-tile. Relative scale for ACF intensity increases with increasing grey value. d) ACF-peaks thresholded at 39% of the peak maximum. e) Anisotropy (aspect ratio), R , and orientation with respect to a horizontal reference line, α , calculated from the best fit ellipse for the thresholded peaks.

between partially glassy basalt and diabase samples after deformation at $T = 500^\circ\text{C}$. For a description of the method of ACF, see Heilbronner Panozzo (1992). Plagioclase has been chosen because (1) it is present in all types of basalt, (2) its elongated mineral shape, and (3) its large ability to reduce its grain shape by fracturing. The ACF has been used previously to describe the microstructures of deformed rocks (e.g. Heilbronner Panozzo, 1992; Heilbronner, 2002; De Ronde et al., 2004). When observing the microstructures in a polarization microscope, one sees that in MD all bright minerals are plagioclase and most darker minerals pyroxene, whereas in BB and VB samples, the bright minerals can be olivine or plagioclase. In order to be able to compare the microstructures of both types of basalt, bitmaps of plagioclase instead of 8-bit grey-value images have been used in this study.

Figure 6.4 illustrates the procedure of the ACF analysis. Using the shareware image analysis program ImageSXM[†] the plane-polarized microscope images (Fig. 6.4a) are thresholded to separate the dark grains (pyroxenes, ore minerals, most minor reaction products, glass pods) from the bright grains (plagioclase, olivine, recrystallized glass) (Fig. 6.4b). The thresholded images are further improved by median ranking filtering and manual separation of the phases with help of the circular polarized or cross-polarized light images. In this way a bit-map showing plagioclase in black and the rest of the sample in white is created. Using the “lazy ACF-tiles”

[†]S. Barrett, <http://www.liv.ac.uk/~sdb/ImageSXM/>

macro[‡] (Heilbronner, 2002) an ACF-tiling of the image is achieved (Fig. 6.4c). Option 7 of the “lazy ACF-tiles” macro is used: this option creates overlapping ACF-squares of which only the central 1/4 area is shown (ACF-tile). The anisotropic shape of the ACF-peaks is quantified by thresholding at 39% of the ACF-peak height (Fig. 6.4d), which is the representative level for a close-packed microstructure (Heilbronner Panozzo, 1992). From the longest and shortest axes of the thresholded peaks, the anisotropy R and the orientation of the longest axis with respect to the horizontal, α , are determined (Fig. 6.4e).

To compare partially glassy basalt with diabase, more than 60% of the six samples has been analyzed in ACF squares measuring 256 pixels, with tiles of ca. 0.29 x 0.29 mm (Fig. 6.5, 6.6). The undeformed samples are rotated to the same orientation as their deformed counterparts. As VB has a small grain size, the pixel size of the ACF-peak is small too. Some sampling effects (i.e. a very pronounced preference for $\alpha = 0, 45, 90, \dots^\circ$) occur after thresholding at 39% peak height in the undeformed sample.

6.3.3 Results of ACF analysis

The ACF analysis of the major part of a partially glassy basalt (VB, Exp. 86nk) and a diabase sample (MD, 30nk), both deformed at $T = 500^\circ\text{C}$, display different spatial distributions of plagioclase grains within both samples (Fig. 6.5). From the bitmaps of both samples it is clear that VB contains less plagioclase and is finer grained than MD. Most of the thresholded ACF-peaks of the VB show an elongated shape and a preferred orientation perpendicular to σ_1 , i.e., parallel to the direction of material flow (shown with dashed lines in Fig. 6.5). In MD most ACF-peaks are nearly round and the plagioclase minerals do not show a preferred orientation that is continuous over several tiles. A strong preferred orientation in the sample is only observed near the fault zone (arrows), where the plagioclase has a preferred orientation with an angle of ca. 20° to the fault zone (Fig. 6.5).

A more quantitative analysis of the ACF-tiling of plagioclase is shown in Figure 6.6. Undeformed MD, BB and VB are compared to samples deformed at $T = 500^\circ\text{C}$ (30nk, 101nk, and 86nk, respectively). The undeformed sample of MD shows a random orientation (Fig. 6.6). Undeformed BB shows a flow-foliation and has a weakly developed preference for $\alpha = 120^\circ$, although a preference for the perpendicular orientation, $\alpha = 30^\circ$ is visible as well. The anisotropy of the ACF-peaks of undeformed VB is very low, indicating that the minor preference for $\alpha \approx 150^\circ$ is only a weakly developed feature.

MD shows approximately the same pattern before and after deformation at $T = 500^\circ\text{C}$ (Fig.

[‡]<http://pages.unibas.ch/earth/micro/software/index.html>

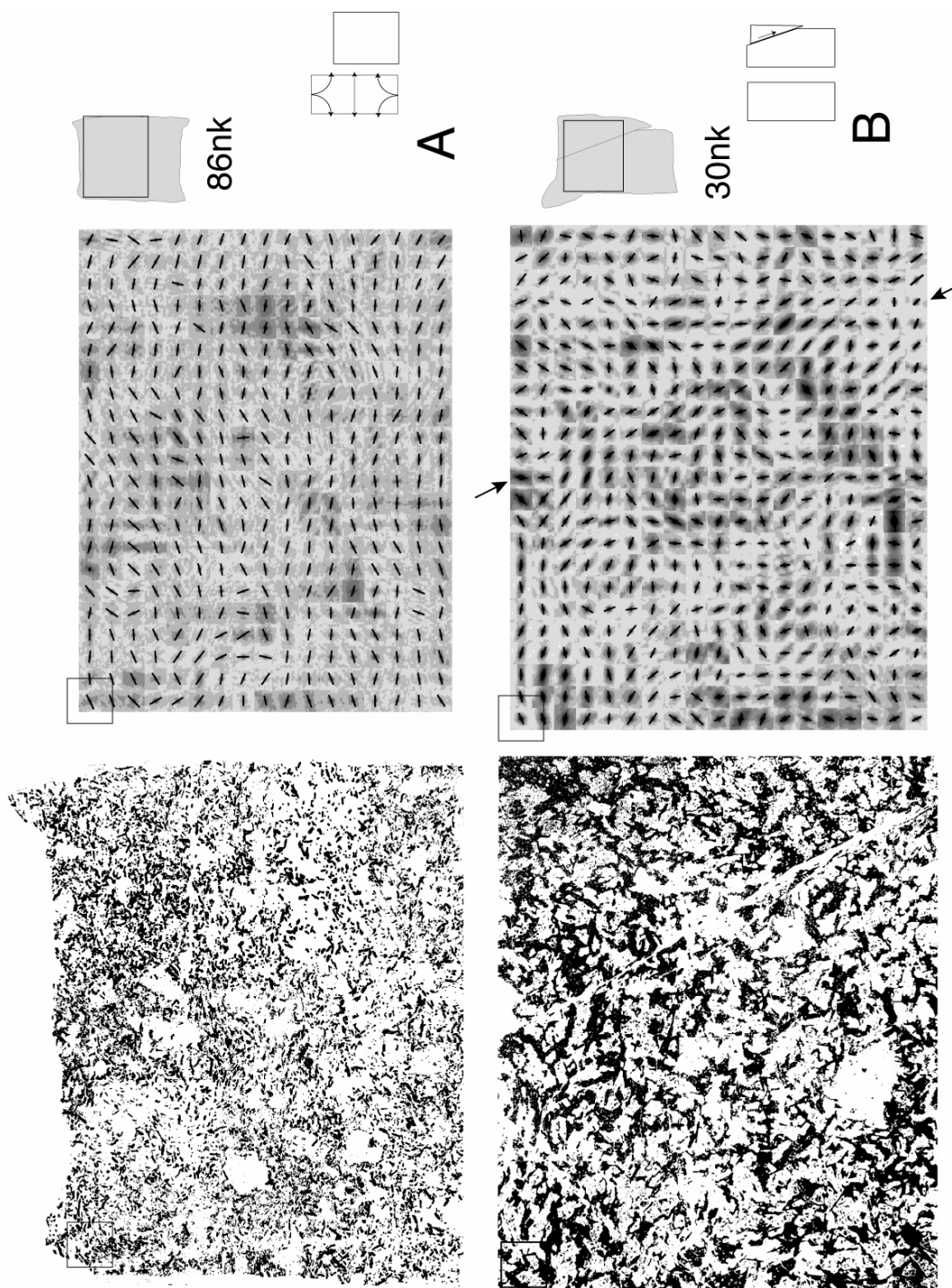


Figure 6.5: ACF-tiles for plagioclase in two samples (a) Vogelsberg Basalt, b) Maryland Diabase) deformed at $T = 500\text{ }^{\circ}\text{C}$. The size of one ACF-square, the area used for the calculation, is indicated. Left: bitmap showing plagioclase grains. Centre: ACF squares of 256 pixels wide; one tile measures 0.29×0.29 mm, the long axis of the ACF-peak is super-imposed on the ACF-tile. Right: sample outline with box indicating location of ACF-tiles and a schematic representation of the deformed sample, a box indicates the analyzed area.

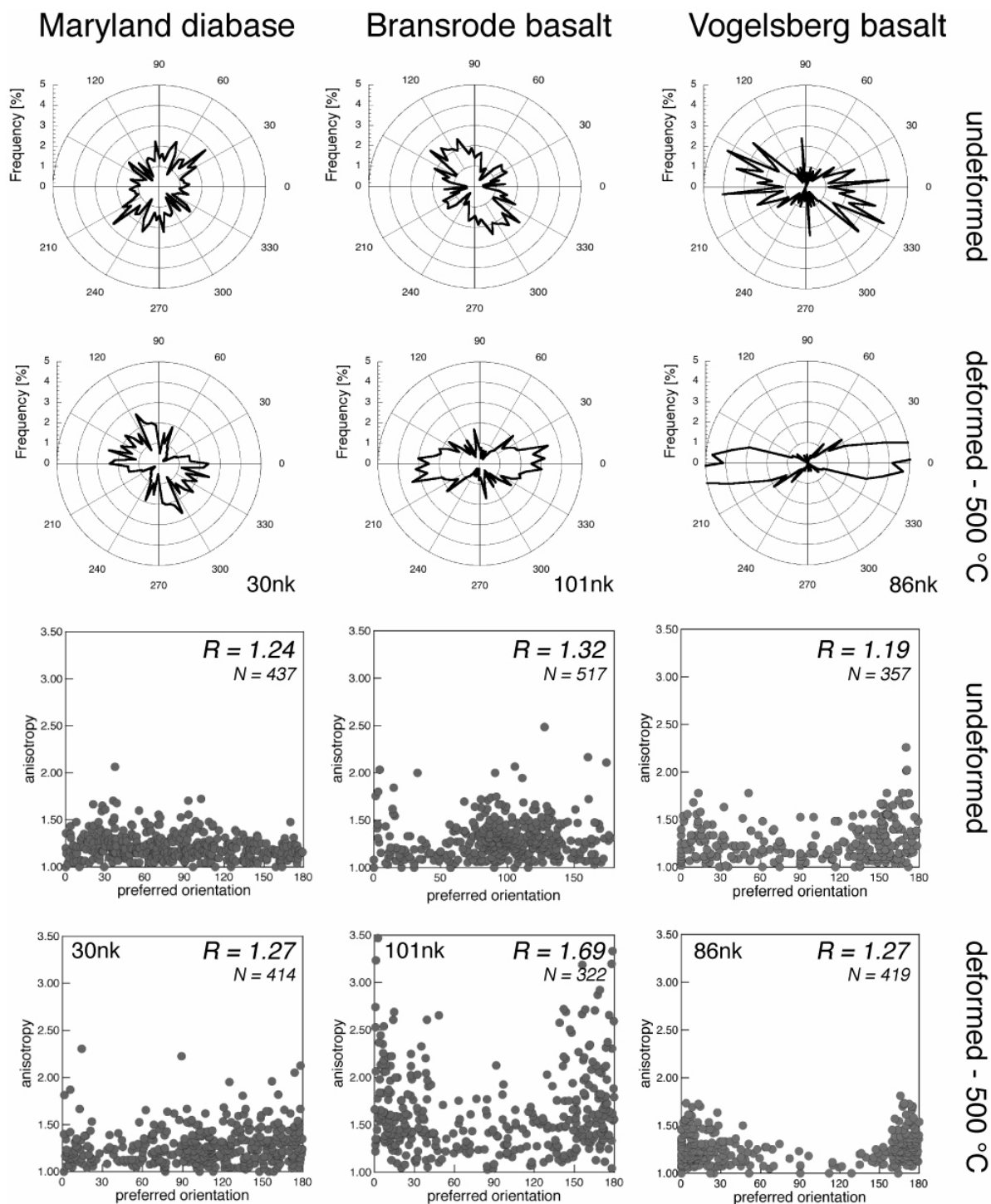


Figure 6.6: Preferred orientation and anisotropy of best fit ellipses representing thresholded ACF-tiles. Rose diagrams show orientation of long axis with respect to a horizontal line, 1.39% indicates the average frequency. Scatter diagrams indicate the relationship between the anisotropy of the axial ratio (R) and the preferred orientation. N is the number of orientations.

6.6), the anisotropy of the pattern remains low. The spatial distribution of plagioclase in MD does not change systematically after deformation under these conditions. From the ACF diagrams of VB and BB in Figure 6.6 three observations can be made. First, the partially glassy basalt deformed at $T = 500^\circ\text{C}$ has a strong shape preferred orientation of plagioclase. Second, the axial ratio of the ACF-peak is increased with respect to the undeformed samples. This means that within an individual ACF square most of the plagioclase grains are orientated in the same direction: commonly in the direction perpendicular to σ_1 . And third, to obtain this high frequency, plagioclase has kept its elongated shape during deformation. For BB, the anisotropy of the ACF-peaks increased to 1.69 and especially for the orientations with a strongly developed preferred orientation (around $\alpha = 0$), a high anisotropy is observed. The same is observed for VB; 72% of α is found in the regions of $160 < \alpha < 200$ and $-20 < \alpha < 20$. Deformation at $T = 500^\circ\text{C}$ strongly changes the spatial distribution of plagioclase in partially glassy basalt, creating a strong shape preferred orientation in the direction perpendicular to σ_1 .

6.3.4 Development of fault zones

Most of the samples deformed at $T = 300^\circ\text{C}$ show a single through-going fault (except the BB deformed at $\dot{\epsilon} = 10^{-6}\text{s}^{-1}$). In sample 105nk a possible evolution of these faults can be studied after deformation. This sample shows a through-going fault, which from the centre of the sample toward the edges develops into a progressively mature fault zone (Fig. 6.7). In the centre of the sample the fault zone has a width of ca. $20\ \mu\text{m}$, a very small amount of gouge, and it cuts through the sample with an angle of 33° towards σ_1 (Fig. 6.7a). The wall-rock of the fault zone shows some cracks, but is largely unaffected by the the fault. On both sides of the fault, at circa $300\ \mu\text{m}$ distance, parallel small faults are developed, with even less gouge.

A bit further away from the centre of the sample, the fault zone has slightly increased in width to ca. $30\ \mu\text{m}$, created more gouge and is rotated to an angle of 38° (Fig. 6.7b). More cracks occur in the wall-rock immediately adjacent to the fault zone. Most of the grains involved in the faulting are stretched with their long axis parallel to the fault zone. About half-way between the centre and the edge of the sample the fault zone has grown to a width of ca. $50\ \mu\text{m}$ (Fig. 6.7c). Slightly more gouge is formed and more cracks have been observed in the wall-rock. The fault zone still has an angle of ca. 38° with σ_1 . The grains within the fault zone however, are stretched with their long axes at an angle of 62° to σ_1 (i.e. 24° towards the fault zone) and form Riedel zones of the fault, as has been observed in the ACF-pattern of MD (Fig. 6.5). The small parallel fault zones have increased in width and in deformation intensity as well and therefore have grown towards the major fault zone. The wall-rock exhibits a ragged contact with the fault zone and forms islands of less intense deformation between the small parallel fault zones.

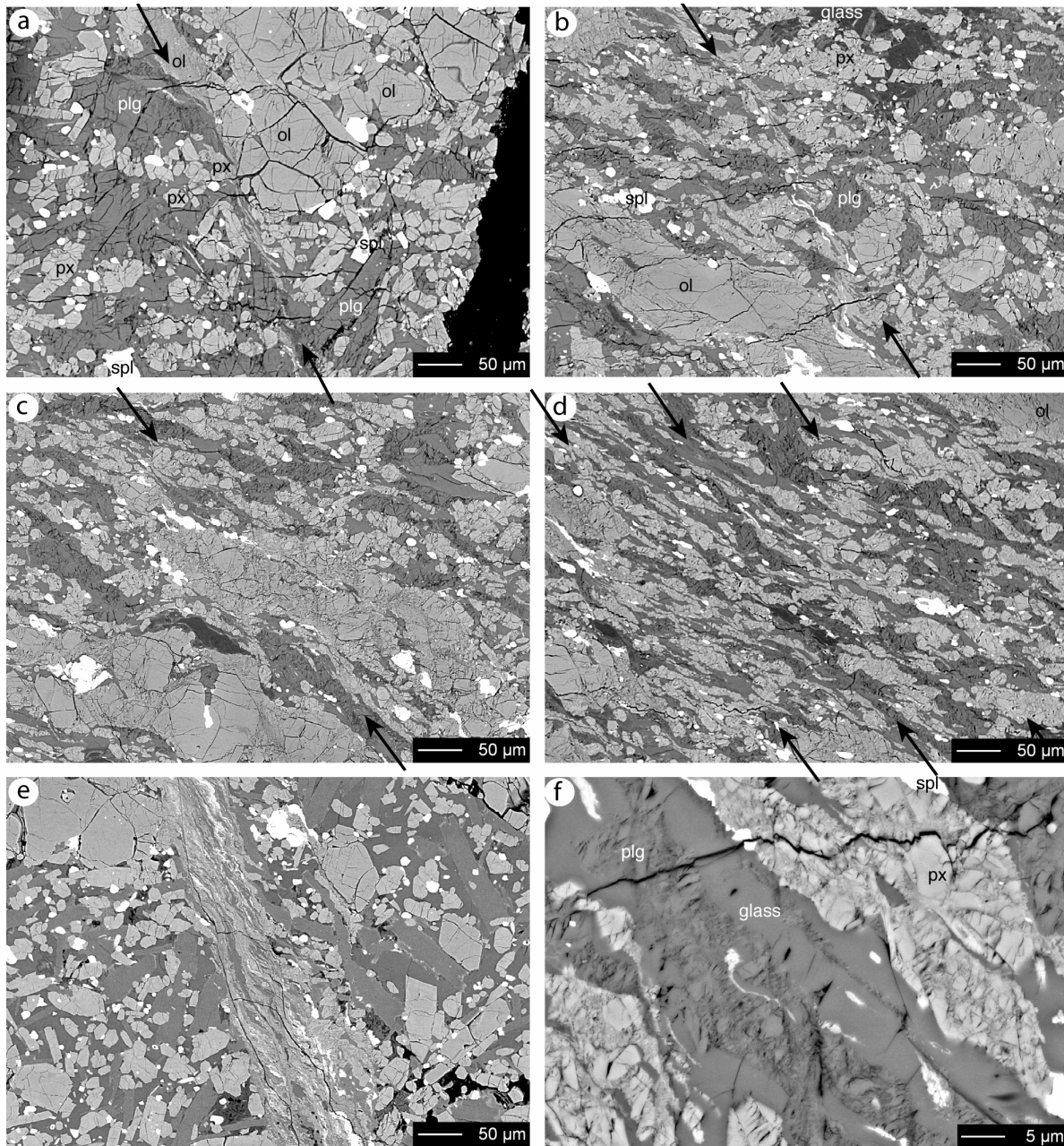


Figure 6.7: BSE micrographs showing the development of fault zones in Vogelsberg Basalt, deformed at $T = 300^\circ\text{C}$. Arrows indicate the orientation of the fault zone, σ_1 is vertical. Black material in a) is glue in a crack resulting from thin section preparation and has no relation with the deformation of the sample. a)-d) and f) show sample 105nk, $\dot{\epsilon} = 3.4 \times 10^{-4} \text{ s}^{-1}$ e) sample shows 87nk, $\dot{\epsilon} = 1 \times 10^{-4} \text{ s}^{-1}$.

Close to the edge of the sample a broad fault zone of ca. $300 \mu\text{m}$ is developed. The grains in the fault zone are flattened due to fracturing with a preferred orientation at an angle of 24° to the fault zone (Fig. 6.7d). The fault zone is broadened due to the lateral integration of the small parallel fault zones with the major fault zone. The contact with the wall-rock is sharper than

at the locality of Figure 6.7c.

However, not all fault zones show a rotation of the fault zone from ca. 33 to 38° and an increase in width from 20 to $300\ \mu\text{m}$ over $3\ \text{mm}$ of fault zone. Sample 87nk was deformed under nearly identical conditions as sample 105nk, except for a two to three times lower strain rate of $\dot{\epsilon} = 1.3 \times 10^{-4}\ \text{s}^{-1}$, but developed a through-going fault zone with a fairly constant thickness of ca. 50 – $100\ \mu\text{m}$ (Fig. 6.7e). The fault zone has sharp contact with the wall-rock and hardly any deformation is observed outside the fault zone. MD, deformed at $T = 300^\circ\text{C}$, has developed the same two types of fault zones; an increasing fault zone width towards the edge of the sample and fractured grains oriented at a low angle to the fault as in sample 105nk have been observed especially in the samples that have rotated during deformation. Other samples show a rather sharp fault zone with even less gouge than 87nk.

The microstructures of these fault zones show an intense fracturing of plagioclase, olivine, pyroxene, and spinel, which has formed a more flattened or lenticular shape of these minerals (Fig. 6.8a,d,e). The gouge that forms as a result of this fracturing is very fine grained; in the large grain size fraction mainly cracked minerals occur (Fig. 6.7f). At a high magnification, it is observed that the lenticular shaped tails of plagioclase and pyroxene grains is caused by the formation of very fine grained gouge in case of plagioclase (Fig. 6.8g), but is formed by a very small scale book-shelf sliding of mainly cracked minerals in pyroxene (Fig. 6.8h). Pyroxene minerals that lie with their c-axis perpendicular to the movement direction are mostly unaffected by the deformation, whereas those grains that have their c-axis parallel to the movement direction are intensely fractured. The glass pods form elongated, lenticular shaped patches, stretching between the cracked grains and do not show many internal fractures after deformation at $T = 300^\circ\text{C}$.

6.3.5 Grain size analysis

To quantify the effect of the comminution in the fault zone, and to compare the fault rock in this study with other natural and experimentally deformed fault rock, a grain size distribution analysis has been performed. For the analysis, two or three series of BSE microraphs representing characteristic areas within the fault rock with a range of magnification of $500\times$ to $20'000\times$ are loaded in the program ImageSXM. The images are thresholded at two different grey-values that represent plagioclase and pyroxene and from the resulting bit-map the size of the grains is measured (see Chapter 4 for details). For the hydrostatically treated samples, the grain size was measured by manual tracing of the grain boundaries of one of the two mineral phases and using the resulting bitmap in the program ImageSXM to measure the grain size (see Chapter

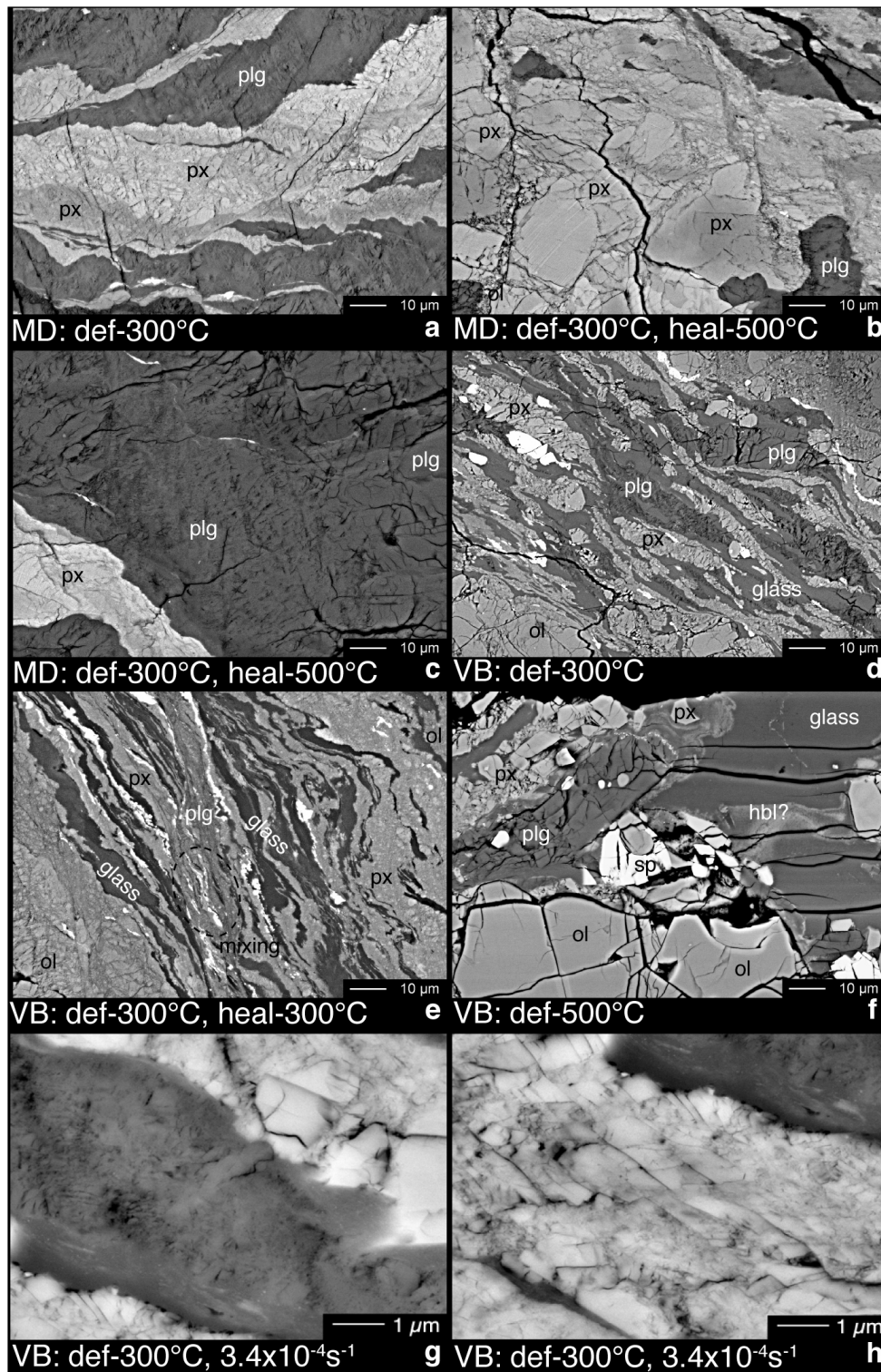


Figure 6.8: Characteristic micrographs of deformed and subsequently healed samples (Back-scatter contrast Scanning Electron Microscopy). MD = Maryland Diabase, VB = Vogelsberg Basalt. Horizontal cracks are extension cracks that developed during retrieving of the sample after the experiment.

5 for details). The grain size distribution is plotted in a log(frequency)-log(radius) histogram. The absolute value of the slope of the best-fit line through the data-points of this grain size distribution is the D -value, which is the power-law exponent of the distribution. It was observed that in granites the fault gouge does not follow a single power-law distribution (see Chapters 3 and 4). Instead, the distribution can be divided into two distributions, one for grains smaller than ca. $3 \mu\text{m}$ in diameter ($D_{<}$ -value) and a second slope, $D_{>}$ -value, for all larger grains measured. The grain size at the slope change, r_K , is related to the grinding limit of the mineral and indicates a change in the dominant comminution mechanism from grinding, for large grains, to attrition and shearing (see Chapter 4).

In the MD sample, deformed at $T = 300^\circ\text{C}$, only small patches of fine grained gouge are observed; at low magnifications there are mainly cracked grains (Fig. 6.8a). The total amount of gouge in the sample is very low. Pyroxene has many intra-granular cracks, but usually these cracks are not matured to trans-granular cracks and thus do not decrease the grain size. Pyroxene is less intensively comminuted than plagioclase. For pyroxene, the more Ca-rich clinopyroxene seems produces more gouge than orthopyroxene.

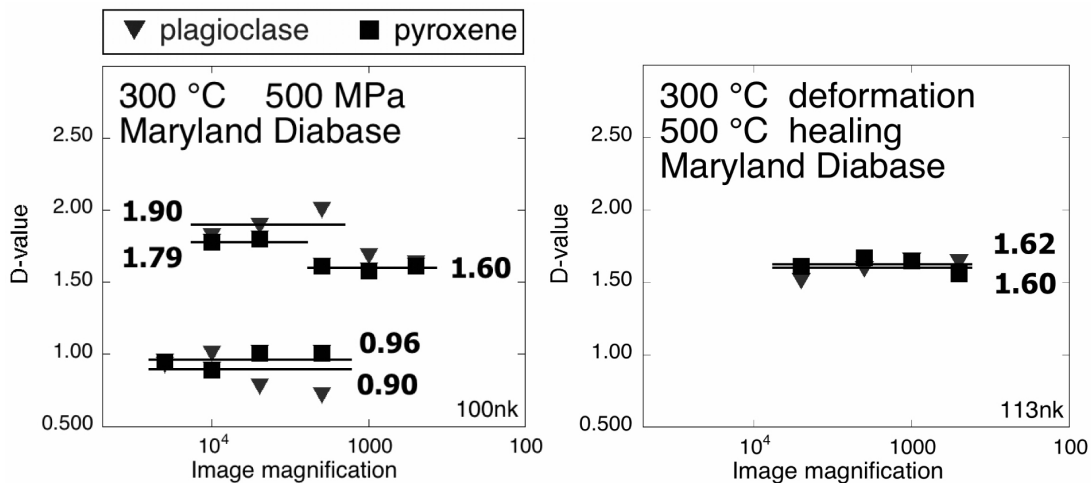


Figure 6.9: Grain size distribution of Maryland Diabase a) after deformation and b) after deformation and heat treatment.

Figure 6.9a shows the grain size distribution of pyroxene and plagioclase for a sample of MD deformed at $T = 300^\circ\text{C}$. The qualitative observations on these samples are reflected in the grain size distribution. A high $D_{>}$ -value could only be measured for the fine grained material in the fault rock: $D_{>} = 1.90$ for plagioclase and $D_{>} = 1.79$ for pyroxene. For the larger grains only cracked material was observed, with $D_{>} = 1.60$. The smallest grain size fraction shows a $D_{<}$ -value of 0.90 and 0.96 for plagioclase and pyroxene, respectively. BB has developed less fractured material than MD at $T = 300^\circ\text{C}$; VB does not form much gouge, but mainly cracked

material (Fig. 6.8d). No grain size distribution was measured for these samples.

6.4 Chemical analysis

After deformation, some of the samples have been kept in the deformation apparatus under hydrostatic conditions, at $T = 300$ or 500°C for two weeks. As a result of this treatment, two different effects on the sample material have been found: (1) mineral reaction of the fine grained gouge and (2) healing (grain growth and loss of porosity due to dissolution-precipitation processes) of the gouge. These two effects will be analyzed in this section.

6.4.1 Reaction within the samples

After deformation and subsequent heat treatment of the samples at $T = 300$ and 500°C some new phases could be observed in the samples (Fig. 6.10). The amount of new phases depends on the starting material and the duration of the heat treatment period, but the reaction progress was small in all of the samples. Figure 6.10 rather shows the locations within the samples with clear evidence of reaction than representative parts of the samples. Measurements of the phases have been performed on the same SEM described above using standard-less EDX analyses. The analyses have been performed using a working distance of 10.0 mm and an acceleration voltage of 20 kV. The spot-size (focussed beam diameter) is approximately $3\ \mu\text{m}$ for the settings used for the measurements. Whereas the composition of the starting material is quite constant and easy to measure, and mainly dependent on systematic errors within the EDX equipment and program, this is not the case for the reaction products, which are usually small in size and in some cases range considerably in composition. The semi-quantitative EDX data are given in Appendix F.

Maryland Diabase: In the samples that are deformed at $T = 500^\circ\text{C}$ (30nk), and deformed at $T = 300^\circ\text{C}$ and heat treated at $T = 500^\circ\text{C}$ for 14 days (113nk) biotite and amphibole (hornblende or actinolite) have been found as new phases. In the sample deformed at $T = 300^\circ\text{C}$ (100nk) no evidence of reaction was found. After deformation at $T = 500^\circ\text{C}$, new phases have only been detected in the 5–30 μm thick gouge zone of the cross-cutting diagonal fault. Even within this gouge, new phases occur only locally and do not exceed a size of 7 μm . The sample that is heat treated at $T = 500^\circ\text{C}$ for 14 days, shows a slightly larger volume of reaction products, still occurring very locally, and the new phases are of the same size as in the deformed-only sample. The increase in volume of reaction products seems to be correlated with the larger amount of gouge rather than the longer time period at $T = 500^\circ\text{C}$. For the samples the following reactions are inferred (all shown in Figs. 6.10 and 6.11), based on BSE and EDX observations

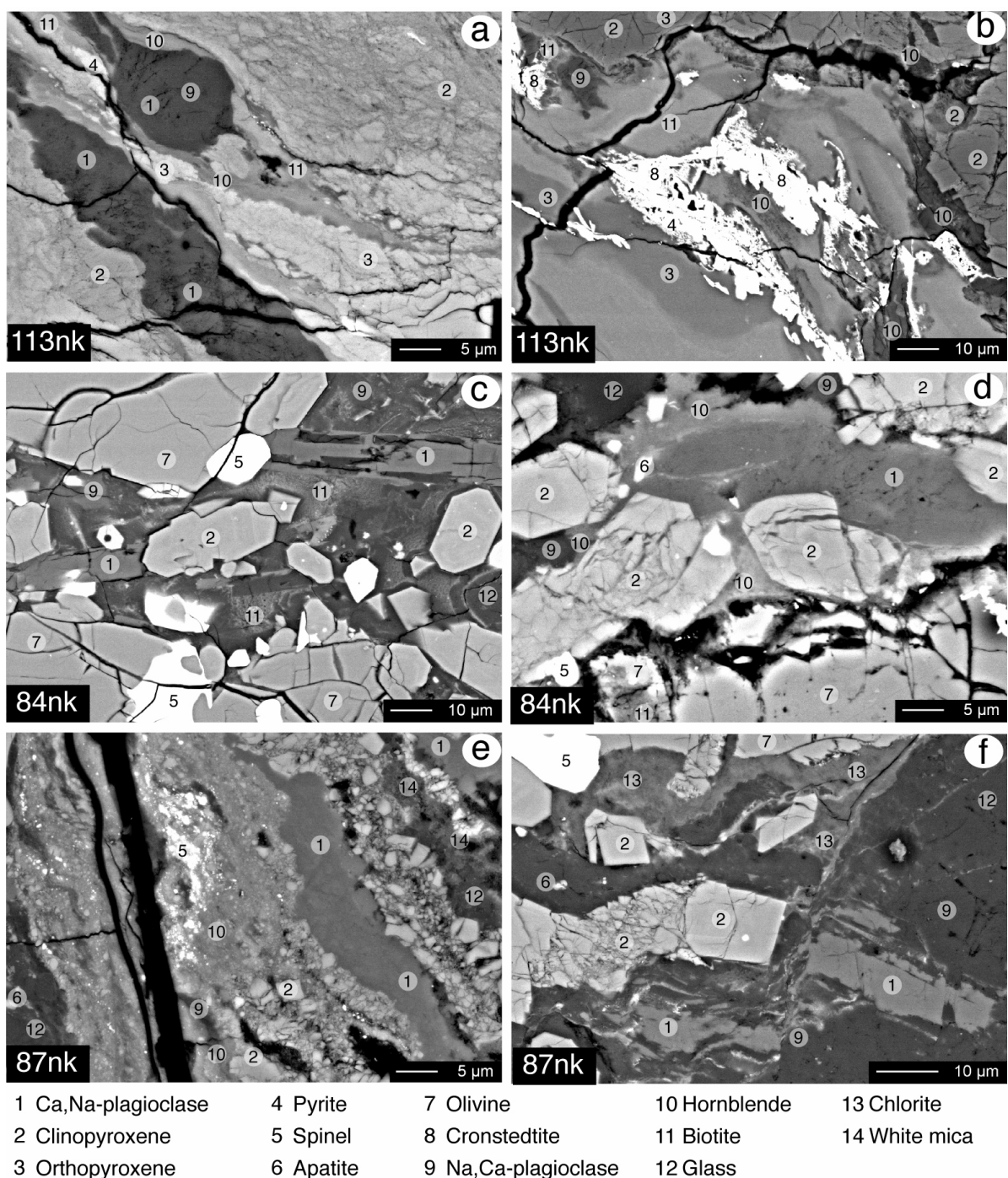


Figure 6.10: Evidence of reaction in deformed basalt samples from backscattered scanning electron micrographs and EDX analyses. 113nk: Maryland Diabase, deformation at $T = 300^{\circ}\text{C}$, heat treatment at $T = 500^{\circ}\text{C}$ for 14 days; 84nk: Vogelsberg Basalt, deformation at $T = 500^{\circ}\text{C}$, heat treatment at $T = 500^{\circ}\text{C}$ for 14 days; 87nk: Vogelsberg Basalt, deformation at $T = 300^{\circ}\text{C}$, heat treatment at $T = 300^{\circ}\text{C}$ for 14 days. Sub-horizontal lines are extension cracks resulting from the retrieving of the sample after deformation. The subvertical crack in sample 87nk indicates the major sharp fault zone cutting through this sample.

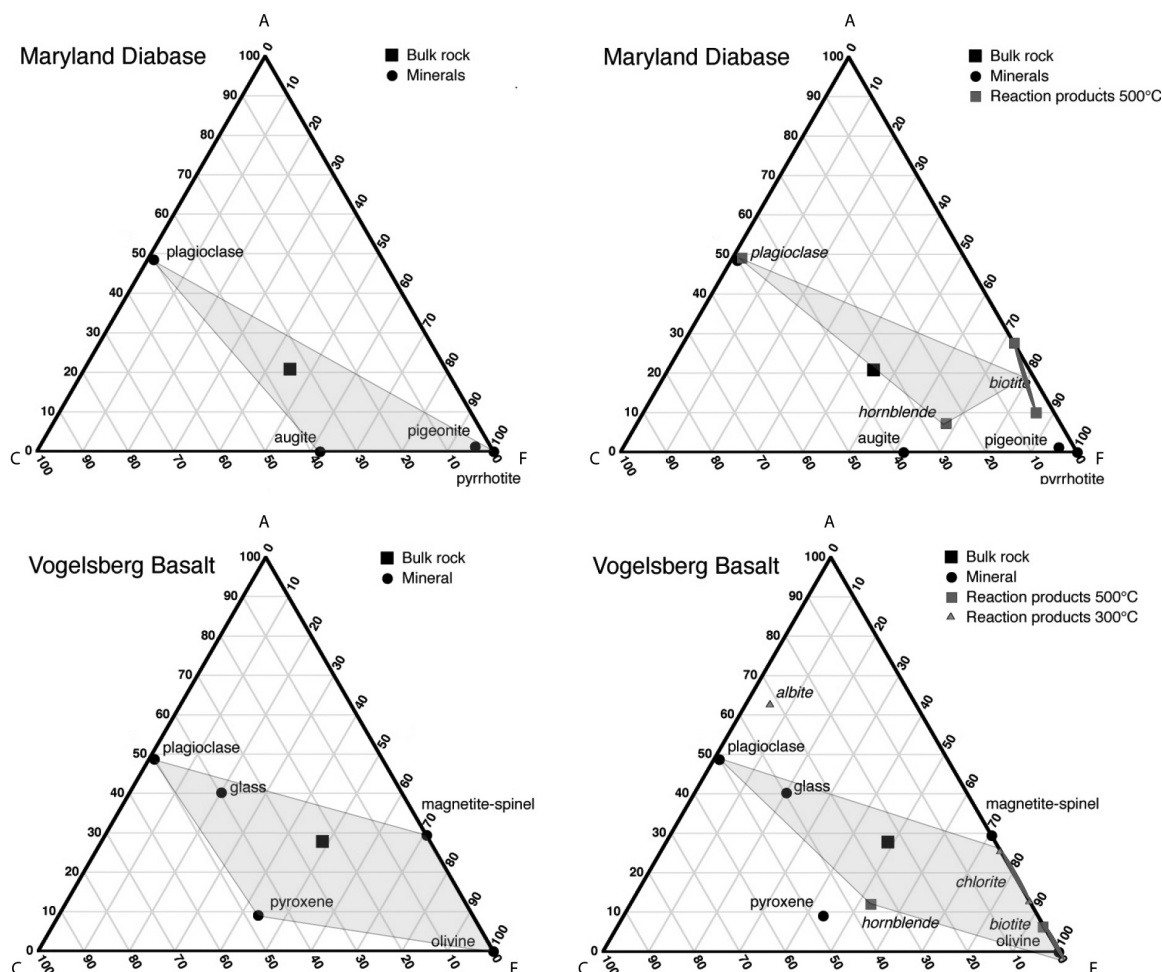
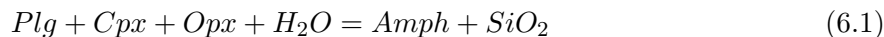


Figure 6.11: ACF-diagrams for undeformed and deformed Maryland Diabase and Vogelsberg Basalt. $A = \text{Al}_2\text{O}_3 + \text{Fe}_2\text{O}_3 - (\text{K}_2\text{O} + \text{Na}_2\text{O})$, $C = \text{CaO}$, $F = \text{FeO} + \text{MnO} + \text{MgO}$. Bulk rock composition of Maryland Diabase estimated from mineral composition, bulk rock composition of Vogelsberg Basalt after Wittenbecher (1992). ACF in this figure refers to the chemical composition and not to the auto correlation function.

and stoichiometry of ideal phases.

Most of the amphibole is formed from plagioclase and pyroxene at $T = 500^\circ\text{C}$ (Fig. 6.10a,b):



Some quartz was observed in the samples, but quartz is already present as a minor phase before deformation. The newly formed silica might be transported away in the fluid. Based on EDX measurements it seems that the plagioclase in the samples partially changes to a more alkali-rich plagioclase. This plagioclase forms biotite together with pyroxene (Fig. 6.10a):



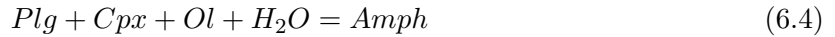
Alternatively, some of the amphibole may have been formed by the reaction of plagioclase and pyroxene with the ores in the sample, pyrrhotite (Po) in the case of MD (Fig. 6.10b):



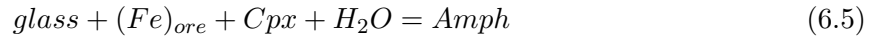
The resulting H₂S or H₂O is added to the fluid present in the sample.

Vogelsberg Basalt: In VB deformed at $T = 500^\circ\text{C}$ (86nk, 89nk) or deformed and healed at $T = 500^\circ\text{C}$ (84nk) the same new phases have been detected as in MD (Figs. 6.10c,d and 6.11). The newly formed phases are of the same size as in MD (1–10 μm), but more abundant and form especially next to and in the glass pods. In samples deformed at $T = 300^\circ\text{C}$ some newly formed phases are found: chlorite, albite and amphibole (hornblende or actinolite). The new phases are very small, only slightly larger than the spot in the EDX-analyses, and usually associated with the glass pods in the samples and, in sample 87nk, with the fault gouge.

At $T = 500^\circ\text{C}$ amphibole is formed from plagioclase, clinopyroxene and olivine (Fig. 6.10d):



The glass pods have a composition close to that of a ternary feldspar and can replace plagioclase in a reaction similar to Equation 6.3 (Fig. 6.10b):



The latter reaction has been observed at $T = 300^\circ\text{C}$ as well (Fig. 6.10e). At $T = 500^\circ\text{C}$ biotite may form in the same way as in Equation 6.2 with glass pods (Fig. 6.10c):



At $T = 300^\circ\text{C}$ chlorite was formed from glass pods and olivine (Fig. 6.10f):



6.4.2 Healing of the samples

Healing is the grain growth and crack closure process resulting from dissolution of the small grains and sharp edges of the larger grains and precipitation of the dissolved material, which causes a rounding of the grains, a closure of small cracks, and an increase in apparent cohesion. Healing has been observed mainly in one of the heat-treated samples: MD deformed at $T = 300^\circ\text{C}$ and kept at $T = 500^\circ\text{C}$ for 14 days (113NK, see Figure 6.8b,c). Both pyroxene and

plagioclase have healed well in this sample. The amount of small grains is reduced with respect to the undeformed sample (Fig. 6.8a), especially in plagioclase (Fig. 6.8c). Pyroxene shows rounded grains and a decrease in the number of intragranular cracks (Fig. 6.8b).

In VB, deformed at $T = 300^\circ\text{C}$, not much gouge is present (Fig. 6.8d), and therefore, after heat treatment at $T = 300^\circ\text{C}$, not much healed gouge has been observed, except within the mainly monomineralic fractions of the sample (e.g. pyroxene on the right side and olivine on the left side of Figure 6.8e). Within the better mixed fraction, mineral reaction seems to have taken place (although the reaction products are very small and therefore hard to identify, see centre of Figure 6.8e). In the sample of VB deformed at $T = 500^\circ\text{C}$ no gouge has been observed, the fractured patch in Figure 6.8f is the largest in the whole sample. The sample that has subsequently been heat treated, does not show evidence of healing, only of reaction. BB has not been heat treated after deformation. The deformed samples show mainly fractured material, especially after deformation at $T = 500^\circ\text{C}$.

The grain size distribution of the healed grains has been measured. The smallest grain size with an abundant appearance is $1\ \mu\text{m}$ for plagioclase and for pyroxene. Only one slope in the grain size distribution is observed, therefore no $D_{<}$ -value is determined. The $D_{>}$ -value for pyroxene is 1.62 and for plagioclase 1.60 (Fig. 6.9b).

6.5 Discussion

6.5.1 Strength of the basalt samples

The samples of the three different materials, MD, BB and VB, deformed at $T = 300^\circ\text{C}$ with 0.2%wt H_2O have a strength of 1.4 – 1.7 GPa. This strength is in good agreement with other experiments: Rutter et al. (1985) found a strength of over 1.4 GPa for wet samples deformed at $T = 20^\circ\text{C}$, Griggs et al. (1960) reported 1.3 GPa for dry basalt experiments performed at $T = 300^\circ\text{C}$, $P_c = 500\ \text{MPa}$ with a high shortening rate (2–4% per minute).

MD deformed at $T = 500^\circ\text{C}$, $\dot{\epsilon} = 10^{-6}\text{s}^{-1}$ has a strength of 1.1 GPa, which is in good agreement with the experiments on dry samples of MD performed by J. Tullis at $T = 600^\circ\text{C}$, which yielded a strength of 1.2 GPa. Griggs et al. (1960) reported 1.1 GPa for dry basalt samples deformed at $T = 500^\circ\text{C}$. Rocchi et al. (2002) collected strength data from experiments on basalts and fitted these in a fracture envelope for brittle failure of basalt. They show that under brittle temperature conditions at $P_c = 500\ \text{MPa}$ the axial stress required to deform basalt is 1.3 GPa. The strength of BB and VB deformed at $T = 500^\circ\text{C}$ and $\dot{\epsilon} = 1 \times 10^{-4}\text{s}^{-1}$ is, at 0.4 GPa, much less than all these reported values. The strength is similar to the strength of dry partially glassy

basalt at $T = 875^\circ\text{C}$ (Hacker and Christie, 1991) or dry diabase at $T = 1000^\circ\text{C}$ (Caristan, 1982; Mackwell et al., 1998).

ACF analysis on plagioclase minerals points to the difference in deformation mechanism between fully crystalline and partially glassy basalts deformed at $T = 500^\circ\text{C}$. MD shows the same spatial distribution of plagioclase in the samples after deformation at $T = 500^\circ\text{C}$ as before deformation (Fig. 6.6). This is caused by the localization of the deformation in Maryland into discrete fault zones (Fig. 6.5) and a deformation with grain size reduction (Fig. 6.3). VB deforms by viscous flow of the glass pods, which leads to a passive rotation of the other minerals with their longest dimension in a position perpendicular to the principal stress (Fig. 6.3). In VB and BB almost all plagioclase rotates into the same orientation without intensive comminution and grain mixing. Compared to MD a variation in the strength of the sample and in the spatial distribution of the deformation was observed.

The main difference between our partially glassy basalt samples and the ones of Hacker and Christie is the presence of water during deformation. Weakening in their samples occurred due to a glass to liquid transition at ca. $T = 800^\circ\text{C}$, visible as melt pocket in cracks. No melt pockets at grain boundaries were observed in our samples however, thus we assume that the water in our samples did not cause a melting of the glass. In our MD samples deformed at $T = 500^\circ\text{C}$ under $\dot{\epsilon} = 1 \times 10^{-6} \text{s}^{-1}$ no weakening was observed. The main difference between these samples and the partially glassy basalt samples is the presence of 10–12% glass pods and 11–12% olivine. BB has more plagioclase and VB less plagioclase than MD. VB has a smaller grain size than MD, but the grain size of BB and VB are comparable. The weakening is therefore not caused by the smaller grain size of VB.

Within the olivine alteration products (chlorite, phlogopite, serpentine, talc) have been detected. These sheet silicates have a low friction coefficient and are known to be able to cause a large weakening of the fault rocks (e.g. Moore et al., 2004; Jefferies et al., 2006). However, hardly any of these sheet-silicates show evidence of accommodation of movement of olivine fragments. These sheet-silicates are not present in a through-going fault zone in the rock; in fact, in most of these weak partially glassy basalt samples no through-going fault has been detected. Therefore, it is unlikely that these alteration products are responsible for the strength reduction within the deformed partially glassy basalt samples when increasing the temperature from $T = 300$ to 500°C .

Instead, we propose that the weakening of the partially glassy basalt is caused by a combined viscous flow of the glass pods in rock samples deformed at $T = 500^\circ\text{C}$. The elongated and lenticular shape and the absence of fractures in the glass pods after deformation point to a viscous deformation mechanism. Rossi (2005); Rossi et al. (subm) performed compaction experiments

on 45–90 μm sized silica glass spheres (72% SiO_2 , 14% Na_2O , 10% CaO and 3% MgO) at $T = 25\text{--}450^\circ\text{C}$, $P_c = 200\text{ MPa}$ in the presence of 0 – 5 vol% fluid and observed that the glass spheres develop flat contacts during the initial stage of the experiment by means of viscous flow under all experimental conditions. This process is enhanced by higher temperatures or by the presence of water and Rossi et al. (subm) explained this weakening by hydration of the glass. This occurs within 6 hours at $T > 350^\circ\text{C}$ and leads to a reduction in the viscosity of the glass. They show that experiments performed on samples consisting of less than 1 vol% fluid show a creep behavior that is typical of glass deformation, following a power law with a high stress exponent in both dry and wet experiments. Furthermore, samples compacted under hydrostatic conditions at $T = 350^\circ\text{C}$ in presence of 5 vol% of H_2O and at $T = 450^\circ\text{C}$ in presence of 1 vol% of H_2O show a nearly complete filling of the pore space (16 and 27 vol%, respectively) and a reduction of the diameter of the spheres within 168 and 6 hours, respectively as the result of viscous flow, eventually combined with a dissolution-precipitation process.

These experiments by Rossi et al. (subm) suggest that the glass pods found in the basalt samples in this study, which have a similar composition, are likely to have been deformed by viscous flow of the glass. Rossi and coworkers showed that viscous flow is relevant in samples compacted under hydrostatic conditions for six hours at $T > 350^\circ\text{C}$, therefore we suppose that this viscous flow can occur within 40 min (the typical duration of our deformation experiments) at $T = 500^\circ\text{C}$ under a high differential stress. Additionally, dissolution, which is very fast in wet glass at $T = 500^\circ\text{C}$, $P_c = 500\text{ MPa}$, may possibly have assisted in this process by filling cracks with reprecipitated material. The dissolution kinetics of glasses are higher than for crystalline materials; Icenhower and Dove (2000) have shown that the dissolution rate of glass is 10-fold increased compared to quartz. The experiments of Rossi were performed under hydrostatic conditions; in our case a high differential stress may have enhanced the rate with which these processes occur. The presence of water is very important: in the experiments performed by Hacker and Christie (1991) on dry samples of partially glassy basalt at higher temperatures ($T = 675\text{--}875^\circ\text{C}$) and partially under lower shortening rates this viscous flow of glass was not observed.

At $T = 300^\circ\text{C}$, however, the viscosity of the glass pods is much higher and therefore the glass pods are not able to deform easily by viscous flow. Instead, the sample deforms by cataclasis. Observations on heat-treated samples show that not all the cracks formed within the glass pods are healed, because dissolution and precipitation are slower at this deformation condition as well. For partially glassy basalt samples deformed at $T = 300^\circ\text{C}$ and for MD deformed at $T = 300$ and 500°C , the strength of the sample is determined by the strength of the pyroxene and plagioclase minerals. A switch in deformation mechanism from cataclasis to viscous flow was observed for the partially glassy basalt samples when increasing the temperature. Possibly,

the cessation of earthquakes in the oceanic crust at temperatures above ca. $T = 400^\circ\text{C}$ may be connected to this change in deformation mechanism (Tapponnier and Francheteau, 1978; Hyndman and Wang, 1995).

6.5.2 Mineral reactions in basalt samples

Within all hydrostatically treated samples and in VB deformed at $T = 500^\circ\text{C}$, $\dot{\epsilon} = 1 \times 10^{-4} \text{s}^{-1}$, new mineral phases have been observed. Although the volume of new phases was very small (a $300 \mu\text{m}$ wide gouge zone cutting at an angle of ca. 30° through a sample of 6.4 mm diameter gives ca. 1 vol% gouge; most gouge zones were narrower and only part of the gouge reacted), it does show that reaction is possible in these samples under the applied conditions.

The observed reactions are hydration reactions of basalt samples corresponding to greenschist or amphibolite facies conditions. These reactions are retrograde reactions in the sense that the undeformed rock has a composition similar to samples metamorphosed or formed at high temperature conditions. The reactions have occurred as an effect of the $P_c T$ -conditions after deformation and as a consequence of deformation a reduction of the grain size and some mixing of the very small grains is detected. Reactions mainly take place in the fine grained, mixed fractions of the gouge. This suggests that the reactions are occurring via dissolution and precipitation and that they can only occur in a measurable amount when the transport path is not too long. The VB samples deformed at $T = 500^\circ\text{C}$ show incipient reaction after deformation. This reaction is not the cause of the extreme weakening of the samples. First, no reaction was observed in the BB samples that showed the same amount of weakening and secondly, not enough reaction material is formed to create a continuous zone of weak phases.

The most abundant reaction in MD is of plagioclase and pyroxene with water forming amphibole. In undeformed VB olivine is present instead of orthopyroxene and glass pods are found together with plagioclase. It is expected that the dissolution of glass is not only faster than for quartz, but faster than for plagioclase as well. Therefore, this reaction occurs in deformed and hydrostatically treated VB, but in MD only after 14 days at $T = 500^\circ\text{C}$, $P_c = 500 \text{ MPa}$. A similar reaction ($\text{plg} + \text{pyx} + \text{H}_2\text{O} = \text{hbl}$), has been observed by Rutter et al. (1985) at $T = 600^\circ\text{C}$. In our samples, biotite has sometimes been found associated with the amphibole.

The assemblage of newly formed minerals, at $T = 500^\circ\text{C}$ biotite, amphibole, plagioclase and at $T = 300^\circ\text{C}$ chlorite, amphibole and albite are both typical for the conditions under which they are formed. However, in both assemblages for both MD and VB, a newly formed calcium-bearing mineral is lacking. No epidote or zoisite is observed. This might have been caused by the Mg-Fe-enriched composition of rocks (Fig. 6.11) compared to most basalts, or, in case of VB,

because the glass pods are richer in K than in Ca. In case of epidote, the reducing conditions during the experiment caused by the graphite-furnaces may have hampered its formation.

6.5.3 Comparison between basalt and granite deformation

Deformation and heat treatment studies are performed on granite samples under the same conditions (see Chapters 4 and 5). Here we will discuss the main similarities and differences between the granite samples and the basalts.

The strength of the granite samples is 100–300 MPa less than the strength of basalts, except for partially glassy basalt deformed at $T = 500^\circ\text{C}$. For both rock types, most samples that were deformed at $T = 300^\circ\text{C}$ formed a single diagonal fault zone or a major diagonal fault zone with small conjugated faults. Most samples deformed at $T = 500^\circ\text{C}$ developed two well developed conjugated faults, or a set of several small conjugated faults. In both rock types, the fracturing of plagioclase and feldspar is very important for the formation of the fault zone. With their cleavage planes, feldspars easily fracture under the applied conditions and these fractures interconnect to a fracture zone (Fig. 6.7a). Micas, especially biotite, add to this process, as they form the weakest phases, they are deformed by a combination of fracturing, sliding and kinking. The fault zones in granite are basically build upon a sliding and kinking mica grains, usually biotite. In basalt samples this biotite is lacking; here the sample forms several parallel thin faults that laterally expand into one fault zone (Fig. 6.7b-d). The absence of mica in basalts explains the difference in strength.

The basalt samples develop less fault gouge than granitic samples. The shortening measured for these samples after deformation is a little less than for granitoid samples deformed with the same amount according to the chart record (see Chapter 2). However, this discrepancy is not enough to explain the difference in the amount of gouge. Furthermore, the fault gouge in the basalt samples is less matured and a large part of the fault zone material consists of cracked minerals, whereas the wall-rock is nearly unaffected by the deformation. In granitoid samples the deformation is less localized. The gouge is only discerned at high magnifications in the SEM; at lower magnifications only cracked grains are visible. The $D_{>}$ -values for the basalt gouge are lower than for quartz (2.26 at $T = 300^\circ\text{C}$ and 2.07 at $T = 500^\circ\text{C}$) and feldspar (2.06 at $T = 300^\circ\text{C}$ and 1.95 at $T = 500^\circ\text{C}$). The $D_{<}$ -values and the $D_{>}$ -value for cracked material are the same as those observed for granitic rocks. This implies that the cracking process, during which a part of the smallest grains was already formed, is not very dependent on the mineral type. Gouge formation for the larger grains is dependent on the mineral properties, as was observed for feldspar and quartz in granite (see Chapter 4).

Because of the small amount of gouge in the basalt samples, healing is not very pronounced in the MD samples. The $D_{>}$ -values for healed gouge (1.62 for pyroxene and 1.60 for plagioclase) are slightly larger than for granitoid samples deformed and hydrostatically treated under the same conditions (1.54 for feldspar and 1.57 for quartz). Healing follows a grain size dependent dissolution-precipitation process (Chapter 5) and therefore especially the very fine grained parts of the fault rock will heal. In VB that was heat treated at $T = 300^{\circ}\text{C}$ healing was very effective (see Fig. 6.8d). This may be caused by the reactions in the glass pods, which adds components to the fluid phase and consequently changes the water salinity and so accelerates the kinetics of dissolution and precipitation within the plagioclase, pyroxene and olivine.

6.5.4 Implications for the deformation of basalts in nature

Basaltic rocks are generally regarded as strong rocks. This is true for fully crystalline rock, but our experiments have shown that partially glassy basalt can change into a very weak rock, deforming under a fraction of its original strength under influence of a moderate temperature and the presence of a fluid. In the laboratory, we observe this weakening effect within a few minutes for a sample deformed at $T = 500^{\circ}\text{C}$, $P_c = 500$ MPa in the presence of de-ionized H_2O . In natural fault zones, like transform faults and subduction zones, more time and a more reactive fluid are present. Therefore, we expect that this weakening effect will even be enhanced compared to laboratory conditions. Since partially glassy basalts are the norm rather than the exception in the oceanic crust, it is important to recognize these processes.

This behaviour of basalt rocks could not have been predicted from room temperature investigations, nor from dry experiments or from experiments performed under higher pressure and temperature conditions. Our experiments were performed under PT -conditions that are realistic for oceanic crust at shallow to intermediate depth. Under these conditions partially glassy basalt is no longer strong, but changes rapidly into a weak rock. This effect is caused by (1) the decrease in viscosity of the glass pods with increasing temperature, (2) by the formation of fault gouge, which increases the amount of mineral reaction and the formation of new weak phases in the rock, and may potentially be enhanced by (3) the much higher dissolution rate of glass, compared to crystalline material, which accelerates granular flow assisted by material transfer within the glass pods. Under the conditions at which the experiments were performed, the weakening effect of the viscous deformation of glass pods is faster than mineral reaction in the samples. Therefore, this aspect of strength reduction in oceanic crust is important to be considered in modeling the oceanic crust.

6.6 Conclusions

We observe for experimental deformation of partially glassy basalt rocks at $T = 500^\circ\text{C}$, $P_c = 500\text{ MPa}$ and $\dot{\epsilon} = 1 \times 10^{-4}\text{ s}^{-1}$ with 0.2 wt% H_2O added a fast and significant weakening of the sample compared to samples deformed at $T = 300^\circ\text{C}$, $\dot{\epsilon} = 0.01\text{--}3.4 \times 10^{-4}\text{ s}^{-1}$ and to deformed samples of fully crystalline basalt. Samples that are only deformed are compared to samples that are heat treated after deformation for 14 days under hydrostatic conditions of $T = 300$ or 500°C , $P_c = 500\text{ MPa}$. Mechanical, microstructural and chemical analyses of the deformed samples are utilized to investigate the samples for their strength, grain size, spatial distribution of their plagioclase minerals, mineral reactions, and healing of the grains. From these investigations, we can conclude the following:

1. Partially glassy basalt deformed at $T = 500^\circ\text{C}$ is weakened as a result of a decrease in viscosity of the glass pods by the presence of a fluid. Deformation is distributed over the sample and concentrated in the glass pods that are deformed by viscous flow. Other minerals, especially elongated plagioclase, are passively rotated and almost undeformed.
2. Partially glassy basalt deformed at $T = 300^\circ\text{C}$ and fully crystalline basalt samples are strong and show localized deformation in discrete fault zones. These fault zones form at an angle of ca. 33° to the compressional axis and widen by incorporating wall-rock as cracked material, by evolving cracked material into a fault gouge, by laterally consuming other small fault zones, and possibly by rotating the fault zone to ca. 38° . Less gouge is formed than in granitoid rock samples deformed under the same conditions.
3. Grain size reduction in the fault zones of diabase produced fine grained gouge with $D_{>}$ -value of 1.90 for plagioclase and 1.79 for pyroxene. For cracked material of both minerals we obtained $D_{>} = 1.60$. The $D_{<}$ -value is 0.90 and 0.96 for plagioclase and pyroxene, respectively. Healing of the gouge during the heat treatment yields a $D_{>}$ -value of 1.60 for plagioclase and 1.62 for pyroxene.
4. In the samples that have been heat treated and the partially glassy basalt deformed at $T = 500^\circ\text{C}$ (for 40 minutes) mineral reactions have been observed. Pyroxene and plagioclase have reacted in the presence of water to amphibole. Biotite has been formed at $T = 500^\circ\text{C}$, and chlorite and albite at $T = 300^\circ\text{C}$. Although only a small volume of new phases is created, these experiments show that reaction is possible and fast in basalts deformed under shallow to mid-crustal conditions.

Chapter 7

Conclusions

The aim of this study is to compare the microstructures of experimental and natural fault rock that formed under conditions near the brittle-ductile and brittle-plastic transition. In this way, the processes that play an important role in fault rock are investigated. This Chapter gives a summary of the main observations and conclusions of this study. In addition to this, possibilities for further research are suggested.

7.1 Summary and conclusions

We studied the deformation and post-deformational heat treatment of granitoid (Verzasca Gneiss) and two partially glassy basalts (Vogelsberg Basalt and Bransrode Basalt) and fully crystalline diabase (Maryland Diabase) in the laboratory and compared the results for granitoid samples to natural granitoid fault rock from three different areas (Nojima Fault Zone, Orobic Thrust and southwestern Black Forest). Deformation experiments were performed in a Griggs type solid-medium deformation apparatus at $T = 300\text{--}500\text{ }^{\circ}\text{C}$, $P_c = 470\text{--}1030\text{ MPa}$ and $\dot{\epsilon} = 1.3 \times 10^{-7}\text{ s}^{-1}\text{--}3.5 \times 10^{-4}\text{ s}^{-1}$ with and without 0.2 wt% H_2O . One experiment was performed at $15\text{ }^{\circ}\text{C}$, low P_c (probably 50 MPa), without added water at a shortening rate of $\sim 10^{-2}\text{ s}^{-1}$. Samples that were only deformed were compared to samples that were heat treated after deformation for 4 hours to 14 days under hydrostatic and non-hydrostatic conditions of $T = 200\text{--}500\text{ }^{\circ}\text{C}$, $P_c = 480\text{--}540\text{ MPa}$. Mechanical, microstructural and chemical analyses of the deformed samples were applied to investigate the samples. From these investigations, the following was concluded:

Geometrical description of fault rock microstructures

An improved version of the image analysis program ‘shapes’ (Fortran source code), the public domain software ‘ImageSXM’ and the macros ‘Lazy D -map’ have been used to investigate the microstructures of experimentally deformed granitoid samples. Several grain shape descriptors, such as the aspect ratio (long axis/short axis), paris- and deltA-factor (difference in shape between the grain and its envelope to indicate the intensity and width of indentations) and the angularity, Ω , (fraction of angles $> 0^{\circ}$ in a histogram of vertex angles), have been used to describe the fault rock. Cracked material displays a higher aspect ratio, a higher paris- and deltA-factor and a larger Ω than gouge. Cracked quartz grains have an especially high aspect ratio and cracked feldspar grains show a high paris-factor. The similarity between deltA- and paris factor values in cracked materials indicates that the indentations are wide and not formed by intra-granular cracks. The distinction between cracked grains and gouge and between cracked feldspar and cracked quartz are clearer when automatic digitization of the grains is applied. For very small grains ($< \sim 1\text{ }\mu\text{m}$) the distinction between feldspar and quartz and cracked minerals and gouge is no longer apparent from the aspect ratio and paris-factor of the grains.

The grain size distribution shows two different slopes, D , in a log(frequency)-log(radius) histogram for all cracked minerals and gouge of quartz, feldspar/plagioclase and pyroxene. The transition point of these two slopes occurs at a grain size of $\sim 1\text{--}2\text{ }\mu\text{m}$ radius and is called r_K . For all mineral types and irrespective of whether the fault rock consists of cracked grains or gouge, the slope of the (2-dimensional) grain size distribution smaller than r_K is ~ 1.0 (labeled $D_{<}$). The smallest grains in the gouge have a radius of $\sim 15\text{ nm}$. For grains larger than r_K cracked grains can be distinguished from gouge by their $D_{>}$ -value; for cracked grains this value

is 1.5–1.6 and for gouge it is dependent on the mineral type, deformation conditions and ranges between 2.27 and 1.76: for deformation at $T = 300\text{ °C}$ and $P_c = 500\text{ MPa}$, the $D_{>}$ of quartz gouge is larger than for feldspar/plagioclase, which in turn is larger than for pyroxene. An increase in confining pressure or in temperature or a decrease in axial shortening rate, decreases $D_{>}$: confining pressure has a larger effect on changes in the $D_{>}$ of gouge than temperature or shortening rate. This distinction in $D_{>}$ -value of cracked material and gouge is reflected in the matrix-content of the fault rock and can be visualized by D -mapping; this mapping is based on the darker average grey-value of matrix compared to intact rock of the same composition in BSE-micrographs.

Implications of the observed grain size distribution and grain shapes of fault rock

The grain size distribution does not show a self-similar distribution within the investigated range of grain sizes (60 nm–100 μm), the grain size distribution is therefore not fractal. Furthermore, values larger than 2.0 are obtained for gouge, so that this distribution cannot be fractal (Turcotte, 1992). The difference in $D_{>}$ -value and in grain shape factors between cracked grains and gouge suggests a two-stage evolution of fault rock. Initial rupturing of intact rock forms cracked grains. Further displacement along the fault cause the evolution of these cracked grains to gouge. As a result of the movement the grains become more equi-dimensional, less indented and less angular. At the same time, the number of small grains increases with respect to larger grains. In the energy-budget equation of earthquakes, a term exists that describes the energy required to create new mineral surfaces in the gouge. To calculate this term, the cracked grains need to be used, as they are developed during the rupturing. The use of cracked grains instead of gouge lowers the surface energy term to an extent that it can be neglected in the energy budget.

The grain size r_K coincides approximately with the grinding limit for quartz and is probably close to this limit for feldspar and pyroxene. The two slopes in the grain-size distribution and the change in grain shape for very small grains is supposed to correspond to a change in the physical process of grain size reduction. Attrition and shear may dominate below the transition value r_K , whereas grinding can be the major grain size reduction mechanism for larger grains.

Effect of temperature, axial shortening rate and time during hydrostatic healing

Monomineralic gouge kept under hydrostatic conditions shows a decrease in $D_{>}$ -value with time that is enhanced by an increase in temperature. The $D_{>}$ -value is observed to approach asymptotically to a value of 1.54–1.58, which is regarded as “healed” gouge. Therefore, a $D_{>}$ -value of 1.5 is chosen as the ultimate value reached in healing. The decay of the $D_{>}$ -value with time can be approached by:

$$\Delta D(t) = D_{>}(t) - D_f = A \cdot e^{(-\lambda t)}$$

in which D_{def} represents the $D_{>}$ -value after deformation. A and λ describe temperature de-

pendent constants. Extrapolation of this function predicts that monomineralic gouge at $T = 200^\circ\text{C}$ and $P_c = 500\text{ MPa}$ will be healed to $D_{>} = 1.5$ in approximately one year.

The influence of temperature and fluid on the strength of and reaction in partially glassy basalt

Partially glassy basalt deformed at $T = 500^\circ\text{C}$ is remarkably weakened (a maximum strength of 400 MPa) compared to fully crystalline Maryland Diabase (1100 MPa) deformed under the same conditions and compared to the same sample material deformed at $T = 300^\circ\text{C}$ (a strength of 1300–1700 MPa). This is a result of a decrease in viscosity of the glass in presence of a fluid. Deformation is distributed over the sample and concentrated in the glass, which deforms by viscous flow.

In the basaltic samples mineral reactions are observed at a small scale within the fine grained gouge. Plagioclase and pyroxene (and olivine) have reacted in the presence of water to amphibole. Biotite has been formed at $T = 500^\circ\text{C}$, chlorite and albite at $T = 300^\circ\text{C}$. Reaction in the partially glassy basalt samples occurs within 40 minutes at $T = 500^\circ\text{C}$.

Effect of pressure, temperature, and shortening rate on the mode of failure and the microstructures of fault rock

All granitoid samples and most basalt samples have been deformed by cataclasis at $P_c = 500\text{ MPa}$. Further movement on the fault zone seems to result in the formation of a wider gouge zone. Deformation occurs by cataclastic flow and is ductile. For samples deformed at $P_c = 1030\text{ MPa}$, shortening takes place by the formation of new sharp faults in the sample, rather than the widening of one fault. This results in a shortening and widening of the sample. The change in mode of fracturing is the result of a transition from mode I to mode II cracking (Tullis and Yund, 1977; Hirth and Tullis, 1994). Deformation at $P_c = 500\text{ MPa}$ occurred above the brittle-ductile transition, as is illustrated by the samples that have been deformed twice with different time periods for healing. Irrespective of the healing time, the sample showed the same resistance against loading in both deformation events and it has thus been deformed by the formation of new fractures rather than by using existing ones. The confining pressure is exhibiting a large influence on the $D_{>}$ -value of the fault rock: increasing the confining pressure from $P_c = 500$ to 1030 MPa is decreasing the $D_{>}$ -value from 2.26 and 2.06 to 1.94 and 1.85 for quartz and feldspar, respectively.

Samples deformed at $T = 300^\circ\text{C}$, $P_c = 500\text{ MPa}$ and $\dot{\epsilon} = 1 \times 10^{-4}\text{ s}^{-1}$ often form a throughgoing fault with or without small conjugated faults, whereas granitoid and diabase samples deformed at the same conditions and $T = 500^\circ\text{C}$ mainly deform by two or more conjugated faults. Deformation of the sample at $T = 300^\circ\text{C}$ may therefore occur closer to the brittle-ductile transition than the sample at $T = 500^\circ\text{C}$. Thus a minor temperature effect on the mode of

failure is displayed. This minor temperature effect is visible as a decrease in $D_{>}$ -value from 2.26 and 2.06 at $T = 300^\circ\text{C}$ to 2.07 and 1.95 at $T = 500^\circ\text{C}$ for quartz and feldspar respectively.

The similarity between the $D_{>}$ -values of experimental and natural fault rock suggests that no distinction is possible between seismic and fast aseismic deformation rates. This suggestion however, may only be valid for fast deformation rates at low temperatures. For deformation at $T = 300^\circ\text{C}$ the same $D_{>}$ -values are obtained for deformation at $\dot{\epsilon} = 1 \times 10^{-4} \text{s}^{-1}$ and $1 \times 10^{-6} \text{s}^{-1}$, but much lower values for $\dot{\epsilon} = 1 \times 10^{-9} \text{s}^{-1}$ (see discussion above). On the other hand, the $D_{>}$ -values of quartz deformed at $T = 300^\circ\text{C}$, $P_c = 500 \text{ MPa}$ and $\dot{\epsilon} = 1 \times 10^{-4} \text{s}^{-1}$ without added water and the sample deformed at room temperature, $P_c \approx 50 \text{ MPa}$ and $\dot{\epsilon} \approx 10^{-2} \text{s}^{-1}$ without added water yield the same $D_{>}$ -value (2.33). A transition of deformation rate insensitive to deformation rate sensitive conditions seems to develop at approximately $T = 300^\circ\text{C}$ and at approximately $\dot{\epsilon} = 1 \times 10^{-6} \text{s}^{-1}$.

For granitoid samples deformed at $T = 500^\circ\text{C}$ and $P_c = 500 \text{ MPa}$ the change from $\dot{\epsilon} = 1 \times 10^{-4} \text{s}^{-1}$ to $\dot{\epsilon} = 1 \times 10^{-6} \text{s}^{-1}$ has a small effect, while the deformation at $\dot{\epsilon} = 1 \times 10^{-7} \text{s}^{-1}$ has a larger effect on the microstructures and $D_{>}$ -value. At $T = 500^\circ\text{C}$ and $P_c = 500 \text{ MPa}$, the $D_{>}$ -value is decreased from 1.95 to 1.68 for feldspar resulting from the decrease in shortening rate with three order of magnitude. Deformation bands and micro-kinking microstructures are observed in the fault zones of the samples deformed at $1 \times 10^{-7} \text{s}^{-1}$. These observations suggest that these are combined effects of cataclasis and diffusive mass-transfer-induced healing of grains. This healing during deformation causes a strong reduction of the $D_{>}$ -value. Healing under differential stress is further enhanced for the samples that were non-hydrostatically healed. Deformation of the small grains ($< \sim 1 \mu\text{m}$) in the gouge at low strain rates ($< \sim 10^{-7} \text{s}^{-1}$) occurs by plastic deformation. For larger grains and the samples deformed at higher strain rates a dominantly brittle mechanism is observed.

Implications for natural fault rock

$D_{>}$ for gouge is a good parameter to compare natural and experimental fault rock. The obtained $D_{>}$ -values for freshly formed gouge ($D_{>} = 2.02$) and for cracked grains ($D_{>} = 1.64$) of the Nojima Fault Zone are the same as for the experimentally deformed granitoids. For natural gouge from different regions in which healing occurred, $D_{>}$ -values of 1.58–1.62 were observed. These $D_{>}$ -values agree well with those of experimentally healed samples, which show $D_{>} = 1.59$ after 4 days at $T = 500^\circ\text{C}$ and almost no further decrease after longer healing times. $D_{>}$ -values of natural and experimental fault rock can be compared directly and the hydrostatic healing law can be used to predict cataclasite healing times in natural systems. However, this law is only valid for monomineral gouge. For polymineralic gouge, the initial grain size distribution of the gouge is preserved. Intense mixing of the different minerals in a gouge impedes grain growth.

In the basalt samples, which were heat treated after deformation and the glassy basalt deformed at $T = 500^\circ\text{C}$ (deformation during 40 minutes) mineral reactions have been identified. Pyroxene and plagioclase have reacted to amphibole in the presence of water. Biotite is created at $T = 500^\circ\text{C}$, and chlorite and albite are formed at $T = 300^\circ\text{C}$. Although the volume of new phases in the experiments is small, with more time or a fluid with a different composition, it is expected that reactions are more abundant in basalts, deformed under shallow to mid-crustal conditions and will probably be important for the strength of the basalt.

7.2 Suggestions for further research

This thesis demonstrates that a range of processes is active during deformation and healing. From the experiments on granitoid and basaltic rock and the comparison of these rocks to natural fault systems new questions arise. In order to address these questions, future studies on fault rock could include research on the following topics:

1. *Influence of muscovite and clay-minerals on the strength of the fault zones:* Feldspar alteration reactions form muscovite, clay-minerals and zeolites during or after deformation in natural granitoid gouge (Wintsch, 1975; Wintsch et al., 1995; Evans and Chester, 1995; Wibberley, 1999, Chapter 5, Appendix E). In experimental basaltic fault rock mineral reactions have been observed as well, while on the contrary no evidence for reaction was detected in experimentally deformed granitoid samples. Mineral reactions will make the fine grained gouge polymineralic and therefore change its healing behavior. Clay- and mica-minerals are able to deform by kinking, dislocation creep and slip on their cleavage planes (Wilson and Bell, 1979; Mares and Kronenberg, 1993), under conditions where quartz and feldspar are deforming by cataclasis (Tullis and Yund, 1977; Shea Jr and Kronenberg, 1993) and thus will have a weakening effect on fault zone (Mitra, 1992; Wintsch et al., 1995).

Alteration reactions, mixing or healing of the gouge and the strength of the fault zone are strongly interrelated features. The precise interactions of these processes, their kinetics, and their dependence on the temperature, deformation rate and fluid chemistry are hardly known, though they are very important for the mechanics of fault zones, especially for the understanding of post-seismic creep. For a further understanding of natural fault rocks more experimental investigations are needed to address these problems. In the current set of experiments on granites no reactions have been observed in feldspar, most likely because the salinity of the water is too low to obtain a reaction that can be observed under the applied experimental conditions. To create a gouge in which these reactions occur, KCl

buffered by HCl could be added as a fluid, which would enhance the following reaction



Alternatively, to investigate the evolution of the strength of the fault zone, muscovite or a clay-mineral could be added to the gouge, either in layers to represent a foliated cataclasite or well mixed with the other minerals to represent a chaotic gouge.

2. *The evolution of fault zones and of the grain size distribution:* In Chapter 4, it was shown that the fault rock evolves from cracked minerals along a single fault to either a set of conjugate fault zones that cross-cut each other or to a progressively widening fault zone. A better understanding of the development of the grain size distribution from cracked grains to gouge during faulting, and the development of fault zone networks is required. To study the evolution of a small crack to a mature fault zone network a set of experiments could be performed with a step-wise (e.g. with steps of 5% shortening) increase of shortening and subsequent study of the microstructures. Features like the onset of gouge formation, the widening of gouge zones related to deformation and the development of conjugate faults are very important for the understanding of fault zones. Important for this kind of experiments is that the pistons are designed in such a way that they do not indent the sample.
3. *TEM-investigations:* Deformation in both laboratory, and natural fault rock produces very small grain sizes. A change in the grain size reduction mechanism has been discussed in Chapter 4. The properties of these small grains are hard to investigate with light and scanning electron microscope. For a better understanding of the mechanism of grain size reduction for small grains a TEM-study is desirable. Such a study would be able to answer whether small grains form dominantly by shearing or by attrition, whether the very small grains are amorphous (Yund et al., 1990) or crystalline (Olgaard and Brace, 1983), and whether some bulging recrystallization microstructures in samples deformed under conditions close to the brittle-plastic transition (regime I deformation of e.g. Hirth and Tullis, 1992) are in fact healed gouges. TEM investigations performed on samples that were healed after deformation could be used to determine the healing mechanisms (see below) and the compositions of newly formed phases, especially for the basalt samples.
4. *Healing mechanism:* The rate of healing defined by changes in the $D_{>}$ -value of gouge has been studied in Chapter 5. The grain size distribution of the experimentally produced fault gouge is changed as a result of dissolution and precipitation in the fault rock. Tentatively, these changes have been connected to healing mechanisms: neck-growth under hydrostatic conditions, pressure solution under non-hydrostatic conditions and perhaps

another mechanism under more shallow crustal levels (e.g. Nakatani and Scholz, 2004). These mechanisms have been inferred from high magnification scanning electron microscope observations: the grain shapes for small grains healed under hydrostatic conditions shows a higher paris-factor (due to agglomeration of small grains). For non-hydrostatically healed grains, more flattening perpendicular to the principal stress was detected, compared to gouge that was only deformed (see the poster of Keulen et al., 2006, for a preliminary study). More high-magnification observations on the microstructures are needed, preferably with cathodoluminescence connected to a transmission scanning electron microscope, to study the relation between newly-grown and already present parts of grains.

5. *Calculation of rates for deformation and healing:* Preliminary calculations (following Paterson, 1995) on the rate of deformation by means of granular flow accommodated by material transfer for very small grains (50 nm–1 μm) of the experimentally created gouge have shown that for these grains, even at temperatures as low as $T = 500^\circ\text{C}$, deformation rates can be on the order of $\dot{\epsilon} = 10^{-7}\text{s}^{-1}$. Therefore, this granular flow is competitive with deformation of the sample by frictional sliding. For a more accurate calculation of this rate, it is important to gain more understanding of which micro-scale mechanism is facilitating these processes (see Den Brok, 1998, for a discussion). In addition, it is important to determine the influence of differential stress on the dissolution-precipitation process and under which conditions stress independent healing mechanisms (like Ostwald-ripening or neck-growth) will become dominant.
6. *Experiments on basaltic samples:* The deformation of basaltic rock, especially the deformation behaviour at middle crustal depth conditions, is hardly investigated. Our experiments are performed under *PT*-conditions that are realistic for upper to middle oceanic crust and show a behavior of basaltic rocks that would not have been predicted from room temperature investigations or from experiments performed under higher pressure and temperature conditions. The deformation behavior of basalts are still poorly understood, especially the combination of deformation with mineral reactions. In the present study only a small amount of reaction products is obtained. Further investigations, possibly with a fluid of a different composition added to the sample, could address (a) the mineral reactions, (b) the rate of dissolution related to granular flow with mass transfer within the gouge, and (c) the viscosity of the glass in relation with temperature, strain rate, stress and water. In the present study the behavior of the gouge is studied under a high deformation rate followed by hydrostatic conditions. Natural conditions would better be represented by a slow shortening rate than by purely hydrostatic conditions.

Appendix A

List of all experiments

The tables on the following pages show the data for all performed experiments. Experiments are sorted by sample material: first Verzasca Gneiss, than mafic samples and further by number. Salt samples are listed in Appendix C.2.

Table A.1: Explanation of the symbols and abbreviations used in the lists of all experiments

Abbreviation	Explanation
heat treatment	healing under hydrostatic or non-hydrostatic conditions
mat	sample material
T	temperature
P_c	confining pressure
$\dot{\epsilon}$	axial shortening rate
<i>ax.</i> ϵ	axial strain
H ₂ O	amount of H ₂ O added inside the jacket before deformation
def.	deformation
TC	thermocouple
nh	non-hydrostatic healing
d	days
m	minutes
GB	Gneiss Berger
P2	Verzasca Gneiss piece 2
MD	Maryland Diabase
BB	Bransrode Basalt
VB	Vogelsberg Basalt
NaCl	sodium chloride
rig	deformation apparatus used
fault	nature of the fault zone
s	single diagonal
sc	single diagonal with small conjugate faults
sb	single broad diagonal fault
c	two conjugated faults
cc	multiple conjugated faults
m	multiple parallel faults
b	barreled without major faults
†	failed experiment

sample	deformation				heat treatment			mat	Comments
	T °C	P_c MPa	$\dot{\epsilon}$ $\times 10^{-4} \text{ s}^{-1}$	ax. ϵ %	H ₂ O wt%	T °C	P_c MPa		
2nk	400	390	0.14	12	0			GB	elastic deformation only
4nk	400	410	1.3	9	0			GB	elastic deformation only
6nk	300	390	0.1.4	8	0			GB	elastic deformation only
8nk	400	500	0.16	11	0			GB	elastic deformation only
9nk	300	510	0.16	11	0			GB	elastic deformation only
10nk	400	600	0.14	23	0			GB	elastic deformation only
11nk	300	400	1.3	37	0			GB	ZrO ₂ -pistons used
12Ank	15	50	100	36	0			GB	manually loaded sample ^a
27nk	500	490	0.016	36	0.2	500	520	GB	nh
29nk	300	470	0.016	33	0.2			GB	
37nk	500	480	0.013	32	0.2			P2	† no deformation, ZrO ₂ -pistons brecciated, CO ₂ pre-dried: $T = 600^\circ\text{C}$, 24h
38nk	300	510	1.5	38	0.2			P2	CO ₂ pre-dried: $T = 600^\circ\text{C}$, 24h
45nk								P2	† TC-problem
46nk	300	560	1.6	39	0.2	500	520	P2	
48nk	300	600	1.4	27	0.2	500	520	P2	
51nk	300	510	1.3	41	0.2	500	560	P2	† salt inside jacket
53nk	500	600	1.4	26+15	0.2	500	520	P2	def. (26%), hydrostatic (14 d), def. (15%)
54nk	500	560	1.4	26+15	0.2	500	530	P2	def. (26%), hydrostatic (14 d), def. (15%)
56nk	500	490	1.6	28	0.2	500	480	P2	
57nk	500	600	1.3		0.2	500	550	P2	† TC-problem, attempt for double cycle
58nk	300	500	1.3	27	0.2	300	510	P2	

^avalues for T, p, $\dot{\epsilon}$ and ax. ϵ are estimated

sample	deformation					heat treatment			mat	Comments
	T °C	P_c MPa	$\dot{\epsilon}$ $\times 10^{-4} \text{ s}^{-1}$	$ax. \epsilon$ wt%	H_2O %	T °C	P_c MPa	$time$ $\times 10^{+3} \text{ s}$		
59nk	500	520	1.4	26+15	0.2			0.66	P2	def. (26%), hydrostatic (11 m), def. (15%) 15% ax. ϵ at 10^{-4} s^{-1} + 19% ax. ϵ at 10^{-7} s^{-1}
60nk	300	1030	1.5	34	0.2				P2	
62nk	300	490	1.4+0.002	15 + 19	0.2	500	480	1207.62	P2	
63nk	300	530	1.4	35	0				P2	
64nk	300	500	1.3	26	0.2				P2	
65nk	500	530	1.4	32	0.2	500	530	1226.50	P2	
66nk	300	490	0.015	38	0.2				P2	
67nk	300	530	1.4	31	0.2	500	510	1213.38	P2	
68nk	500	520	1.4	37	0.2				P2	
70nk	500	500	0.013	24	0.2				P2	
71nk	300	830	1.5	34	0.2				P2	
72nk	500	470	0.0013	39	0.2				P2	
77nk	300	580	1.3	27	0.2	300	550	1198.91	P2	
91nk	400	530	1.3	38	0.2				P2	
92nk	300	500	1.4	31	0.2	400	500	1209.12	P2	
95nk	300	540	1.3	31	0.2	500	540	13.80	P2	
97nk	300	500	1.3	29	0.2	300	520	13.80	P2	
102nk	300	510	1.3	57	0.2				P2	
104nk	300	490	1.2	31	0.2	400	500	13.80	P2	
116nk	300	530	1.4	35	0.2	400	530	1209.3	P2	
119nk	300	550	1.5	34	0.2	200	510	330.12	P2	

Table A.2: All deformation experiments performed on Verzasca Granite, continued from previous page

sample	deformation				heat treatment			mat	Comments
	T °C	P_c MPa	$\dot{\epsilon}$ $\times 10^{-4} \text{ s}^{-1}$	$ax. \epsilon$ wt%	H_2O %	T °C	P_c MPa		
12nk	650	700	0.12		0.0			MD	† no deformation, ZrO ₂ -pistons brecciated
14nk	650	850	0.15	32	0.0			MD	
15nk	650	800	0.16	30	0.0	650	800	MD	nh
30nk	500	480	0.13	34	0.2			MD	
31nk	500	500	0.014		0.2			MD	† sample rotated
39nk	300	480	0.018	39	0.2			BB	predried at $T = 900 \text{ }^\circ\text{C}$, 24 h:
41nk	500	510	0.01	15	0.2			BB	13.1 ml CO ₂ /min & 3.6 ml CO/min
84nk	500	500	1.0	25	0.2	550	480	VB	predried at $T = 900 \text{ }^\circ\text{C}$, 26.5 h:
86nk	500	510	1.2	30	0.2			VB	13.1 ml CO ₂ /min & 3.6 ml CO/min
87nk	300	490	1.3	30	0.2	300	500	VB	
88nk	300	510	1.3	35	0.2			VB	
89nk	500	540	1.3	40	0.2			VB	
100nk	300	480	1.3	39	0.2			MD	
101nk	500	560	1.3	37	0.2			BB	
105nk	300	520	3.4	35	0.2			VB	
113nk	300	510	1.3	37	0.2	500	560	MD	

Table A.3: All deformation experiments performed on Vogelsberg Basalt, Bransrode Basalt and Maryland Diabase

sample	dimensions		rig	shortening			Comments
	length <i>mm</i>	diameter <i>mm</i>		chart <i>mm</i>	screw <i>mm</i>	fault	
11nk	11.952	6.28	1	4.41	2.71	c	ZrO ₂ -pistons
27nk	9.442	6.413	1	3.42	2.83	s	ZrO ₂ -pistons
29nk	9.004	6.410	2	2.99	2.90	c	ZrO ₂ -pistons
37nk	12.627	6.50	2	4.05	4.80	sc	ZrO ₂ -pistons
38nk	10.44	6.416	2	4.01	3.55	sc	
46nk	10.326	6.36	2	4.06	4.14	sb	
48nk	10.721	6.372	2	2.85	2.44	c	
51nk	10.58	6.372	2	2.34	2.30	sc	
53nk	11.188	6.38	2	4.45	4.11	sc	
54nk	11.001	6.38	2	4.20	3.85	sc	
56nk	11.104	6.38	2	3.21	2.74	sc	
57nk	10.285	6.379	1	2.73	2.91	c	
58nk	10.315	6.39	2	2.72	3.21	c	
59nk	12.749	6.384	1	3.61	3.27	cc	
60nk	10.127	6.395	1	3.649	2.93	m	five parallel faults
62nk	11.906	6.409	2	2.88	3.31	c	
63nk	12.11	6.398	1	4.25	4.12	s	
64nk	12.327	6.404	1	3.18	3.59	c	
65nk	12.561	6.381	2	4.05	3.80	cc	
66nk	12.373	6.384	1	4.64	5.06	sc	
67nk	10.615	6.408	1	3.31	4.20	s	
68nk	10.318	6.431	1	3.8	3.8	c	
70nk	12.945	6.411	1	4.97	5.0	sc	sample tilted
71nk	10.581	6.383	2	3.58	3.25	cc	
72nk	10.184	6.423	2	3.96	4.04	s	
77nk	12.621	6.423	2	3.69	3.85	cc	
91nk	11.501	6.407	2	4.34	3.85	s	
92nk	11.212	6.431	2	3.50	2.92	cc	
95nk	11.333	6.427	2	3.66	3.31	c	
97nk	10.859	6.421	2	3.14	2.35	cc	
30nk	13.786	6.50	1	4.67	3.37	sc	
39nk	10.385	6.40	2	4.05	2.98	c	
84nk	11.721	6.448	2	2.98	2.21	b	
86nk	11.827	6.391	2	3.60	2.60	b	
87nk	11.720	6.387	2	3.49	2.52	s	
88nk	11.351	6.396	1	4.01	2.94	cc	
89nk	11.870	6.395	1	4.70	2.31	b	
100nk	11.505	6.415	2	4.22	3.37	sc	
101nk	11.493	6.480	2	4.45	3.46	b	
105nk	11.719	6.374	1	4.10	3.28	sc	
113nk	11.987	6.3910	2	4.22	3.70	sc	

Table A.4: Dimensions of the granitoid and mafic samples that were used to calculate the difference between the shortening calculated from the chart record and the shortening measured after deformation. Additionally some experiments performed on samples with zirconia pistons are given for comparison.

Appendix B

Mechanical data

This Appendix shows the mechanical data of 44 deformation experiments in ten diagrams. The experiments were grouped in such a way that the effect of confining pressure, temperature and shortening rate is visible, as well as the degree in which the data can be reproduced. The first seven diagrams are drawn for granitoid samples, the other three for mafic samples. The mechanical data for the salt experiments is given in Appendix C. All data are for samples with 0.2 wt% H₂O added inside the jacket, unless indicated differently.

Each diagram consists of two parts, first the force-displacement measurements and second the stress-shortening recalculation of these data. Displacement is as measured from chart record; data is corrected for distortion of the apparatus, except for 11nk–30nk. The recalculation of to stress and shortening was done with the Fortran program rigC, see the Chapter 2 for details and comments.

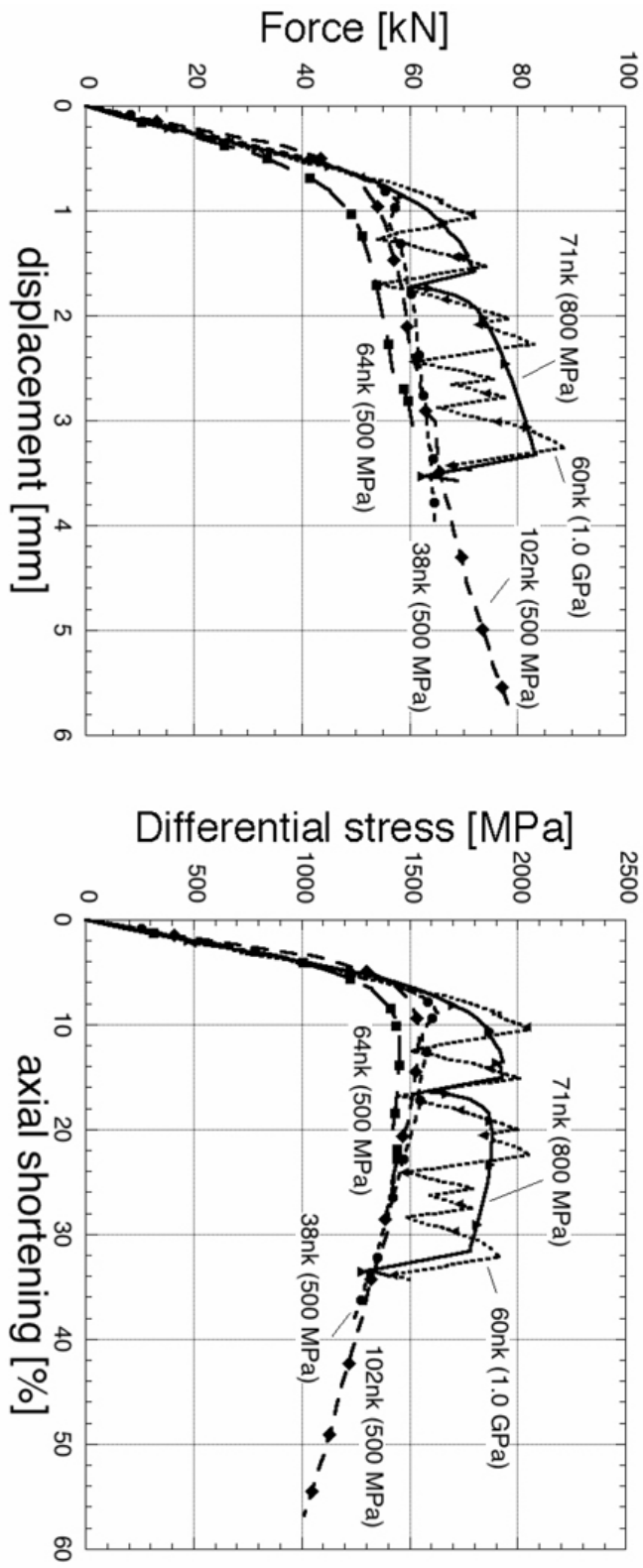


Figure B.1: Force-displacement and stress-shortening diagrams for deformation experiments on Verzasca Gneiss. All samples were deformed at $T = 300\text{ }^{\circ}\text{C}$, $\dot{\epsilon} = 1 \times 10^{-4} \text{ s}^{-1}$. The confining pressure covers 500 MPa, 800 MPa and 1.0 GPa, indicated in brackets.

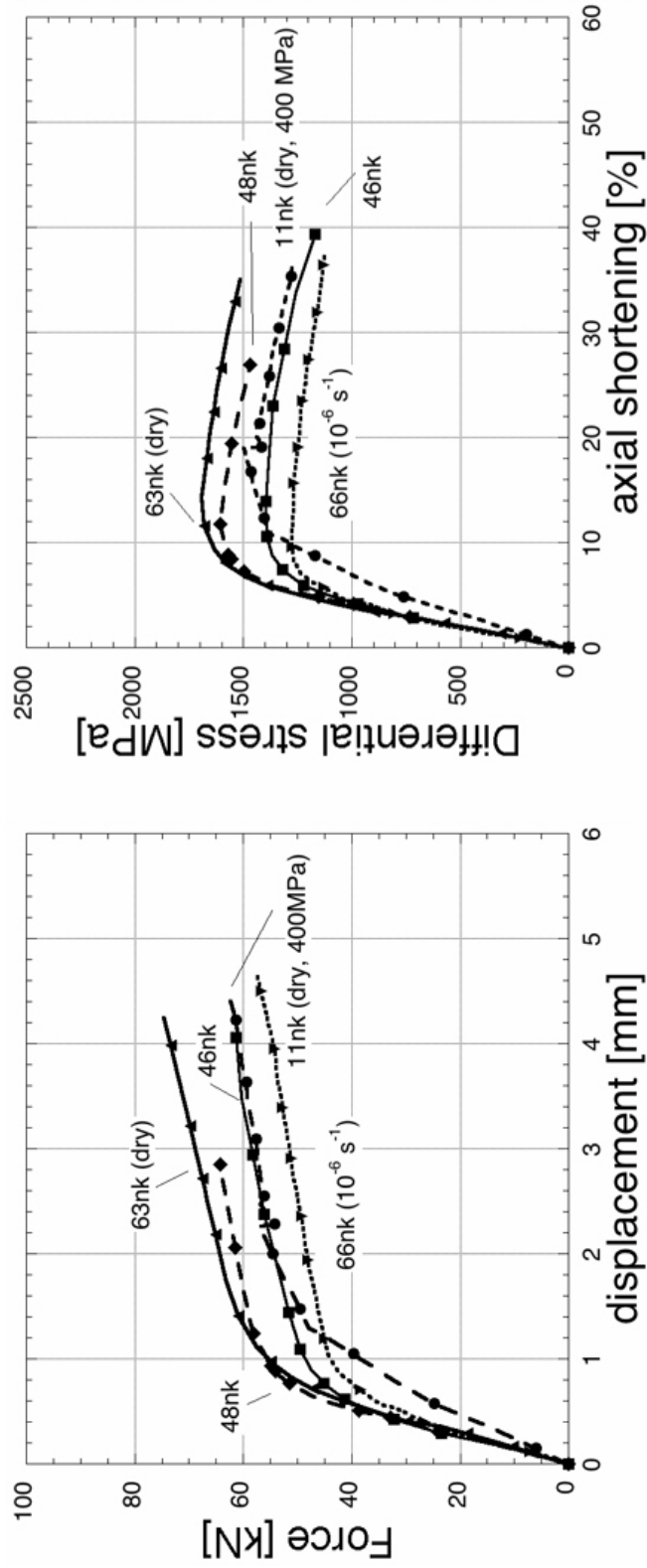


Figure B.2: Force-displacement and stress-shortening diagrams for deformation experiments on Verzasca Gneiss. All experiments were performed at $T = 300\text{ }^{\circ}\text{C}$, $\dot{\epsilon} = 1 \times 10^{-4}\text{ s}^{-1}$, $P_c = 500\text{ MPa}$. One experiment was performed with a lower shortening rate, one with a lower confining pressure and two experiments without H_2O (dry) added to the sample. Exceptions indicated in brackets.

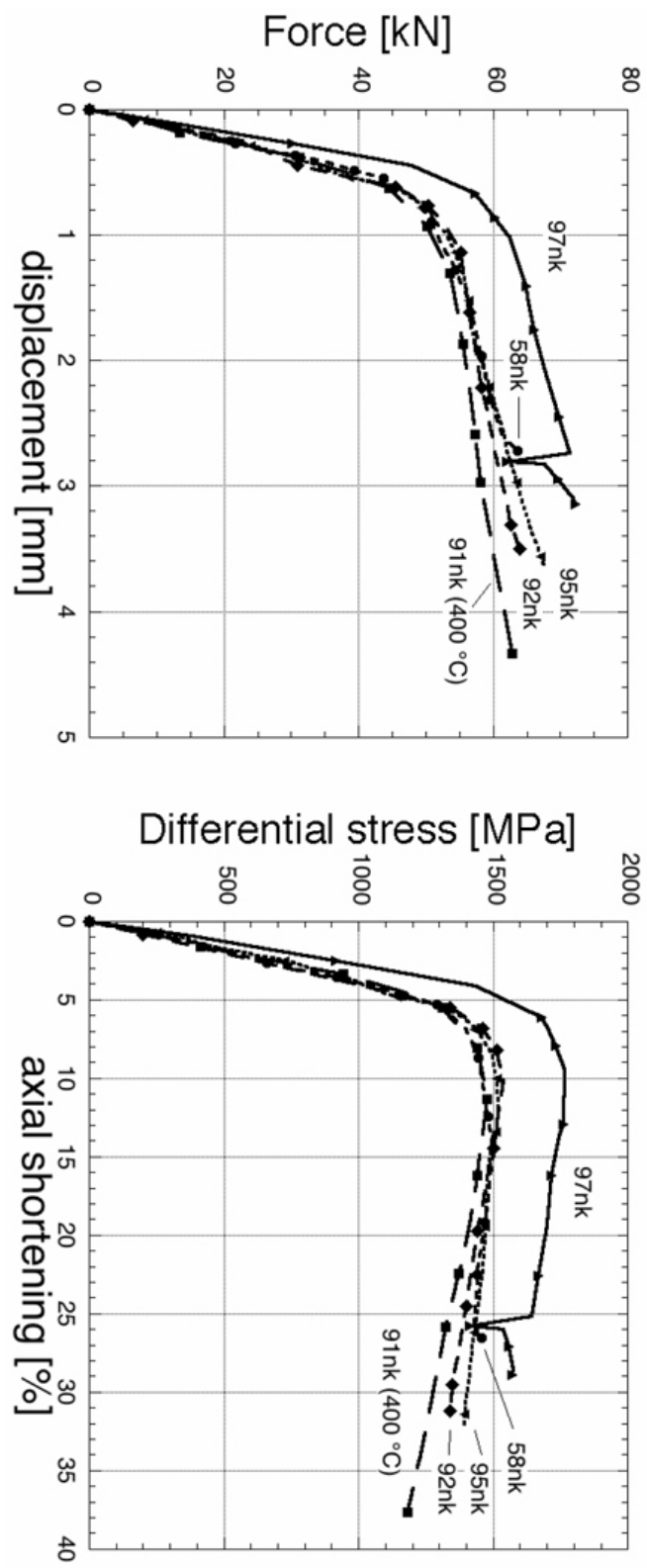


Figure B.3: Force-displacement and stress-shortening diagrams for deformation experiments on Verzasca Gneiss. All shown experiments display deformation at $T = 300\text{ }^{\circ}\text{C}$, $\dot{\epsilon} = 1 \times 10^{-4}\text{ s}^{-1}$, $P_c = 500\text{ MPa}$. One experiment was performed at $T = 400\text{ }^{\circ}\text{C}$, indicated in brackets.

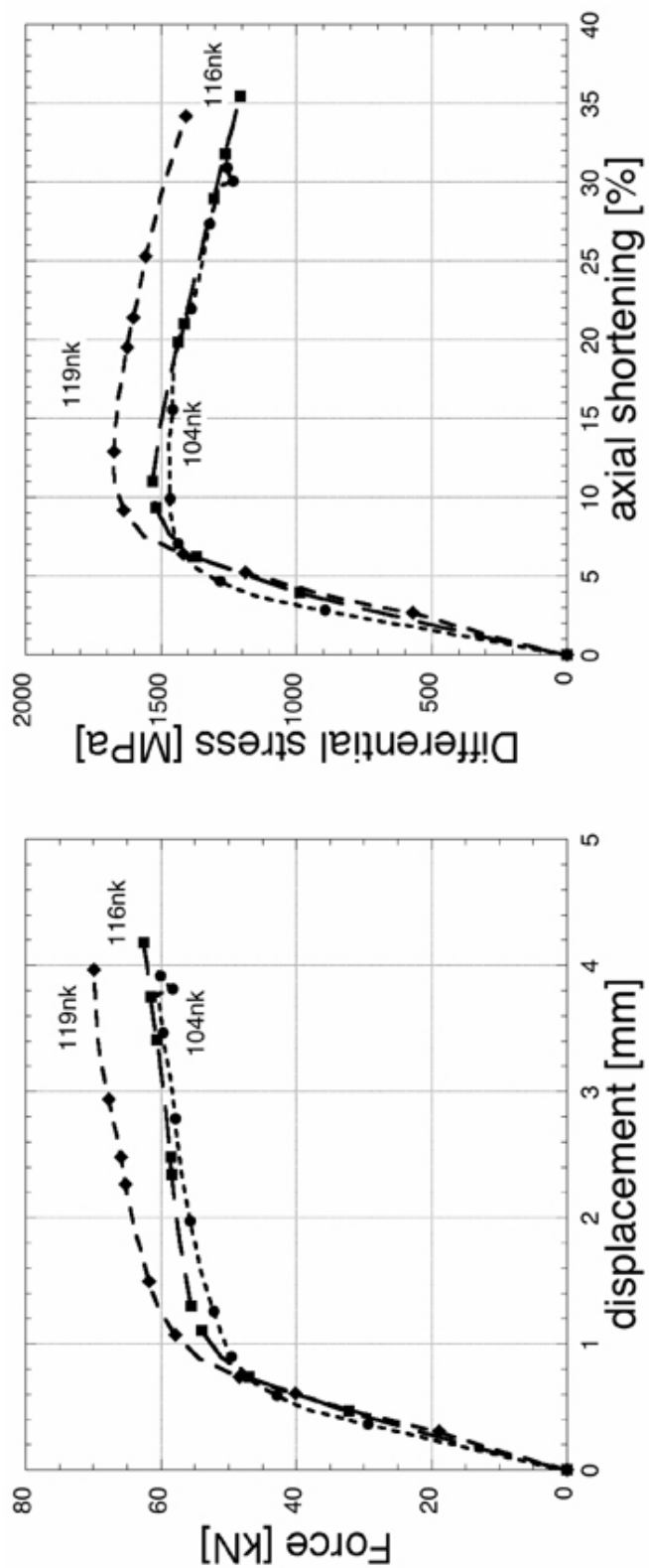


Figure B.4: Force-displacement and stress-shortening diagrams for deformation experiments on Verzasca Gneiss. All deformation experiments conducted at $T = 300\text{ }^{\circ}\text{C}$, $P_c = 500\text{ MPa}$ and $\dot{\epsilon} = 1 \times 10^{-4}\text{ s}^{-1}$.

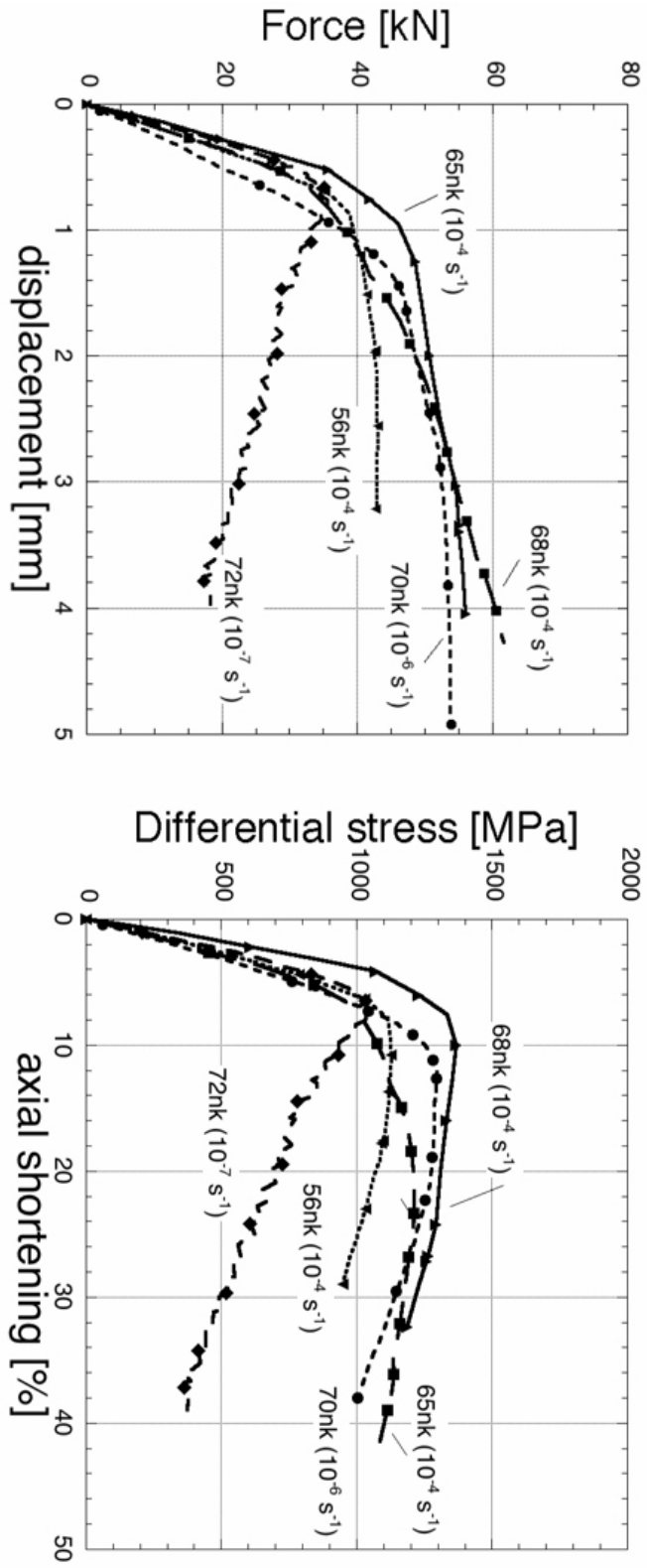


Figure B.5: Force-displacement and stress-shortening diagrams for deformation experiments on Verzasca Gneiss. All experiments were performed at $T = 500 \text{ }^\circ\text{C}$ and $P_c = 500 \text{ MPa}$. Two experiments were deformed at a lower shortening rate: $\dot{\epsilon} = 1 \times 10^{-6} \text{ s}^{-1}$ and 10^{-7} s^{-1} , indicated in brackets.

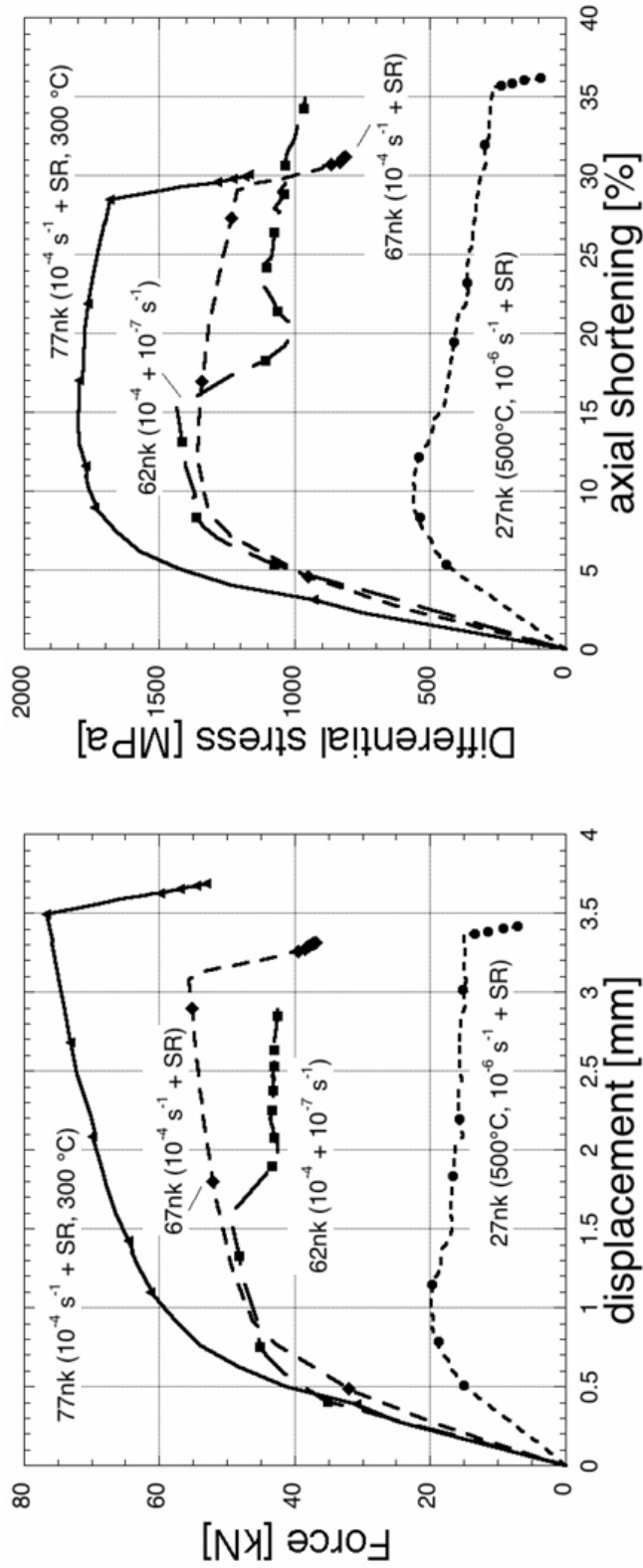


Figure B.6: Force-displacement and stress-shortening diagrams for deformation experiments on Verzasca Gneiss at $T = 300^\circ\text{C}$ followed by non-hydrostatic healing (SR) or deformation at a very low shortening rate $\dot{\epsilon} = 1 \times 10^{-7} \text{ s}^{-1}$ at $T = 500^\circ\text{C}$. All experiments were performed at $P_c = 500 \text{ MPa}$. Precise conditions during deformation and healing in brackets and in Appendix A

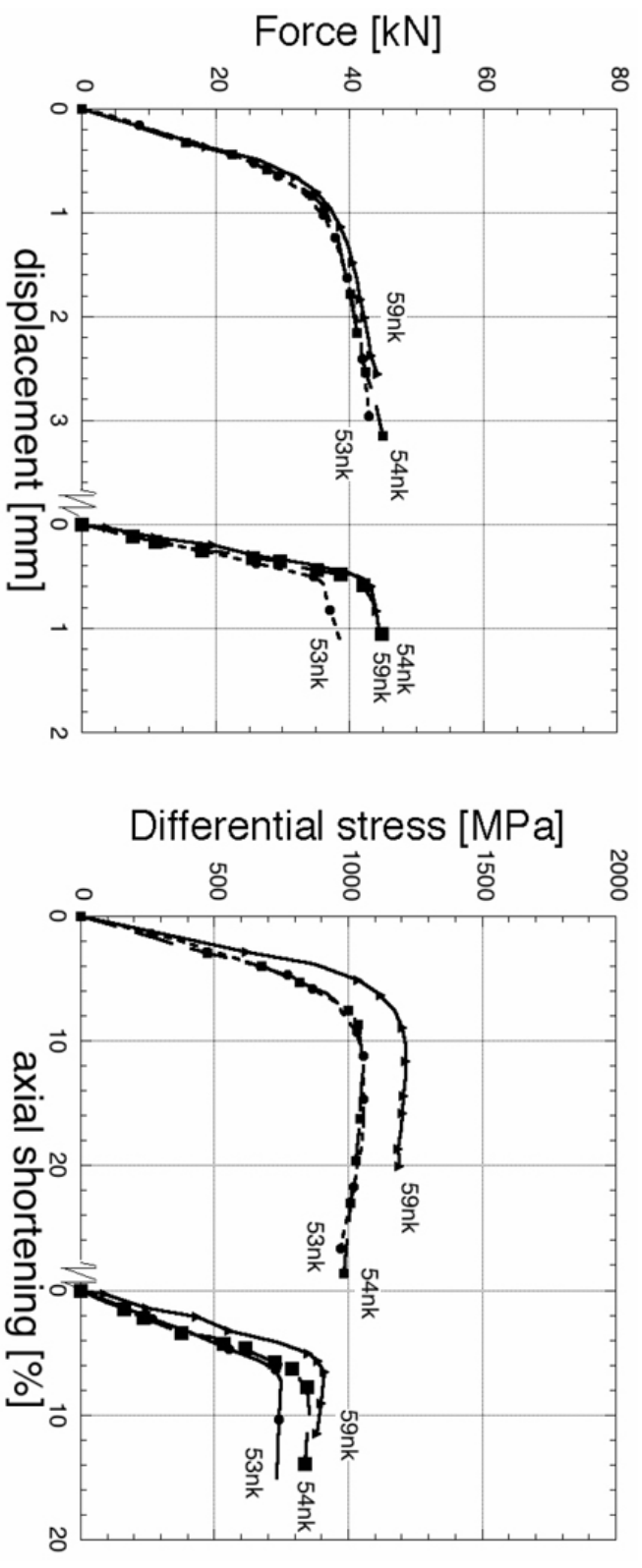


Figure B.7: Force-displacement and stress-shortening diagrams for repeated deformation on samples of Verzasca Gneiss. Deformation of all samples at $T = 500\text{ }^{\circ}\text{C}$ and $P_c = 500\text{ MPa}$. Between the first and second deformation samples were at hydrostatic conditions during 14 days (53nk, 54nk) or 11 minutes (59nk).

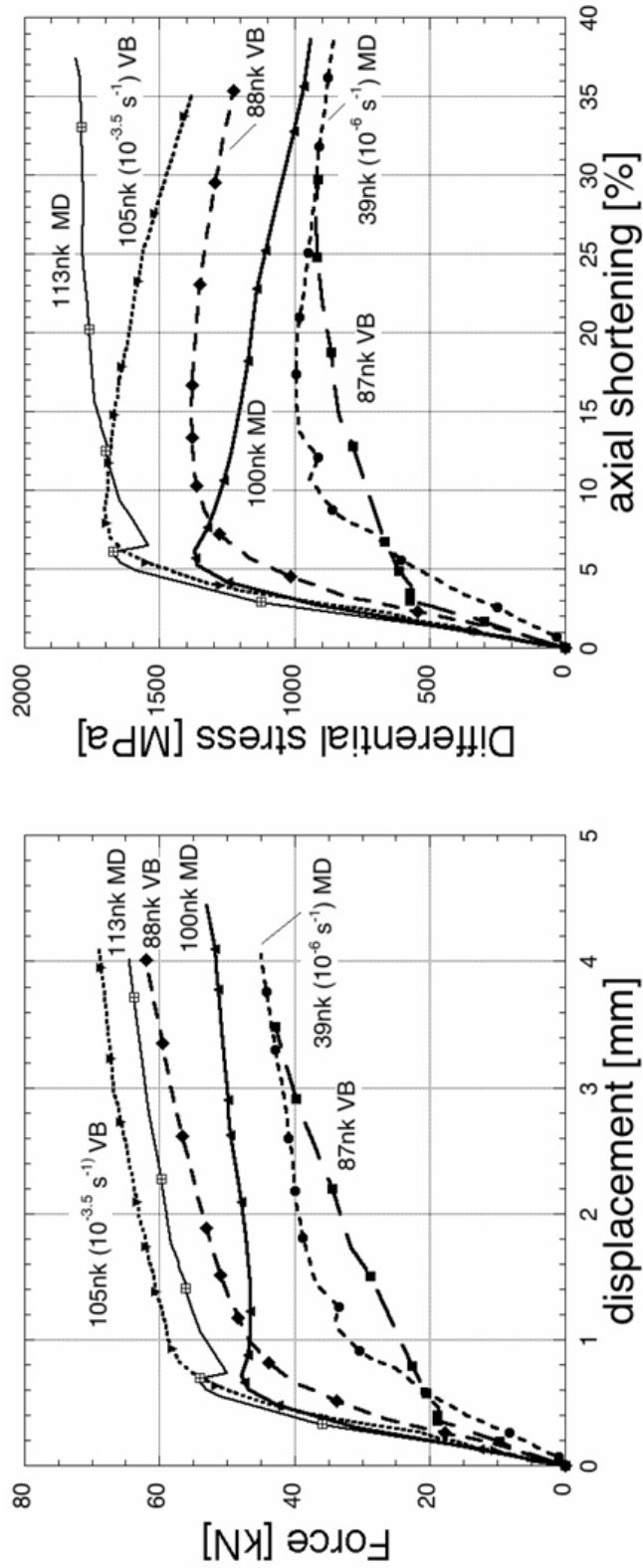


Figure B.8: Force-displacement and stress-shortening diagrams for deformation experiments on Vogelsberg Basalt (VB), Bransrode Basalt (BB) and Maryland Diabase (MD). All experiments show deformation at $T = 300 \text{ }^\circ\text{C}$, $P_c = 500 \text{ MPa}$ and $\dot{\epsilon} = 1 \times 10^{-4} \text{ s}^{-1}$, with two exceptions for the shortening rate. Details are indicated in brackets.

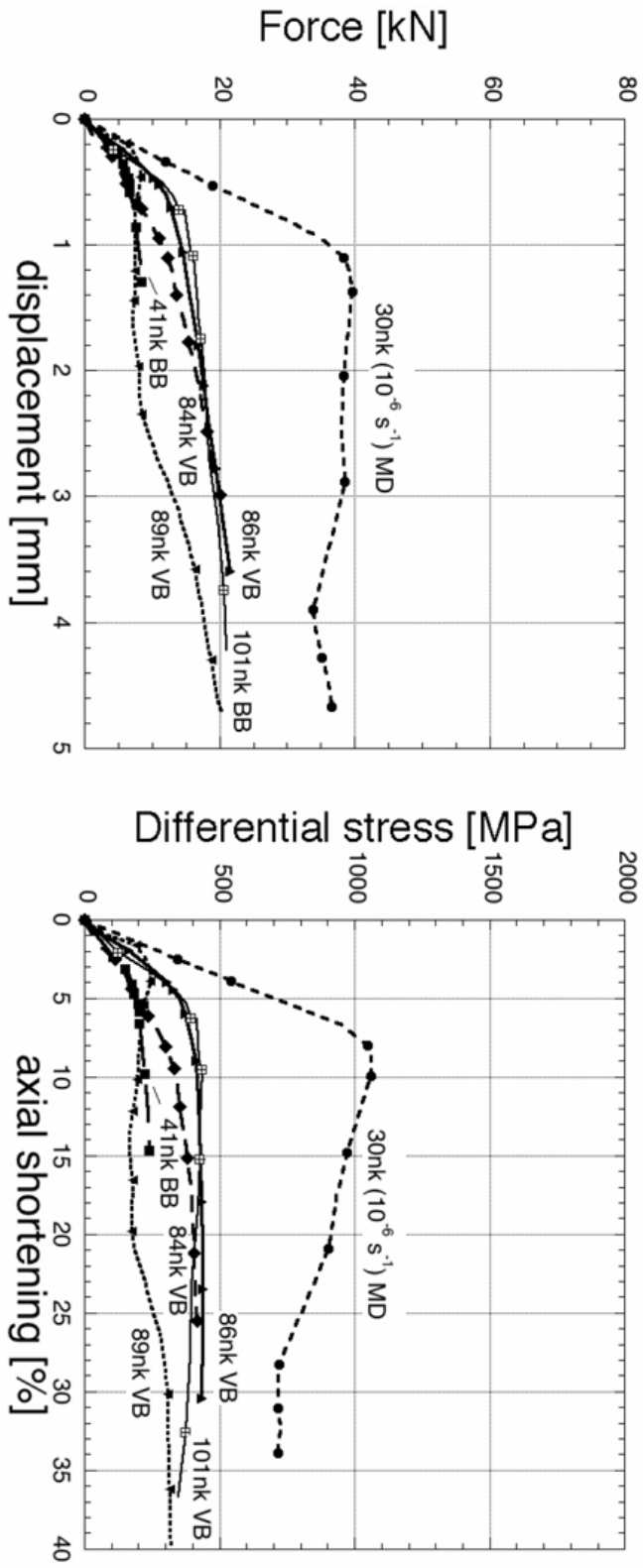


Figure B.9: Force-displacement and stress-shortening diagrams for deformation experiments on Vogelsberg Basalt (VB), Branströde Basalt (BB) and Maryland Diabase (MD). All samples have been deformed at $T = 500^\circ \text{C}$ and $P_c = 500 \text{ MPa}$. $\dot{\epsilon} = 1 \times 10^{-6} \text{ s}^{-1}$ (30nk and 41nk) or 10^{-4} s^{-1} for all other experiments. Details are indicated in brackets.

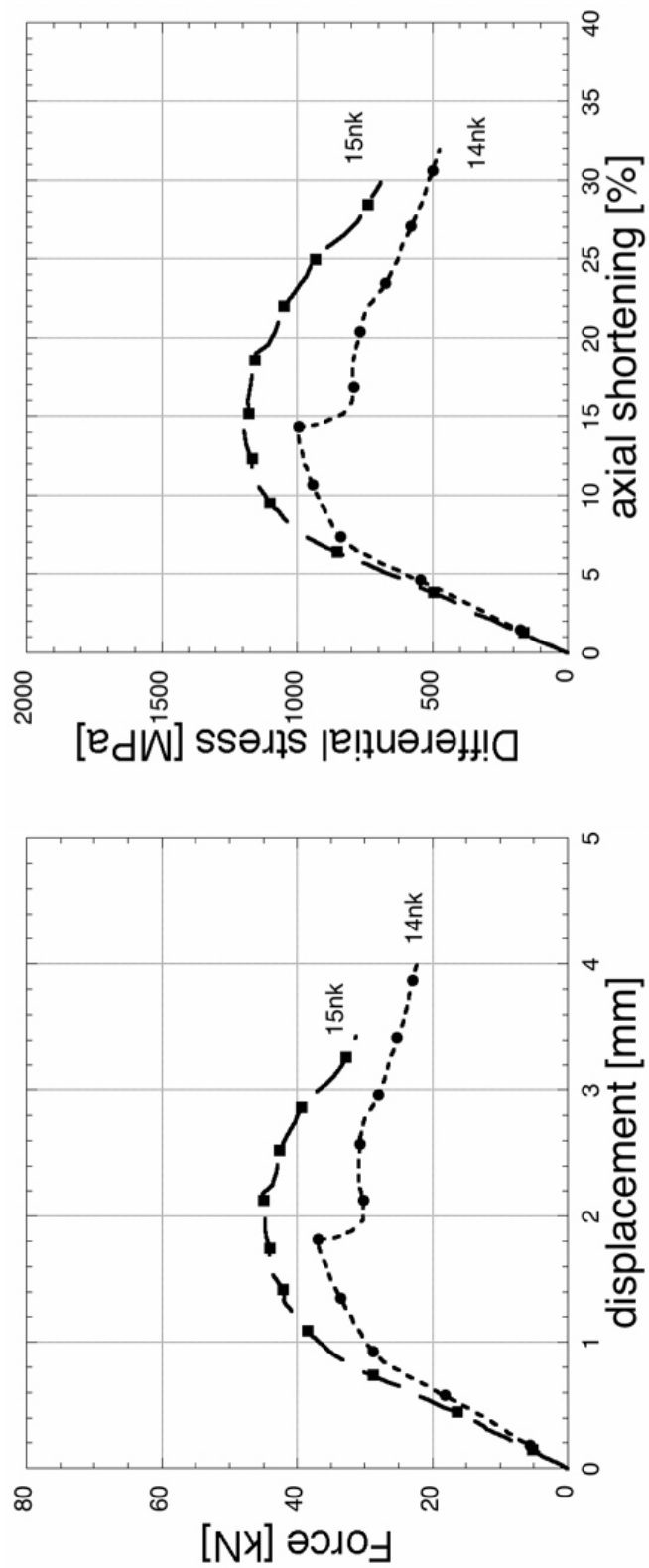


Figure B.10: Force-displacement and stress-shortening diagrams for deformation experiments on Maryland Diabase. Deformation at $T = 650\text{ }^{\circ}\text{C}$, $P_c = 800\text{ MPa}$ and $\dot{\epsilon} = 1 \times 10^{-5}\text{ s}^{-1}$.

Appendix C

Experiments on salt samples

To study the behavior of the sodium-chloride confining medium and to get a measure for the friction effects in the Griggs-type deformation apparatus, a series of ten salt sample deformation experiments has been performed.

C.1 Preparation of the salt samples

To be able to study the behavior of the sodium-chloride confining medium during an experiment, the samples were prepared in the same way as the confining medium. 0.8 grams of sodium chloride were ground to powder and pressed with one drop of water under 2 tons, using the set-up shown in Figure C.1 to create a sample of ca. 10 mm length. In this way the salt sample was formed under the same stress and with the same amount of water present during the pressing as the inner and outer salt liners.

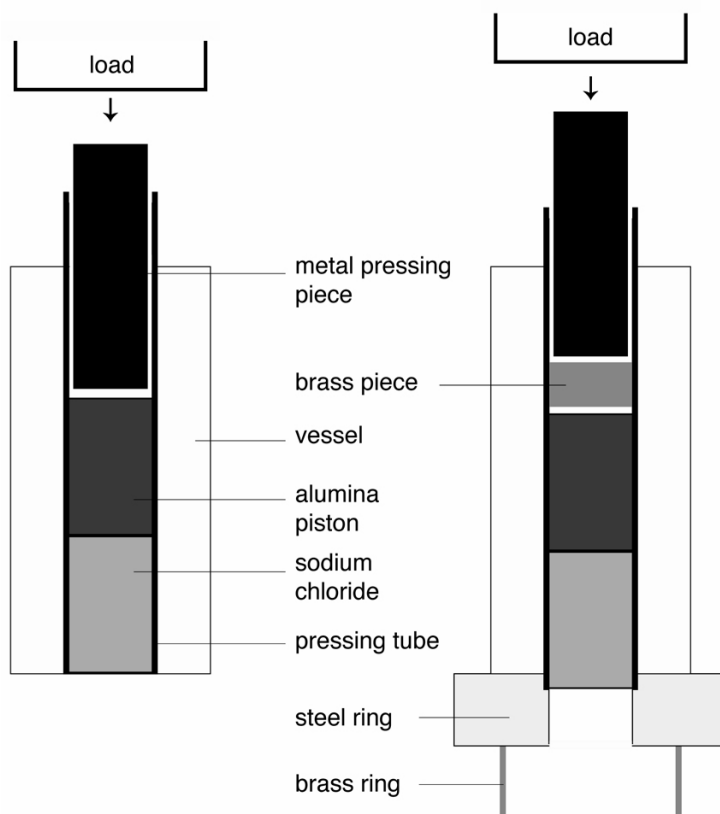


Figure C.1: Set-up for the creation of salt samples. Sketch on the left shows the pressing, on the right the set-up to press the salt out of the vessel again. Vertical dimensions not to scale.

The salt samples are pressed in the same vessel, which is used to make inner salt liners. Their diameter is determined by the inner diameter of the piston salt pieces pressing tube. The salt and water are filled into the pressing tube and pressed with an alumina piston (zirconia will break) and a 6 mm diameter metal pressing piece. To remove the salt from the vessel a brass piece is put between the pressing piece and the piston to dampen the applied load when pressing the salt out. Friction inside the vessel, stress relaxation cracking, too much water and a hard landing are the most likely causes for damage of the salt piece.

sample	temperature °C	ax. $\dot{\epsilon}$ $\times 10^{-4} s^{-1}$	rig	length ₀ mm	Δ length mm	slope N/mm	peak stress MPa
test11	300	1.3	2	10.3	7.3	8.7×10^2 ^a	122
test12	300	1.3	2	12.52	7.6	8.2×10^2	159
test12A			2	11.6	9.6		
test13	300	1.3	1	12.5	10.42	8.2×10^2	191
test14	500	1.3	2	11.74	11.7	6.2×10^2 ^a	
test15	500	1.3	2	11.52	1.73	6.8×10^2	11.0
test16	300	0.013	2	11.99	2.71	4.9×10^3 ^a	17.7
test17	500	1.3	2	11.49	1.01		17 ^a
test18			2	11.59	10.1		
test19	300	0.013	2	11.3	2.44	9.4×10^2	14.5

Table C.1: Overview of the experiments performed on wet-pressed NaCl samples. All experiments were performed at 500 MPa. ax. $\dot{\epsilon}$ = axial shortening rate, rig = the number of the deformation apparatus, slope = steepness of the run-in curve before the hit-point, length₀ = initial length, Δ length = measured change in length.

^a estimated value

C.2 Salt experiments

To study the behaviour of the sodium-chloride confining medium and to get a measure for the friction effects in the Griggs-type deformation apparatus, a series of ten salt sample deformation experiments has been performed. Table C.1 gives an overview of all experiments.

Rheology of the salt samples and implications for the deformation of other sample material.

Test12A and test18 are salt sample experiments in which the sample was retrieved from the deformation apparatus before the actual deformation of the sample was initiated. Test 12A was pumped to $P_c = 100$ MPa, without heating of the sample; test18 was pumped to $P_c = 100$ MPa and heated to $T = 232$ °C. Both samples show significant shortening (2.0 mm in test12A, 1.5 mm in test18).

Indications that at low PT-conditions the salt liners do not act as a confining medium are derived from experiments carried out in Griggs type solid medium apparatuses in Basel and at the ETH, Zurich: (1) Vernooij (2005) has demonstrated that a sample (single crystal quartz), which has been brought hydrostatically to $P_c = 1200$ MPa and $T = 800$ °C during 9 hours, with two intermediate equilibration periods at $P_c = 100$ MPa and $T = 25$ °C during > 15 hours and at $P_c = 1150$ MPa and $T = 800$ °C during > 16 hours, shows partially healed longitudinal cracks

and newly formed small grains at the contact to the pistons. (2) A. Tarantola has performed an experiment (118AT) with a single crystal quartz, at $P_c = 100$ MPa and $T = 275^\circ\text{C}$ that has remained at these conditions for 10 minutes. After deformation an initially 2 mm thick salt disc between the upper alumina pistons is shortened to 1.2 mm. The outer salt liners in this experiment appear undeformed and are only recrystallized within the first 0.5 mm adjacent to the furnace. The lead piece used in this experiment shows some deformation. After deformation, the sample showed vertical radial cracks.

These experiments indicate that below approximately $P_c = 100$ MPa, at temperatures of 200 to 250°C the outer salt liners are not recrystallized and do not fully confine the sample. Lowering the σ_3 -piston to build-up the confining pressure below these conditions effectively exerts a force on the sample through the rigid lead piece in the σ_1 -direction. The experimental procedure may be improved by initially pumping to $P_c = 50 - 100$ MPa, increasing the temperature to $T = 250^\circ\text{C}$ and then waiting at these conditions for some time before continuing with the pumping or the heating of the samples.

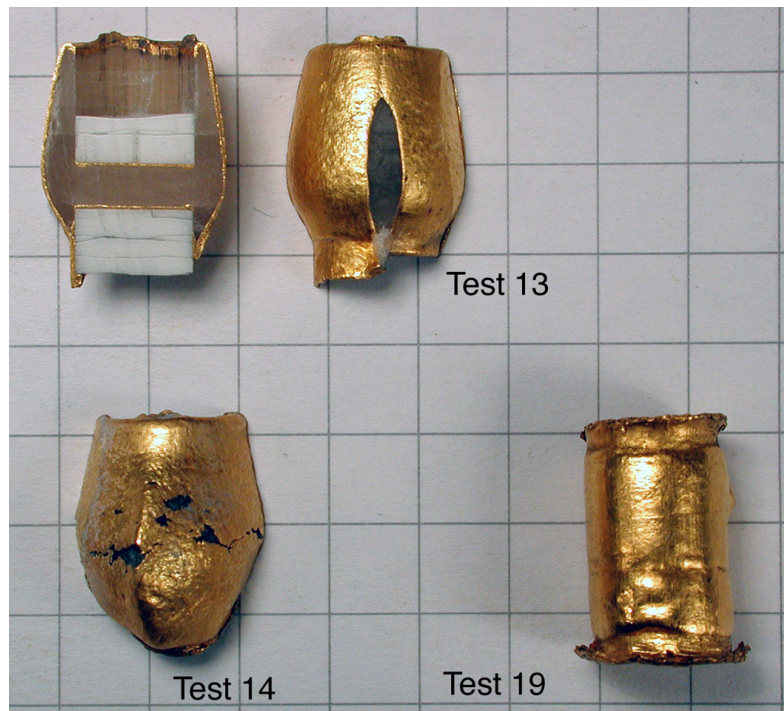


Figure C.2: Examples of salt samples in gold jacket after deformation. Parts of zirconia pistons are visible as white in-transparent material in the cross-sectional view of test 13. Equi-distance of lines in background is 5 mm.

The salt samples that have been deformed (Table C.1) show extrusion of the salt and tearing of the gold jacket (Fig. C.2). Granite and basalt samples do not usually show tearing of the

jacket, except for very large displacements (> 5 mm) on a single fault plane. The extrusion of the salt has led to a strong increase in confining pressure during the deformation, which was not observed for stronger samples. Salt samples deformed with less finite displacement usually show barrelling of the samples (e.g. test19 in Figure C.2).

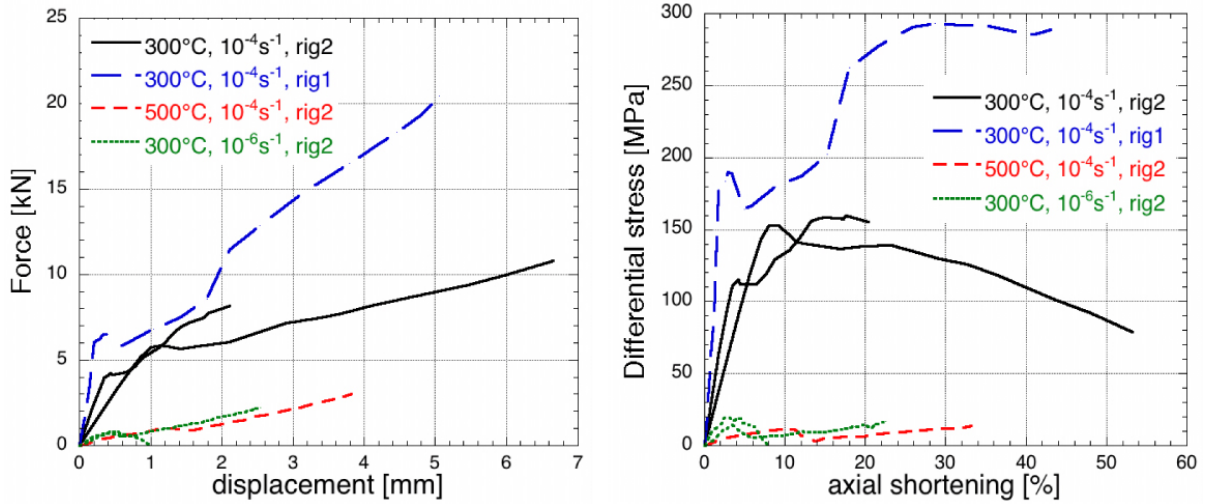


Figure C.3: Force-displacement and stress-strain plots for experiments on NaCl samples.

The mechanical data for these experiments are shown in Figure C.3. The chart records show a very irregular behaviour. After 0.3 – 1.2 mm displacement (2 – 11 % axial shortening) a peak in the strength is reached, followed by a decrease in strength. Further loading of the sample leads to a strengthening or a weakening of the samples, no systematic correlation can be observed with changing deformation conditions, neither is the data reproducible for experiments performed under the same conditions. For most samples a second peak stress is observed after 15 – 30 % axial shortening. This second peak may correlate to the tearing of the gold jacket. Some of the salt samples were shortened so much that the σ_1 -piston intruded the upper copper disc. In these samples, this might have caused an increase in strength due to increased friction, but second peaks have been observed in samples where the piston did not touch the copper disc as well.

The peak stress of the salt (first peak in the curves) is indicated in Table C.1 and ranges from approximately 150 MPa for deformation at $T = 300^\circ\text{C}$, $1.3 \times 10^{-4} \text{ s}^{-1}$ and ca. 15 MPa for a temperature increase to 500°C or a shortening rate decrease to $1 \times 10^{-6} \text{ s}^{-1}$. Mafic or granitoid samples, deformed at $T = 300^\circ\text{C}$, $\dot{\epsilon} = 1.3 \times 10^{-4} \text{ s}^{-1}$ have a peak strength of ca. 1500 MPa. Thus, in $T = 300^\circ\text{C}$ experiments 10% of the sample strength may be attributed to the relatively rigid salt confining medium, for all other experiments it is 1–2% of the sample strength, although axial shortening of salt samples might not be directly comparable to the radial force effected by salt confining a sample.

The observed peak stress values for the deformation of the salt samples are ca. 140 MPa higher for the samples deformed at $T = 300\text{ }^\circ\text{C}$, $\dot{\epsilon} = 1.3 \times 10^{-4}\text{ s}^{-1}$ and ca. 10 MPa higher for the salt samples deformed at $500\text{ }^\circ\text{C}$ or with a shortening rate of $1 \times 10^{-6}\text{ s}^{-1}$, than those observed for the deformation of wet polycrystalline halite (for a comparison of data from this study to work performed by Ter Heege et al. (2005) see Figure C.4). Extrapolating from the data of Ter Heege and coworkers, the peak stress of salt is $\approx 4\text{ MPa}$ for deformation at $T = 300\text{ }^\circ\text{C}$, $\dot{\epsilon} = 10^{-6}$, and $\approx 8\text{ MPa}$ at $\dot{\epsilon} = 10^{-4}\text{ s}^{-1}$; deformation at $T = 500\text{ }^\circ\text{C}$, $\dot{\epsilon} = 10^{-4}\text{ s}^{-1}$ yields $\approx 6\text{ MPa}$. The additional stress applied to deform the salt samples is necessary to overcome the friction of the deformation apparatus and the sample assembly, to deform the gold jacket and nickel foil around the sample and to push aside the furnace.

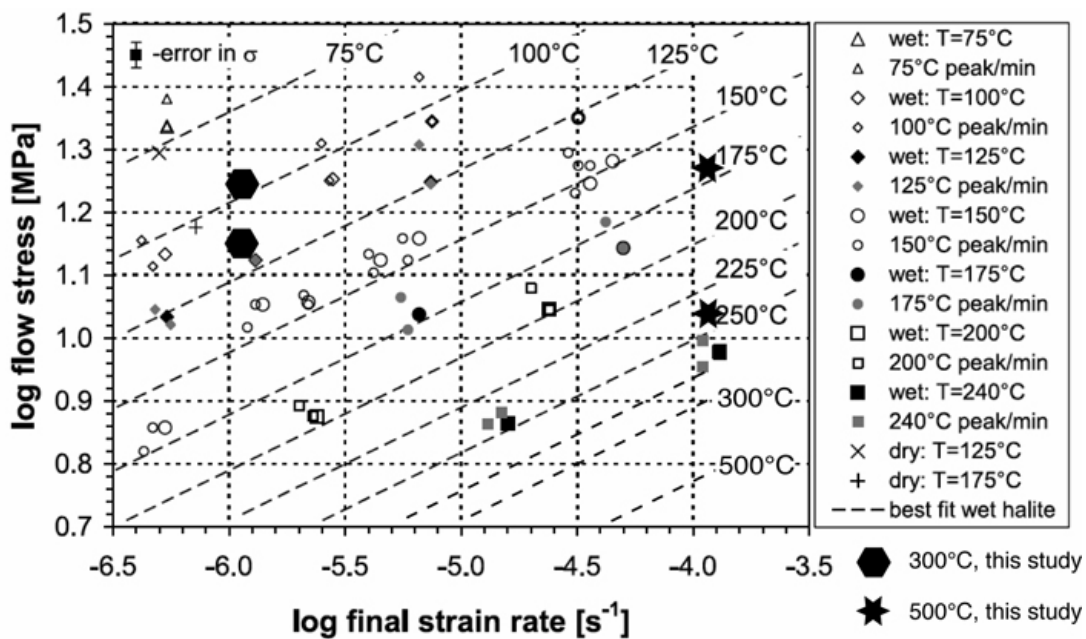


Figure C.4: Peak strength of the samples plotted against their strain rate in a flow stress diagram for wet polycrystalline halite, altered after Ter Heege et al. (2005). Samples deformed at $T = 300\text{ }^\circ\text{C}$, $1.3 \times 10^{-4}\text{ s}^{-1}$ plot outside the diagram.

Deformation at $T = 300\text{ }^\circ\text{C}$, $\dot{\epsilon} = 1 \times 10^{-4}\text{ s}^{-1}$, $P_c = 500\text{ MPa}$ might therefore be the lower limit to obtain reasonable mechanical results for deformation in the Griggs-type solid medium deformation apparatus. For samples deformed at these conditions some correction of the data for the strength of the salt may be necessary. However, no correction is applied to the data of granite and basalt samples, since the scatter in the data of the salt samples is too large. It is not possible to subtract the force-curve for salt deformation under certain conditions from the curve for a silicate rock sample, because of the poor reproducibility of the data.

Samples were cut into two halves; one of the cut samples (test 11) was polished with oil and

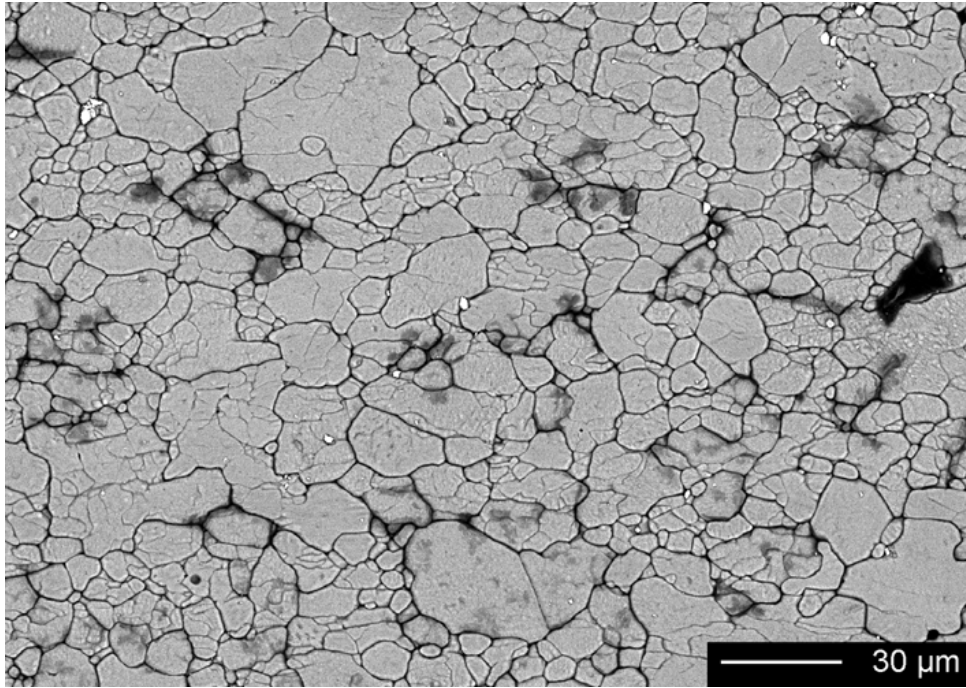


Figure C.5: Backscatter-contrast scanning electron microscope image of test11 after deformation. σ_1 -orientation is vertical.

studied with back-scatter contrast electron scanning electron microscopy (Fig. C.5). The sample shows no evidence for cataclasis of the salt. The grain size ranges over one order of magnitude (ca. 5 – 50 μm), the grains have straight to gently curved grain boundaries with locally some serration. Inside the larger grains, structures are seen that are either sub-grains or remnants of the original crushed salts. The grains are flattened with respect to the principal stress. These observations depict either crystal plastic or pressure-solution creep dependent deformation mechanism for this salt sample.

C.3 Correction of the mechanical data for friction

It has been suggested to correct for the friction (the proportion of shear stress to normal stress, dimensionless) inside the assembly and the Griggs-type deformation apparatus by linear extrapolation of the run-in curve of the experiments (Den Brok, 1992; Rybacki et al., 1998) beyond the hit-point and to subtract this curve from the force data recorded for the experiment (see Figure 2.4 for an explanation of the run-in curve and the hit-point). It is assumed that the friction increases linearly during a deformation experiment and has a unit expressed in Newton. In the case of weak samples, this may lead to a negative strength of the samples (Vernooij, 2005).

However, the run-in curve of an experiment describes a complex interplay of several features.

During the run-in before the hit-point the lead is compressed and squeezed out between the σ_1 -piston and the upper alumina piston. The gold-ends around the sample are shortened as well. Furthermore, there is friction inside the apparatus and in the sample assembly due to the movement of the σ_1 -piston. Therefore, the run-in curve describes a combination of dislocation creep of lead and gold together with an additional friction term. The slope of the run-in curve depends on the deformation conditions (Figure C.6), as was obtained from the run-in curve of the salt samples. For deformation at $T = 300^\circ\text{C}$, $\dot{\epsilon} = 1 \times 10^{-4} \text{ s}^{-1}$ this slope is $8.2 \times 10^2 \text{ N}$ for each mm displacement of the piston. Decreasing the axial shortening rate increase this value to $9.8 \times 10^2 \text{ N/mm}$; a temperature increase to $T = 500^\circ\text{C}$ decrease the value to $6.8 \times 10^2 \text{ N/mm}$.

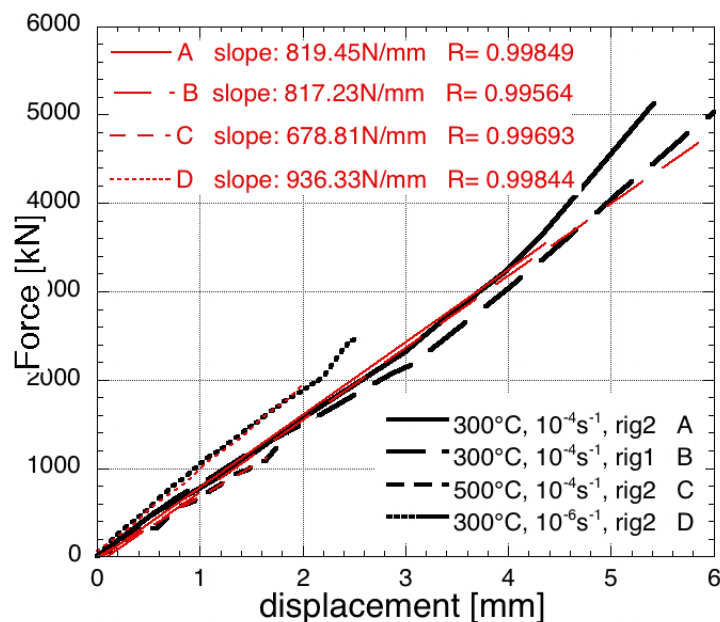


Figure C.6: Force-displacement record of the of the run-in curve before the hit-point (black) with best-fit curves (red). Steepness of the slope is indicated for test12, test13, test15, and test19, respectively.

Other ways to correct for the frictional stress in the sample assembly and in the deformation apparatus are described by Stipp and Tullis (2003): (1) performing of an additional run-in and hit of the samples after deformation (Gleason and Tullis, 1995) or (2) measuring the strength of salt samples and subtracting these data from data for the studied rock specimens. The second method was tried and proven unsuccessful due to too large differences between the salt experiments performed under identical conditions, both for molten salt and for the salt samples in this study. Salt samples should not be used to correct for the frictional stress in the sample assembly in a quantitative way.

Appendix D

*Structural evolution of the Nojima fault
(Awaji Island, Japan) revisited from the
GSJ drill hole at Hirabayashi**

This Appendix provides information on the Nojima Fault Zone, as background for the fault gouge analyses performed in Chapters 4 and 5.

*Published as: A.-M. Boullier, K. Fujimoto, H. Ito, T. Ohtani, N. Keulen, O. Fabbri, D. Amitrano, M. Dubois, P. Pezard, (2004) Structural evolution of the Nojima fault (Awaji Island, Japan) revisited from the GSJ drill hole at Hirabayashi. *Earth Planets Space*, 56, 1233–1240.

Abstract

Following the Hyogoken Nanbu earthquake (January 17, 1995, Mw=7.2), three drillholes were sunk through the Nojima Fault (Awaji Island, Japan). Textural and petrographic studies of the Geological Survey of Japan (GSJ) drill cores allow recognition of two deformation episodes. The first one is older than the deposition of the Middle to Late Eocene Kobe Group, corresponds to a left-lateral movement on the Nojima fault and is expressed by pseudotachylytes, kinking of biotite crystals in the low-strain rocks and an intensive laumontite hydrothermal alteration. The second one displaces the basal unconformity of the Kobe group, corresponds to a right-lateral reverse displacement and is expressed at least by carbonate-filled hydraulic fractures and thin gouge zones. Different important deformation mechanisms are recorded by the fault rocks, but questions relating to the attribution of deformation and alteration features to one or other deformation episodes remain unresolved.

D.1 Introduction

The Nojima fault (Awaji Island, Japan) has been extensively studied after the Hyogo-ken Nanbu earthquake (January 17, 1995, Mw=7.2). Three drill holes (drilled by GSJ, NIED and University group) have encountered the fault at different depths and have allowed structural observations of the fault imprint on the surrounding rocks. This paper summarizes the results of a textural and petrographic study of the drill cores from the GSJ borehole, and points out the different important mechanisms recorded by the fault rocks and some unresolved questions.

D.2 The Geodynamic Context of the Nojima Fault

The Nojima fault has a N45°E orientation and a subvertical dip (85°SE). Left-lateral transcurrent faults with identical N45°E orientation were formed in southwest Japan during the Late Cretaceous-Palaeocene (Kanaori, 1990) and are interpreted to belong to a fault network defining a regional block structure. Reactivation of these faults occurred in pre-5 Ma times (left-lateral) and in Late Pliocene to Quaternary times (right-lateral) (Fig. D.1; Fabbri et al., 2004).

On the Awaji Island (Fig. D.2), the Nojima fault cross-cuts the Cretaceous Nojima granodiorite (K-Ar ages on minerals ranging from 70 to 90 Ma, Takahashi, 1992; cooling age at 74 ± 3 Ma by zircon fission track method, Murakami and Tagami, 2004) and its porphyry dykes. The granodiorite is unconformably overlain by the Kobe Group, the base of which has been dated at Middle to Late Eocene (Yamamoto et al., 2000), and by the Plio-Pleistocene Osaka Group (Mu-

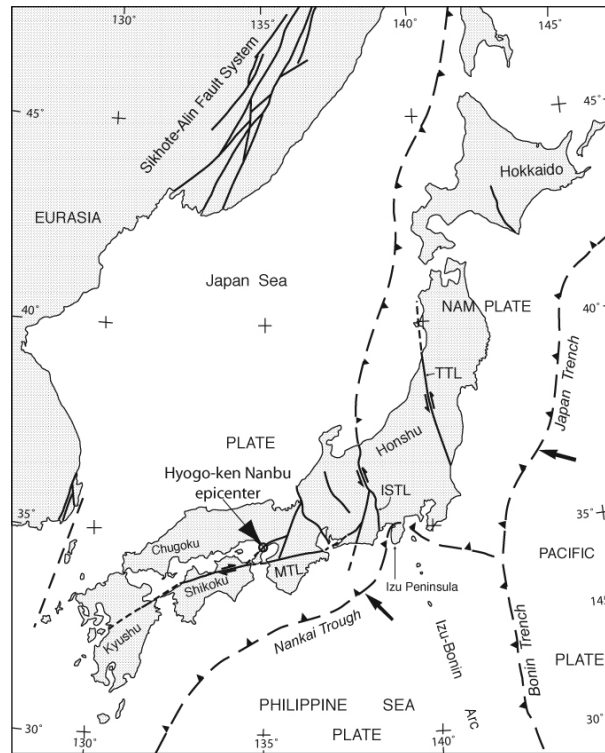


Figure D.1: Tectonic framework of Japan with localization of the Hyogo-ken Nanbu earthquake epicenter on the Nojima fault.

rata et al., 2001). The Quaternary vertical offset is 490 to 540 m as determined by the vertical displacement of the Kobe Group basal unconformity (Murata et al., 2001). The corresponding average slip rate (0.4–0.5 m/10³ years down-dip and 0.9–1.0 m/10³ years right-lateral) of the Nojima fault has been estimated by Mizuno et al. (1990).

Studies of deformation and alteration textures indicate that the fault damage zone is >46.5 m wide and the fault core itself is 30 cm wide (Ohtani et al., 2000, 2001; Tanaka et al., 2001; Fujimoto et al., 2001). However, if the Nojima fault has followed the same two-stage evolution of the N45°E fault system, the present-day thickness of the fault is the result of deformation accumulated over its whole history and it is important to understand what are the deformation and alteration structures related to each episode. In order to decipher this two-stage history, it should be pointed out that deformation structures related to the recent activity of the fault could not have formed at a depth greater than the present-day depth of the sample within the drill hole plus the Quaternary 490–540 m vertical offset. Conversely, any structure formed at a depth greater than the present-day depth of the sample within the drill hole plus the Quaternary 490–540 m vertical offset should have been formed before the displacement of the Kobe Group basal unconformity.

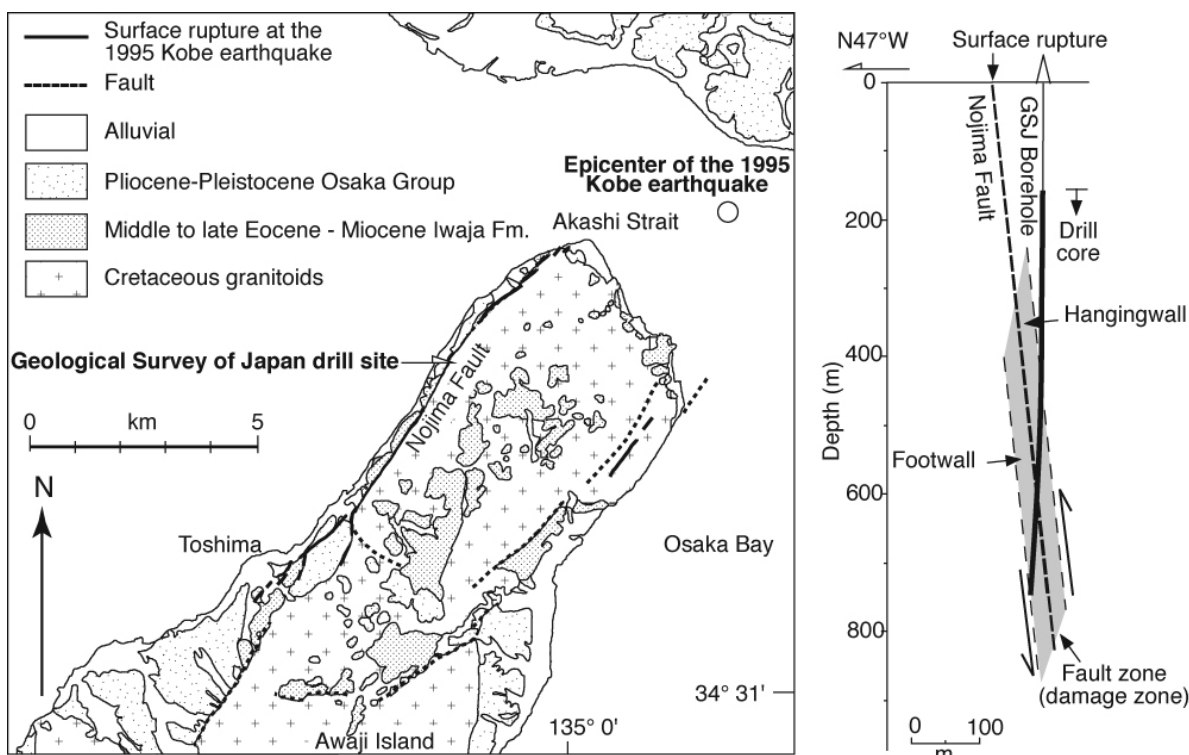


Figure D.2: Geological map of the Awaji Island and sketch of the Hirabayashi borehole showing the relative orientations of the fault and borehole (after Ohtani et al., 2000). The shaded pattern on the sketch represents the fault zone (i.e. damage zone).

D.3 Microstructural Studies of the Fault Rocks

D.3.1 Low strain rocks

Outside the fault zone, the granodiorite may appear as undeformed. However, careful observations indicate that some strain is recorded in these rocks. Two directions of horizontal shortening are observed in the Nojima granodiorite in the GSI borehole. They can be deduced from the orientation of fluid inclusion planes (mode I cracks), and kink-bands in quartz and biotite (Fig. D.3). Following Boullier et al. (2000), the first shortening event recorded by kinked cleavage planes in biotites (Fig. D.4) is NNW-SSE orientated and coincides with the principal orientation of fluid inclusion planes (Takeshita and Yagi, 2000), and with cracks sealed by albite and chlorite. Consequently, they probably appeared in greenschist facies conditions (around 300°C). Takeshita and Yagi (2000) suggest that this first shortening event, which is consistent with a left-lateral movement on the N45°E Nojima fault, occurred in Late Cretaceous times (around 85 Ma) just after the solidification of the granodiorite.

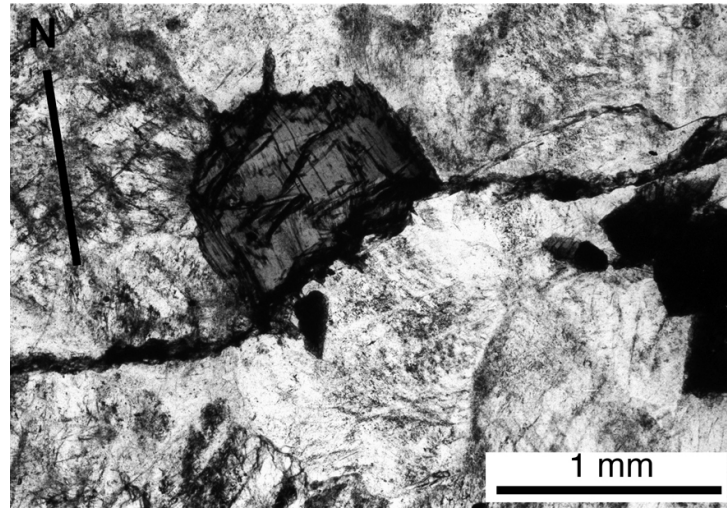


Figure D.3: Microphotograph of shortened cleavages in biotite in an oriented horizontal thin section at 352 m depth. North is indicated by the thick black line. Note also the black trace of a fracture acting as a dissolution or stylolite-like plane.

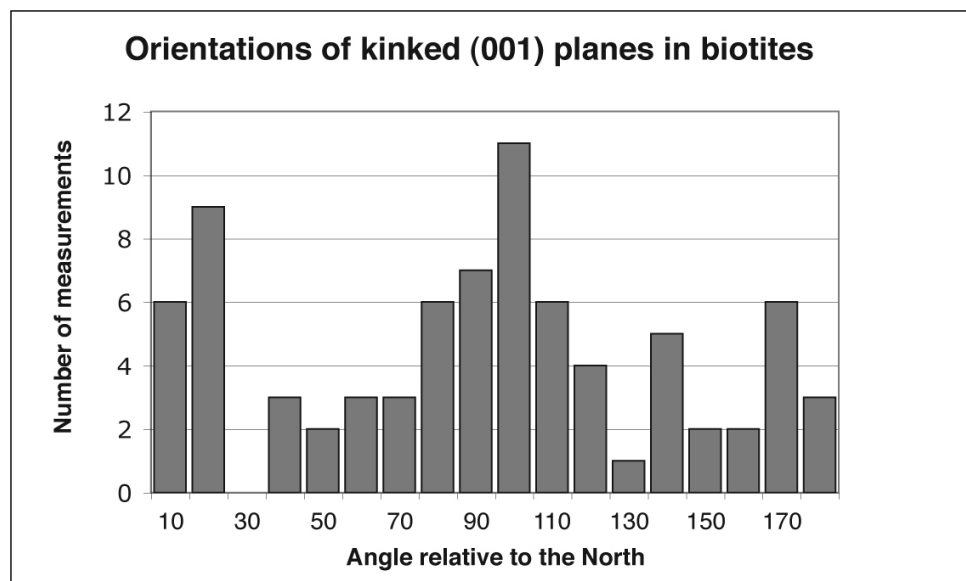


Figure D.4: Histogram of the orientation of shortened biotite cleavage planes relative to the North in the thin section shown in Fig. D.3 at 352 m depth. Two maxima are observed at N15E and N100E respectively.

D.3.2 Pseudotachylytes

Pseudotachylytes are observed in the fault core (Ohtani et al., 2000, 2001; Tanaka et al., 2001; Boullier et al., 2001; Otsuki et al., 2003). They are closely related to some fine-grained fault gouges (Otsuki et al., 2003), which are characterized by an isotropic or homogeneous texture without any strain localization (no shear plane), and have experienced fluidization (Otsuki et al., 2003).

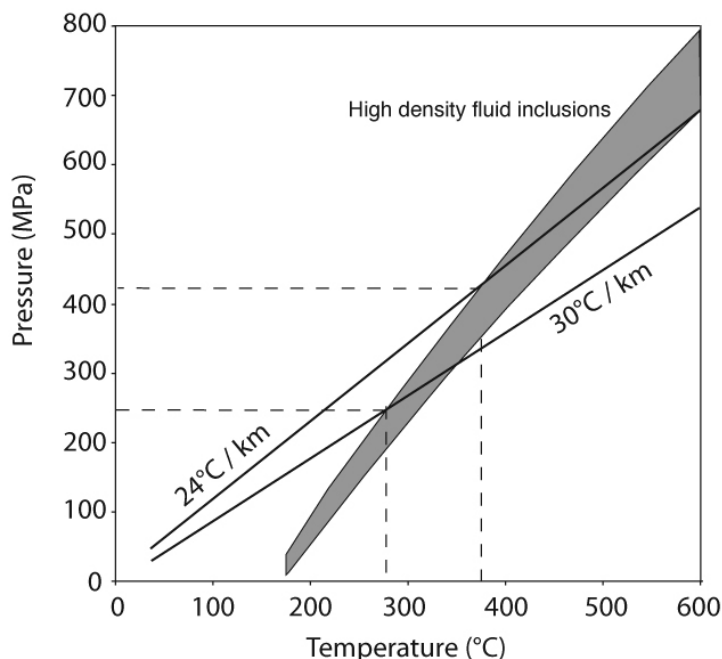


Figure D.5: Isochoric lines calculated from the microthermometric data on fluid inclusions in pseudotachylytes, after Boullier et al. (2001).

Boullier et al. (2001) described fluid inclusions within pseudotachylytic glass in the fault core at 624.59 m in the GSJ drill hole. The fluid inclusions are filled with a high density $\text{H}_2\text{O}+\text{CO}_2$ fluid. Isochoric lines calculated from these fluid inclusions (Fig. D.5) indicate that they were formed at a minimum depth of 15 km for a $24^\circ\text{C}/\text{km}$ geothermal gradient (Kitajima et al., 1998; Yamaguchi et al., 1999) or 10 km if a slightly higher $30^\circ\text{C}/\text{km}$ geothermal gradient is chosen. Consequently, the pseudotachylytes which contain these fluid inclusions and which originated by friction melting during earthquakes were interpreted to have formed in greenschist facies P-T conditions at depths greater than 10 km and temperatures higher than 280°C . Therefore, the pseudotachylytes and the associated fine-grained ultracataclasites cannot correspond to the Quaternary activity of the Nojima fault. These events have been interpreted to have occurred after the solidification of the granodiorite but before the deposition of the Kobe Group (Boullier et al., 2001), that is some time between 80 Ma and 40 Ma. Recent dating of pseudotachylyte at

Table D.1: Principal occurrences and features of the hydrothermal minerals in the GSJ drillhole.

Mineral	Chlorite	Zeolite: laumontite	Siderite	Carbonate
Stability field	ca. 300°C	ca. 150-280°C		less than 100°C
Texture	as rosettes in small cavities, in cracks with albite	in veins, blocky coarse-grained filling, in hydraulic fractures, with small fragments of cataclasites or minerals	in thin veinlets parallel to the flattening plane within the fault core	calcite: blocky coarse-grained veins, with scarce analcite, in hydraulic fractures close to the fault core, with fragments of cataclasite or minerals (ankerite and siderite)
Alteration product	alteration of biotite and amphibole	in-situ replacement product of plagioclase		alteration product of plagioclase, biotite and amphibole
Mechanisms of formation		hydraulic fracturation	Taber growth	hydraulic fracturation
Subsequent deformation		dissolution processes: stylolites, brecciation in the fault zone	brecciation	dissolution processes: stylolites and schistosity, brecciation and comminution in thin fine-grained gouge zones
Suggested relative age	prior to the Kobe Group deposition	prior to the Kobe Group deposition	quiescence stage	Quaternary to recent

56±4 Ma using the zircon fission-track method (Murakami and Tagami, 2004) confirms our assumption and confirms previous fission-track data obtained on GSJ borehole samples indicating that the rocks around the fault have been reheated around 30–40 Ma ago, well after the initial cooling of the granodiorite to 210°C–310°C that occurred at 74±3 Ma (Murakami et al., 2002).

D.3.3 Hydrothermal alteration

Ohtani et al. (2000) and Fujimoto et al. (2001) distinguished three major episodes of hydrothermal alteration within the fault granodioritic wall rocks in the GSJ drill hole. These episodes are characterized successively by chlorite, zeolite and then carbonates. Some clays have also been observed within the fault at Hirabayashi village (Otsuki et al., 2003) and detected by X-ray diffraction in the core samples (Fujimoto et al., 2001) but will not be described in this study. Table 1 gives the principal occurrences and features of these hydrothermal minerals.

The structures accompanying laumontite alteration are very similar to those described by Blenk-

insop and Sibson (1992) in the Cajon Pass drill hole. First, laumontite veins with straight boundaries and blocky internal structures (Bons, 2000) are observed in the whole drill hole (Fig. D.6(a)). Then, hydraulic fractures occur where angular fragments of neighbouring minerals or cataclasites are embedded in a fine-grained matrix of laumontite (Fig. D.6(b)). Laumontite is the main product of transformation of plagioclase and a common infill of fractures within quartz (Fig. D.6(a)). Similarly, blocky calcite veins are also observed in the drill hole (Fig. D.7(a)) and are clearly later than laumontite.

Within the fault zone, very thin siderite veinlets are parallel to the fault plane (Fig. D.7(b)) and postdate the veins described above. They display fibrous internal structure and may have formed by Taber-growth (Means and Li, 2001). Above the fault core, these siderite veinlets are crosscut by hydraulic fractures showing jigsaw contours and fragments of neighbouring minerals or cataclasites in a mixture of euhedral ankerite and siderite crystals (Fig. D.7(c); Boullier et al., 2004). The fine-grained laumontite and carbonate veins display deformation structures such as stylolites or dissolution features (Fig. D.6(c); Boullier et al., 2004, figures 9 and 10).

The similarity of textures suggests that zeolites and carbonates may be attributed to comparable hydrothermal and deformation processes that occurred at different depths and temperatures. The succession (1) laumontite, (2) calcite±analcite, (3) siderite±ankerite can be deduced from thin sections observations. This mineralogical succession is consistent with decreasing temperature conditions by comparison with hydrothermal alteration parageneses in Cajon Pass (James and Silver, 1988; Vincent and Ehlig, 1988). The stability field of laumontite could be estimated between 150°C and 280°C depending on the pressure (Zen and Thompson, 1974). The presence of laumontite within pseudotachylyte-associated ultracataclasites has been demonstrated by X-ray diffraction (Otsuki et al., 2003). All together, these observations suggest that laumontite alteration as well as friction melting should be related to the first stage of the structural evolution of the Nojima fault.

In contrast, the carbonate-filled hydraulic fractures are compatible with the composition of the fluid which is presently percolating through the fault (Sato and Takahashi, 1999) and, therefore, may have been formed during the Quaternary activity of the Nojima fault (Boullier et al., 2004). The siderite veinlets which are younger than laumontite alteration but older than carbonate-filled hydraulic fractures, could have formed during the quiescent period between the two stages of deformation on the Nojima fault.

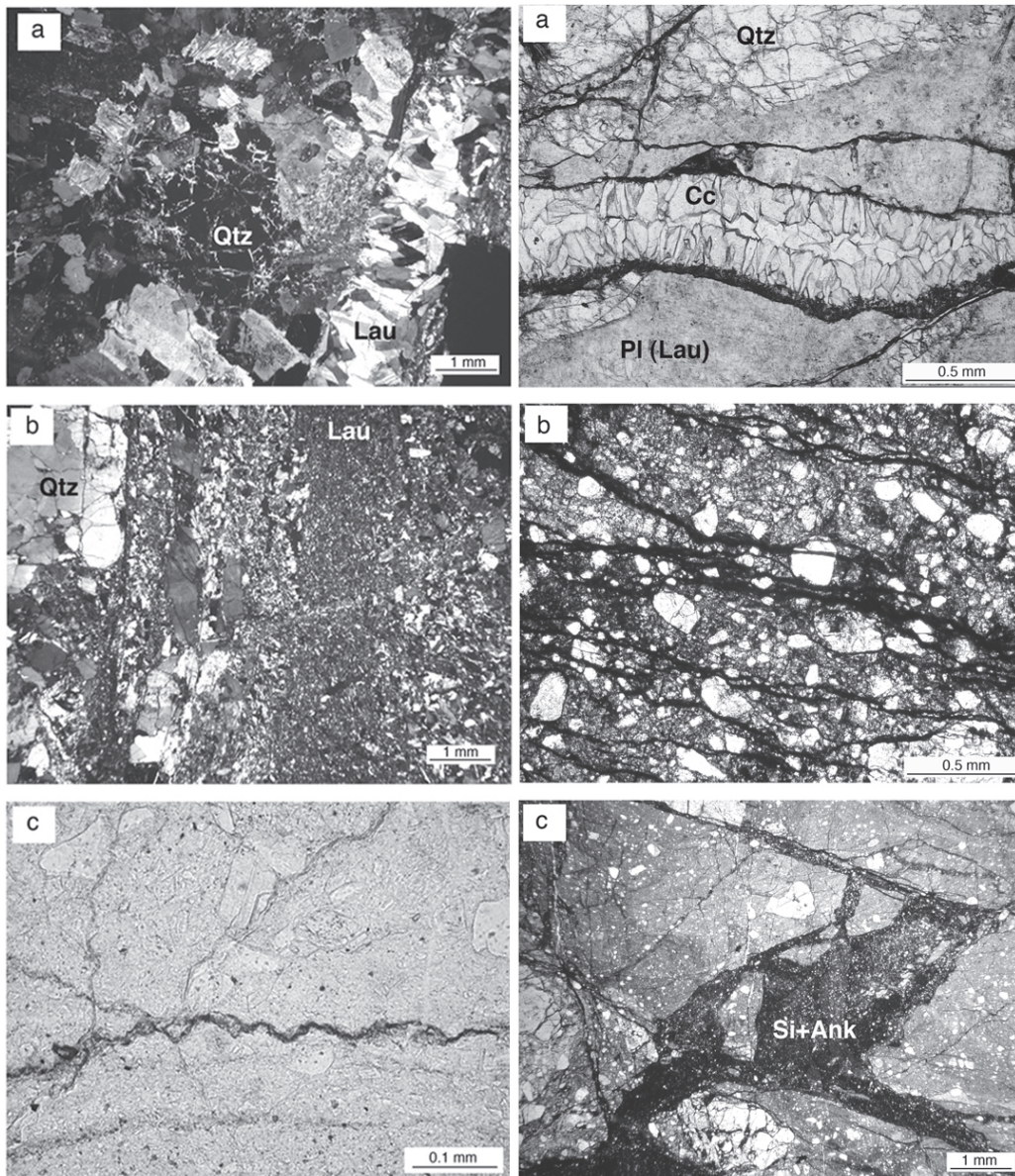


Figure D.6

Figure D.7

Figure D.6: Textural features in laumontite veins. (a) Blocky internal structure in a fractured granodiorite at 659.45 m depth; note the fractured quartz grain (Qtz, black in the center) cemented by laumontite. Crossed polars. (b) Fine-grained hydraulic fracture containing fragments of surrounding minerals in a matrix of very fine-grained laumontite (Lau, 588.75 m depth, crossed polars). (c) Stylolite developed in the fine-grained laumontite matrix of a hydraulic fracture (586.50 m depth). The orientation of the stylolite is subvertical and parallel to the fault plane.

Figure D.7: Textural features in carbonate veins. (a) blocky calcite (Cc) vein in a fractured and altered granodiorite (501 m depth). Note the fractured quartz grains (Qtz) and the plagioclase (Pl) entirely replaced by laumontite (Lau). (b) Very thin siderite veinlets cross-cutting a compacted cataclasite. The actual orientation of the veinlets is subvertical and parallel to the fault plane (623.50 m depth). (c) Fine-grained hydraulic fracture (black on the microphotograph) containing fragments of the surrounding cataclasite in a matrix of very fine-grained siderite and ankerite (Si+Ank, 623.50 m depth). Same sample as in Fig. D.7(b).

D.3.4 The latest events: thin fault gouge zones

The youngest structures observed in the GSJ borehole are symptomatic of two types of deformation processes: pressure solution expressed by dissolution features (stylolites, Fig. D.6(c)) and brecciation/comminution expressed by thin fault gouges which are especially numerous below the fault core (i.e. in 625–635 m interval in the GSJ borehole). These two processes correspond to very low and high strain-rate mechanisms respectively and may tentatively be attributed to interseismic and seismic periods, although a controversy still exists on the seismic or aseismic character of cataclasites and gouges (see the review by Snoke and Tullis, 1998). In order to understand the deformation processes within the gouge zones (comminution, compaction, dissolution, recrystallization), the 2D grain-size distribution has been measured (Fig. D.8(a)) in fault rocks using back-scattered SEM images with different magnifications. With help of the public domain software ImageJ (<http://rsb.info.nih.gov/ij/>), grain boundary maps were drawn using a combination of automatic and manual grain boundary tracing. For automatic tracing a method similar to that described by Heilbronner (2000) was used. The grain size in Fig. D.8 is the equivalent radius of a circle having the same area as the grain. An image at x100 magnification covers an area of 11 mm². For each sample at each magnification, at least 500 grains were counted. For the grain size distribution of the rock, we have distinguished fractured fault rocks in which the fragments or counterparts could be fitted together (522.88 m depth), from the cataclasites in which counterparts cannot be identified (624.41 m depth). The grain size distribution can also be displayed as magnification of the images versus the fractal dimension (D-value) observed in each image (Fig. D.8(b)). On these Figures (D.8(a) and D.8(b)) it appears that:

- for large grain sizes (low magnifications) the D values are 1.6 for fractured rocks and 2.5 for cataclasites.
- for small grain sizes (high magnifications) the slope of the distribution approaches 1 in both cases.
- the pinning point between large and small grain sizes is close to the grinding limit (1.7 μm diameter for quartz; Prasher, 1987).
- much smaller particles than the grinding limit are observed (ca. 50 nm).

Blenkinsop (1991) has studied the grain size distribution and fractal dimension of cataclastic granitoid samples from the Cajon Pass drilling project. These granitoid cataclasites originate from various depths, up to 2807 m and have 2D fractal dimensions of 0.88–2.08. The fractal dimensions we found are higher, possibly because our samples were deformed later again during

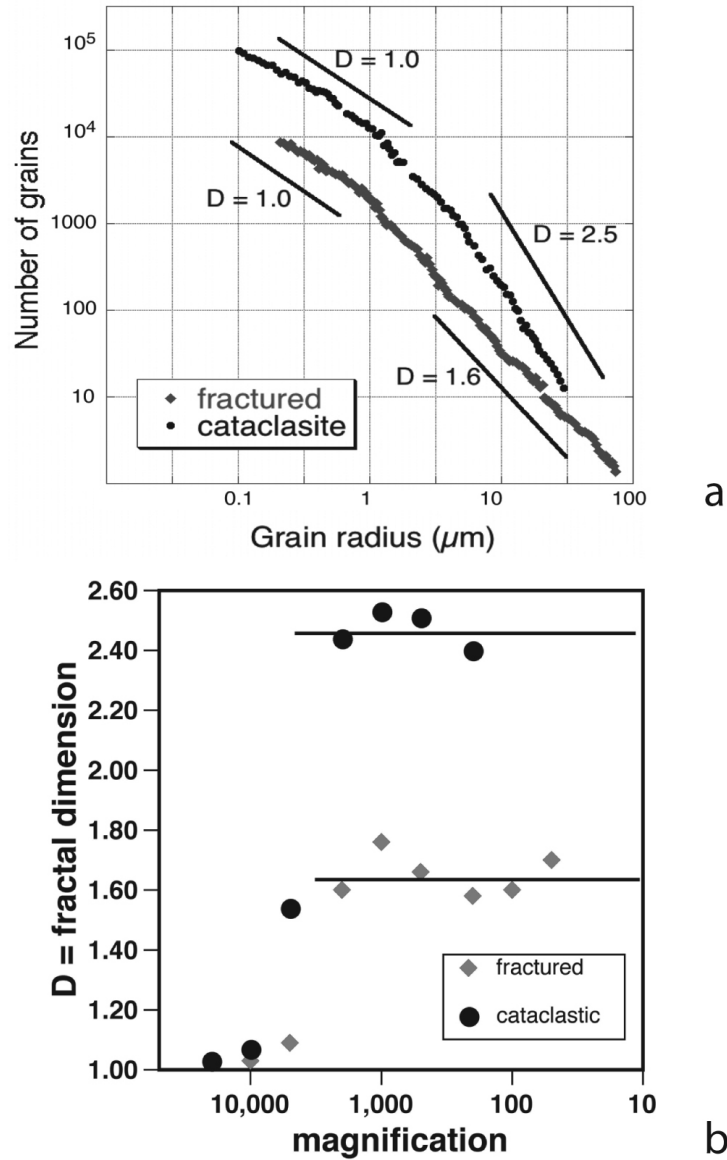


Figure D.8: (a) Grain size distribution obtained from SEM-images of thin sections of fractured rocks (522.88 m depth) and of cataclasites (624.41 m depth). The negative of the slope is the fractal dimension, D . (b) Variations of D values for fractured rocks (522.88 m depth) and cataclasites (624.41 m depth) as a function of the magnification of the images. A high magnification relates to a small grain size. The cataclasites have a higher D -value (2.5) than the fractured grains (1.6).

a subsequent episode, or because we analyzed more grains and studied a wider range of smaller grain sizes. Our results for the pseudotachylyte-related ultracataclasites of the Nojima fault (624.41 m depth) are comparable to the observations of Monzawa and Otsuki (2003), who studied the grain size distribution of larger grains for the Nojima and three other fault zones. We were able to measure the sizes of the very small grains with the Scanning Electron Microscope. These grains have a diameter that is much smaller than the grinding limit. Therefore, grinding is not the only effective mechanism to decrease the grain size. Abrasion or dissolution might be involved in the grain size reduction of the smallest particles. We report higher D values for cataclasites (2.5) than for fractured fault rocks (1.6) within the Nojima fault. The difference may be due to increasing strain or variations in confining pressure (Amitrano and Schmittbuhl, 2002) or to additional active processes in cataclasites such as fluidization as suggested by Monzawa and Otsuki (2003). However, more measurements are needed on different types of fault rocks in order to test the response of the grain size distributions to quiescent periods during which compaction or recrystallization mechanisms may occur as suggested by studies of experimental and naturally deformed fault rocks (Keulen et al., 2003a, b).

Since they are the youngest observed deformation structures in the drill hole, the thin gouge zones are tentatively attributed to recent and near-surface seismic activity.

D.4 Remaining Questions and Conclusions

The Nojima fault has undergone a multistage evolution. At least two main periods can be distinguished. The first one occurred before the deposition of the Kobe Group (<40 Ma) and before the uplift of the granodioritic basement. The second (Late Pliocene to Quaternary) corresponds to the 490 to 540 m vertical offset of the unconformity at the base of the Kobe Group. Therefore, the structures observed in the drill hole can be attributed to either one or the other period.

Given our data and observations, the imprint of the first period is represented by the pseudotachylytes and a NNE-SSW compressional event expressed by shortened biotite cleavage planes and healed fluid inclusion planes. The later structures correspond to a sinistral strike-slip movement on the Nojima fault. As laumontite is stable between 150 and 280°C (Zen and Thompson, 1974), it was probably formed also prior to the deposition of the Kobe Group and, therefore, it is tentatively related to the first period. If friction melting (pseudotachylytes) and laumontite alteration were contemporaneous at ca. 56 Ma (Murakami and Tagami, 2004), it means that the temperature deduced from fluid inclusions in pseudotachylytes (>280°C, Boullier et al., 2001) may have been slightly overestimated.

On the basis of similar composition between carbonate infill and the fluid sampled in the fault after drilling, Boullier et al. (2004) have interpreted the carbonate-filled hydraulic fractures as due to co-seismic circulation of fluids during Quaternary or Recent activity of the fault. Consequently, the thin gouge zones being younger than the carbonate hydraulic fractures are themselves attributable to the latest period of activity of the Nojima fault. Thickness of the fault zone (>46.5 m) is determined from alteration and deformation features (Tanaka et al., 2001; Ohtani et al., 2000) and most of the width of the fault is characterized by laumontite alteration (Fujimoto et al., 2001). Therefore, there is no correlation between the present-day width of the fault zone and the measured vertical Quaternary (ca. 500 m) movement and this set of data should be used with caution to assess a relationship between thickness of the gouge zone and total displacement along faults (Scholtz, 1990). Some questions remain: should we consider some quiescent intervals between the major periods of activity? If yes, what could be the textures indicative of this quiescence? Significant changes in the fluid composition percolating through the fault probably occurred between the laumontite and the carbonate episodes. Could it be correlated with a change in the origin or the main fluid reservoirs or with different circulation or mixing paths?

If it is often possible to interpret the different structures observed in the fault zone in terms of low or high strain rate processes, it is still difficult, if not impossible, to interpret them in terms of kinetics or dynamics. What is the duration of the aseismic intervals? Are all the cataclases seismic or not? If they are seismic, what could be the corresponding earthquake magnitudes?

The evolution of the Nojima fault appears more complex than firstly expected. At least two periods of activity are suspected which are very difficult to decipher from the observation of the drill cores alone. More data are needed on the age of the laumontite or carbonate alteration stages, on the origin of the percolating fluids and on the fluid-rock exchanges. Nevertheless, and even if some questions remain, the GSJ and other drill holes through the Nojima fault represent an important opportunity to study the mechanisms of deformation in active faults and the interactions between fluids and deformation.

Appendix E

Setting and structures of the sample localities

This Appendix gives the topographic setting and a short geological background of the sample localities in the Black Forest and along the Orobic Thrust. The information on the Kandern Fault Zone is partially included in a paper in press in the International Journal of Earth Sciences as: Dresmann H., Keulen, N., Timar-Geng, Z., Fügenschuh, B., Wetzel, A. and Stünitz H.: The south-western Black Forest and the Upper Rhine Graben Main Border Fault: thermal history and hydrothermal fluid flow. doi: 10.1007/500531-008-0391-3.

E.1 Black Forest

Topographic setting

Two fault zones in the southwestern Black Forest, southwestern Germany, were sampled: the Kandern Fault Zone and the Wehratal Fault Zone (Fig. E.1). The Kandern Fault Zone is found East of the village Kandern where it is traversed by the road to Schlächtenhaus. The village Kandern lies at the border of the Rhine valley, between the mountains of the Black Forest and the hills of the Dinkelberg area. The Wehratal lies further to the east, at the other side of the Dinkelberg area and forms an North-South stretching valley between Hausen and Säckingen. Samples were collected along the northern lake-side of the Wehra storage reservoir (see Figure E.2).

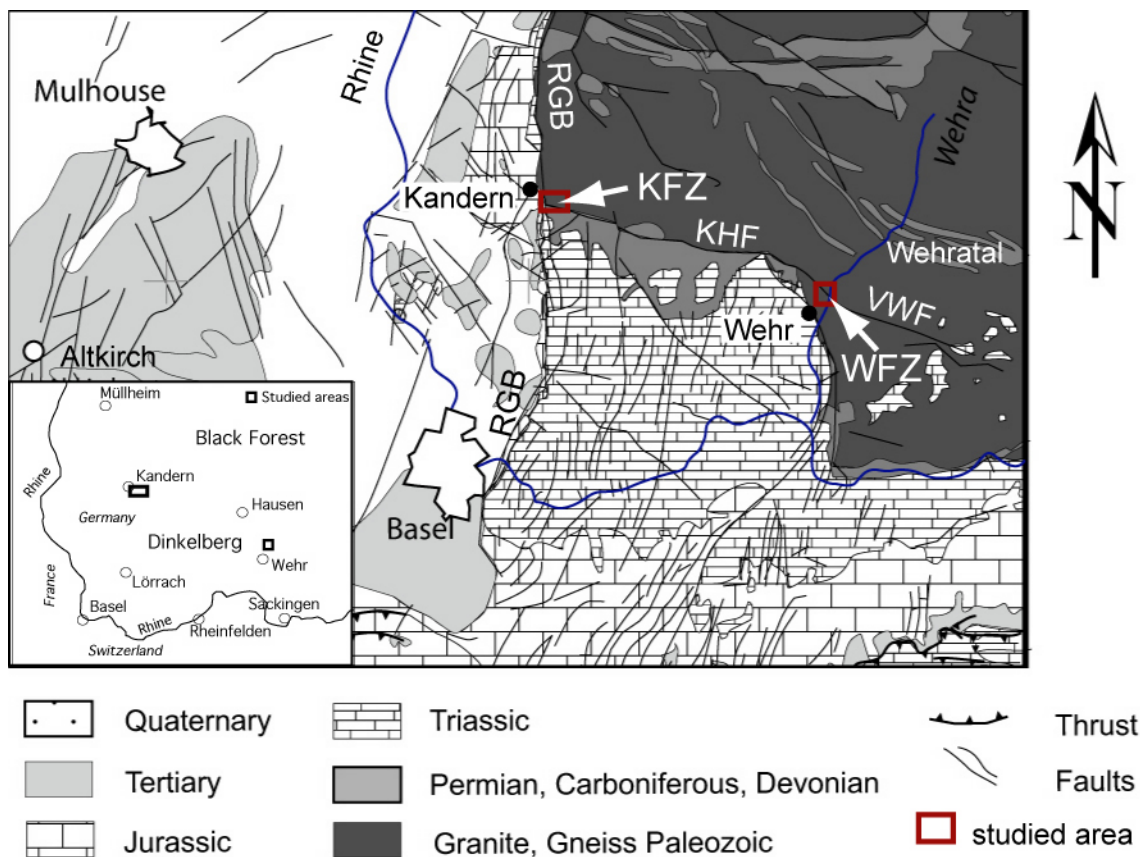


Figure E.1: Geological map of the southwestern Black Forest, Dinkelberg and Rhine Graben valley. KHF = Kandern Hausen Fault, VWF = Vorwald Fault, KFZ = Kandern Fault Zone, WFZ = Wehratal Fault Zone, RGB = Rhine Graben border fault. Map adapted from Chatraïne et al. (1996); Ustaszewski et al. (2005); Dresmann (inprep.)

Geological setting

Both studied fault zones, are situated at the contact between the crystalline (granitoid and gneissic) basement of the Black Forest and the sediments of the Dinkelberg block (Fig. E.1). During the Variscan orogeny large scale thrusting, intensive metamorphism of Palaeozoic sediments and extrusives, as well as anatexis, granitic intrusions and extrusions led to the formation of a crystalline basement (Geyer and Gwinner, 1986). Simultaneously, during the Carboniferous and Permian, large WNW-ESE striking intramontane basins were formed in central Europe and filled with locally derived sediments (Ziegler and Dèzes, 2005). A WNW-striking, N-dipping fault was formed between Kandern and Hausen during the Late Carboniferous as a dextral compressional mylonite (Echtler and Chauvet, 1992). During the Upper Carboniferous two extensional shear zones were developed east of Wehr, accommodating E-W extension of the area. Anatexis and emplacement of large granite intrusions are related to this extension. The Kandern-Hausen Fault was reactivated as a dextral transtensional shear zone (Wirth, 1984; Echtler and Chauvet, 1992). The formation of the Permian grabens probably led to a cataclastic reactivation of both studied fault zones (Echtler and Chauvet, 1992). The opening of the Rhine Graben was associated with a reactivation of the Kandern-Hausen Fault, normal (West-down) faulting along the Wehratal fault and a structural descent of the Dinkelberg Block with respect to the Black Forest Basement. Within the Dinkelberg Block a set of N-S striking faults developed parallel to the Rhine Graben border fault and the N-S-striking Wehr Fault (Geyer and Gwinner, 1986).

The Wehratal Fault Zone consists of a cataclastic zone, which is part of the WNW-ESE striking Vorwald Fault (Sawatzki et al., 1998, Fig. E.2), that is cross-cut by the N-S striking normal Wehr Fault along the border of the Wehra storage basin (Fig. E.2). The Vorwald Fault is the northeastern of the Carboniferous transtensional shear zones (described above) and accommodated dextral shear under HT/LP conditions (Echtler and Chauvet, 1992). A extensional reactivation of the Vorwald Fault under colder (“non-metamorphic”, Echtler and Chauvet, 1992) temperatures probably happened during the Permian. The Wehr Fault is associated to the opening of the Rhine Graben, which started in the Eocene (Schumacher, 2002), causing a renewed activity of the Wehratal Fault Zone. The Wehr Fault is the Tertiary reactivation of the western Carboniferous shear zone. This shear zone used to be the high angle normal west-dipping Wehra Shear Zone. The Vorwald Fault cuts through granitoids, amphibolites and gneisses (Huber and Huber-Aleffi, 1990; Sawatzki et al., 1998).

The Kandern Fault zone forms the intersection between the NNE striking Rhine Graben border fault and the WNW striking Kandern-Hausen fault (Fig. E.3). The area between Kandern and Hausen was affected by Carboniferous (HT/LP) compressional shearing, followed by cataclastic faulting in the Permian. Hydrothermal activity is reported for the area during Late

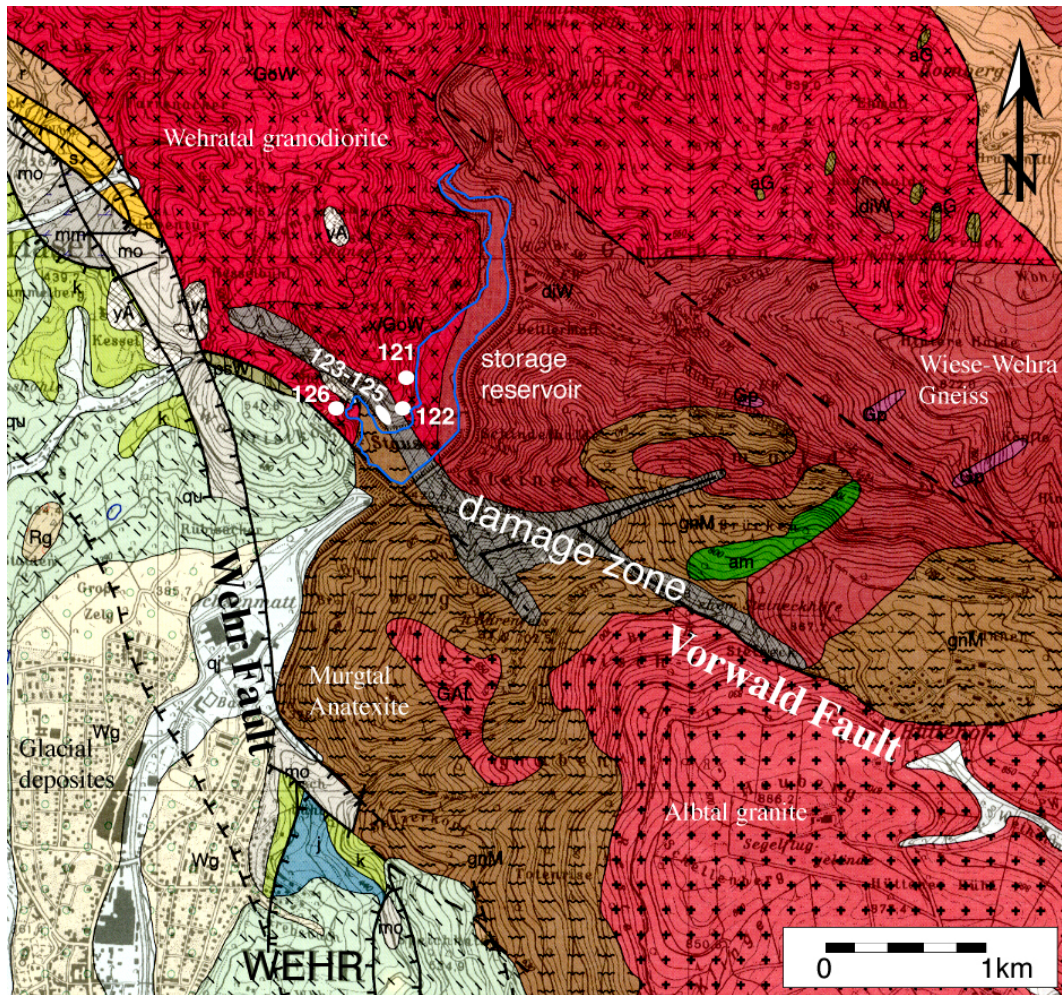


Figure E.2: Geological map of the area around the village Wehr, adapted from Sawatzki et al. (1998). Samples were collected from the northwestern shore of the storage-reservoir (outlined in blue), numbers indicate approximate localities of samples 01NK121–126.

Cretaceous and Early Tertiary (Werner and Franzke, 2001), followed by rift-related volcanism in the early Paleocene (Keller et al., 1992). The Rhine Graben started to open during the Eocene (Schumacher, 2002). This opening caused dextral transtensional movements along the Kandern-Hausen Fault and normal faulting along the Rhine Graben border fault. A paleo-depth of approximately 1800 meters was estimated for the cataclastically deformed granites in the Kandern Fault Zone area that outcrop today on the Black Forest side of the zone (Dresmann et al., 2009). The reactivation of the Kandern Fault Zone in the Eocene is associated with a local heating event (Dresmann et al., 2009).

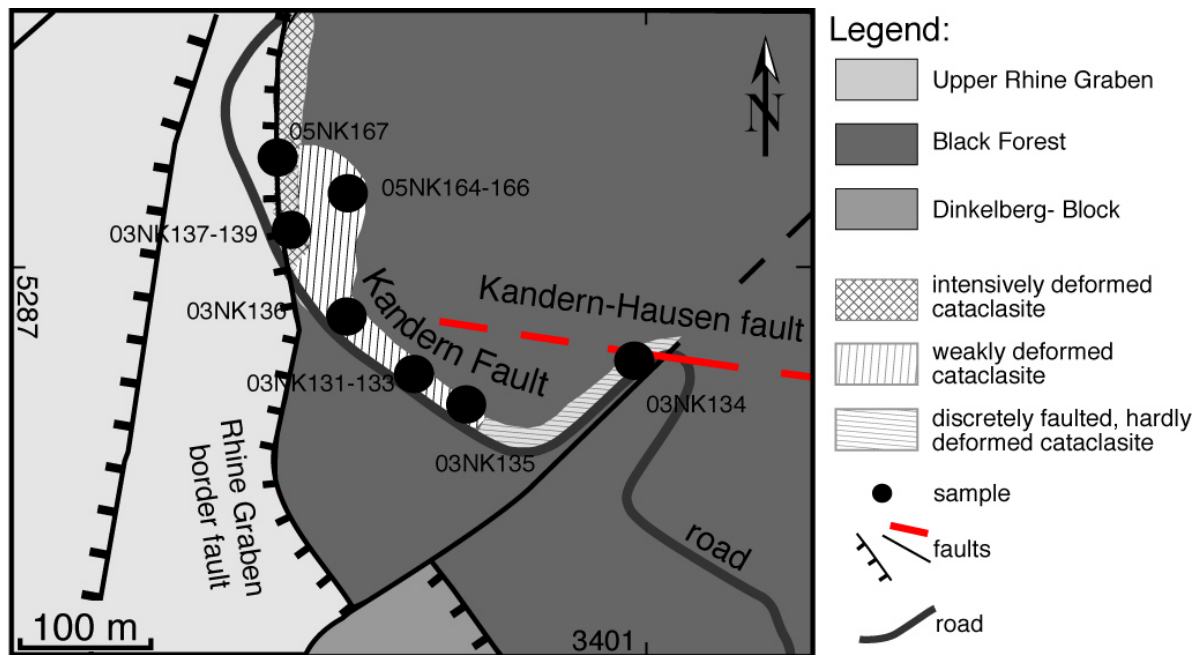


Figure E.3: Schematic overview of the localities sampled along the Kandern Fault Zone. The Kandern Hausen fault (in red) is cut by the Rhine Graben border fault, leading to an increase in deformation along the Kandern Fault zone from east to west. Map altered after Dresmann et al. (2009).

Outcrop scale

Wehratal: A road section along the dam of the water storage reservoir is cutting through the Wehratal Fault zone and along this road the samples 01NK121-126 have been collected. The fault zone consists of a broad (~ 150 m) zone, indicated in Figure E.2 as “damage zone” with rigorous cataclastic deformation and some less intensively affected granitic rock outside this zone. To be able to study cataclastic deformation of different intensity, but especially the most deformed fault rock, six samples have been collected. Sample numbers increase from East to West, 01NK121 is nearly undeformed granite, 01NK123-125 consist of granites with intensive cataclastic deformation and 01NK122 and 01KN126 show moderately deformed granite. An example of cataclastically deformed granite is shown in Figure E.4a, taken from the broad cataclastically deformed damage zone. Within the damage zone a network with varying spacing (generally centimeter-meter spaced) of cataclasites is found. Samples from the damage zone have been used for the grain size analysis, Table E.1 at the end of this Appendix gives an overview of the important thin sections.

Kandern: A newly built road intersects the Kandern Fault zone over 400m at a low angle (Figs. E.3, E.4b). Along this road-section the plagioclase-rich biotite-hornblende-bearing Malsburg Granite is found in the west of the outcrop, whereas most of the outcrop was formed

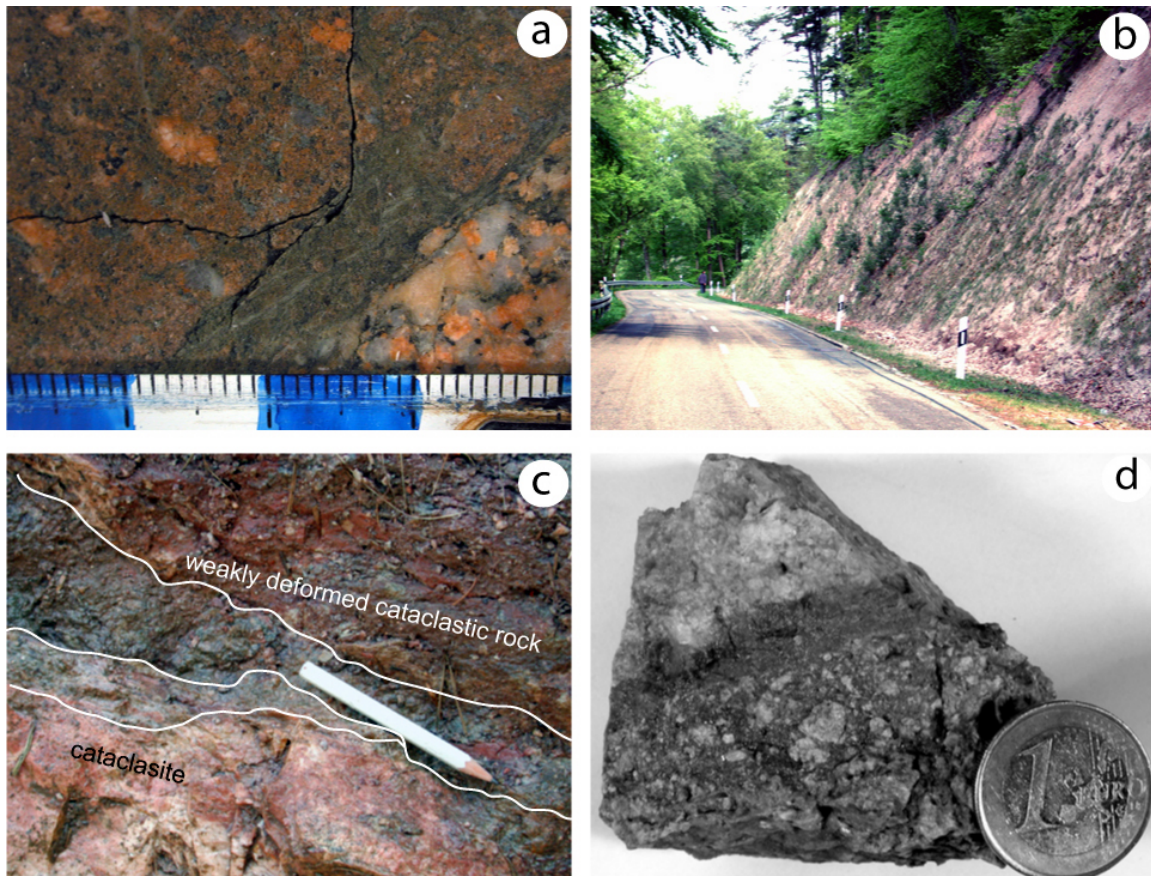


Figure E.4: Outcrop and sample photographs of the Wehratal and Kandern Fault zone. a) Detail of handspecimen 01NK124, originating from the damage zone in the Wehratal Fault zone. Scale in cm. b) Overview of the Kandern Fault cut by the road. Image taken in the direction of Kandern. c) Cataclasite, photograph taken at 0.5 m from sample locality 03NK132, Kandern Fault zone. d) Hand specimen taken from sample locality 03NK136, Kandern Fault zone.

by the K-feldspar-rich biotite-muscovite Schlächtenhaus Granite. Along the outcrop, the cataclastic fault rocks change their movement direction from NNE-SSW (rhenish) to WNW-ESE (Kandern-Hausen Fault strike). Deformation progressively decreases in intensity from West to East. The cataclasites form a meter-spaced network of varying intensity. Individual cataclasites are approximately 5 to 30 cm wide (Fig. E.4c,d). The cataclasites are unfoliated and locally cut by decimeter to decameter spaced 0.5–5 cm wide quartz veins. From this outcrop thirteen samples have been collected evenly distributed along the outcrop (Fig. E.3). In this way the decrease in deformation intensity of the samples can be studied. Samples 03NK134, 03NK132 and 03NK138 have been analysed for apatite and zircon fission tracks by H. Dresmann as sample HD128, HD129 and HD130, respectively. For the grain size analysis samples 03NK138 and 03NK132 have been used, see Table E1.

Microstructural observations

Wehratal Fault zone: The intact granitoid rock (sample 01NK121) has a granitic to granodioritic composition and is rich in K-feldspar. The sample has as an average grain size of approximately 0.1–0.5 mm. In thin section the rock shows grains with straight or mildly curved and pinned grain boundaries. Some melt pockets were observed. The grains show no internal deformation (no sub-grains, no undulatory extinction, no cracks), except for some kinks in biotite. Some of the K-feldspar grains reacted to clay-minerals (kaolinite?), biotite is partly replaced by chlorite, muscovite and quartz.

A network of fault zones cut through the intensely deformed samples. Thin (1 mm – 1 cm) ultracataclasites are usually bordered by very weakly deformed granite at one side and cataclastically deformed granite ($\sim 1 - 10$ cm) at the other side (see Fig. E.4a). The deformed samples (01NK123-125) show a wide range of grain sizes (~ 100 nm – 2mm, occasionally > 0.5 cm). In thin sections, at least two deformation phases could be detected, where the fragments of the earlier generation were reworked during the later deformation. Most of the fragments are very angular and show a random distribution within the rock (Fig. D.12a). Quartz forms larger (up to 100 – 300 μ m) fragments than K-feldspar (< 100 μ m). Biotite was deformed by kinking, shearing and fracturing. The spatial distribution of the fragments has a chaotic appearance, they are intensively fragmented, but do not appear to have accommodated much displacement. Most of the deformation seems to have taken place along small intensively comminuted zones directly next to the weakly deformed wall rock (Fig. D.12a). With cathodoluminescence microscopy two different episodes of cataclasis have been observed; an earlier one under diagenetic temperature conditions (creating luminescent cementation material) and one colder episode (with non-luminescent material deposited between the grains, see Fig. 5.3.2). During or after (one of) the earlier deformation events, calcite is deposited in the rock as ca. 2 – 20 μ m veins and as crack and pore space fillings. These calcite veins were fractured during later deformation and fragments were found in the younger cataclasite (Fig. D.12b). The granitoid wall-rock of the cataclasites shows crystal-plastic deformation features, formed previous to the brittle deformation structures. Feldspars show deformation bands and an undulatory extinction, quartz locally shows some sub-grain rotation and grain boundary migration recrystallization. These deformation structures may originate from the Carboniferous shearing movement on the zone, and show that the shear zone has been reactivated as brittle fault.

Kandern Fault zone Within the microstructures of the Kandern Fault zone two cataclastic deformation episodes can be distinguished. Evidence for the older episode are multi-component fragments within the matrix of the younger cataclasite as well as locally observed cataclastic wall-rock along the younger cataclasite. At thin-section scale, the younger cataclasite forms a

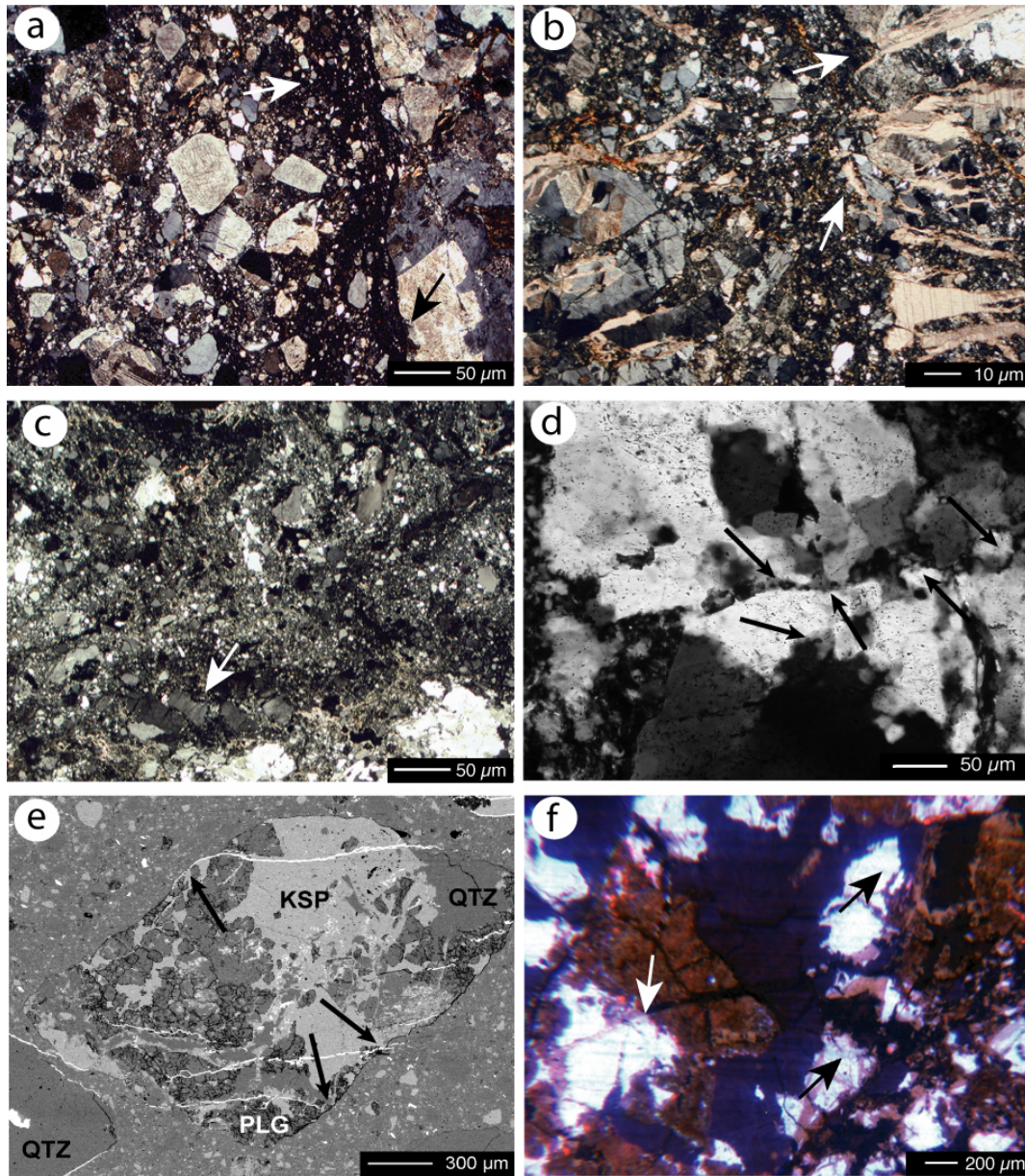


Figure E.5: Crossed polarized light (LM), Cathodoluminescence camera LM, and backscatter-contrast scanning electron (BSE) micrographs showing structures from the Wehratal Fault zone and the Kandern Fault zone. a) Angular fragments in mostly unfoliated cataclasite. Cataclasite, ultracataclasite and more intact wall rock (from left to right), Wehratal, LM. Grain size analysis performed in cataclastic matrix. b) Calcite veins cut by later cataclasis, Wehratal, LM. c) Cataclasite with book-shelf structure of quartz (arrow), Kandern, LM. Grain size analysis performed in fine grained matrix. d) Cataclastic fragments, consisting mainly of quartz, in fine grained matrix of younger cataclasite. Along healed cracks quartz is deforming by bulging recrystallisation (arrows), Kandern, LM. e) Fragment, consisting of older cataclasite in fine grained matrix of younger cataclasite. Barite veins (white) cut older cataclasite, but do not continue into matrix of younger cataclasite (arrows), Kandern, BSE. f) Remnants of earlier fracturing-cementation event within K-feldspar (white mineral) filled with light blue luminescent material (black arrows). The latest veins cut through all minerals and are cemented with low-luminescent (dark-grey and violet) material (white arrows), Kandern, CL. Thin sections: a) NK123, b) NK124, c) NK138, d) NK131, e) NK131, f) NK166.

network of fractures, which measure 20 micrometer to several centimetres in cross-section (Fig. D.12c).

Quartz that has been deformed during the formation of the earlier cataclasite shows bulging recrystallization along healed fractures (Fig. D.12d). Biotite fragments at the edges of the multi-component fragments have been deformed by kinking and gliding, but these crystal-plastic features can not always unambiguously be assigned to the formation of the earlier cataclasite. K-feldspar deformed during this episode is fractured and granulated. After formation of this cataclasite, a set of thin barite veins has cut through the rocks (Fig. D.12e). The barite veins are more localized phenomena than the hematite precipitations.

For naturally deformed quartz, bulging recrystallization has been observed for temperatures above approximately $T = 280^\circ\text{C}$ (Stipp et al., 2002). Laboratory experiments on granites under high strain rates ($\dot{\epsilon} = 10^{-4} - 10^{-6}\text{s}^{-1}$) at $T = 300^\circ\text{C}$ indicated that biotite deforms by a combination of fracturing, gliding and kinking (Tullis and Yund, 1977; Kato et al., 2003). A temperature of $T = 250\text{--}280^\circ\text{C}$ is assumed for the earlier cataclastic deformation episode of the Kandern Fault Zone. Deformation is estimated to be Permian or Mesozoic in age, based on zircon fission track analysis (Dresmann et al., 2009).

During the deformation episode that created the younger cataclasite, fragmented and granulated quartz, feldspars, biotite, muscovite, hematite and multi-component fragments originating from the earlier cataclasite has been formed within a fine-grained matrix (Fig. D.12c). All minerals have deformed by fracturing. The fault rock shows a wide range of grain sizes ($\sim 200\text{ nm} - 2\text{mm}$, occasionally $> 1\text{ cm}$); the quartz forms slightly larger fragments than feldspar. No evidence for crystal plasticity has been observed in the quartz minerals. Quartz shows fewer fractures than feldspar minerals and most of the larger grains in the matrix are quartz, indicating temperatures below approximately $T = 250^\circ\text{C}$ (Passchier and Trouw, 1998). Lin (1999b) assumes that the transition from brittle to semi-brittle behavior for biotite lies at $T = 150^\circ\text{C}$. Kato et al. (2003) observe mainly brittle behavior of biotite in experimentally deformed granite at $T = 180^\circ\text{C}$. This colder deformation phase is assumed to be related to the opening of the Rhine Graben (Dresmann et al., 2009).

By means of cathodoluminescence two generations of silicate deposition have been observed. The earlier one cements fractures in quartz, plagioclase and K-feldspar with luminescent material of the same phase (black arrow in Fig. D.12f). The closed fractures have the same optical orientation as the minerals in which the fractures occur and are hardly visible with LM or SEM (BSE contrast). The second generation is formed by the late silicate-veins described above and is low-luminescent (Fig. D.12f). The change from quartz deposition to adularia deposition can be observed as a color-change of the vein material from dark violet to dark grey (white arrow).

E.2 Orobic Thrust

Topographic setting

The Orobic Thrust is located in the Lombardic Alps, northern Italy. This thrust forms the main mountain chain in the Orobic Alps and stretches roughly West-East between the Lake Como and the Adamello Mountains. The Passo di San Marco in the Orobic Alps lies on the road between Morbegno in Valtellina and Bergamo (see inset in Figure E.6). Samples have been collected in the area between the Passo di San Marco, Lago di Pescegallo (above Gerola Alta) and Monte Avaro. Most of the studied samples have been collected at the Passo di Verrobbio.

Geological setting

The Orobic Thrust is part of a South-vergent fold and thrust belt (e.g. De Sitter and De Sitter-Koomans, 1949; Laubscher, 1985; Schoenborn, 1992), in which the Variscan basement is thrust over a series of Verrucano Lombardo, and Triassic sandstones, siltstones, sandy dolomites and locally cellular dolomites (Schoenborn and Schumacher, 1994), see Figure E.6. The Variscan metamorphic basement in the Passo di San Marco area consists of paragneisses, schists and locally metapelites and meta-intrusives (Milano et al., 1988; Carminati and Siletto, 2005) and shows a paragenesis of garnet, brownish biotite, white mica, quartz and plagioclase.

The top-most nappe of the Variscan Basement is formed by the Gneiss Chiari, an intrusion that probably formed during the Late Caledonian (Milano et al., 1988; Schoenborn, 1992). The rocks crop out as white orthogneisses and are up to 1 km thick (Schoenborn and Schumacher, 1994) and show the same metamorphism as the contacting paragneisses.

Alpine deformation in the Orobic area started between the Late Cretaceous (Bernoulli and Winkler, 1990; Schoenborn and Schumacher, 1994) and before the 43–30 Ma Adamello intrusions (Brack, 1981; Del Moro et al., 1983). At least three nappes were formed, all consisting of basement and sediment units (Schoenborn, 1992). The Alpine deformation caused open chevron folds in the quartz-rich layers and a crenulation or kinking in the more mica-rich series (Milano et al., 1988; Carminati and Siletto, 2005). This deformation phase formed mylonites and catclasites in the basement rocks; some of the mylonites were folded (Milano et al., 1988). The Alpine deformation phase might have extend over a longer time (Milano et al., 1988). Carminati and Siletto (2005) suggested a two-phase deformation: first SSE-thrusting, than strike-slip along the same fault. Later deformation (very late-Alpine) caused kink bands, chevron fault and a fracture cleavage dipping parallel to the Orobic thrust (50–80° to N-NW).

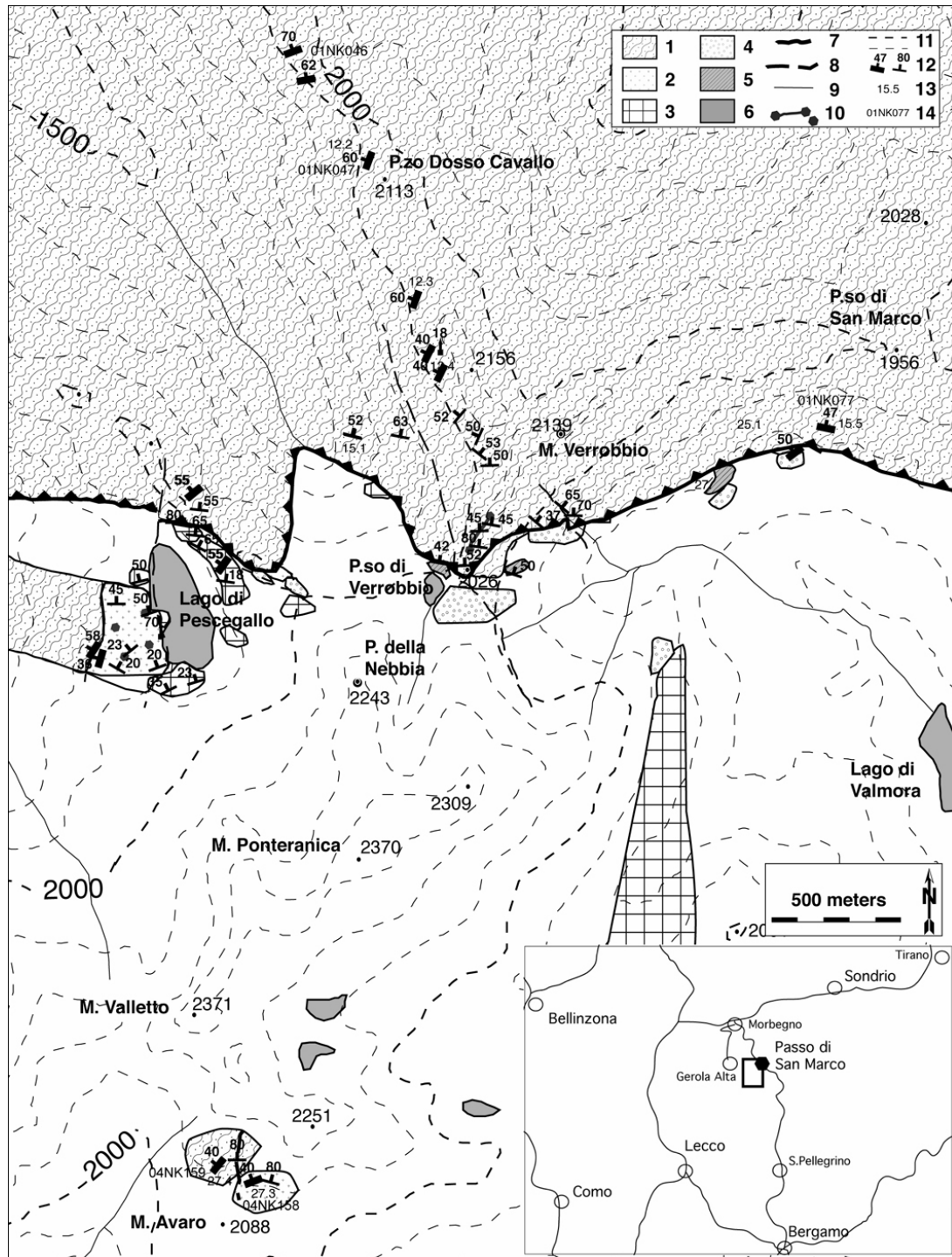


Figure E.6: Sample localities and field observation on the Orobic Thrust. 1) crystalline Basement (paragneisses and schists), 2) Gneiss Chiara, 3) Collio formation (conglomerates, locally sandstone), 4) Verucano (conglomerates), 5) Servino (sandstone, dolomites), 6) lakes, 7) Orobic Thrust, 8) other fault, 9) river, 10) discussed sample localities, 11) altitude contour lines, 12) mylonitic (left) and cataclastic foliation (right), 13) locality without measurements, 14) sample locality. Details of Passo di Verrobbio and Lago di Pescegallo in Figures E.7 and E.9, respectively.

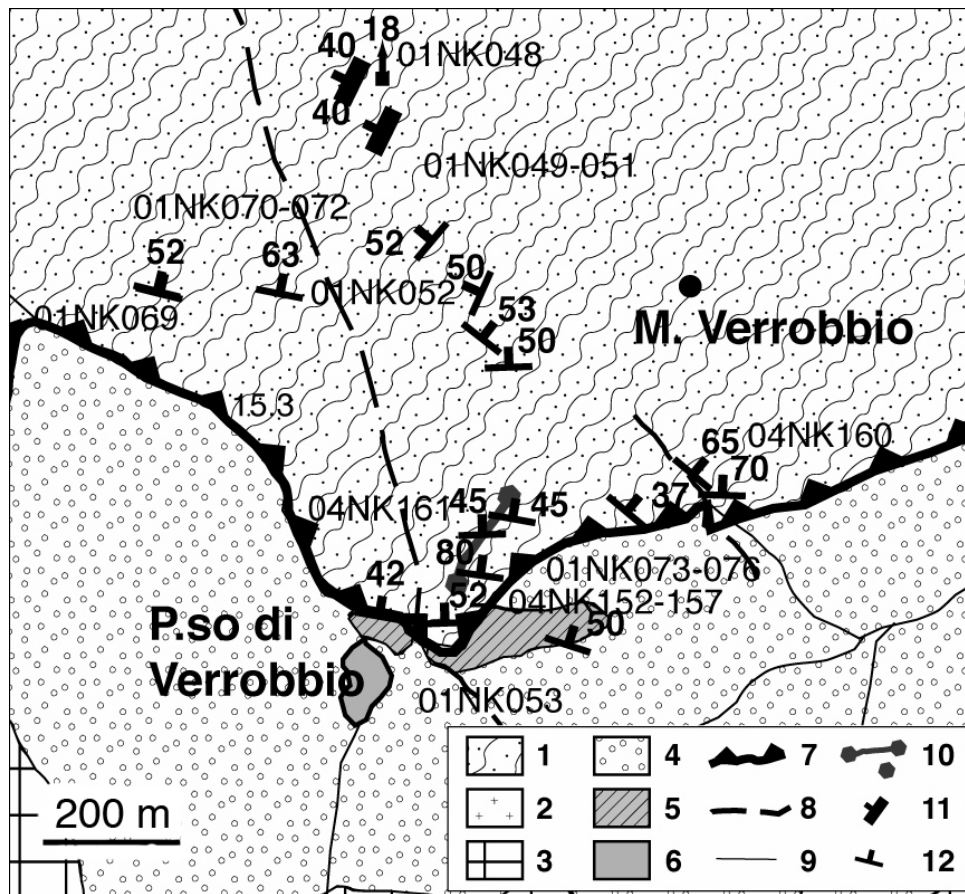


Figure E.7: Simplified geological map of the Orobic Thrust area near Passo di Verrobbio, detail of Figure E.6. 1) crystalline Basement (paragneisses and schists), 2) Gneiss Chiara, 3) Collio formation (conglomerates, locally sandstone), 4) Verrucano (conglomerates), 5) Servino (sandstone, dolomites), 6) lakes, 7) Orobic Thrust, 8) other fault, 9) river, 10) discussed sample localities, 11) mylonitic 12) cataclastic foliation. Redrawn after Schoenborn and Schumacher (1994) and own observations (2001, 2004).

Outcrop scale

Going upward from the Passo di Verrobbio, the slope of the Monte Verrobbio is nearly perpendicular to the foliation of the Basement rocks. Here the cataclasites that are formed in the paragneissic basement have been studied (Figs. E.7). The intensity of their deformation is partly determined by the composition of the host-rock. The cataclastic foliation is superimposed on the mylonitic foliation of the paragneiss. The mylonitic foliation originates from the early Alpine deformation and is defined by aligned epidote, chlorite, stilpnomelane, isoclinaly folded quartz veins and locally by mylonites. The cataclastic foliation has a spacing of 0.5 - 5 mm. The foliation is very penetrative where mica is abundant, whereas in feldspar/quartz-rich parts, it is more spaced and discontinuous. The fragments consist mainly of quartz, some lenses of gneissic material and fine grained cataclastic material originating from an earlier deformation

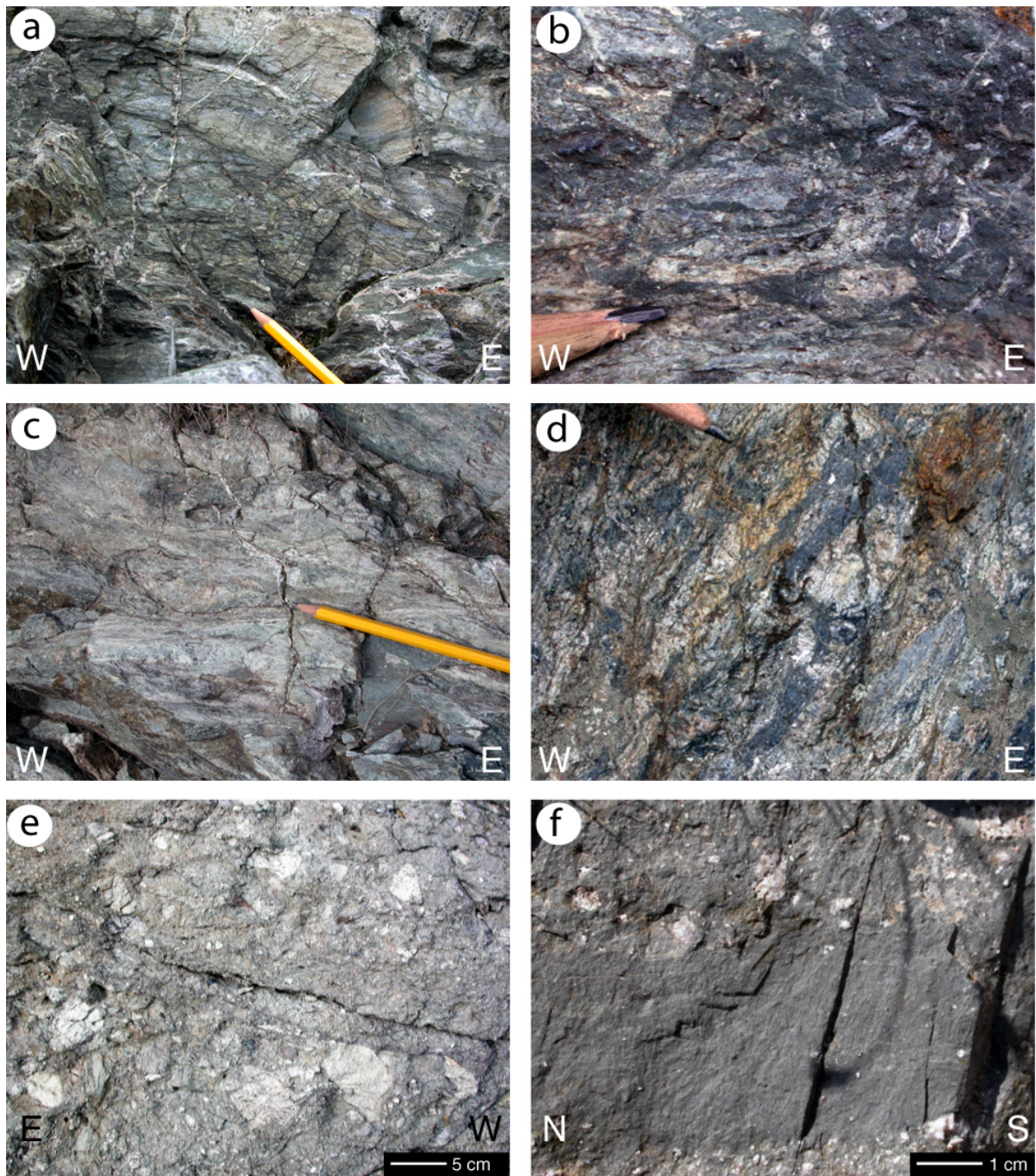


Figure E.8: Outcrop photographs of cataclasites from the Orobic Thrust. a) Cataclasite from Passo di Verrobio, with a greenish alteration color (chlorite) (01NK73). b) Less intensely deformed, not very altered cataclasite (04NK154). c) Cataclasite with white alteration color (white mica) (04NK157). d) Intensely deformed cataclasite with ultra-cataclasites and pseudotachylytes (04NK160). e) Gneiss Chiara, western shore of Lago di Pescegallo, f) ultracataclasite in Gneiss Chiara (01NK66). See Figures E.7 and E.9 for sample localities.

phase; the larger fragments are mainly subrounded (well rounded to subangular) and occasionally lenticular shaped, and are ca. 0.5 – 10 cm in size. Some Fe-ore minerals are found within the fragments, marked by rust-colored dots. Further away from the thrust contact the fragments are more angular. The larger fragments are mainly matrix-supported with ca. 50–80% matrix, in quartz-rich parts less matrix (20–40%) is observed.

The cataclasites at the thrust contact near the Passo di Verrobbio (2026 m altitude) towards the top of the Monte Verrobbio (2139 m) have been studied; the first 14 m of this section were studied in greater detail and are described here. In the first few meters (ca. 3–4 m perpendicular to the foliation) from the thrust contact of the sediments with the basement at Passo di Verrobbio towards the top the paragneiss shows a green-grey alteration color, blue-grey fresh colour (Fig. E.8a). Here the mm-spaced (ca. 0.5–5 mm) foliation is defined by dark colored sheet silicates (mainly chlorite, some clay minerals) and aligned elongated felsic minerals (quartz and albite). Locally, pseudotachylytes and a color-banding (green, blue) exists. The foliation forms a cataclastic S-C-structure, which is not observed further away from the thrust contact.

The next meters (ca. 9–11 m) the cataclasite varied in intensity, mainly defined by the composition of the gneiss. The matrix is dark colored and has a high white mica content; in the finer grained parts, the fragments are smaller. The paragneiss has a blue-greyish alteration colour (Fig. E.8b). Many adularia veins, which are locally fractured, cut through the rock. Some of the cataclasites show an intense white or light-grey alteration colour (Fig. E.8c). Here the cataclasite is formed by a felsic mineral-rich paragneiss with a white, wide-spread alteration cut by many post-deformational veins (containing mainly adularia). In the more sheet-silicate-rich parts, the paragneiss is finer grained, strongly foliated and more altered, the fragments are subrounded and the matrix content is high, ca. 60–90%. The fragments in the less sheet-silicate-rich parts are angular.

Within these first 14 meters of the section, intensively deformed zones are found, consisting of ultracataclasite with pseudotachylytes. The alteration color is grey, with black (mainly pseudotachylytes) and brown (iron oxidation) patches (Fig. E.8d). The intensity of alteration is not clearly visible due to the small grain size of the cataclasite. The intensively foliated fault rock has a micro-scale spacing, (maximum ca. 2 mm) and is quartz-rich. The foliation is defined by color-banding, bands of fine grained material, alignment of elongated fragments and forms a braided network around quartz-fragments. The fragments are not very abundant, smaller than 1 cm, elongated and rounded in shape and consist of quartz or reworked cataclasite. The matrix (70–90 %) is even finer grained than in other parts, the individual minerals cannot be distinguished with a hand lens. The matrix has a brown, black, dark-blue or grayish color. Such ultracataclasites and pseudotachylytes have been detected abundantly around 2030 m, 2036 m,

2038 m, 2043 m, 2053 m, 2065 m, and 2080 m altitude.

The most intensive alteration of the fault rock is observed close to the contact with the sediments. Laterally the same types of cataclasite were found; white altered and very intensively deformed cataclasites close the thrust plane, have been less intensively deformed further away. Only the cataclasite type with the green alteration colour was not found at other locations. Its greenish alteration color might result from the thrust-contact with the Servino dolomites rather than the Verrucano conglomerate. The most intensive deformation has been observed in the first 14 meters from the thrust contact and very locally afterwards. Samples were taken from these first 14 meters, especially within the first few meters from the thrust contact (Fig. E.7). See Table E.1 at the last page of this Appendix.

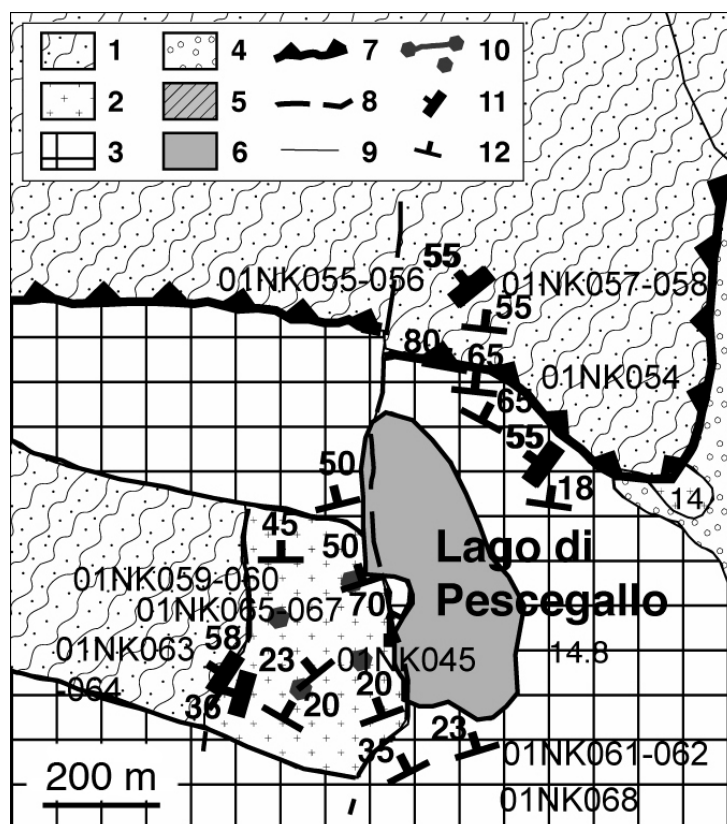


Figure E.9: Simplified geological map of the area near Lago di Pescegallo. Detail of Figure E.6, legend as in Figure E.7. Redrawn after Schoenborn and Schumacher (1994) and own observations (2001, 2004).

The Gneiss Chiara outcrop West of the Lago di Pescegallo developed several near-horizontal black ultracataclasites of ca. 1–10 cm thickness (Fig. E.8e and f). These ultracataclasites developed a mm - cm spaced color-banding (black, dark grey, dark brown, white-greyish fine material). Some quartz and earlier cataclasite remained as larger fragments (up to 5 mm in size) in the latest cataclasite, and are rounded to subrounded. The contact with the white

orthogneiss is very sharp. These black ultracataclasites could be traced laterally over several meters. Other, still white, parts of this orthogneiss were intensively deformed as well. However, the total width of the zone of deformation is only a few meters, whereas in the paragneisses the cataclastic deformation zone stretches over ca. 50 m. The Gneiss Chiara cataclasites have a weakly developed, spaced foliation with very angular fragments with rather large (up to several cm) to very fine grained fragments.

Microstructural observations

The paragneiss basement along the Monte Verrobbio profile and the orthogneissic Gneiss Chiara near Lago di Pescegallo (see Fig. E.6 for localities) were deformed under lower amphibolite facies conditions, visible in quartz as elongated subgrains, rotated subgrains, irregular formed and sized recrystallised grains. The later lower greenschist facies condition deformation can be observed in quartz as undulatory extinction, serrated grain boundaries and bulging recrystallisation. The mylonitic foliation (early Alpine), observed at the outcrop scale, is slightly overprinting this structure at thin section scale and is mainly visible as a crenulation in the micas.

The rocks are cut by an anastomosing network of cataclasites, which are visible as an SC-like structure at the outcrop scale and in thin section (Fig. E.10a). The cataclasites are characterized by up to 10 μm - 1 dm spaced fracture zones of varying width. The amount of fracturing is irregular, but generally decreasing with increasing distance from the fault zone. The cataclastic network was active at several times, producing fragments consisting of earlier cataclasites (Fig. E.10b). Up to three generations of reworked cataclastic fragments were observed, showing progressively cooler (i.e., less pressure solution after deformation, more intensive cataclasis of quartz, more angular fragments) deformation conditions. Feldspars are very intensively fractured and subsequently altered to white mica. Quartz is fractured as well, but forms most of the larger fragments that are still present in the matrix. Muscovite of the original paragneiss was fractured. Biotite was both fractured and deformed in a more plastic manner.

With backscatter contrast scanning electron microscopy, the healing structures of the grains can be observed. Healing is visible as rounding of edges, cementation, closure of cracks and the agglomeration of small grains. The amount of healing is qualitatively depending on the amount of mixing of minerals (poorly mixed minerals heal better) and on the composition (quartz heals better than feldspars) (Fig. E.10c). Alteration of feldspar forms another type of healing structure, linking the individual fragments with micas (Fig. E.10d). Within the samples evidence for pressure solution was found: rounded, slightly flattened grains with straight grain boundaries and stylolites are abundant in some thin sections.

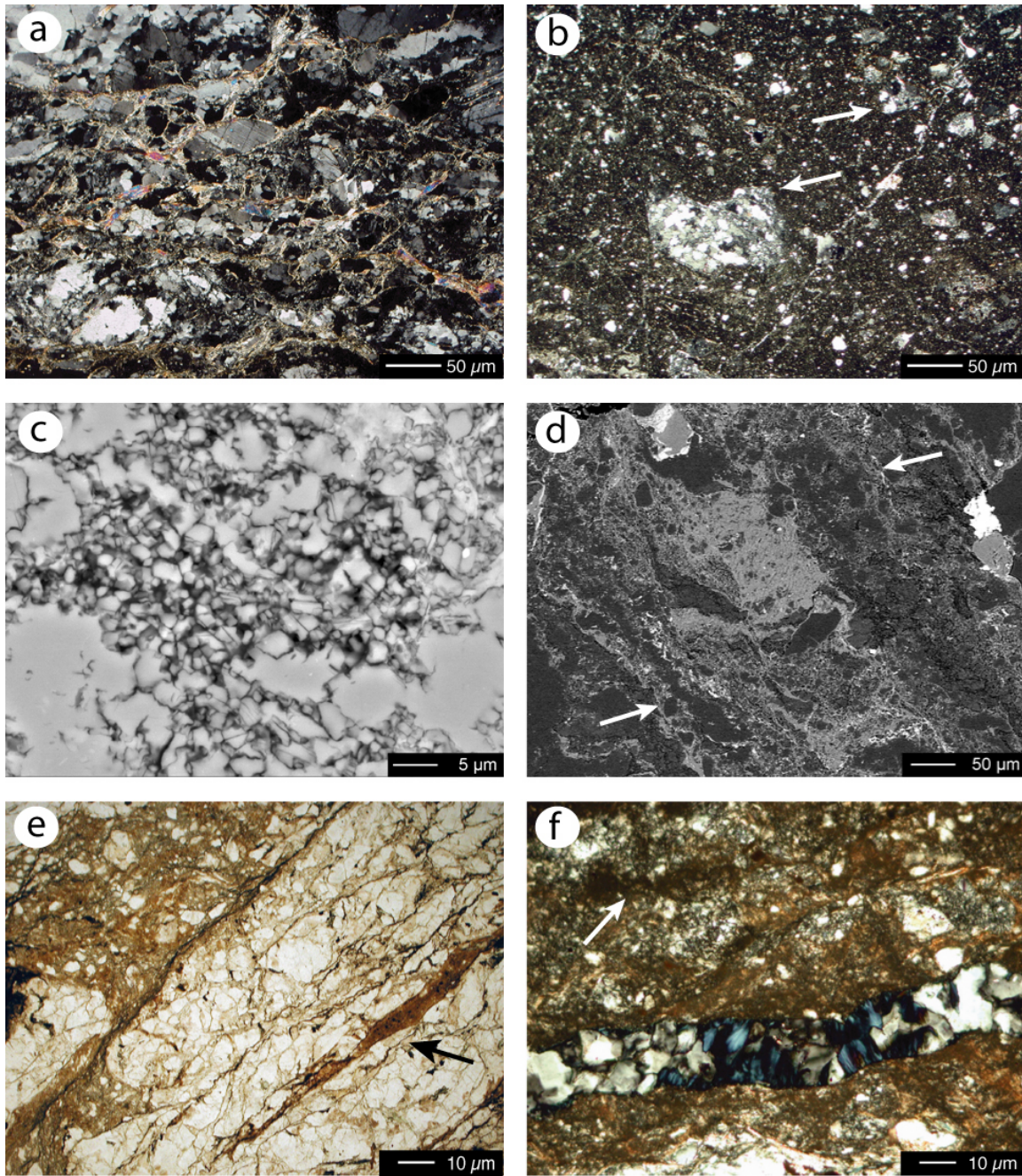


Figure E.10: Cross-polarized light (LM) and backscatter-contrast scanning electron microscopy (BSE) micrographs showing structures of the basement fault rock of the Orobic Thrust. a) S-C-structure in foliated ultracataclasite, Gneiss Chiari, LM. b) fragments consisting of earlier generation cataclasite (arrows) with ultracataclasite, Gneiss Chiara, LM. c) Monomineralic aggregate of Gneiss Chiara, BSE. d) Cataclasite in paragneiss, consolidation by formation of mica minerals, BSE. e) Plane polarized light: Pseudotachylyte (arrow) adjacent to ultracataclasite, Passo di Verrobbio, LM. f) Vein of adularia and chlorite in cataclasite with fragment of pseudotachylyte (arrow), Monte Verrobbio, LM. Thin sections: a) NK060, b) NK112, c) NK065, d) NK154, e) NK154, f) NK157. See Figures E.7 and E.9 for sample localities.

Pseudotachylytes, associated with these cataclasites, are observed in the paragneiss of Monte Verrobbio. Pseudotachylytes are visible as dark (brown, black or grey) planar features, usually immediately next to fine grained cataclasites, separated by a sharp straight boundary. Part of the pseudotachylytes are fractured, forming fragments in the cataclasites (Fig. E.10e). Near Monte Verrobbio many thin pseudotachylytes are observed in some samples. Quartz forms most of the bigger fragment in the cataclasites and usually has an angular shape. Remnant feldspars are smaller and rounder. Micas are not observed as large inclusions, but show a ragged structure at contacts to intact rock.

Thin sections

Sample number	locality	$D_{>}$ -value	remarks
<i>Wehratal:</i>			
01NK123	damage zone	1.60	small ultracataclasite
01NK124	damage zone		carbonate veins
01NK125	damage zone	1.60	CL
<i>Kandern:</i>			
03NK131	centre outcrop		barite veins
03NK132	centre outcrop	1.58	fission track
03NK134	east of outcrop		fission track
03NK138	west of outcrop	1.72	fission track, CL
05NK164	centre of outcrop		hematite
05NK166	centre of outcrop		CL
<i>Orobic Thrust:</i>			
01NK060	Pescegallo		contact cataclasite/ultracataclasite
01NK065	Pescegallo	1.59	Gneiss Chiari cataclasite
01NK066	Pescegallo		ultracataclasite
01NK073	Verrobbio		multiple deformation events, CL
01NK076	Verrobbio	1.62	multiple deformation events, CL
04NK154	Verrobbio		pseudotachylytes
04NK160	Verrobbio	1.59	ultracataclasite, CL

Table E.1: Overview of most important thin sections of natural samples. Remarks lists representative features of the thin sections and methods of analysis. CL = cathodoluminescence.

Appendix F

EDX data of basalt samples

The tables on the following pages show the EDX-data for minerals in the basalt samples that have been described in Chapter 6.

The tables in this Appendix show the chemical data for minerals in the basalt samples. Analysis have been performed with an electron dispersive X-ray detector (EDX) connected to a scanning electron microscope in back-scattered electron mode. Measurements of the phases are performed without the application of standards by using a working distance of 10.0 mm and an acceleration voltage of 20 kV. The spot-size (focussed beam diameter) is approximately 3 μm for the settings that were applied. Results of the analyses are given in Tables E.1 – E.3. In these analysis no adjustment for the possible presence of H_2O , CO_2 or other light element-oxides is made. The applied EDX-program (edxi32) is automatically recalculating the measurements to 100 mol%. While the starting material of the samples is quite constant in composition and easy to measure, this is not the case for the reaction products, which are usually small in size and in some cases range considerably in composition. Accuracy of the measurements depends on systematic errors within the EDX equipment and program. None of these data, but especially not those of the reaction products, should be regarded in an other way than as indication of possible values for the observed phases.

Data for Maryland Diabase are given in Table F.1, for Bransrode Basalt in Table F.2 and for Vogelsberg Basalt in Table F.3.

	Starting material				$T = 500^\circ\text{C}$		
	Di	Pgt	An	Crn	Plg	Amp	Bt
[mol%]							
Na_2O			3.40		5.0	0.3	0.2
MgO	22.39	25.52		2.25		19.2	21.1
Al_2O_3	1.75	0.79	20.08		17.9	4.3	8.7
SiO_2	50.3	50.4	59.04	35.12	64.0	50.9	45.3
K_2O			0.19		1.1	0.6	4.3
CaO	17.6	1.71	17.00		11.7	11.9	1.7
TiO_2						0.1	0.6
FeO	7.98	21.61	0.40	69.80	10.4	12.7	14.8
ClO_2							0.08

Table F.1: Mineral compositions of Maryland Diabase - starting material and newly formed minerals after deformation and heat treatment at $T = 500^\circ\text{C}$. Mineral abbreviations after Kretz (1983); all Fe is reported as FeO. Crn = cronstedtite.

	Starting material					Alteration products				
	Aug	Ol	Plg	Mag	Ilm	glass	Chl	Bt	Tlc	
[mol%]										
Na ₂ O			3.98			5.53	0.64			
MgO	17.63	43.62		4.01	5.15	2.25	28.64	25.69	31.04	
Al ₂ O ₃	2.01	0.11	18.91	0.75		16.10	8.77	8.74	1.75	
SiO ₂	48.30	34.31	62.33			66.37	38.37	43.26	54.21	
K ₂ O			0.91			3.55	0.57	5.74		
CaO	23.90	0.10	13.1			24.60	1.84			
TiO ₂	1.44			19.47	48.28			4.38		
FeO	6.68	21.55	0.63	73.64	46.57	1.85	21.82	12.32	12.99	
Cr ₂ O ₃				0.33						
MnO ₂		0.26		0.60						

Table F.2: Mineral compositions of Bransrode Basalt - starting material and pre-existing alteration products. Mineral abbreviations after Kretz (1983).

	Starting material						$T = 300^\circ\text{C}$			$T = 500^\circ\text{C}$		
	Di	Ol	An	Spl	g-Fsp	g-rim	Ab	Amp	Chl	Amp	Bt	An
[mol%]												
Na ₂ O	0.50		4.29		7.36	5.75	8.92	1.11		1.8	0.6	5.9
MgO	16.35	52.92		12.26		4.01		11.85	38.3	13.3	29.7	
Al ₂ O ₃	5.34		19.43	4.30	15.81	14.30	16.88	9.70	7.77	9.0	8.6	17.6
SiO ₂	43.76	34.74	60.53		65.33	61.93	68.09	55.16	41.88	52.2	43.8	65.0
K ₂ O			0.52		5.69	3.52	1.19	3.67	0.53	2.6	5.3	1.3
CaO	24.27		14.73	0.14	2.15	4.97	4.19	12.91		13.1	0.6	10.8
TiO ₂	3.25		0.11	16.00	1.24	1.36	0.43	1.41		1.9	0.9	
FeO	6.53	12.33	0.40	65.86	3.31	3.19	0.40	3.56	11.6	6.3	10.1	
P ₂ O ₅						0.84						
SO ₃						0.85						
Cr ₂ O ₃				1.16								
MnO				0.30								
ClO ₂											1.01	

Table F.3: Mineral compositions of Vogelsberg Basalt - starting material and newly formed minerals after deformation and heat treatment at $T = 300$ and 500°C . Mineral abbreviations after Kretz (1983); g-Fsp and g-rim show the range in glass composition.

Bibliography

- Amitrano, D. and Schmittbuhl, J. (2002). Fracture roughness and gouge distribution of a granite shear band. *Journal of Geophysical Research*, 107(12):2375–2390.
- An, L.-J. and Sammis, C. (1994). Particle size distribution of cataclastic fault materials from southern California: A 3-D study. *Pure & Applied Geophysics*, 143(1/2/3):203–227.
- Anderson, J., Osborne, R., and Palmer, D. (1980). Petrogenesis of cataclastic rocks within the San Andreas Fault Zone of southern California, U.S.A. *Tectonophysics*, 67:221–249.
- Anderson, J., Osborne, R., and Palmer, D. (1983). Cataclastic rocks of the San Gabriel Fault—An expression of deformation at deeper crustal levels in the San Andreas Fault Zone. *Tectonophysics*, 98:209–251.
- Avé Lallemant, H. (1978). Experimental deformation of diopside and websterite. *Tectonophysics*, 48:1–27.
- Bass, J. (1995). Elasticity of Minerals, Glasses, and Melts. In Ahrens, T., editor, *Mineral Physics & Crystallography - A handbook of Physical Constants*, volume 2 of *AGU Reference Shelf*, pages 45–63. AGU, Washington.
- Bernoulli, D. and Winkler, W. (1990). Heavy mineral assemblages from Upper Cretaceous South- and Austroalpine flysch sequences (northern Italy and southern Switzerland): source terrains and palaeotectonic implications. *Eclogae geologicae Helveticae*, 83:287–310.
- Biegel, R., Sammis, C., and Dietrich, J. (1989). The frictional properties of a simulated gouge having a fractal particle distribution. *Journal of Structural Geology*, 11(7):827–846.
- Billi, A., Salvini, F., and Storti, F. (2003). The damage zone-fault core transition in carbonate rocks: implications for fault growth, structure and permeability. *Journal of Structural Geology*, 25:1779–1794.
- Blanpied, M., Lockner, D., and Byerlee, J. (1995). Frictional slip of granite at hydrothermal conditions. *Journal of Geophysical Research*, 100(B7):13045–13064.
- Blanpied, M., Tullis, T., and Weeks, J. (1998). Effects of slip, slip rate, and shear heating on the friction of granite. *Journal of Geophysical Research*, 103:489–512.
- Blenkinsop, T. (1991). Cataclasis and Processes of Particle Size Reduction. *Pure & Applied Geophysics*, 136:60–86.
- Blenkinsop, T. and Rutter, E. (1986). Cataclastic deformation of quartzite in the Moine thrust zone. *Journal of Structural Geology*, 8(6):669–681.

- Blenkinsop, T. and Sibson, R. (1992). Aseismic fracturing and cataclasis involving reaction softening within core material from the Canjon Pass drill hole. *Journal of Geophysical Research*, 97:51355144.
- Bons, P. (2000). The formation of veins and their microstructures. In Jessell, M. and Urai, J., editors, *Stress, Strain and Structure, A volume in honour of W. D. Means*, volume 2.
- Borg, I., Friedman, M., Handin, J., and Higgs, D. (1960). Experimental deformation of Saint Peter sand—A study of cataclastic flow. In Griggs, D., editor, *Memoir - Geological Society of America*, pages 133–191. Geological Society of America, Boulder, CO.
- Borg, I. and Handin, J. (1966). Experimental deformation of crystalline rocks. *Tectonophysics*, 3(4):249–368.
- Bos, B., Peach, C., and Spiers, C. (2000). Slip behaviour of simulated gouge-bearing faults under conditions favoring pressure solution. *Journal of Geophysical Research*, 105(B7):16699–16717.
- Bos, B. and Spiers, C. (2002). Fluid-assisted healing processes in gouge-bearing faults: insights from experiments on a rock analogue system. *Pure & Applied Geophysics*, 159:2537–2566.
- Boullier, A.-M., Fujimoto, K., Ito, H., Ohtani, T., Keulen, N., Fabbri, O., Amitrano, D., Dubois, M., and Pezard, P. (2004a). Structural evolution of the Nojima Fault (Awaji Island, Japan) revisited from the GSJ drillhole at Hirabayashi. *Earth Planets Space*, 56:1233–1240.
- Boullier, A.-M., Fujimoto, K., Ohtani, T., Roman-Ross, G., Lewin, E., Ito, H., Pezard, P., and Ildefons, B. (2004b). Textural evidence for recent co-seismic circulation of fluids in the Nojima Fault zone, Awaji Island, Japan. *Tectonophysics*, 378:165–181.
- Boullier, A.-M., Ildefonse, B., Gratier, J.-P., Fujimoto, K., Ohtani, T., and Ito, H. (1999). Deformation textures and mechanisms in the granodiorite from the Nojima Hirabayashi borehole. In Ito, H., Fujimoto, K. and Tanaka, H., and Lockner, D., editors, *International workshop of the Nojima fault core and borehole data analysis*, page 111117. Geological Survey of Japan, Tsukuba.
- Boullier, A.-M., Ohtani, T., Fujimoto, K., Ito, H., and Dubois, M. (2001). Fluid inclusions in pseudotachylytes from the Nojima fault, Japan. *Journal of Geophysical Research*, 106:21965–21977.
- Brack, P. (1981). Structures in the southwestern border of the Adamello intrusion (Alpi bresciane). *Schweizerische Mineralogische und Petrographische Mitteilungen*, 61(1):37–50.
- Brodie, K. and Rutter, E. (1985). On the relationship between deformation and metamorphism, with special reference to the behaviour of basic rocks. In Thompson, A. and Rubie, D., editors, *Metamorphic reactions - kinetics, textures, and deformation*, pages 138–179. Springer.
- Byerlee, J. (1967). Frictional characteristics of granite under high confining pressure. *Journal of Geophysical Research*, 72:3639–3648.
- Byerlee, J. (1978). Friction of rocks. *Pure Applied Geophysics*, 116:4741–4750.
- Byerlee, J. and Brace, W. (1968). Stick slip, stable sliding, and earthquakes - effect of rock type, pressure, strain rate, and stiffness. *Journal of Geophysical Research*, 73(18):6031–6037.
- Caristan, Y. (1982). The transition from high temperature creep to fracture in Maryland Diabase. *Journal of Geophysical Research*, 87(B8):6781–6790.
- Carmichael, R. (1989). *Practical Handbook of Physical Properties of Rocks and Minerals*. CRC-Press, Boca Raton.

- Carminati, E. and Siletto, G. (2005). The Central Southern Alps (N.Italy) paleoseismic zone: a comparison between field observations and predictions of fault mechanisms. *Tectonophysics*, 401(3-4):179–197.
- Carpenter, M. (1992). Thermodynamics of phase transitions in minerals; a macroscopic approach. In Price, G. and Ross, N., editors, *The stability of minerals*, volume 3, pages 172–215. Mineralical Society of Great Britain, London.
- Carter, N., Anderson, D., Hansen, F., and Kranz, R. (1981). Creep and creep rupture of granitic rocks. In Carter, N., Friedman, M., Logan, J., and Stearns, D., editors, *Geophysical Monograph: Mechanical behavior of crustal rocks; the Handin volume*, volume 24, pages 61–62. American Geophysical Union, Washington, DC, United States.
- Chatraine, J., Autran, A., Cavelier, C., et al. (1996). *Carte géologique de la France à l' échelle du millionième*, volume 6e édition. BRGM, Orléans.
- Chester, F., Evans, J., and Biegel, R. (1993). Internal structure and weakening mechanisms of the San Andreas Fault. *Journal of Geophysical Research*, 98(B1):771–786.
- Chester, F., Friedman, M., and Logan, J. (1985). Foliated cataclasites. *Tectonophysics*, 111:139–146.
- Chester, J., Chester, F., and Kronenberg, A. (2005). Fracture surface energy of the Punchbowl fault, San Andreas system. *Nature*, 437:133–136.
- Cladouhos, T. (1999). Shape preferred orientation of survivor grains in fault gouge. *Journal of Structural Geology*, 21:419–436.
- Clark, S. J. (1966). *Geological Society of America Memoir*, volume 97. Yale University Press.
- De Ronde, A. (2004). *Mineral Reaction and Deformation in Plagioclase-Olivine Composites: An Experimental Study*. PhD thesis, Basel University.
- De Ronde, A., Heilbronner, R., Stünitz, H., and Tullis, J. (2004). Spatial correlation of deformation and mineral reaction in experimentally deformed plagioclase-olivine aggregates. *Tectonophysics*, 389(1-2):93–109.
- De Ronde, A., Stünitz, H., Tullis, J., and Heilbronner, R. (2005). Reaction-induced weakening of plagioclase-olivine composites. *Tectonophysics*, 409:85106.
- De Sitter, L. and De Sitter-Koomans, C. (1949). The Geology of the Bergamase Alps, Lombardia, Italy. *Leidse Geologische Mededelingen*, XIVB:1–257.
- Del Moro, A., Pardini, G., Quercioli, C., Villa, I., and Callegari, E. (1983). Rb/ Sr and K/ Ar chronology of Adamello granitoids, southern Alps. *Memorie della Societa Geologica Italiana*, 26:285–299.
- Den Brok, S. (1998). Effect of microcracking on pressure-solution strain rate: The Gratz grain-boundary model. *Geology*, 26(10):915–918.
- Den Brok, S. B. (1992). *An experimental investigation into the effect of water on the flow of quartzite*. PhD thesis, Utrecht University.
- Di Toro, G. and Pennacchioni, G. (2005). Fault plane processes and mesoscopic structure of a strong-type seismogenic fault in tonalites Adamello batholite, Southern Alps. *Tectonophysics*, 402:55–80.
- Dietrich, J. (1972). Time dependent friction in rocks. *Journal of Geophysical Research*, 77:3690–3697.

- Dietrich, J. (1979). Modeling of rock friction, 1. Experimental results and constitutive equations. *Journal of Geophysical Research*, 84(B5):2161–2168.
- Dietrich, J. and Kilgore, B. (1994). Direct observations of frictional contacts: new insights for state-dependent properties. In Marone, C. and Blanpied, M., editors, *Faulting, Friction, and Earthquake Mechanics*, volume 2, page 41964202. Birkhauser, Basel.
- Dor, O., Ben-Zion, Y., Rockwell, T., and Brune, J. (2006). Pulverized rocks in the Mojave section of the San Andreas Fault Zone. *Earth and Planetary Science Letters*, 245:642–654.
- Dove, P. and Crerar, D. (1990). Kinetics of silica-water reactions. *Geochimica Cosmochimica Acta*, 54:955–969.
- Dresmann, H., Keulen, N., Timar-Geng, Z., Fügenschuh, B., Wetzel, A., and Stünitz, H. (in press, 2009). The south-western Black Forest and the Upper Rhine Graben Main Border Fault: thermal history and hydrothermal fluid flow. *International Journal Earth Sciences*, doi: 10.1007/500531-008-0391-3.
- Echtler, H. and Chauvet, A. (1992). Carboniferous convergence and subsequent crustal extension in the Southern Schwarzwald (SW Germany). *Geodinamica Acta*, 5(1-2):37–49.
- Engelder, J. (1974). Cataclasis and the generation of fault gouge. *Bulletin of the Geological Society of America*, 85:1515–1522.
- Evans, J. and Chester, F. (1995). Fluid-rock interaction in faults of the San Andreas system: Inferences from San Gabriel fault rock geochemistry and microstructures. *Journal of Geophysical Research*, B7:13007–13020.
- Fabbri, O., Iwamura, K., Matsunaga, S., Coromina, G., and Kanaori, Y. (2004). Distributed strike-slip faulting, block rotation, and possible intracrustal vertical decoupling in the convergent zone. In Grocott, J., Tikoff, B., McCaffrey, K., and Taylor, G., editors, *Vertical coupling and decoupling in the lithosphere*, volume 227, pages 141–166. Geological Society London Special Publications, London.
- Faulkner, D., Lewis, A., and Rutter, E. (2003). On the internal structure and mechanics of large strike-slip fault zones: field observations of the Carboneras fault in southeastern Spain. *Tectonophysics*, 367:235–251.
- Fernlund, J. (1998). The effect of particle form on sieve analysis: a test by image analysis. *Engineering Geology*, 50:111–124.
- Fredrich, J. and Wong, T.-F. (1986). Micromechanics of thermally induced cracking in three crustal rocks. *Journal of Geophysical Research*, 91(B12):12743–12746.
- Fujimoto, K., Tanaka, H., Higuchi, T., Tomida, N., Ohtani, T., and Ito, H. (2001). Alteration and mass transfer inferred from the Hirabayashi GSJ drill core penetration the Nojima Fault, Japan. *The Island Arc*, 10(401-410).
- Fusseis, F., Handy, M., and Schrank, C. (2006). Shear zone networks at the brittle-to-viscous transition (Cap de Creus, NE Spain). *Journal of Structural Geology*, 28(7):1228–1243.
- Geyer, O. and Gwinner, M. (1986). *Geologie von Baden-Württemberg*. Schweizerbart, Stuttgart.
- Giger, S., Tenthorey, E., Cox, S., and FitzGerald, J. (2006). Permeability and porosity evolution of quartz fault gouges during hot pressing under hydrothermal conditions. *Eos Trans. AGU Fall Meet. Suppl.*, 87(52):S41D06.
- Gleason, G. and Tullis, J. (1995). A flow law for dislocation creep of quartz aggregates determined with the molten salt cell. *Tectonophysics*, 247:1–23.

- Griggs, D. (1967). Hydrolitic weakening of quartz and other silicates. *Geophysical Journal of the Royal Astronomical Society*, 30(14):19–31.
- Griggs, D., Turner, F., and Heard, H. (1960). Deformation of rocks at $T = 500^{\circ}\text{C}$ to $T = 800^{\circ}\text{C}$. In Griggs, D. and Handin, J., editors, *Geological Society of America, Memoir*, volume 79, pages 39–104. Waverly Press, Baltimore, MD.
- Guo, Y. and Morgan, J. (2002). Influence of grain fracture and shape evolution on fault gouge strength in particle dynamics simulations. *Eos Transactions AGU Fall Meeting Supplement*, 83(47):F1375–1376.
- Hacker, B. and Christie, J. (1991). Experimental deformation of a glassy basalt. *Tectonophysics*, 200:79–96.
- Hadzadeh, J. and Johnson, W. (2003). Estimating local strain due to comminution in experimental cataclastic textures. *Journal of Structural Geology*, 25:1973–1979.
- He, C., Yao, W., Wang, Z., and Zhou, Y. (2006). Strength and stability of frictional sliding of gabbro gouge at elevated temperatures. *Tectonophysics*, doi:10.1016/j.tecto.2006.05.023(427).
- Heard, H. (1960). Transition from Brittle to Ductile Flow in Solenhofen Limestone as a function of temperature, confining pressure, and interstitial fluid pressure. In *Rock Mechanics (A symposium)*, volume 79, pages 193–226. Waverly Press, Baltimore, MD.
- Heilbronner, R. (2000). Automatic grain boundary detection and grain size analysis using polarization micrographs or orientation images. *Journal of Structural Geology*, 22:969–981.
- Heilbronner, R. (2002). Analysis of bulk fabrics and microstructure variations using tessellations of autocorrelation functions. *Computers and Geosciences*, 28(4):447–455.
- Heilbronner, R. and Keulen, N. (2006). Grain size and grain shape analysis of fault rocks. *Tectonophysics*, 427(1-4):Pages 199–216.
- Heilbronner, R. and Tullis, J. (2002). The effect of static annealing on microstructure and crystallographic preferred orientations of quartzites experimentally deformed in axial compression and shear. In de Meer, S., Drury, M. R., de Bresser, J. H. P., and Pennock, G. M., editors, *Deformation Mechanisms, Rheology and Tectonics: Current Status and Future Perspectives*, volume 200, pages 191–218. Geological Society London, Special Publication.
- Heilbronner Panozzo, R. (1992). The autocorrelation function: an image processing tool for fabric analysis. *Tectonophysics*, 212:351–370.
- Heki, K., Miyazaki, S., and Tsuji, H. (1997). Silent fault slip following and interplate thrust earthquake at the Japan Trench. *Nature*, 386:695–698.
- Hinsken, S. (2003). *Geologische Untersuchungen an Syn-riftsedimenten des südlichen Oberrheingraben*. Master Thesis, Geologisch-Paläontologisches Institut, University Basel.
- Hirose, T. and Shimamoto, T. (2003). Fractal dimension of molten surfaces as a possible parameter to infer the slip-weakening distance of faults from natural pseudotachylytes. *Journal of Structural Geology*, 25(10):1569–1574.
- Hirth, G. and Tullis, J. (1989). The effects of pressure and porosity on the micromechanics of the brittle-ductile transition in quartzite. *Journal of Geophysical Research*, 94(B12):17825–17838.
- Hirth, G. and Tullis, J. (1992). Dislocation creep regimes in quartz aggregates. *Journal of Structural Geology*, 14(2):145–159.

- Hirth, G. and Tullis, J. (1994). The brittle-plastic transition in experimentally deformed quartz aggregates. *Journal of Geophysical Research*, 99(B6):11731–11747.
- Hoffmann, N. and Schönert, K. (1971). Bruchanteil von Glaskugeln in Packungen von Fraktionen und binären Mischungen. *Aufbereitungstechnik*, 9:513–518.
- Huber, M. and Huber-Aleffi, A. (1990). Zur Tektonik des Südschwarzwaldes. In *Nagra Technischer Bericht*, volume 90-03, pages 7–8. Nagra, Baden.
- Hyndman, R. and Wang, K. (1995). The rupture zone of Cascadia great earthquakes from current deformation and the thermal regime. *Journal of Geophysical Research*, 100(B11):22133–22154.
- Icenhower, J. and Dove, P. (2000). The dissolution kinetics of amorphous silica into sodium chloride solutions: Effects of temperature and ionic strength. *Geochimica et Cosmochimica Acta*, 64(24):4193–4203.
- Ito, H., Fujimoto, K., Tanaka, H., and Lockner, D. (1999). *Proceedings of the international workshop on the Nojima fault core and borehole data analysis*, volume GSJ Interim report No. EQ/00/1, USGS Open-File Report 000-129. Geological Survey of Japan, Tsukuba, Japan.
- Jaeger, J. (1967). Failure of rocks under tensile conditions. *International Journal of Rock Mechanics and Mining Sciences*, 4:219–237.
- James, E. and Silver, L. (1988). Implications of zeolites and their zonation in the Cajon Pass deep drill hole. *Geophysical Research Letters*, 15:973–976.
- Jefferies, S., Holdsworth, R., Wibberley, C., Shimamoto, T., Spiers, C., Niemeijer, A., and Lloyd, G. (2006). The nature and importance of phyllonite development in crustal-scale fault cores; an example from the Median Tectonic Line, Japan. *Journal of Structural Geology*, 28(2):220–235.
- Kanagawa, K., Cox, S., and Zhang, S. (2000). Effects of dissolution-precipitation processes on the strength and mechanical behavior of quartz gouge at high-temperature hydrothermal conditions. *Journal of Geophysical Research*, 105:11115–11126.
- Kanamori, H. (1994). Mechanics of earthquakes. *Annual Review of Earth and Planetary Sciences*, 22:207–238.
- Kanaori, Y. (1990). Late Mesozoic-Cenozoic strike-slip and block rotation in the inner belt of Southwest Japan. *Tectonophysics*, 177:381–399.
- Karner, S., Marone, C., and Evans, B. (1997). Laboratory study of fault healing and lithification in simulated fault gouge under hydrothermal conditions. *Tectonophysics*, 277:41–55.
- Kato, A., Ohnaka, M., and Mochizuki, H. (2003). Constitutive properties for the shear failure of intact granite in seismogenic environments. *Journal of Geophysical Research*, 108(B1):doi:10.1029/2001JB000791.
- Kay, M., Main, I., Elphick, S., and Ngwenya, B. (2006). Fault gouge diagenesis at shallow burial depth: Solution-precipitation reactions in well-sorted and poorly sorted powders of crushed sandstone. *Earth and Planetary Science Letters*, 243:607–614.
- Keller, J., Kraml, M., and Henjes-Kunst, F. (1992). Schweizerische mineralogische und petrographische mitteilungen. ⁴⁰Ar/³⁹Ar single crystal laser dating of early volcanism in the Upper Rhine Graben and tectonic implications, 82(1):121–130.
- Kendall, K. (1978). The impossibility of comminuting small particles by compression. *Nature*, 272:710–711.

- Keulen, N., Heilbronner, R., Stünitz, H., and Ramseyer, K. (2006). Microstructures of healed granitoid Fault Gouge - a Combination of Cathodoluminescence and BSE-Contrast SEM Imaging. In *Geophysical Research Abstracts*, volume 8, pages EGU06–A–08088. EGU, Vienna.
- Keulen, N., Heilbronner, R., Boullier, A.-M., and Stünitz, H. (2003a). What happens after fracturing? Particle size distribution and grain growth in experimentally deformed granitoids. In *1st Swiss Geoscience Meeting*, page 54. University of Basel, Basel.
- Keulen, N., Heilbronner, R., and Stünitz, H. (2003b). Microstructures and grain size distribution of naturally and experimentally deformed polyphase cataclasites - some preliminary results. In *Deformation Mechanisms, Rheology and Tectonics*, page 93. University of Rennes, Saint Malo, France.
- Keulen, N., Stünitz, H., and Heilbronner, R. (2008). Healing microstructures of experimental and natural fault gouge. *Journal of Geophysical Research*, 113(B06205):doi:10.1029/2007JB005039.
- Kirby, S. and Kronenberg, A. (1984). Deformation of clinopyroxenite; evidence for a transition in flow mechanisms and semibrittle behavior. *Journal of Geophysical Research*, 89(B5):3177–3192.
- Kitajima, T., Kobayashi, Y., Ikeda, R. and Iio, Y., and Omura, K. (1998). Terrestrial heat flow in Nojima-Hirabayashi, Awaji Island. *Chikyū Monthly, in Japanese*, 21:108–113.
- Kohlstedt, D., Evans, B., and Mackwell, S. (1995). Strength of the lithosphere: Constraints imposed by laboratory experiments. *Journal of Geophysical Research*, 100(B9):17587–17602.
- Korvin, G. (1992). *Fractal Models in the Earth Sciences*. Elsevier, Amsterdam.
- Kretz, R. (1983). Symbols for rock-forming minerals. *American Mineralogist*, 68:277–279.
- Kronenberg, A. and Shelton, G. (1980). Deformation microstructures in experimentally deformed Maryland Diabase. *Journal of Structural Geology*, 2(3):341–352.
- Kumar, A. (1968). The effect of stress rate and temperature on the strength of basalt and granite. *Geophysics*, 33:501–510.
- Laubscher, H. (1985). Large-scale, thin-skinned thrusting in the Southern Alps: Kinematic models. *Geological Society America Bulletin*, 96:710–718.
- Lin, A. (1999a). Roundness of clasts in pseudotachylytes and cataclastic rocks as an indicator of frictional melting. *Journal of Structural Geology*, 21:473–478.
- Lin, A. (1999b). S-C cataclasite in granitic rock. *Tectonophysics*, 304:57–273.
- Lockner, D., Summers, R., and Byerlee, J. (1986). Effects of temperature and sliding rate on frictional strength of granite. *Pure & Applied Geophysics*, 124(3):445–469.
- Mackwell, S., Zimmerman, M., and Kohlstedt, D. (1998). High-temperature deformation of dry diabase with application to tectonics on Venus. *Journal of Geophysical Research*, 103(B1):975–984.
- Mair, K., Frye, K., and Marone, C. (2002). Influence of grain characteristics on the friction of granular shear zones. *Journal of Geophysical Research*, 107(B10):ECV 4–1; doi: 2001JB000516.
- Mandelbrot (1982). *The fractal Geometry of Nature*. Freeman and Co., New York.
- Manning, C. (1994). The solubility of quartz in H₂O in the lower crust and upper mantle. *Geochimica et Cosmochimica Acta*, 58:4831–4839.

- Mares, V. and Kronenberg, A. (1993). Experimental deformation of muscovite. *Journal of Structural Geology*, 15(9/10):1061–1076.
- Marone, C. (1998). The effect of loading rate on static friction and the rate of fault healing during the earthquake cycle. *Nature*, 391:69–72.
- Marone, C. and Scholz, C. (1989). Particle-size distribution and microstructures within simulated fault gouge. *Journal of Structural Geology*, 11(7):799–814.
- Marone, C., Vidale, J., and Ellsworth, W. (1995). Fault healing inferred from time dependent variations in source properties of repeating earthquakes. *Geophysical Research Letters*, 22(22):3095–3098.
- Means, W. and Li, T. (2001). A laboratory simulation of fibrous veins: Some first observations. *Journal of Structural Geology*, 23:857–863.
- Mei, S., Bai, W., Hiraga, T., and Kohlstedt, D. (2002). Influence of melt on the creep behavior of olivine-basalt aggregates under hydrous conditions. *Earth and Planetary Science Letters*, 201:491–507.
- Milano, P., Pennacchioni, G., and Spalla, M. (1988). Alpine and pre-Alpine tectonics in the Central Orobic Alps (Southern Alps). *Eclogae geologicae Helveticae*, 81(2):273–293.
- Mitra, G. (1978). Ductile deformation zones and mylonites; the mechanical processes involved in the deformation of crystalline basement rocks. *American Journal of Science*, 278:1057–1084.
- Mitra, G. (1992). Deformation of granitic basement rocks along fault zones at shallow to intermediate crustal levels. In Mitra, S. and Fisher, G., editors, *Structural Geology of Fold and Thrust Belts.*, pages 123–144. John Hopkins University Press, Baltimore.
- Mitra, G. (1993). Deformation processes in brittle deformation zones in granitic basement rocks: A case study from the Torrey Creek area, Wind River Mountains. In Schmidt, C., Chase, R., and Erslev, E., editors, *Laramide Basement Deformation in the Rocky Mountains Foreland of the Western United States*, volume 280 of *Geological Society of America Special Paper*, pages 177–195. Boulder, Colorado.
- Mitra, G. and Ismat, Z. (2001). Microfracturing associated with reactivated fault zones and shear zones: what can it tell us about deformation history? In Holdsworth, R., Strachan, R., Magloughlin, J., and Knipe, R., editors, *The nature and significance of fault zone weakening*, volume 186, pages 113–140. Geological Society Special Publication, London.
- Mizuno, K., Hattori, H., Sangawa, A., and Takahashi, H. (1990). *Geology of the Akashi district with geological sheet map, in Japanese with English abstract*. Geological Survey of Japan, Tsukuba.
- Monzawa, N. and Otsuki, K. (2003). Comminution and fluidization of granular fault materials: implications for fault slip behavior. *Tectonophysics*, 367:127–143.
- Moore, d., Lockner, D., Tanaka, H., and Iwata, K. (2004). The coefficient of friction of chrysotile gouge at seismogenic depths. In Ernst, W., editor, *Serpentine and serpentinites. Mineralogy, Petrology, Geochemistry, Ecology, Geophysics, and Tectonics*, volume 8, pages 525–538. Bellweather Publishing for the Geological Society of America, Columbia, MD.
- Morgan, J. (1999). Numerical simulations of granular shear zones using the distinct element method. 2. Effects of particle size distribution and interparticle friction on mechanical behavior. *Journal of Geophysical Research*, 104(B2):2721–2732.
- Morgan, J. and Boettcher, M. (1999). Numerical simulations of granular shear zones using the distinct element method. 1. Shear zone kinematics and the micromechanics of localization. *J. Geoph. Res.*, 104(B2):2703–2719.

- Morrow, C. and Byerlee, J. (1989). Experimental studies of compaction and dilatancy during frictional sliding on faults containing gouge. *Journal of Structural Geology*, 11(7):815–826.
- Muhuri, S., Dewers, T., Thurman, E. J., and Reches, Z. (2003). Interseismic fault strengthening and earthquake-slip instability: Friction or cohesion? *Geology*, 31(10):881–884.
- Murakami, M. and Tagami, T. (2004). Dating pseudotachylyte of the Nojima fault using the zircon fission-track method. *Geophysical Research Letters*, 31:doi: 10.1029/2004GL020211.
- Murata, A., Takemura, K., Miyata, T., and Lin, A. (2001). Quaternary vertical offset and average slip rate of the Nojima Fault on Awaji Island, Japan. *The Island Arc*, 10:360–367.
- Nadeau, R. and McEvilly, T. (1999). Fault slip rates at depth from recurrence intervals of repeating microearthquakes. *Science*, 285:718–721.
- Nakamura, M., Yurimoto, H., and Watson, E. (2005). Grain growth control of isotope exchange between rocks and fluids. *Geology*, 33(10):829–832.
- Nakatani, M. and Scholz, C. (2004). Frictional healing of quartz gouge under hydrothermal conditions: 1. Experimental evidence for solution transfer healing mechanism. *Journal of Geophysical Research*, 109(B07201):doi:10.1029/2001JB001522.
- Olgaard, D. and Brace, W. (1983). The microstructure of gouge from a mining-induced seismic shear zone. *International Journal of Rock Mechanics and Mining Science & Geomechanical Abstracts*, 20(1):11–19.
- Olgaard, D. and Evans, B. (1988). Grain growth in synthetic marbles with added mica and water. *Contributions to Mineralogy and Petrology*, 100:246–260.
- Olsen, M., Scholz, C., and Léger, A. (1998). Healing and sealing of a simulated fault gouge under hydrothermal conditions: implications for fault healing. *Journal of Geophysical Research*, 103:7421–7430.
- Otsuki, K., Monzawa, N., and Nagase, T. (2003). Fluidization and melting of fault gouge during seismic slip: Identification in the Nojima fault zone and implications for focal earthquake mechanisms. *Journal of Geophysical Research*, B4:ESE 4-1 – 4-18.
- Panozzo, R. (1984). Two-dimensional analysis of shape-fabric using projections of digitized lines in a plane. *Tectonophysics*, 95(3-4):279–294.
- Panozzo, R. and Hürlimann, H. (1983). A simple method for the quantitative discrimination of convex and convex-concave lines. *Microscopica Acta*, 87:169–176.
- Panozzo Heilbronner, R. (1988). Distortion of orientation data introduced by digitizing procedures. *Journal of Microscopy*, 149:83–96.
- Passchier, C. and Trouw, R. (1998). *Microtectonics*. Springer, Berlin, 2nd edition.
- Paterson, M. (1978). *Experimental Rock Deformation - the Brittle Field*, volume 13. Springer-Verlag, Heidelberg.
- Paterson, M. (1995). A theory for granular flow accommodated by material transfer via an intergranular fluid. *Tectonophysics*, 245:135–151.
- Pennacchioni, G., Di Toro, G., Brack, P., Menegon, L., and Villa, I. (2006). Brittle-ductile-brittle deformation during cooling of tonalite (Adamello, Southern Italian Alps). *Tectonophysics*, 427(1-4):171–197.

- Pittarello, L., Di Toro, G., Bizzarri, A., Hadizadeh, J., and Pennacchioni, G. (2006). Seismic energy partitioning inferred from pseudotachylite-bearing faults (Gole Larghe Fault, Adamello batholith, Italy). In *Geophysical Research Abstracts*, volume 8, pages EGU06–A–01883. EGU, Vienna.
- Prasher, C. (1987). *Crushing and Grinding Process Handbook*. Wiley, New York.
- Ramseyer, K., Fischer, J., Matter, A., Eberhardt, P., and Geiss, J. (1989). A cathodoluminescence microscope for low intensity luminescence. *Journal of Sedimentary Petrology*, 59:619–622.
- Ramseyer, K. and Mullis, J. (2000). Geological application of cathodoluminescence of silicates. In Pagel, M., Barbin, V., Blanc, P., and Ohnenstetter, D., editors, *Cathodoluminescence in Geosciences*, pages 177–191. Springer, Berlin.
- Rawling, G. and Goodwin, L. (2003). Cataclasis and particulate flow in faulted, poorly lithified sediments. *Journal of Structural Geology*, 25:317–331.
- Reches, Z. and Dewers, T. (2005). Gouge formation by dynamic pulverization during earthquake rupture. *Earth and Planetary Science Letters*, 235:361–374.
- Rocchi, V., Sammonds, P., and Kilburn, C. (2002). Flow and fracture maps for basaltic rock deformation at high temperatures. *Journal of Volcanology and Geothermal Research*, 120:25–42.
- Rossi, M. (2005). *Déformation, transferts de matière et de fluide dans la croûte continentale: application aux massifs cristallins externes des Alpes*. PhD thesis, Université Joseph Fourier - Grenoble 1.
- Rossi, M., Vidal, O., Wunder, B., and Renard, F. (subm). Experimental study of deformation processes in aggregates made of spherical grains: time-dependent changes and effects of temperature, isostatic confining pressure and fluid content. *Tectonophysics*, x:xx.
- Rutter, E. (1986). On the nomenclature of mode of failure in rocks. *Tectonophysics*, 122(3/4):381–387.
- Rutter, E. and Maddock, R. (1992). On the mechanical properties of synthetic kaolinite/quartz fault gouge. *Terra Nova*, 4:489–500.
- Rutter, E., Peach, C., White, S., and Johnston, D. (1985). Experimental ‘syntectonic’ hydration of basalt. *Journal of Structural Geology*, 7(2):251–266.
- Rybacki, E., Renner, J., Konrad, K., Harbott, W., Rummel, F., and Stöckhert, B. (1998). A servohydraulically-controlled deformation apparatus for rock deformation under conditions of ultra-high pressure metamorphism. *Pure & Applied Geophysics*, 152:579–606.
- Sammis, C., King, G., and Biegel, R. (1987). The kinematics of gouge deformation. *Pure & Applied Geophysics*, 125:777–812.
- Sammis, C., Osborne, R., Anderson, J., Banerdt, M., and White, P. (1986). Self-similar cataclasis in the formation of fault gouge. *Pure & Applied Geophysics*, 124(1-2):53–78.
- Sato, T. and Takahashi, M. (1999). Chemical and isotopic compositions of groundwater obtained from the Hirabayashi well, in international workshop of the Nojima fault core and borehole data analysis. *GSI Interim report No. EQ/00/1, USGS Open-File Report 000-129*, page 187192.
- Sawatzki, G., Hincke, E., and Piepjohn, K. (1998). Wehr. In *Geologische Karte von Baden-Württemberg 1:25000*, volume 8313. Geologisches Landesvermessungsamt Baden-Württemberg, Freiburg i. Br.

- Schmid, S. and Handy, M. (1991). Towards a genetic classification of fault rocks: Geological usage and tectonophysical implications. In Müller, D., McKenzie, J., and Weissert, H., editors, *Controversies in Modern Geology*, pages 339–361. Academic Press, London.
- Schoenborn, G. (1992). Alpine tectonics and kinematic model of the central Southern-Alps. *Memorie della Societa Geologica Italiana*, 44:229–393.
- Schoenborn, G. and Schumacher, M. (1994). Controls on thrust tectonics along basement-cover detachment. *Schweizerische Mineralogische und Petrographische Mitteilungen*, 74:421–436.
- Scholz, C. (1990). *Mechanics of Earthquakes and Faulting*. Cambridge University Press, Cambridge.
- Scholz, C. and Engelder, T. (1976). Role of asperity indentation and ploughing in rock friction. *International Journal of Rock Mechanics Mining Sciences*, 13:149154.
- Schumacher, M. (2002). Upper Rhine Graben: The role of pre-existing structures during rift evolution. *Tectonics*, 21(1):DOI: 10.1029/2001TC900022.
- Shao, S.-M. and Zou, J.-C. (1996). Fractal research of fault gouge. *Acta Seismologica Sinica*, 9(3):485–491.
- Shea Jr, W. and Kronenberg, A. (1993). Strength and anisotropy of foliated rocks with varied mica contents. *Journal of Structural Geology*, 15(9/10):1097–11122.
- Sheu, S.-Y. and Shieh, C.-F. (2004). Viscoelastic-afterslip concurrence; a possible mechanism in the early post-seismic deformation of the M_w 7.6, 1999 Chi-Chi (Taiwan) earthquake. *Geophysical Journal International*, 159(3):1112–1124.
- Shigematsu, N., Fujimoto, K., Ohtani, T., and Goto, K. (2004). Ductile fracture of fine-grained plagioclase in the brittle-plastic transition regime: implication for earthquake source nucleation. *Earth and Planetary Science Letters*, 222:1007–1022.
- Shimamoto, T., Kanaori, Y., and Asai, K.-I. (1991). Cathodoluminescence observations on low-temperature mylonites: potential for detection of solution-precipitation microstructures. *Journal of Structural Geology*, 13(8):967–973.
- Sibson, R. (1977). Fault rocks and fault mechanisms. *Journal of the Geological Society of London*, 133:191–213.
- Sleep, N. (1994). Grain size and chemical controls on the ductile properties of mostly frictional faults at low temperature hydrothermal conditions. *Pure and Applied Geophysics*, 143:41–60.
- Snoke, A. and Tullis, J. (1998). An overview of fault rocks. In Snoke, W., Tullis, J., and Todd, V. R., editors, *Fault Related Rocks, a Photographic Atlas*, page 318. Princeton University Press, Princeton, New Jersey.
- Stesky, R., Brace, W., Riley, D., and Robin, P.-Y. (1974). Friction in faulted rock at high temperature and pressure. *Tectonophysics*, 23:177–203.
- Stewart, M., Holdsworth, R., and Strachan, R. (2000). Deformation processes and weakening mechanisms within the frictional-viscous transition zone of major crustal-scale faults: insights from the Great Glen fault zone, Scotland. *Journal of Structural Geology*, 22:543–560.
- Stipp, M., Stünitz, H., Heilbronner, R., and Schmid, S. (2002). The eastern Tonale fault zone: a 'natural laboratory' for crystal plastic deformation of quartz over a temperature range from 250 – 700 °C. *Journal of Structural Geology*, 24:1861–1884.

- Stipp, M. and Tullis, J. (2003). The recrystallized grain size piezometer for quartz. *Geophysical Research Letters*, 30(21):SDE3-1, doi:10.1029/2003GL018444.
- Storti, F., Billi, A., and Salvini, F. (2003). Particle size distributions in natural carbonate fault rocks; insights for non-self-similar cataclasis. *Earth and Planetary Science Letters*, 206(1-2):173.
- Stünitz, H., Fitz-Gerald, J., and Tullis, J. (2003). Dislocation generation, slip systems, and dynamic recrystallization in experimentally deformed plagioclase single crystals. *Tectonophysics*, 372:215-233.
- Stünitz, H. and Tullis, J. (2001). Weakening and strain localization produced by syn-deformational reaction of plagioclase. *International Journal of Earth Sciences*, 90:136-148.
- Takahashi, M., Nagahama, H., Masuda, T., and Fujimura, A. (1992). Fractal analysis of experimentally, dynamically recrystallized quartz grains and its possible application as a strain rate meter. *Journal of Structural Geology*, 20(2/3):269-275.
- Takahashi, M., Nagahama, H., Masuda, T., and Fujimura, A. (1998). Fractal analysis of experimentally, dynamically recrystallized quartz grains and its possible application as a strain rate meter. *Journal of Structural Geology*, 20(2/3):269-275.
- Takeshita, T. and Yagi, K. (1999). Dynamic analysis based on 3-D orientation distribution of microcracks in quartz from the Cretaceous granodiorite core samples drilled along the Nojima fault, southwest Japan. In Ito, H., Fujimoto, K., Tanaka, H., and Lockner, D., editors, *Proceedings of the international workshop on the Nojima fault core and borehole data analysis*, volume GSJ Interim report No. EQ/00/1, USGS Open-File Report 000-129, pages 133-140. Geological Survey of Japan, Tsukuba, Japan.
- Tapponnier, P. and Francheteau, J. (1978). Necking of the lithosphere and the mechanics of slowly accreting plate boundaries. *Journal of Geophysical Research*, 83n:3955-3970.
- Tenthorey, E. and Cox, S. (2006). Cohesive strengthening of fault zones during the interseismic period: An experimental study. *Journal of Geophysical Research*, 111:doi:10.1029/2005JB004122.
- Tenthorey, E., Cox, S., and Todd, H. (2003). Evolution of strength recovery and permeability during fluid-rock reaction in experimental fault zones. *Earth and Planetary Science Letters*, 206:161-172.
- Ter Heege, J., De Bresser, J., and Spiers, C. (2005). Rheological behaviour of synthetic rocksalt: the interplay between water, dynamic recrystallization and deformation mechanisms. *Journal of Structural Geology*, 27:948-963.
- Tsutsumi, A. (1999). Size distributions of clasts in experimentally produced pseudotachylytes. *Journal of Structural Geology*, 21:305-312.
- Tullis, J. and Yund, R. (1977). Experimental deformation of dry Westerly Granite. *Journal of Geophysical Research*, 82(36):5705-5718.
- Tullis, J. and Yund, R. (1980). Hydrolytic weakening of experimentally deformed Westerly Granite and Hale Albite rock. *Journal of Structural Geology*, 2(4):439-451.
- Tullis, J. and Yund, R. (1987). Transition from cataclastic flow to dislocation creep of feldspar: Mechanisms and microstructures. *Geology*, 15:606-609.
- Tullis, J. and Yund, R. (1992). The brittle-ductile transition in feldspar aggregates: An experimental study. In Evans, B. and Wong, T.-f., editors, *Fault Mechanics and transport properties of Rocks*, pages 89-117. Academic Press, San Diego.

- Tullis, T. and Tullis, J. (1986). Experimental rock deformation techniques. In Hobbs, B. and Heard, H., editors, *Mineral and rock deformation: Laboratory Studies - The Paterson Volume*, volume 36, pages 297–324. AGU Geophysical Monograph.
- Turcotte, D. (1986). Fractals and fragmentation. *Journal of Geophysical Research*, 91(1921–1926).
- Turcotte, D. (1992). *Fractals and chaos in geology and geophysics*. University Press, Cambridge.
- Underwood, E. (1970). *Quantitative stereology*. Addison-Wesley series in metallurgy and materials. Addison-Wesley Publishing Company, Reading, Massachusetts.
- Ustaszewski, K., Schumacher, M., and Schmid, S. (2005). Simultaneous normal faulting and extensional flexuring during rifting: an example from the southernmost Upper Rhine Graben. *International Journal of Earth Sciences*, 94(4):680–696.
- van Daalen, M., Heilbronner, R., and Kunze, K. (1999). Orientation analysis of localized shear deformation in quartz fibres at the brittle-ductile transition. *Tectonophysics*, 303(1–4):83–107.
- Vernooij, M. (2005). *Dynamic recrystallisation and microfabric development in single crystals of quartz during experimental deformation*. PhD thesis, ETH Zurich.
- Vernooij, M., Kunze, K., and Den Brok, B. (2006). 'Brittle' shear zones in experimentally deformed quartz single crystals. *Journal of Structural Geology*, 28:1292–1306.
- Vincent, M. W. and Ehlig, P. L. (1988). Laumontite mineralization in rocks exposed north of the San Andreas fault at Cajon Pass, southern California. *Geophysical Research Letters*, 15:977–980.
- Voisin, C., Renard, F., and Grasso, J. (2007). Long-term friction: From stick-slip to stable sliding. *Geophysical Research Letters*, 34:L13301, doi:10.1029/2007GL029715.
- Werner, W. and Franzke, H. (2001). Postvariszische bis neogene Bruchtektonik und Mineralisation im südlichen Zentralschwarzwald. *Zeitschrift der deutschen Geologischen Gesellschaft*, 152(2–4):405–437.
- White, S. (1982). Fault rocks of the Moine thrust zone: a guide to their nomenclature. *Textures and microstructures*, 4:211–221.
- Wibberley, C. (1999). Are feldspar-to-mica reactions necessarily reaction-softening processes in fault zones? *Journal of Structural Geology*, 21:1219–1227.
- Wibberley, C. and Shimamoto, T. (2005). Earthquake slip weakening and asperities explained by thermal pressurisation. *Nature*, 436:689–692.
- Wilson, B., Dewers, T., Reches, Z., and Brune, J. (2005). Particle size and energetics of gouge from earthquake rupture zones. *Nature*, 434:749–752.
- Wilson, C. and Bell, I. (1979). Deformation of biotite and muscovite: optical microstructure. *Tectonophysics*, 58:179–200.
- Wilson, J., Chester, J., and Chester, F. (2003). Microfracture analysis of fault growth and wear processes, Punchbowl Fault, San Andreas system, California. *Journal of Structural Geology*, 25(11):1855–1873.
- Wintsch, R. (1975). Solid-fluid equilibria in the system $\text{KAlSi}_3\text{O}_8\text{-NaAlSi}_3\text{O}_8\text{-Al}_2\text{SiO}_5\text{-SiO}_2\text{-H}_2\text{O-HCl}$. *Journal of Petrology*, 16(1):57–79.

- Wintsch, R., Christoffersen, R., and Kronenberg, A. (1995). Fluid-rock reaction weakening of fault zones. *Journal of Geophysical Research*, 100(B7):13021–13032.
- Wirth, G. (1984). Kleintektonische Untersuchungen im Grund- und Deckgebirge des Südostschwarzwaldes (Baden-Württemberg). *Arbeiten des Instituts für Geologie und Paläontologie Universität Stuttgart*, 78:85–136.
- Wise, D., Dunn, D., Engelder, J., Geiser, P., Hatcher, R., Kish, S., Odom, A., and Schamel, S. (1984). Fault-related rocks: Suggestions for terminology. *Geology*, 12:391–394.
- Wittenbecher, M. (1992). Geochemie tholeiitischer und alkaliolivinbasaltischer Gesteine des Vogelsberges. *Geologische Abhandlungen Hessen*, 97:52.
- Xie, Z. and Walther, J. (1993). Quartz solubilities in NaCl solutions with and without wollastonite at elevated temperatures and pressures. *Geochimica et Cosmochimica Acta*, 57:1947–1955.
- Yamaguchi, T., Yamamoto, M., Nagao, T., and Goto, S. (1999). Temperature monitoring in a borehole drilled into the Nojima fault and radioactive heat production of core samples. In Ito, H., Fujimoto, K., Tanaka, H., and Lockner, D., editors, *Proceedings of the international workshop on the Nojima fault core and borehole data analysis*, volume GSJ Interim report No. EQ/00/1, USGS Open-File Report 000-129, pages 277–282. Geol. Surv. Japan, Tsukuba, Japan.
- Yamamoto, Y., Kurita, H., and Matsubara, T. (2000). Eocene calcareous nannofossils and dinoflagellate cysts from the Iwaja Formation in Awajishima Island, Hyogo Prefecture, southwest Japan. *Journal of the Geological Society of Japan (in Japanese with English abstract)*, 106:379–382.
- Yoshinobu, A. and Hirth, G. (2002). Microstructural and experimental constraints on the rheology of partially molten gabbro beneath oceanic spreading centers. *Journal of Structural Geology*, 24:1101–1107.
- Yund, R., Blanpied, M., Tullis, T., and Weeks, J. (1990). Amorphous material in high strain experimental fault gouge. *Journal of Geophysical Research*, 95,(B10):15589–15602.
- Zen, E. and Thompson, A. (1974). Low grade regional metamorphism: Mineral equilibrium relations. *Annual Review of Earth and Planetary Sciences*, 2:197–212.
- Ziegler, P. and Dèzes, P. (2005). Evolution of the lithosphere in the area of the Rhine rift system. *International Journal of Earth Sciences*, 94(4):594–614.

Presentations

Own presentations:

- Keulen, N., Stünitz, H., Heilbronner, R., Ramseyer, K., Healing mechanisms and healing period of granitoid fault gouge at hypocentre depth pT-conditions, Abstr. Vol. Swiss Geoscience Meeting, 2006 (poster)
- Keulen, N., Stünitz, H., Heilbronner, R., Healing rates of natural and experimental granitoid fault gouges, Geophys. Res. Abstr. V8, EGU-A07900, 2006 (oral)
- Keulen, N., Heilbronner, R., Stünitz, H., Ramseyer, K., Microstructures of healed granitoid fault gouge - a combination of cathodoluminescence and BSE-contrast SEM Imaging, Geophys. Res. Abstr. V8, EGU-A08088, 2006 (poster)
- Keulen, N., Stünitz, H., Heilbronner, R., Deformation and Healing Processes in granitoid Fault Rock in Experiments and Nature. Geophys. Res. Abstr. V7, EGU-A10000, 2005 (oral)
- Keulen, N., Heilbronner, R., Stünitz, H., Interaction of cataclasis and healing processes in experimental and natural fault gouge. DRT abstract volume p. 122, 2005 (oral)
- Keulen, N., Heilbronner, R., Stünitz, H., Preservation of fault rocks and their microstructures. Abstr. Vol. Swiss Geoscience Meeting, 2004 p. 208 (oral)
- Keulen, N., Stünitz, H., Heilbronner, R. Grain size evolution in wet experimentally deformed granitoids. Gordon Conference Mt. Holyoke, MA, USA, 2004 (poster)
- Keulen, N., Stünitz, H. and Heilbronner, R., The influence of temperature, time fluids and strain on the texture of caclasites: grain size reduction versus grain growth in experimentally deformed granitoids, Terra Nostra, 01, 2004, p. 43 (oral)
- Keulen, N., Stünitz, H. and Heilbronner, R., The influence of temperature, time, fluids and strain on the texture of caclasites: grain size reduction versus grain growth in experimentally deformed granitoids, Lithos, Vol. 73, 1-2, p S57, 2004 (oral)
- Keulen, N., Heilbronner, R., Stünitz, H., Microstructural comparison of Black Forest Variscan fault rocks with recent seismogenic fault rocks (San Andreas, Nojima): Earthquakes in the Black Forest? Eucor-Urgent meeting Abstr. Vol. p. 28, 2003, (oral)
- Keulen, N., Heilbronner, R., Stünitz, H., What happens after fracturing? Particle size reduction and annealing in experimentally deformed granitoid and diabase, Abstr. Vol. Swiss Geoscience Meeting, 2003 p. 54 (poster)
- Keulen, N., Stünitz, H., Heilbronner, R. Microstructures and grain size distribution of natural and experimentally deformed polyphase cataclasites - some preliminary results, DRT Abstr. Vol. p. 93. 2003 (poster)
- Keulen, N., Stünitz, H., Heilbronner, R., Grain size distribution and microstructures of granitoid cataclasites, Lithos, Vol. 71, 1-2, 2002

Presentations by other persons:

- Heilbronner, R.(*), Keulen, N.T. and Stünitz, H. Mapping grain size distributions and surface density in experimentally faulted granitoids, *Eos Trans. AGU*, 87(52), Fall Meet. Suppl., Abstract T43A-1631 (poster)
- Keulen, N., Heilbronner, R., and Stünitz, H.(*), Fault gouge healing in granitoid rocks, *Eos Trans. AGU*, 87(52), Fall Meet. Suppl., Abstract S33B-0240, 2006 (poster)
- Stünitz, H.(*), Keulen, N., Heilbronner, R., Healing of cataclastic rocks in nature and experiment, AOGS conf. AO308, 2006 (oral)
- Stünitz, H., Keulen, N., Heilbronner, R., Rupture and gouge formation in fault zones - a two-stage process? *Geophys. Res. Abstr.* V8, EGU-A07914, 2006 (poster)
- Keulen, N. Stünitz, H., Heilbronner, R.(*), Grain scale processes during cataclasis and healing in granitoid fault rocks: results from experiments and nature, AGU-Fall meeting, EOS Abstr. nr. 7313, 2005 (oral)
- Heilbronner, R., Keulen, N., Boullier, A.-M., Grain shape factors for natural and experimental fault rocks. DRT abstract volume p. 110, 2005 (poster)
- Heilbronner, R., Keulen, N., Shape Analysis of experimental and natural fault rocks. *Geophys. Res. Abstr.* V7, 09915, 2005 (poster)
- Dresmann, H., Keulen, N., Ustaszewski, K., Kock, S., Hinsken, S., Timar-Geng, Z., Wetzell, A., Heilbronner, R., Fügenschuh, B., Stünitz, H., Palaeo- earthquakes in the southern Black-Forest, *Abstr. Vol. Swiss Geoscience Meeting*, 2004 p. 121 (poster)
- Keulen, N., Stünitz, H.(*), Heilbronner, R., Seismic or aseismic? Grain size reduction and grain growth in naturally and experimentally fractured granitoids. *Abstr. IGC Florence*, 2004 (oral)
- Boullier A.M.(*), Fujimoto, K., Ito, H., Ohtani, T., Amitrano, D., Fabbri, O., Keulen, N., Pezard, P. Structural evolution of the Nojima fault, Awaji Island, Japan, Inland seismics conference *Abstr. Vol.*, 2004 (oral)

Curriculum Vitae

Name: Nynke Thera Keulen
Nationality: Dutch
Date of Birth: 24 March 1978
City of Birth: Leeuwarden, Netherlands

Education:

- Geological Institute, University of Basel, Switzerland, 2001-2006.
PhD in Natural Sciences,
Area of specialization: Microstructures of Fault Rocks
Doctoral Research Supervisors: Renée Heilbronner, Holger Stünitz (Basel)
- Faculty of Earth Sciences, University of Utrecht, Netherlands, 1996-2001:
Master in Earth Sciences, 2001
Master Thesis: "*Force of crystallisation of gypsum during the hydration of synthetic anhydrite rock.*"
Supervisors: Bas den Brok (ETH, Zurich), Chris Spiers (Utrecht)
- Department of Earth Sciences, ETH Zurich, Switzerland, 1999-2000,
Exchange year (14 months)
- ExxonMobil Chemical, Machelen, Belgium, 2001, Internship (3 months),
Calibration of EDX on TEM and SEM for use on zeolites
Supervisors: Anton-Jan Bons (ExxonMobile), Martyn Drury (Utrecht)
- Secondary school: Christelijk Gymnasium, Leeuwarden, 1990-1996.